Kinetic investigation of the impulsive penetration mechanism of 2D plasma elements into the Earth's magnetosphere

Marius M. Echim

May 3, 2004

Părinţilor mei

"The forest hides the trees for those who think that they disengage themselves from atomistics by the consideration of differential equations"

Ludovic Boltzmann, *1905*

FOREWORD

At the beginning I wish to express my sincere gratitude to the persons who have continuously and actively supported my work during the time spent to accomplish the scientific mission of this thesis.

I should probably never had realized the strength of the kinetic theory without meeting Professor Joseph Lemaire. I thank him for his careful guidance in the world of kinetics, for his patience and understanding and for all the things he encouraged me to discover on my own. I am grateful for his ongoing support and generosity and for helping me to "fulfill my dream", comme Jacques Brel le disait. To Professor Lemaire and to Madame Lemaire I owe many wonderful moments spent in Belgium, that helped me feel comfortable away from my home country.

I am much indebted to those who at the Belgium Institute for Space Aeronomy in Brussels have helped me in many respects during my research stages there. I thank Professor Paul Simon, the Director of BISA, for his long term hospitality. My thanks go also to Vivianne Pierrard for her solidarity and for many discussions giving me valuable clues concerning the kinetic theory. I thank all the colleagues at BISA, Fabien Darouzet, Hervé Lamy, Vladimir Cadez, Daniel Heyndericks, Bart Quaghebeur, Johan DeKeyzer, Michel Kruglanski for their friendship. It is due to Leonardo Fedullo that the data of my kinetic models was never lost. The help of Mr. Edwin Rigo was decisive for building the reference data.

I am most grateful to Dr. Michel Roth who always found the time to read carefully and repeatedly my research notes. This way he contributed significantly to the improvement of my thesis.

I am very grateful to Professors Ghislain Grégoire, Jean-Pierre Antoine, Guy Schayes, Pierre Defrance and Tom Chang for accepting being members of the Jury.

Part of this work was carried on in Romania and at the Institute for Space Sciences in Bucharest. I thank my colleagues Horia Comişel, Octav Marghitu, Dragoş Constantinescu, Adrian Blăgău and Mircea Ciobanu for believing in our small Group of Magnetometry and Space Plasma. Their commitment to genuine research made things easier.

Without the encouragements, patience and confidence offered generously and continuously by my family I would have never been here. I thank them all, Corina especially for the grace, generosity and beauty she brings into our life. I thank my parents for all the things they taught me. This work is a tribute to their honesty and faith.

SUMMARY

In this thesis I investigate the dynamics of charged particles and plasma into non-uniform distributions of the electric and magnetic fields.

In the first part attention is focused on the motion of test particles. The interaction between particles as well as the perturbations they might produce to the external charge and current density is neglected. I investigate a distribution of the magnetic field that depends on only one spatial coordinate, x, with the B_x component of the magnetic field being equal to zero everywhere, like in tangential discontinuities. The magnetic vector, $\boldsymbol{B}$, can rotate across the discontinuity by an angle $\alpha \in [0^0, 180^0]$. In addition to the B-field distribution I assumed different distributions of the electric field, $\boldsymbol{E}$, with $E_x = 0$. I have considered three cases: (A) a uniform electric field; (B) a non-uniform electric field perpendicular everywhere to $\boldsymbol{B}$ and conserving the zero order drift, and (C) a non-uniform electric field, perpendicular everywhere to $\boldsymbol{B}$ and conserving the magnetic moment of the drifting particles. The particles are drifting into these steady state electromagnetic field distributions; their orbits together with the path of the first order guiding center are integrated numerically.

The numerical results show that the "antiparallel" distribution of the magnetic field (obtained when $\alpha = 180^0$) with $B = 0$ at $x = 0$ does not produce anomalous acceleration of the test-particle as assumed in some steady state reconnection models. Although the zero and first order guiding center approximations diverge where $B = 0$, the exact equation of motion is not singular, it can be integrated throughout the integration time. The mathematical singularity of the approximative solutions does not correspond to a "true" (physical) singularity of the exact equation of motion. When the magnetic field is sheared with a non-zero B_y-component, and $\boldsymbol{B}$ can rotate with respect to $\boldsymbol{E}$ (case A), the particle orbit is confined into a sheath centered onto the x-position where $\boldsymbol{B}$ becomes parallel to $\boldsymbol{E}$. Partial or total penetration of the test-particle is equally possible, as demonstrated for the E-field distributions of case B and case C. In case C the distance of penetration depends on the initial total energy of the test particles. Except for one of six different configurations considered, the reversal point of B_z does not correspond to a point of particle acceleration in the direction normal to $\boldsymbol{B}$ nor is the stopping point of the particle's motion in the direction normal to $\boldsymbol{B}$. Indeed, it is the relative orientation between $\boldsymbol{E}$ and $\boldsymbol{B}$, together with the

total initial energy of the particle that determine the distance of penetration across the sheared magnetic field distribution. Penetration into the region of non-uniform magnetic field produces separation of charges. Particles with the highest energy are deflected the most.

In the second part of the thesis I treat the dynamics of an "ensemble" of electrons and protons forming a plasma stream. The plasma flow is spatially two-dimensional. In this case the plasma "internal" contribution to the external fields is evaluated and self-consistently computed. The method adopted is the kinetic theory approximation of plasma physics instead of one-fluid magnetohydrodynamic (MHD) approximation or the Particle-In-Cell (PIC) generally used. Both the ensembles of electrons and protons are described by their velocity distribution function (VDF) that has to satisfy the Vlasov equation derived from the general Liouville theorem for a collisionless plasma. The VDFs are given in terms of the two constants of mechanical motion, the total energy, $\mathcal{H}$, and one canonical momentum, p_x. The first adiabatic invariant, μ - the magnetic moment which is almost conserved when the Alfven conditions are satisfied, approximates a third constant of motion. I have found a velocity distribution function that describes a plasma moving in the Ox direction with a two-dimensional bulk velocity $V_x(y, z)$ depending both on y and z. The moments of the VDFs of electrons and ions were computed analytically. The self-consistent electromagnetic potentials are found by solving the Maxwell equations and the plasma quasineutrality equation. The partial current densities, $j_x(y, z)$, determined by the first order moments of the VDFs were introduced into Ampere's equation in order to compute $A_x(y, z)$, the component of the magnetic vector potential. The charge densities of the component species, $q_\alpha n_\alpha$, determined by the zero order moments of the VDFs have been introduced into the quasineutrality equation, $\sum_\alpha q_\alpha n_\alpha = 0$, from which the distribution of the electric potential, $\Phi(y, z)$, is computed. The solutions for the electromagnetic potentials are found numerically.

I have obtained a kinetic model that describes a two-dimensional plasma stream whose perpendicular bulk velocity varies (or is sheared) both in the direction *normal* to the magnetic field (*perpendicular shear*) and *parallel* to the magnetic field (*parallel shear*). The parallel shear of velocity has never been modeled before using kinetic equations. On the other hand the two dimensional models proposed till now for the dynamics of magnetospheric plasma did not consider differential (or sheared) plasma motion across magnetic field lines.

Several kinetic solutions are given for two-dimensional plasma flows and for different values of asymptotic densities, temperatures and bulk velocity. The key-feature of these numerical models is the existence of a parallel component of the electric field, $E_{parallel}$. It is shown that the parallel electric field is sustained by the parallel shear of the perpendicular plasma velocity. The amplitude of the parallel electric field depends on the value of the magnetic-field-aligned gradient of the perpendicular plasma velocity and also on the relative density and temperature of the moving stream with respect to the background, stagnant plasma. This is a new mechanism to generate parallel electric fields that adds to the ones already described in the literature and that are discussed in part 2 of this Thesis.

In the kinetic models presented in the second part I have adopted a set of plasma densities and temperatures typical for the terrestrial magnetopause region. A parallel gradient of the density or electronic pressure enhances the intensity of the parallel electric field. The scale length of the boundary layer of transition from moving to stagnant regime can be of the order of the electron Larmor radius ("electron layer") or the proton Larmor radius ("proton layer"). The scaling of the boundary layer is determined by the relative orientation of the magnetic field and the plasma bulk velocity. $E_{parallel}$ is stronger in the case of Parallel Sheared Electron Layer than in the case of Parallel Sheared Proton Layer.

The existence of a parallel component of the electric field invalidates the MHD approximation. In the case of the two-dimensional plasma flow studied in this Thesis the MHD convection velocity, $\boldsymbol{U}_E = \boldsymbol{E} \times \boldsymbol{B}/B^2$ is not a satisfying approximation of the plasma bulk velocity, $\boldsymbol{V}$. I illustrate the differences between $\boldsymbol{U}_E$ (assigned in MHD approximations to a "frozen-in" motion of B-field lines) and $\boldsymbol{V}$ obtained by the kinetic models described in part 2. It is shown that the "de-freezing" is produced in those regions where a non-vanishing parallel electric field component was determined.

The kinetic treatment of the plasma dynamics adopted in this Thesis evidence kinetic effects disregarded in the one-fluid approximations: finite Larmor radius effects that are illustrated in Part I and non-MHD parallel electric fields that are described in Part II. These effects play an important role in the processes taking place at the magnetopause, the interface region between the solar wind and the terrestrial magnetosphere.

Contents

Introduction **1**

I Charged particles across sheared fields **11**

1 Equations for particle and fields **13**

1.1 Newton-Lorentz and first order drift 13
1.1.1 Larmor gyration 14
1.1.2 Alfvén conditions 14
1.1.3 Guiding center equation of motion 15
1.1.4 First order perpendicular drift 17
1.1.5 First order parallel drift 18
1.2 Electric and magnetic fields distribution 18
1.2.1 B-field distribution 19
1.2.2 E-field distribution 20

2 Numerical orbits of test-particle **25**

2.1 **Case A**: uniform electric field 27
2.1.1 Antiparallel B-field distribution 27
2.1.2 Sheared B-field distribution 29
2.2 **Case B**: Non-uniform E-field conserving U_E 34
2.2.1 Antiparallel B-field distribution 34
2.2.2 Sheared B-field distribution 35
2.3 **Case C**: Non-uniform E-field conserving $\overline{\mu}$ 43
2.3.1 Antiparallel B-field distribution 44
2.3.2 Sheared B-field distribution 45
2.4 Summary and conclusions 51

II Kinetic treatment of sheared plasma flows 53

3 Kinetic model 55
3.1 Vlasov-Poisson-Ampere equations . . . 57
3.2 Equations governing fields . . . 58
3.2.1 Flow and field geometry . . . 58
3.2.2 Maxwell's equation . . . 60
3.2.3 Asymptotic values. Boundary conditions . . . 61
3.3 Kinetic solution 2D . . . 65
3.3.1 Constants of motion . . . 66
3.3.2 Asymptotic values of VDF . . . 67
3.3.3 Solution of Vlasov equation . . . 68
3.4 Moments of the VDF . . . 72
3.4.1 Accessibility condition . . . 73
3.4.2 Densities . . . 79
3.4.3 Currents . . . 81
3.4.4 Bulk velocity . . . 83

4 Vlasov numerical models 85
4.1 Numerical method . . . 86
4.2 Sestero Tangential Discontinuity . . . 89
4.2.1 SETD . . . 90
4.2.2 SPTD . . . 95
4.3 $2D$ sheared flow: solutions . . . 99
4.3.1 PSEL1 . . . 100
4.3.2 PSEL2 . . . 111
4.3.3 PSEL3 . . . 115
4.3.4 PSPL1 . . . 118
4.3.5 PSPL2 . . . 124
4.3.6 PSPL3 . . . 128
4.4 Decoupling of plasma motion . . . 132
4.5 Conclusions and comments . . . 137

5 Comparison with previous results 141
5.1 Kinetic models . . . 141
5.2 Kinetic (PIC) simulations . . . 142
5.3 MHD models and numerical simulations . . . 146

6 Summary and perspectives 149

References 155

APPENDIX **169**

Scaling factors **171**

Analytical moments of the truncated VDF **173**

Analytical moments of the nontruncated VDF **177**

Fifth-order Runge Kutta integrator of ODE **179**

Gauss-Seidel iterative method **181**

Bracketing and bisection method **185**

Introduction

Plasma dynamics and its self-consistent interaction with non-uniform electric and magnetic fields is a topic of interest for the theoretical investigator as well as for the laboratory experimenter and the space physicist. Laboratory experiments and in-situ measurements of plasma parameters in space contribute to accumulate large collection of data that can be used to study the value and evolution in time for a broad range of physical parameters characterizing the plasma state like : Debye length, screened free mean path, plasma frequency, (Larmor) gyration radius, etc.

The aim of this work is to investigate the electrodynamics of a non-uniform, classical, sub-Alfvenic plasma flow in the presence of an external magnetic field. I have been led into this field of investigation by my interest in understanding the physical processes that take place at the interface between the solar wind and the Earth's magnetosphere.

Solar Wind, Magnetosphere, Magnetopause

The plasma stream ejected continuously from the Sun, the *solar wind*, convects through interplanetary space with supersonic/super-alfvenic velocities ranging from 350 km/s to 1000 km/s. At 1 AU the solar wind "collides" with the obstacle formed by the geomagnetic field and the terrestrial plasma shell - the *magnetosphere*. A bow shock is formed that slows down the plasma to a subsonic/sub-alfvenic regime. It is this "shocked" plasma stream that "flows" quasi-permanently over the outer layers of the magnetosphere.

The latter takes an elongated shape, having a long tail in the antisunward direction as illustrated schematically in figure 1. In the antisunward direction the magnetosphere extends beyond $200 - 300$ Earth radii (R_E) while in the sunward direction the magnetosphere extends to $10 - 15$ R_E. The "lateral" extension of the magnetosphere, in the plane $(YOZ)_{GSE}$ [1] is equal

[1] the GSE reference system is determined by the Sun-Earth direction (Ox), the Earth's axis of rotation (Oz) and the normal on the plane determined by the two directions.

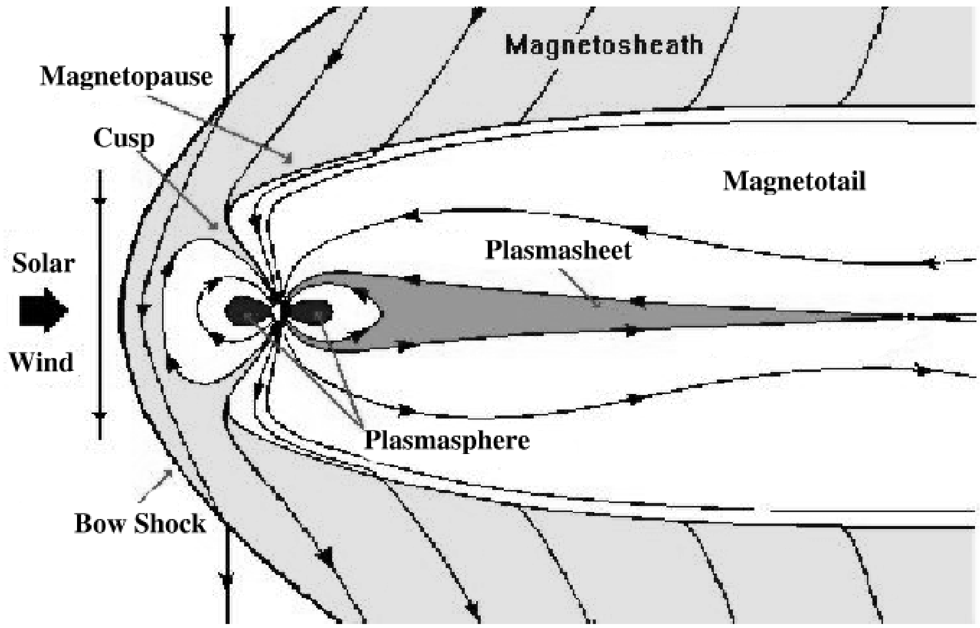

Figure 1: Schematic illustration of a meridional, $(xOz)_{GSE}$, cross section through the main magnetospheric regions.

to 20-25 R_E. The outer boundary of the magnetosphere is a 3D surface - the *magnetopause*.

The inner boundary of the magnetosphere is the electrically conducting ionosphere - the ionized layer on top of the neutral atmosphere. At lower magnetospheric altitudes the gravitational force plays an important role in determining the distribution of the cold ionospheric plasma versus altitude. At higher altitudes the role of gravity diminishes and the most significant forces of the system are of electromagnetic origin. Therefore, a proper assessment of the electric and magnetic fields at high altitudes is essential.

The plasma density in the magnetosphere (in the region Earthward of the magnetopause) is of the order of 5 cm^{-3}, approximately ten times smaller than upstream, in the magnetosheath. The temperature in the outer parts of the magnetosphere is of the order of 10^2 eV, i.e. one order of magnitude larger than in the magnetosheath. The value of the magnetic induction at the magnetopause is of the order of 10 nT. In a plasma with average parameters defined above the screened free mean path between two binary collisions is approximately equal to $L_{DH} = 346.000.000$ km (or $\approx$ 54000 Earth radii, or 2 AU); the screening distance of the Coulomb field due to collective effects (or the Debye length) is equal to $\lambda_D = 7,43$ m; the radius of gyration in the external magnetic field (or Larmor radius) of an electron is equal to

$r_{Le} = 1,06\ km$ while the proton Larmor radius is equal to $r_{Li} = 45,69\ km$.

Experimental data from laboratory and space

Some relevant laboratory experiments can illustrate globally the interaction of fast plasma stream with external magnetic fields and plasma. Their results are challenging and do not always support the standard predictions of the one-fluid, magnetohydrodynamic approximation of plasma physics.

The experiment of *Baker and Hammel* (1965), illustrated and briefly commented in figure 2, addresses the question whether the deflection of the solar wind plasma around the magnetosphere is mainly due to the effects of local magnetic forces on the impacting charged particles. The interaction of solar wind particles with the geomagnetic field was reviewed in the seminal papers of *Willis* (1975, 1978). The non-local effects of the conducting ionosphere short-circuiting the convection electric field in the external plasma stream is an additional mechanism that plays also a key role to stop the impacting solar wind plasma. Laboratory experiments that studied plasma convection across magnetic field were carried on successfully by *Bostick* (1956), *Demidenko et al.* (1967, 1969, 1972), *Wessel and Robertson* (1981), *Wessel et al.* (1988), *Dimonte et al.* (1991) and very recently by *Hurtig et al.* (2003).

On the other hand active experiments in the Earth's magnetosphere (*Haerendel et al.*, 1967; *Bernhard et al.*, 1987; *Kazeminezhad et al.*, 1993) provide data concerning the dynamics of artificial ion clouds injected above the Earth's ionosphere. The results show that the ion clouds drift across the geomagnetic field, experience deformations and eventually dissipate in the background plasma. There are many examples of artificial plasma clouds moving distances inside the magnetosphere orders of magnitude deeper than predicted by MHD theory or approximation of plasma physics. Indeed, optical observations show snapshots of artificial clouds "skidding" across geomagnetic field lines over distances in the range of 5 to 10 proton Larmor radius (*Delamere et al.*, 2002). The mechanism enabling the perpendicular drift is not fully understood.

Naturally occuring plasma irregularities or clouds have been detected in the inner magnetosphere and/or ionosphere (*Perkins et al., 1973*, *Zabuski et al., 1973*, *Kelley et al.*, 2003). There is increasing evidence (*Walbridge*, 1967; *Sperling and Glassman*, 1985; *Sperling*, 1986) that, as in the experiments of *Baker and Hammel* (1965), the kinetic energy of plasma irregularities drifting in the magnetosphere is Joule dissipated in the ionosphere, contrary to the models of plasma-field coupling proposed in MHD approximations (*Wright*, 1996).

Spacecraft observations put in evidence, upstream of the magnetopause, the existence of moving plasma structures, often called plasma or magnetic

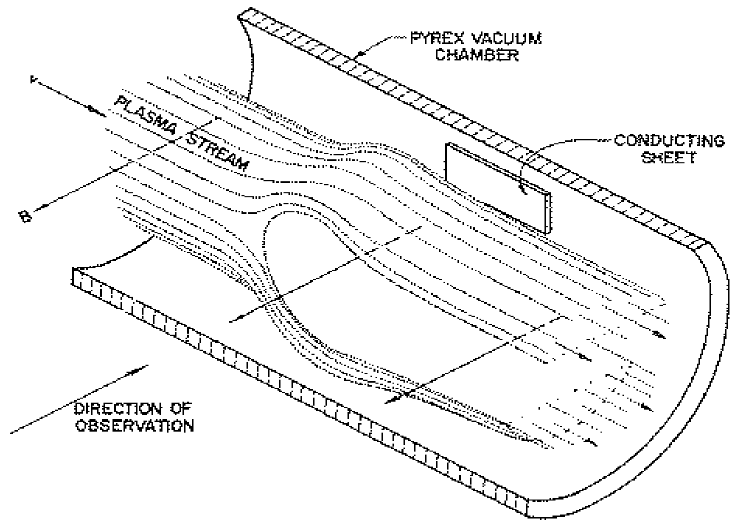

Figure 2: Laboratory experiment of *Baker and Hammel* (1965): a plasma flow injected normal to an external magnetic field into a vacuum chamber having insulating walls. An electrically conducting plate is attached to one of the walls. The stream is slowed down/stopped when it crosses the region where the magnetic field lines are connected to the conducting plate. Note the peculiar, elongated shape of the stream in the wedge of the conducting region resembling the Earth's magnetotail. Note that this tail is not formed by the presence of a non-uniform B-field distribution as in Birkeland Terella experiments or in *Demidenko et al.* (1967, 1969, 1972) ones.

clouds, with scale lengths comparable with the magnetospheric size (*Lepping et al.*, 1997; *Farrugia et al.*, 1998). Plasma irregularities with scales smaller than 1 R_E are also always present in the solar wind (see *Celnikier et al.*, 1987). The borders of these solar wind irregularities, large or smaller one, are the sites of sharp gradients in the plasma momentum density, number density, bulk velocity and higher order moments of the particle velocity distribution function, as well as gradients of the total magnetic field (*Burlaga*, 1971; *Burlaga and Lemaire*, 1977).

Kinetic and fluid treatment of plasma dynamics

In-situ satellite measurements in the transition region between magnetosheath and the magnetosphere show that the magnetopause has a thickness, l_{MP}, of the order of $500 - 1000$ km or $0.1 - 0.3$ R_E. Considering the range of plasma average temperature and density at the magnetopause the following inequality holds:

$$\lambda_L \ll r_{Le} < r_{Li} \approx l_{MP} \ll L_{DH} \tag{1}$$

where λ_L is the Debye length, r_{Le}, r_{Li} are the electron and ion Larmor radius respectively, L_{DH} is the screened mean free path. This shows that the plasma is collisionless and that the kinetic approximation holds to model the transport of plasma in this region.

Without collisions to randomize the thermal motion of particles there is no *a-priori* reason to treat the plasma at the magnetopause as a fluid. *Chew, Goldberger and Low* (1956) show that whenever the effects of *kinetic pressure* along magnetic field cannot be neglected (e.g . when there are significant gradients parallel to $\boldsymbol{B}$) the plasma must be treated kinetically and not in the fluid approximation. In the second part of this thesis an addition to this constrained will be discussed

Kinetic models of tangential discontinuities

Sestero (1964, 1965, 1966, 1967) pioneered the first kinetic models describing the E-field and B-field transition across discontinuities in monoionic collisionless plasmas when magnetic field lines are parallel to each other and the component of $\boldsymbol{B}$ normal to the discontinuity surface is equal to zero. The first application of kinetic models to tangential discontinuities (TD) observed in the solar wind plasma was proposed by *Lemaire and Burlaga* (1976) and *Burlaga and Lemaire* (1977). Their kinetic model of a TD extended *Sestero* collisionless model to take into account sheared B-field distributions where magnetic field lines rotate about $\boldsymbol{k}$ the normal to the TD's surface.

The one-dimensional model of *Roth* (1984) (see review in *Roth et al.*, 1996) is the first one in the literature that takes into account simultaneous large perpendicular shears of the plasma flow and of the B-field. Using this one-dimensional model and assuming an empirical model of the solar wind flow around the magnetopause based on satellite observations, *DeKeyzer and Roth* (1997a, 1997b, 1998) predicted which region of the magnetopause correspond to equilibrium configuration for a given B-field rotation.

The TD models of the magnetopause are only valid for steady state flow in the magnetosheath when the total pressure balance between inner and outer plasmas and fields has been achieved (*Mead and Beard*, 1964; *Schield*, 1967; *Sotirelis and Meng*, 1999). Satellite measurements show examples of magnetopause crossings for which the magnetopause can be approximated by a tangential discontinuity (*Papamastorakis*, 1984).

In "open" magnetospheric models geomagnetic field lines interconnect or reconnect over a larger portion of the magnetopause surface, $\boldsymbol{B} \cdot \boldsymbol{k} \neq 0$, and the magnetopause (MP) is then better approximated by a rotational discontinuity (RT). Experimental observations show also examples of MP crossings when the magnetopause can be approximated by a RT (*Lee and*

Kan, 1982; *Berchem and Russell*, 1982; *Sanchez and Siscoe* 1990; *Phan and Paschmann*, 1996a,b) . The kinetic solutions for the Vlasov equilibrium problem of a rotational discontinuity have not yet been resolved.

In MHD theories a TD is a nonpenetrable surface: mass and energy transport across this surface is not possible unless some instabilities disrupt the sheet and "open" it to the external flow (*Petchek*, 1964; *Kiendl et al., 1997*). In the view of MHD approximation a rotational discontinuity may be penetrable provided a peculiar, antiparallel magnetic field distribution exists at the magnetopause such that an anomalous process, called *magnetic reconnection*, may act to transfer plasma from outside into the magnetosphere (*Dungey*, 1961; *Vasyliunas*, 1975; *Pudovkin and Semenov*, 1985). The magnetic reconnection mechanism is based on the "frozen-in" field concept that implies complete coupling between the convection of plasma and "motion" of magnetic field lines.

Impulsive entry of plasma inside the magnetosphere

Lemaire (1977, 1985) and *Lemaire and Roth* (1978, 1991) have proposed the *impulsive penetration* mechanism as an non-steady state alternative process for the steady-state "closed" and "open" magnetospheric models under debate at that time (*Dungey*, 1961; *Axford and Hines*, 1961).

A magnetosheath plasma irregularity (or *plasmoid*) impacting on the magnetopause with an excess density and/or bulk velocity with respect to the background plasma has an excess of the tensor of the momentum flux density given by :

$$\Delta\overline{\overline{P}} = m\Delta n\boldsymbol{V}\boldsymbol{V} + mn\Delta\left(\boldsymbol{V}\boldsymbol{V}\right) + \Delta\overline{\overline{p}}$$

(in the rest of the Thesis vector quantities are notated with bold fonts; tensor variables are notated with a double bar on top). As a consequence of its excess momentum the plasma element penetrates the magnetopause and moves inside the magnetosphere. The polarization drift of ions and electrons sustains a polarization electric field that enables the forward motion (*Schmidt*, 1960, *Lemaire*, 1985).

Figure **3** shows a schematic view of the distribution of the electric field in the plane normal to the magnetic field. Inside the magnetosphere the plasmoid is braked by two competing processes: *(i)* adiabatic breaking due to the conservation of the average magnetic moment of ions and electrons (*Lemaire*, 1985) and *(ii)* non adiabatic (Joule) breaking by short circuiting of the polarization electric field in the resistive (ohmic) ionosphere (similar to the process simulated in the laboratory by *Baker and Hammel*, 1965). The

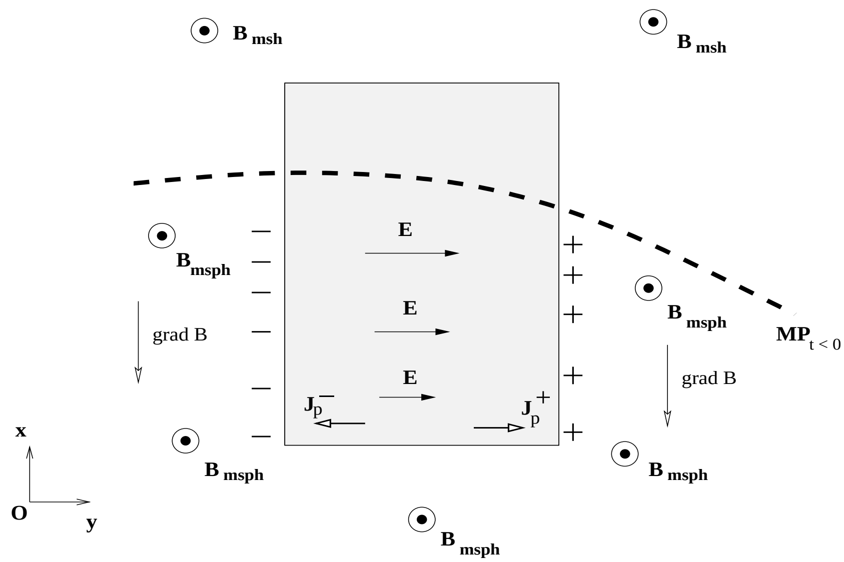

Figure 3: Schematic illustration of a cross (xOy) section through an impulsive penetrating plasmoid at the dayside magnetopause. Differential drifts (grad-B and polarization) sustain the convection electric field. Space charge layers can exist for time scales less than that associated with the depolarization rate. Adapted from *Echim and Lemaire* (2002a).

edges of the impacting plasmoid are sites of gradients of the velocity and/or density in direction parallel and perpendicular of the magnetic field.

The model of impulsive penetration is not constrained to the Chew-Goldberger-Low fluid approximation and does not rely on a peculiar magnetic field distribution. Reviews of the impulsive penetration model were proposed by *Lemaire and Roth* (1991) and *Echim and Lemaire* (2000).

Experimental data at high latitudes detected the propagation of magnetosheath plasma blobs across the magnetopause, inside the magnetosphere (*Lundin and Dubinin*, 1985; *Woch and Lundin*, 1992). A controversial fluid model of the impulsive penetration was proposed by *Heikkila* (1982, 1986).

Objectives of Part 1

The first part of the thesis is devoted to numerical integration of test-particle orbits injected in three different electric field distribution superimposed over a magnetic field distribution of a tangential discontinuity.

In *case A* the electric field is uniform and the magnetic field is sheared as in the steady-stade reconnection models. In *case B* we test a non-uniform distribution of $\boldsymbol{E}$ that conserves exactly the zero order drift. In *case C* the electric field distribution is non-uniform and conserves exactly the **average** (over the velocity distribution function) of the magnetic moment. The objectives of the section devoted to numerical integration of orbits are:

- to study the dynamics of the test-particle in regions where the magnetic field is equal to zero and to compare it with the dynamics of the corresponding first order guiding center;

- to identify the magnetic and electric field distribution that lead to a non-adiabatic acceleration of particles in a localized region where $B = 0$ and can therefore be called a region of reconnection or merging;

- to study the effect of magnetic shearing on the particle and guiding center orbits injected into non-uniform E-field distributions;

- to study the dynamics of test-particle and its corresponding first order guiding center injected into E-field distributions proposed theoretically by the model of the impulsive penetration.

Objectives of Part 2

The dynamics of test-particles is a first approximation to the plasma flow only when the particle density is very small and the binary and collective interactions between particles can be completely neglected. The orbits of individual charges can then be considered as “tracers” of the global dynamics of the collisionless rarefied plasma (*Longmire*, 1963; *Karlson*, 1962, 1963). In general, however, the collective interactions of plasma particles cannot be neglected and a self-consistent treatment must therefore be considered. This is precisely the objective of Part 2.

We give a self-consistent, kinetic description for a two-dimensional flow across a magnetic field distributions of a plasma formed by electrons and protons. The main objectives of Part 2 are :

- to find the velocity distribution function for each species, electron and proton, describing the transition from two-dimensional moving plasma to stagnant plasma regime;

- to compute analytically the moments of the VDF and to develop the appropriate numerical method to solve the Maxwell equations for computing the self-consistent electromagnetic potentials;

- to check the kinetic model and the numerical method by simulating the case of the one-dimensional Sestero Tangential Discontinuity;

- to compute the self-consistent distribution of the electric and magnetic potential, of the electric and magnetic field and of the plasma density and bulk velocity for boundary conditions corresponding to a non-uniform, two-dimensional plasma flow.

Part I

Motion of charged particles across sheared electric and magnetic fields

Chapter 1

Equation of motion and field distribution

This section describes the system of equations that will be integrated numerically as well as the electric and magnetic field distributions that will be used in these numerical experiments.

1.1 Equation of motion for charged particle and its associated guiding center

The equation of motion of a particle of mass m_α and electric charge q_α is given by:

$$\ddot{\boldsymbol{r}} = \frac{q_\alpha}{m_\alpha}\left(\boldsymbol{E} + \dot{\boldsymbol{r}} \times \boldsymbol{B}\right) + \boldsymbol{g} \tag{1.1}$$

where $\boldsymbol{r}$ is the position vector of the particle, $\boldsymbol{E}$ and $\boldsymbol{B}$ are the electric and magnetic fields (can be nonuniform and time-dependent), and $\boldsymbol{g}$ is the total non electromagnetic (in general gravitational) force per unit mass. An analytical solution of equation (1.1) for general non-uniform and non-stationary fields is generally not available. Throughout this study the non-electromagnetic force will be neglected as well as the time dependence of the electric and magnetic fields. Indeed in the region of the magnetopause the gravitational force and binary collisions can be neglected. The equation of motion (1.1) is solved numerically for different one-dimensional distributions of $\boldsymbol{E}$ and $\boldsymbol{B}$.

The magnetic field is assumed strong enough or the electric current density carried by the charge is small enough so that $\boldsymbol{B}$ is not perturbed by the current carried by the moving test particle. It is also assumed that $\boldsymbol{B}$ is not rapidly changing with time and in space, i.e. both types of Alfven conditions are satisfied. The electric field intensity is also assumed to be sufficiently weak such that E/B is much smaller than the velocity of the particle.

1.1.1 Larmor gyration

The simplest possible solution of equation (1.1) is found in the case of a vanishing electric field and a uniform and steady-state magnetic field. If the initial parallel velocity of a particle (whose species is indexed with α) is zero then its trajectory is two-dimensional: it is a circle confined in the plane perpendicular to $\boldsymbol{B}$ whose radius is equal to:

$$r_{L\alpha} = \frac{m_\alpha V_\perp}{q_\alpha B} \tag{1.2}$$

where m_α and q_α are the mass and charge of the particle. The period of gyration on the circle is equal to:

$$T_{L\alpha} = \frac{2\pi m_\alpha}{q_\alpha B} \tag{1.3}$$

If the particle has an initial non-zero velocity in the direction of $\boldsymbol{B}$ then the orbit is three-dimensional: it is a helix centered on a magnetic field line.

1.1.2 Alfvén conditions

It is *Alfven* (1940) who, inspired by the pioneering work of *Störmer* (1907, 1913), gave a first perturbative analysis of the dynamics of the charged particle in non-uniform magnetic field. In *Alfven*'s own words: "*... if a charged particle (mass=m, charge=e, energy $E = E_\parallel + E_\perp$) moves in a magnetic field H and* [conditions] *are satisfied, it is convenient to substitute the spiraling particle with a small >>equivalent magnet<< which is antiparallel to the magnetic field and has the moment*

$$\mu = \frac{E_\perp}{H}.$$

This moment remains constant during the motion" (*Alfven*, 1940). Alfven's small magnet has been later on called the "guiding center" of the particle's motion (*Alfven*, 1953). The instantaneous center of curvature of the trajectory (i.e. the center of the oscillatory circle tangent at each point to the actual trajectory) should not be confused with the guiding center which is the origin of a non-Galilean frame of reference.

The conditions that need to be fulfilled in order for the guiding center approximation to be valid were given by *Alfven* and are listed below:

1. very smooth spatial variation of the magnetic field with respect to the ion Larmor radius (first type of Alfven condition):

$$r_L|\boldsymbol{\nabla} B| \ll B \tag{1.4}$$

2. very slow time variation of B with respect to the Larmor period (second type of Alfven condition):

$$T_L \frac{dB}{dt} \ll B \tag{1.5}$$

3. the longitudinal advancement of the particle must be much smaller than the radius of curvature R of the magnetic line of force (third type of Alfven condition):

$$r_L \frac{v_\parallel}{v_\perp} \ll R \tag{1.6}$$

4. the non-magnetic force $\boldsymbol{g}$ must be much smaller than the Lorentz force (fourth type of Alfven condition):

$$mg \ll eBv_\perp \tag{1.7}$$

The conditions above outline the framework of Alfven's perturbative theory.

1.1.3 Guiding center equation of motion

The mathematical formalism for treating a classical perturbation theory existed before *Alfven*(1940). Indeed *Born* (1936) developed a formalism for treating quasi-periodic motions. More formal derivations of the guiding center approximation were proposed only later on by *Kruskal* (1962) and others. A deductive analysis starting from the first principles was given later by *Northrop* (1963), and this is the work that we will follow in treating the dynamics of the guiding center in the first order approximation.

The equation of motion of the guiding center is obtained by substituting in equation (1.1) the following expansion:

$$\boldsymbol{r} = \boldsymbol{r}_{gc} + \boldsymbol{r}_L \tag{1.8}$$

As illustrated by figure (1.1), $\boldsymbol{r}$ is the position of the particle, $\boldsymbol{r}_{gc}$ is the position of the guiding center (Alfven's "small magnet") and $\boldsymbol{r}_L$ is a vector from the guiding center's position to the particle position whose length is equal to the Larmor radius defined by (1.2). In the first order approximation the perpendicular component of the velocity of the particle in the guiding

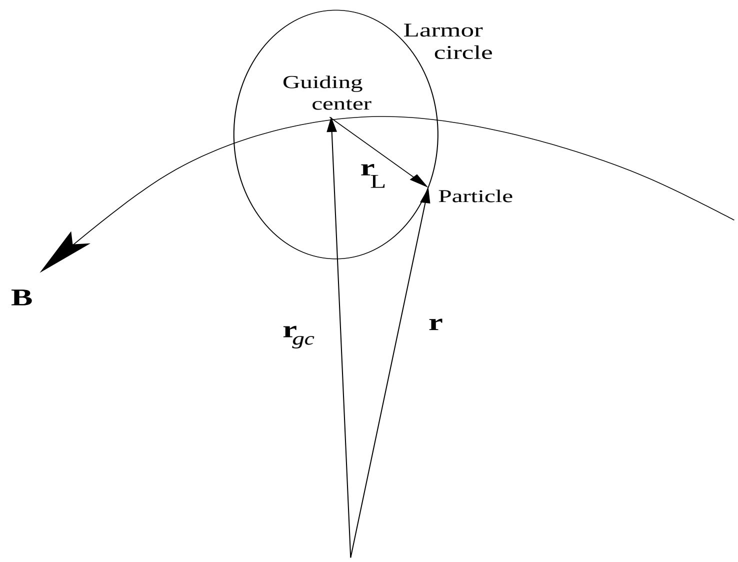

Figure 1.1: Guiding center position, Larmor radius and particle position with respect to the local magnetic field line. Adapted from *Northrop* (1963).

center frame is evaluated as the difference between particle's instantaneous velocity and the zero order drift velocity:

$$\boldsymbol{w}_{\perp}(\boldsymbol{r}) = \boldsymbol{v}_{\perp} - \boldsymbol{v}_{gc0\perp} \tag{1.9}$$

The vector Larmor radius is determined by:

$$\boldsymbol{r}_L = \left(\frac{m_\alpha}{q_\alpha B^2}\right) \boldsymbol{B} \times \boldsymbol{w}_{\perp} \tag{1.10}$$

Assuming that the Alfven conditions (1.4)-(1.7) are satisfied, r_L is much smaller than the scale of variation of $\boldsymbol{E}$ and $\boldsymbol{B}$. *Northrop* (1963) showed that the first order Taylor expansion of equation (1.1) about $\boldsymbol{r}_{gc}$ is given by:

$$\begin{aligned}\ddot{\boldsymbol{r}}_{gc} + \ddot{\boldsymbol{r}}_L = \frac{q_\alpha}{m_\alpha} \{ & \boldsymbol{E} + \boldsymbol{r}_L \cdot \boldsymbol{\nabla}\boldsymbol{E} + (\dot{\boldsymbol{r}}_{gc} + \dot{\boldsymbol{r}}_L) \times \\ & [\boldsymbol{B} + \boldsymbol{r}_L \cdot \boldsymbol{\nabla}\boldsymbol{B}]\} + \mathcal{O}(\epsilon^2)\end{aligned} \tag{1.11}$$

where $\mathcal{O}(\epsilon^2)$ defines second order terms in r_L/r.

In a reference system whose z-axis is parallel to $\boldsymbol{B}$, the Larmor circle is confined in the xOy plane. Since the average of $\boldsymbol{r}_L$, $\dot{\boldsymbol{r}}_L$ and $\ddot{\boldsymbol{r}}_L$ over a Larmor period is equal to zero, the average over a Larmor period of equation (1.11) is equal to:

$$< \ddot{\boldsymbol{r}}_{gc} >= \frac{q_\alpha}{m_\alpha} [\boldsymbol{E} + (< \dot{\boldsymbol{r}}_{gc} > \times \boldsymbol{B}(\boldsymbol{r}_{gc}))] - \frac{\mu_\alpha}{m_\alpha} \boldsymbol{\nabla} B + \mathcal{O}(\epsilon^2) \tag{1.12}$$

where $\mu_\alpha = m_\alpha {w_\perp}^2/2B$ is the magnetic moment. This is the basic differential equation that determines the acceleration of the guiding center's motion.

1.1.4 First order perpendicular drift

Taking the vectorial product of equation (1.12) with $\hat{\boldsymbol{b}}$, the unit vector parallel to $\boldsymbol{B}$ one obtains after some algebra:

$$< \dot{\boldsymbol{r}}_{gc,\perp} >= \frac{\boldsymbol{E}\times\hat{\boldsymbol{b}}}{B} + \frac{\mu_\alpha}{q_\alpha}\left(\frac{\hat{\boldsymbol{b}}\times\boldsymbol{\nabla}B}{B}\right) + \frac{m_\alpha}{q_\alpha}\left(\frac{< \ddot{\boldsymbol{r}}_{gc} > \times\hat{\boldsymbol{b}}}{B}\right) + \mathcal{O}(\epsilon^2) \quad (1.13)$$

where in the first order approximation $< \ddot{\boldsymbol{r}}_{gc} >$ the acceleration of the guiding center, is defined by:

$$< \ddot{\boldsymbol{r}}_{gc} >= \frac{d}{dt}\left[\frac{\boldsymbol{E}\times\hat{\boldsymbol{b}}}{B} + \hat{\boldsymbol{b}}\left(< \dot{\boldsymbol{r}}_{gc} > \cdot\hat{\boldsymbol{b}}\right)\right]$$

where $d/dt = \partial/\partial t + \boldsymbol{v}_{gc0\perp}\cdot\boldsymbol{\nabla}$ is the Lagrange derivative.

The first order drift in the direction perpendicular to the magnetic field is determined by :

$$< \dot{\boldsymbol{r}}_{gc,\perp} >= \frac{\boldsymbol{E}\times\boldsymbol{B}}{B^2} + \frac{m_\alpha {w_\perp}^2}{2q_\alpha B^3}\boldsymbol{B}\times\boldsymbol{\nabla}(B) + \frac{m_\alpha {v_\parallel}^2}{q_\alpha B^4}\boldsymbol{B}\times(\boldsymbol{B}\cdot\boldsymbol{\nabla})\boldsymbol{B} + \frac{m_\alpha v_\parallel}{q_\alpha B^3}\boldsymbol{B}\times(\boldsymbol{U}_E\cdot\boldsymbol{\nabla})\boldsymbol{B} + \frac{m_\alpha}{q_\alpha B^2}\boldsymbol{B}\times\frac{d}{dt}\left(\frac{\boldsymbol{E}\times\boldsymbol{B}}{B^2}\right) \quad (1.14)$$

The first term corresponds to the zero order (or *electric*) drift:

$$\boldsymbol{v}_{gc0\perp} = \boldsymbol{U}_E = \frac{\boldsymbol{E}\times\boldsymbol{B}}{B^2} \quad (1.15)$$

The following three terms in (1.14) are first order terms proportional to r_L or ϵ. The second term in (1.14) corresponds to the *gradient-B* drift, the third term and fourth term corresponds to the *inertial* drift. In stationary fields and when the electric field is weak the third term is dominant. It corresponds to the *curvature drift*. The curvature drift is identically equal to zero when magnetic field lines are straight lines as in TDs where $\boldsymbol{B}(x)$ is a function of x only. Indeed in this case $(\boldsymbol{B}\cdot\boldsymbol{\nabla})\boldsymbol{B}$ is equal to zero.

The last term in (1.14) corresponds to the polarization drift; it is often ignored in the first order guiding center approximation, when $v_{gc} \ll V_\perp$ (*Banos*, 1965). The polarization drift will be however considered here although it is a second order term and under some circumstances it may be small compared to the gradient-B drift and/or curvature drift. *Schmidt* (1960) and *Lemaire*

(1985) have emphasized that the small polarization drift is essential in transporting charges across magnetic field lines and producing inside the plasma an internal polarization electric field, $\boldsymbol{E}_p$, which is perpendicular to $\boldsymbol{B}$. It is only recently that the role of the polarization drift has been recognized by the MHD plasma physicists. *Vasyliunas* (2001) recognized that the polarization drift maintains the forward motion of plasma flows across magnetic fields and sustains the polarization electric field that drives the convection of plasma with the velocity $\boldsymbol{U}_E$ (eq. 1.15).

The values of $w_\perp$, $\boldsymbol{B}$ and $\boldsymbol{\nabla} B$ in (1.14) must be evaluated at the position of the guiding center, $\boldsymbol{r}_{gc}$, instead of the position $\boldsymbol{r}$ of the particle. The differences resulting from these approximations are second order corrections which will be neglected in the (first order) guiding center approach.

Note that for a planar, one-dimensional tangential discontinuity (TD) the gradient-B drift velocity is perpendicular to the magnetic field direction and parallel to the surface of the TD.

1.1.5 First order parallel drift

Generally the guiding center has also a non-zero parallel velocity in the direction of the magnetic field. Its value is found by computing the scalar product of equation (1.12) with $\hat{\boldsymbol{b}}$:

$$< \ddot{r}_{gc,\parallel} >= \frac{q_\alpha}{m_\alpha} E_\parallel - \frac{\mu_\alpha}{m_\alpha}\frac{\partial B}{\partial s} + \boldsymbol{U}_E \cdot \left(\frac{\partial \boldsymbol{b}}{\partial t} + v_{gc,\parallel}\frac{\partial \boldsymbol{b}}{\partial s} + \boldsymbol{U}_E \cdot \boldsymbol{\nabla b} \right) \qquad (1.16)$$

where $\boldsymbol{b}$ is the unit vector in the direction parallel to the magnetic field, s is the curvilinear coordinate along the magnetic field line and $\mu_\alpha = \frac{m_\alpha {V_\perp}^2}{2B}$ is the magnetic moment of the particle.

1.2 Electric and magnetic fields distribution

In the following we describe the magnetic and electric field distributions used in the numerical integration of test-particle trajectories. Inductive effects are disregarded, since the electromagnetic fields are assumed stationary in all our case studies. The contribution of the particle charge and drift to the space charge density and to the electric current density is assumed negligibly small everywhere.

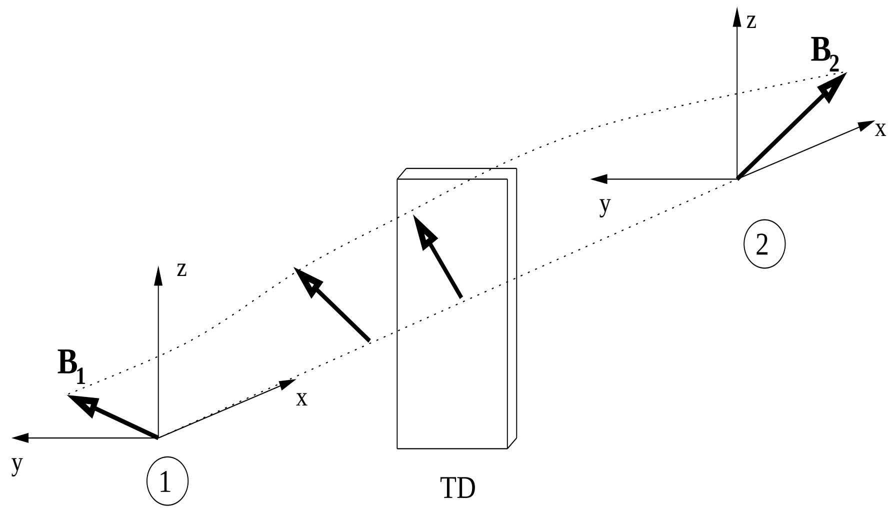

Figure 1.2: Sheared magnetic field across a tangential discontinuity (from *Roth et al.* 1996)

1.2.1 B-field distribution

We consider a stationary magnetic field that depends on a single spatial coordinate, x. Let us first consider a magnetic field distribution for which $B_x = 0$ and for which the components B_y and B_z are a function of x given by the following equation :

$$\boldsymbol{B}(x) = \frac{\boldsymbol{B}_1}{2} erfc\left(\frac{x}{L}\right) + \frac{\boldsymbol{B}_2}{2}\left[2 - erfc\left(\frac{x}{L}\right)\right] \tag{1.17}$$

where the complementary error function is defined by:

$$erfc(x) = \frac{2}{\sqrt{\pi}} \int_x^{\infty} e^{-t^2} dt \tag{1.18}$$

with $erfc(\infty) = 0$, $erfc(0) = 1$ and $erfc(-\infty) = 2$ (*Abramowitz and Stegun*, 1964). Here, $\boldsymbol{B}_1$ and $\boldsymbol{B}_2$ correspond to the magnetic intensity at $x = -\infty$ and $x = +\infty$ respectively. At $x = 0$, $\boldsymbol{B} = \frac{1}{2}(\boldsymbol{B}_1 + \boldsymbol{B}_2)$. The B_y and B_z components of $\boldsymbol{B}_1$ and $\boldsymbol{B}_2$ can both be different from zero.

This particular dependence of $\boldsymbol{B}$ on x is not essential for this study; it is dictated by the need to use a mathematically simple model of a sheared B-field distribution. The magnetic field distribution adopted here is similar to that of a tangential discontinuity (TD) for which the value L is the characteristic scale length (along the x-axis) over which the B-field components change significantly. The B-field distribution is prescribed, it is not computed self-consistent as in the kinetic models of *Sestero* (1964), *Lemaire and*

Burlaga (1976), *Roth* (1978, 1984), *Lee and Kan* (1979), *Roth et al.* (1996) or in chapter 4 of this thesis.

The magnetic field distribution assumed in steady state reconnection theories can be considered as a limiting ideal case for which the magnetic field changes from $\boldsymbol{B}_1$ at $x = -\infty$ to $\boldsymbol{B}_2 = -\boldsymbol{B}_1$ at $x = +\infty$ and becoming equal to zero at $x = 0$, i.e. inside a neutral sheet where $\boldsymbol{B} = 0$; this neutral sheet corresponds to the neutral line generally considered in reconnection models, e.g. the "open" magnetospheric model of *Dungey* (1961).

1.2.2 E-field distribution

Let us first consider a uniform electric field, indeed is closest to the case considered in steady-state reconnection models.

<u>Case A</u>: uniform electric field

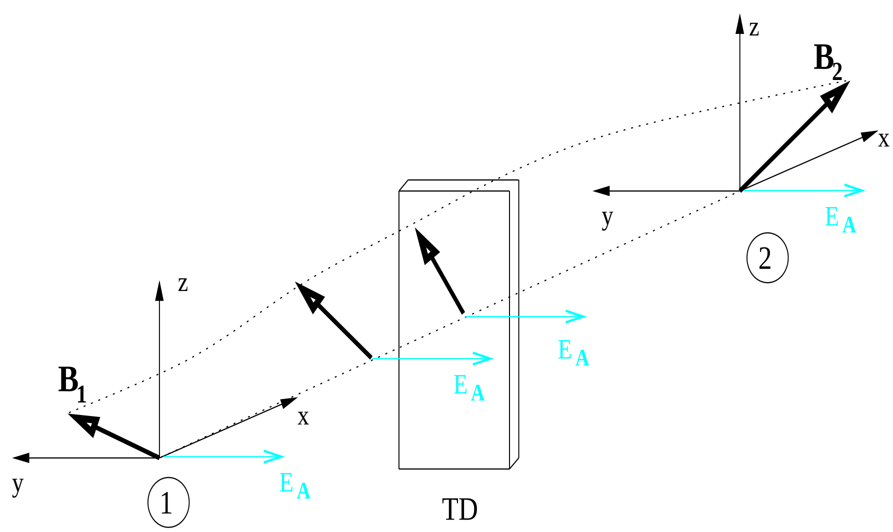

Figure 1.3: Superposition of a sheared magnetic field (illustrated by black arrows) of a tangential discontinuity and a uniform electric field (blue arrows).

The simplest electromagnetic field distribution is given by the superposition of a uniform electric field:

$$\boldsymbol{E}(x) = \boldsymbol{E}_A = ct. \tag{1.19}$$

and the "sheared" B-field distribution (1.17). This is an electromagnetic field distribution where the parallel component of $\boldsymbol{E}$ may have a nonzero component:

$$E_{\parallel} = \boldsymbol{E} \cdot \boldsymbol{B} \neq 0$$

i.e. when one of the condition on which MHD theories are based is violated and when reconnection takes place. Its role will be discussed in section **2.1**.

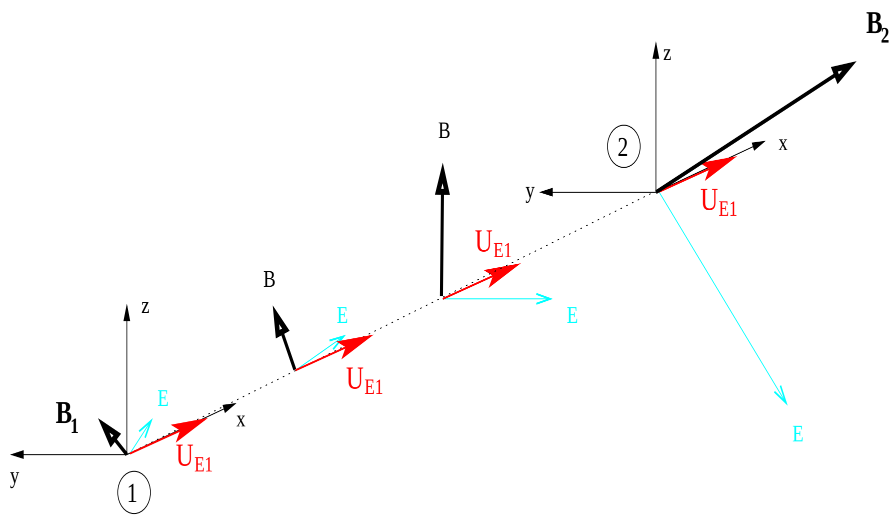

Figure 1.4: Superposition of a sheared magnetic field of a tangential discontinuity and a non-uniform electric field. $\boldsymbol{B}$ (solid black arrows) rotates and increase from "left" to "right" side of the discontinuity; when $\boldsymbol{B}$ rotates about the Ox-axis the vector $\boldsymbol{E}$ (solid blue arrows) rotates also and satisfies everywhere the condition $\boldsymbol{E} \cdot \boldsymbol{B} = 0$ and $\left|\frac{\boldsymbol{E} \times \boldsymbol{B}}{B^2}\right| = U_{E1}$; the convection velocity (red arrows) is everywhere parallel to the Ox direction.

<u>Case B</u>: non-uniform electric field conserving $\boldsymbol{U_E}$

Unlike in the previous case A, one can assume that the direction of $\boldsymbol{E}(x)$ remains perpendicular to $\boldsymbol{B}(x)$: i.e. the condition $\boldsymbol{E} \cdot \boldsymbol{B} = 0$ is satisfied everywhere. So far we did specify the orientation of the electric field vectors (shown in blue in fig. **1.4**) but not yet the distribution of their modulus, $E(x)$, as a function of x. We assume this distribution could be any continuous function of x without further discussion of the origin of any particular function adopted. We will consider two particular limiting cases that are different from the uniform electric field (case A', see below) for which steady-state reconnection occurs.

In **case** B we assume that the electric field intensity, $E(x)$, is such that the electric drift $U_E(x) = U_{E1}$ is constant:

$$\boldsymbol{E}_B(x) = -\boldsymbol{U}_{E1} \times \boldsymbol{B}(x) \tag{1.20}$$

$\boldsymbol{U}_{E1}$ is parallel to the Ox axis and independent of the coordinate x. This implies also that the polarization drift, fourth term in equation (1.14), is everywhere equal to zero. When the B-field rotates around the Ox axis, the E-field vector rotates by the same angle and $E(x)/B(x)$ is independent of x.

Case C: non-uniform electric field conserving μ

In **case C** we will assume that $\boldsymbol{E} \perp \boldsymbol{B}$ everywhere and that $E(x)$ is chosen such that the magnetic moment of electrons, μ^-, and ions, μ^+, drifting across the TD is an adiabatic invariant. This is precisely the E-field distribution expected to exist inside of a plasmoid or plasma element moving across a non-uniform magnetic field satisfying the Alfven conditions (*Schmidt*,1960; *Lemaire*, 1985).

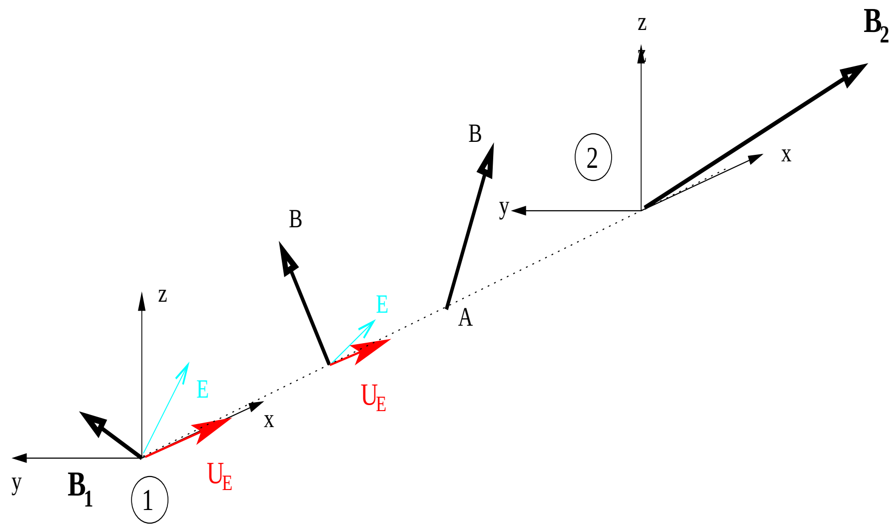

Figure 1.5: Electric field (solid blue arrows) conserving the average magnetic moment of ions traversing the sheared TD magnetic field. It illustrates the situation when the particle is stopped at point (A) where its initial convection energy has been completely transformed into gyromotion perpendicular to the magnetic field $\boldsymbol{B}$.

When the magnetic moment is conserved

$$\mu^{\pm} = \frac{m^{\pm}|\boldsymbol{v}_{\perp} - \boldsymbol{U}_E|^2}{2B} = ct. \tag{1.21}$$

with U_E defined by equation (1.15), the following equation is valid (*Lemaire*, 1985):

$$\frac{1}{2}\left(m^+ + m^-\right) U_E{}^2(x) + \left(\overline{\mu^+} + \overline{\mu^-}\right) B(x) = ct. \tag{1.22}$$

where the bars over quantities indicate averaging over the velocity distribution functions of electrons or ions. The electric field, $E_C(x)$, in case C is determined from :

$$\boldsymbol{E}_C(x) = -\boldsymbol{U}_E(x) \times \boldsymbol{B}(x) \tag{1.23}$$

The function $U_E(x)$ is determined such that $\overline{\mu^+}+\overline{\mu^-}$ is a constant independent of x:

$$\overline{\mu^+} + \overline{\mu^-} = \frac{1}{B_0}\left[\frac{1}{2}m^+\overline{(w_\perp{}^+)^2} + \frac{1}{2}m^-\overline{(w_\perp{}^-)^2}\right]_0 \stackrel{\text{def}}{=} \frac{(m^+ + m^-)\,\overline{w_{\perp 0}{}^2}}{2B_0} \tag{1.24}$$

where $\overline{w_{\perp 0}{}^2}$ is considered here as a free input initial parameter in the numerical integration of the particle orbit and guiding center path. It will be further called *initial averaged thermal velocity*.

In the following chapter we give the results obtained by integrating numerically the orbits of test-particles injected into these non-uniform distributions of the electromagnetic field.

Chapter 2

Numerical orbits of test-particles injected into the sheared electromagnetic field of a 1D tangential discontinuity

We integrate simultaneously the system of equations of motion of the particle and of its guiding center (gc) :

$$\frac{d^2\boldsymbol{r}}{dt} = \frac{q_\alpha}{m_\alpha}\left[\boldsymbol{E} + \frac{d\boldsymbol{r}}{dt} \times \boldsymbol{B}\right] \tag{2.1-a}$$

$$\frac{d\boldsymbol{r}_{gc,\perp}}{dt} = \boldsymbol{v}_{gc,\perp} \tag{2.1-b}$$

$$\frac{d^2 r_{gc,\parallel}}{dt^2} = \frac{dv_{gc,\parallel}}{dt} \tag{2.1-c}$$

where the right hand side of the equations (2.1-b) and (2.1-c) were defined by eqs. (1.14) and (1.16) respectively. In the simplified geometry of a one-dimensional, planar TD illustrated in figure **1.2**, the curvature drift is equal to zero. In this case equations (1.14) and (1.16) are reduced to simpler expressions. The perpendicular drift and parallel acceleration of the guiding center become:

$$\boldsymbol{v}_{gc,\perp} = \frac{\boldsymbol{E}\times\boldsymbol{B}}{B^2} + \frac{m_\alpha {w_\perp}^2}{2q_\alpha B^3}\boldsymbol{B}\times\boldsymbol{\nabla}(B) + \frac{m_\alpha v_\parallel}{q_\alpha B^3}\boldsymbol{B}\times(\boldsymbol{U}_E\cdot\boldsymbol{\nabla})\,\boldsymbol{B} + \frac{m_\alpha}{q_\alpha B^2}\boldsymbol{B}\times\frac{d}{dt}\left(\frac{\boldsymbol{E}\times\boldsymbol{B}}{B^2}\right) \tag{2.2-a}$$

$$\frac{dv_{gc,\parallel}}{dt} = \frac{q_\alpha}{m_\alpha}E_\parallel \tag{2.2-b}$$

In the simulations discussed in this chapter the test-particle is injected on the left hand side of the TD, at the initial position $\boldsymbol{r}_1 = (x_1, 0, 0)$ with an initial velocity equal to $\dot{\boldsymbol{r}}_1 = v_{1\perp}\hat{\boldsymbol{x}} + v_{1\parallel}\hat{\boldsymbol{b}}$ where $\hat{\boldsymbol{x}}$ is the unit vector parallel to the Ox direction, $\hat{\boldsymbol{b}}$ is the unit vector in the direction of the local magnetic field. $\boldsymbol{B}_1 = (0, B_{1y}, B_{1z})$ and $\boldsymbol{B}_2 = (0, B_{2y}, B_{2z})$ are the asymptotic fields of the distribution (1.17). $\boldsymbol{E}_1 = (0, E_{1y}, E_{1z})$ is the electric field intensity at $x = x_1$; it is also an initial value for integration. Indeed, E_1/B_1 determines the perpendicular velocity of the guiding center at $x = x_1$; the parallel velocity of the *gc* is equal to $v_{1\parallel}$, the parallel velocity of the particle at $x = x_1$. Thus x_1, $v_{1\perp}$, $v_{1\parallel}$, B_{1y}, B_{1z}, E_{1y}, E_{1z} are free parameters that are inputs of the numerical integration code. We will work with the dimensional equation in order to obtain results easier to apply to the physical space in the magnetopause region.

The role of the "adiabaticity" parameter (see below) is formally played by $\epsilon = \frac{m_\alpha}{q_\alpha}$, the ratio between mass and charge of the test-particle (*Northrop*, 1963). The initial conditions for all the simulations discussed here are introduced in Table 2.1. The differential equations (2.1-a)-(2.1-c) have been integrated by the Cash-Karp-Runge-Kutta (CKRK) fifth order algorithm with adaptive step size (*Press et al.*, 1992) and is briefly described in the Appendix.

Table 2.1: Initial conditions for the integration of test-particle orbits

Fig./Case	L	B_{1y}	B_{2y}	B_{1z}	B_{2z}	E_{1y}	E_{1z}	$v_{1\perp}$	$v_{1\parallel}$	α
$2.1/A'$	10^3	0	0	-3	$+5$	-0.3	0	3	0.5	180^0 n
$2.2/A$	10^3	$+2$	$+6$	-3	$+5$	-0.3	-0.2	3	0.5	95^0 n
$2.4/A$	10^3	$+2$	$+5$	$+3$	$+7$	-0.3	-0.2	3	0.5	10^0 p
$2.5/B'$	10^3	0	0	-3	$+5$	-0.3	0	3	0.5	180^0 p
$2.6/B$	10^3	$+2$	$+6$	-3	$+5$	-0.3	-0.2	3	0.5	95^0 p
$2.8/B$	10^5	$+2$	$+6$	-3	$+5$	-0.3	-0.2	3	0.5	95^0 p
$2.7/B$	10^3	$+2$	$+5$	$+3$	$+7$	$+0.3$	-0.2	3	0.5	10^0 p
$2.11/C'$	10^3	0	0	-3	$+5$	-0.3	0	3	0.5	180^0 n
$2.12/C'$	10^3	0	0	-3	$+5$	-0.7	0	4	0.5	180^0 p
$2.13/C$	10^3	$+2$	$+6$	-3	$+5$	-0.9	-0.6	5	0.5	95^0 p

B_{1y}, B_{1z}, B_{2y}, B_{2z} = asymptotic values (in nT) of B;
E_{1y}, E_{1z} = initial values (in mV/m) of the electric field;
$v_{1\perp}$, $v_{1\parallel}$ = initial components (in 10^2 km/s) of test-particle velocity;
α = angle of shear across the TD;
L = scale-length of the TD (in km);
p: indicates a penetrating orbit, n: indicates a non-penetrating orbit

2.1 Case A: uniform electric field

When $E_A = 0$ the particle spirals along an helicoidal trajectory centered on the local magnetic field line. Its guiding center drifts in planes parallel to the TD surface.

When $E_A \neq 0$ the particle drifts across $\boldsymbol{B}$. The zero order drift velocity has also a component normal to the TD. The initial velocity of the guiding center is equal to:

$$\begin{aligned} v_{gc0\parallel} &= v_{0\parallel} \\ v_{gc0x} &= v_{gc0\perp} = U_{E1} = E_A/B_1 \end{aligned} \tag{2.3}$$

Since the E-field and B-field distributions are stationary the polarization drift velocity (fourth term in eq. 2.2-a) can be transformed into :

$$\frac{m_\alpha}{q_\alpha B^2}\boldsymbol{B} \times [(\boldsymbol{U}_E \cdot \boldsymbol{\nabla})\, \boldsymbol{U}_E] = -\frac{m_\alpha {U_E}^2}{q_\alpha B^3}\boldsymbol{B} \times \boldsymbol{\nabla} B \tag{2.4}$$

2.1.1 Antiparallel B-field distribution

Figures **2.1 c, d** show two projections of the 3-D trajectory of the test-proton for the initial conditions specified in table 2.1. The magnetic field is zero at $x = 0$ (figure **2.1 a**) where the B_z component changes sign from a negative ("Southward") value to a positive ("Northward") value. The B_y component is everywhere equal to zero. The electric field is everywhere perpendicular to $\boldsymbol{B}$: thus $E_\parallel = 0$. This electric and magnetic field distribution is quite similar to that considered in MHD steady-state reconnection models since $B = 0$ at $x = 0$. Note that here $B = 0$ in the whole yOz plane not only along an X-line as in the reconnection model of *Dungey* (1961). (This special case is labeled *case A'*)

The insert of figure **2.1 e** shows that close to $x = 0$ where $B = 0$ the velocity of the guiding center diverges. Indeed, $U_E = \frac{\boldsymbol{E}\times\boldsymbol{B}}{B^2} \to \infty$ when $B \to 0$. The integration of the guiding center trajectory is then interrupted. This constitutes a mathematical singularity of the first order guiding center equation, similar to that occuring at the X-line in MHD reconnection models where the convection velocity, $\boldsymbol{U}_E$, also becomes infinitely large. However, the integration of the exact equation of motion of the particle continues since the actual velocity of the particle does not diverge where $B = 0$. There is no true physical singularity, but a mathematical one both in the first order *gc* approximation and MHD approximation.

The proton oscillates in the region centered on $x = 0$, and its pitch angle tends asymptotically to 90^0. The particle moves parallel to the current sheet and oscillate about the plane where $B = 0$.

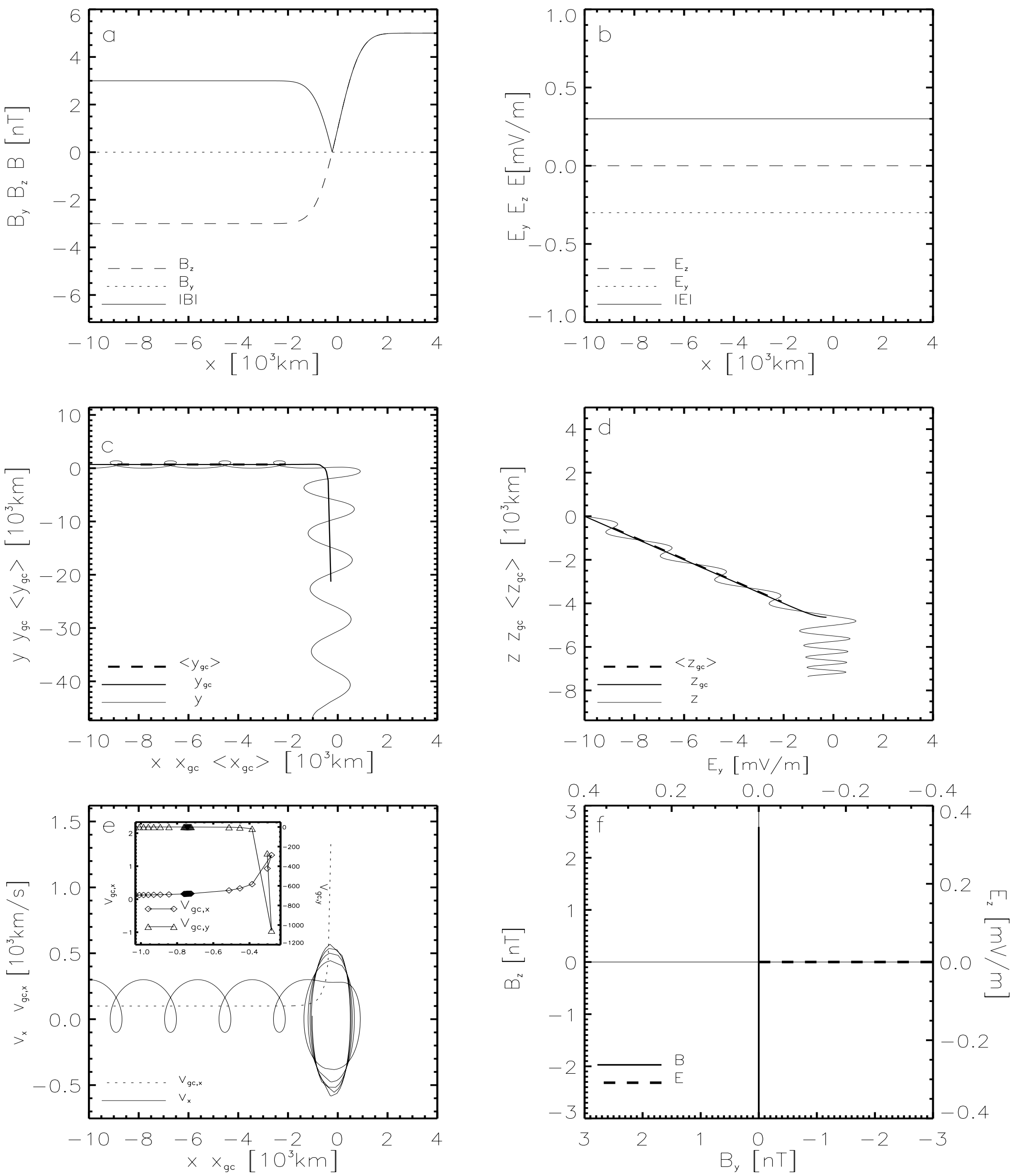

Figure 2.1: *case A′*; panels show: ***a***) the B-field distribution; ***b***) the E-field distribution; ***c***) the xOy projection of trajectories: particle, guiding center (y_{gc}), and averaged gc ($< y_{gc} >$); ***d***) gives the xOz projections; panel ***e***) shows the velocities of the particle (v_x) and gc ($v_{gc,x}$); panel ***f***) shows the changes of B_y and B_z (solid thick line) and of E_y and E_z (dashed thick line) as "seen" by the drifting particle while it moves across the TD.

Similar results were obtained previously by *Speiser* (1965, 1967) and *Speiser et al.* (1981) in their studies of the motion of charged particles at the neutral sheet of the magnetotail where $\boldsymbol{B}$ reverses. The downward oscillatory motion of the particle observed in the xOz projection of the orbit (figure **2.1 d**) is due to the initial non-zero parallel velocity of the particle. In this case $\boldsymbol{v}_{\parallel}$ remains constant during the whole simulation time.

In the region where the magnetic field tends to zero the particle is accelerated by the electric field in the $-Oy$ direction as along X-lines in MHD reconnection models. The electrons and ions can be accelerated respectively in the $+Oy$ and $-Oy$ direction to any energy by the electric field, E_A. This is a configuration that can produce *jetting* of energized charged.

2.1.2 Sheared B-field distribution

When a non-zero component B_y is added in equation (**1.17**), the B-field does not vanish at $x = 0$ nor at any other point. The B-field rotates around and all along the Ox axis. The orbit of a test-proton injected into such a B-field distribution is shown in figure **2.2**. The total angle of rotation, or *shear angle* in the case simulated in figures **2.2 a-f** is equal to $\alpha = 95^0$. The particle is accelerated in the direction parallel to the magnetic field (see figure **2.2 e**). The parallel component of the electric field "seen" by the particle increase along its orbit due to the rotation of $\boldsymbol{B}$ with respect to the uniform E-field. When $\boldsymbol{B}$ becomes exactly parallel to $\boldsymbol{E}$ (and $E_\perp = 0$) the advancement in the direction normal to $\boldsymbol{B}$ stops and the particle gyrates around the field line of "maximum penetration" ($x \approx 500\ km$).

The pitch angle decreases asymptotically towards 0^0. This would be an interesting way to produce thin sheets of accelerated particles and at the same time to inject them into the loss cone along polar cusps. The location of the field line of "maximum penetration" depends on the relative orientation of $\boldsymbol{B}$ and $\boldsymbol{E}$ vectors but not on the location of the reversal of the B_z component as in case A'. This is shown by the "hodogram" of $\boldsymbol{B}$ and $\boldsymbol{E}$ in figure **2.2 f**.

Since there is no point where $B = 0$, the convection velocity and guiding center velocity does no more diverge, unlike in case A'. The gc trajectory could be integrated over the whole time interval, as show figures **2.2 c**, **d**. Nevertheless, the guiding center path failed to follow exactly the average particle orbit because $r_L/L \approx 1$ and the first type of Alfven condition (eq. 1.4) is then not satisfied. The insert of figure **2.2 c** shows that the sharp gradient of $\boldsymbol{B}$ around $x = 0$ produces the offset between the *gc* path and the exact trajectory.

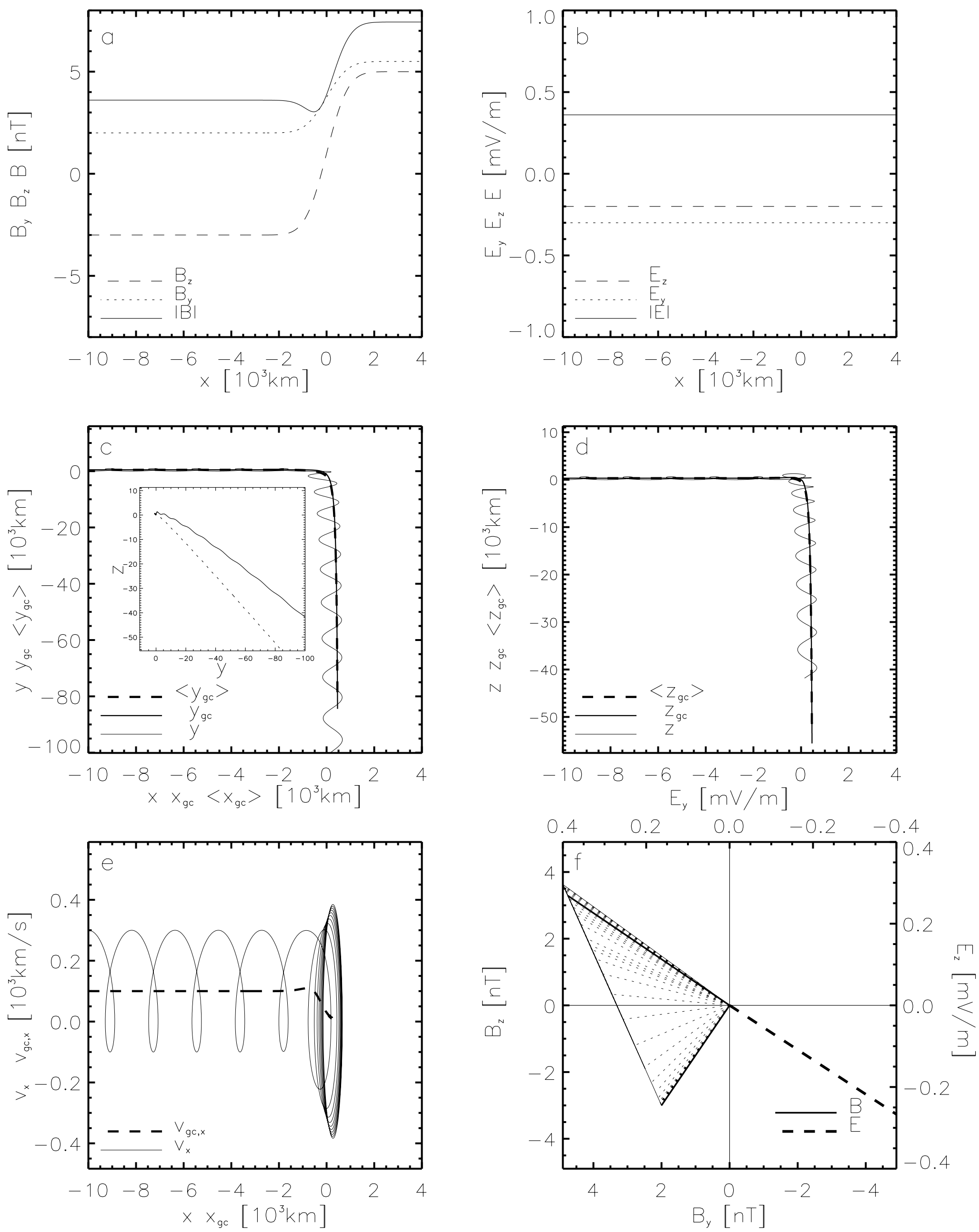

Figure 2.2: *Case A:* same panel distribution as in figure **2.1** but for a higher shear-angle α. The advancement in the Ox direction stops at $x \approx 500$ km where the magnetic field is parallel to the uniform E-field and $\boldsymbol{E} \times \boldsymbol{B}/B^2 = 0$; the particle is then accelerated in the parallel direction.

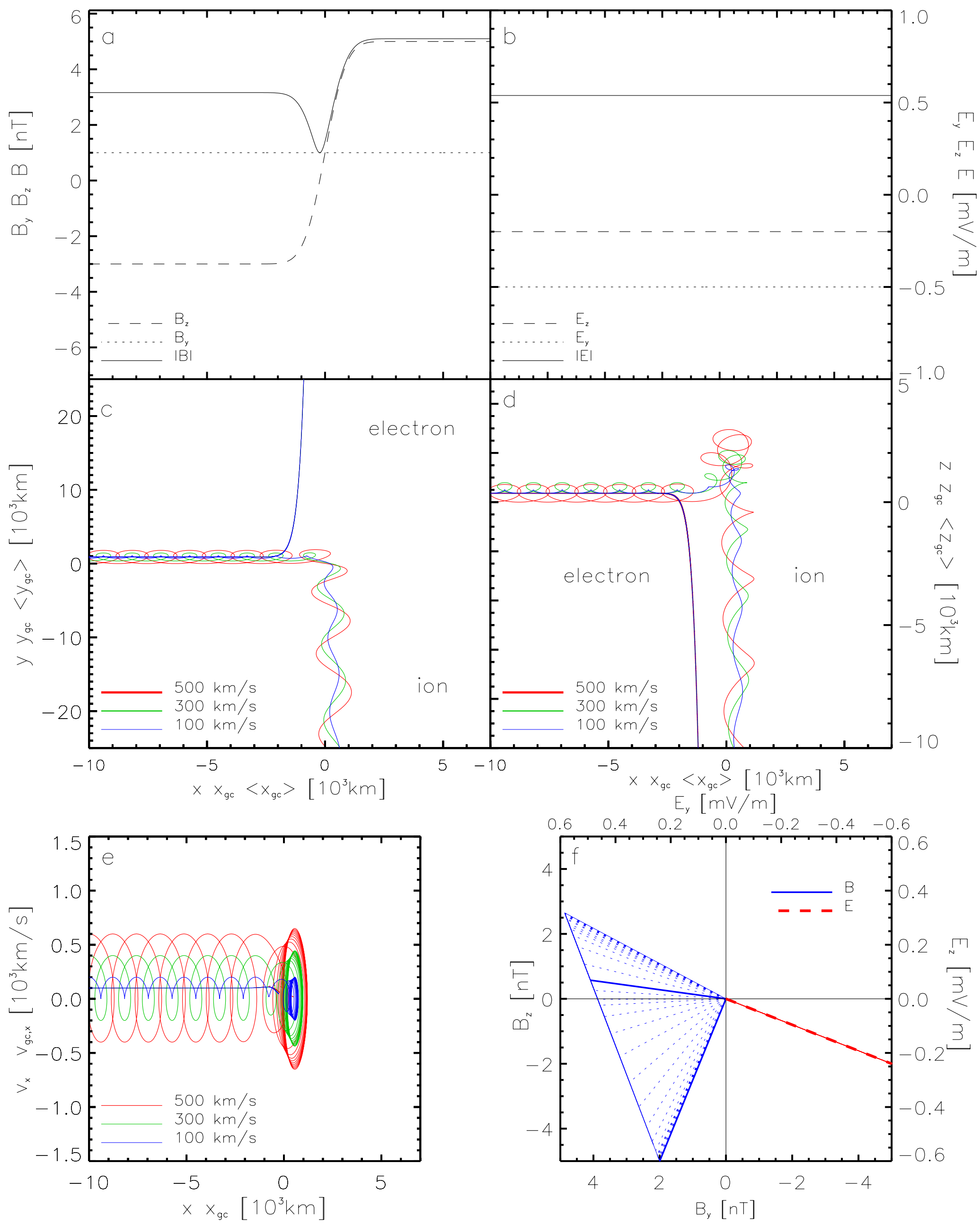

Figure 2.3: *Case A:* same panel distribution as in figure **2.1** but with $B_y \neq 0$ and a large magnetic shear angle, α. Different colors correspond to different initial energies of the three pairs ion-electron. Each electron is initialized with the same energy as the corresponding ion.

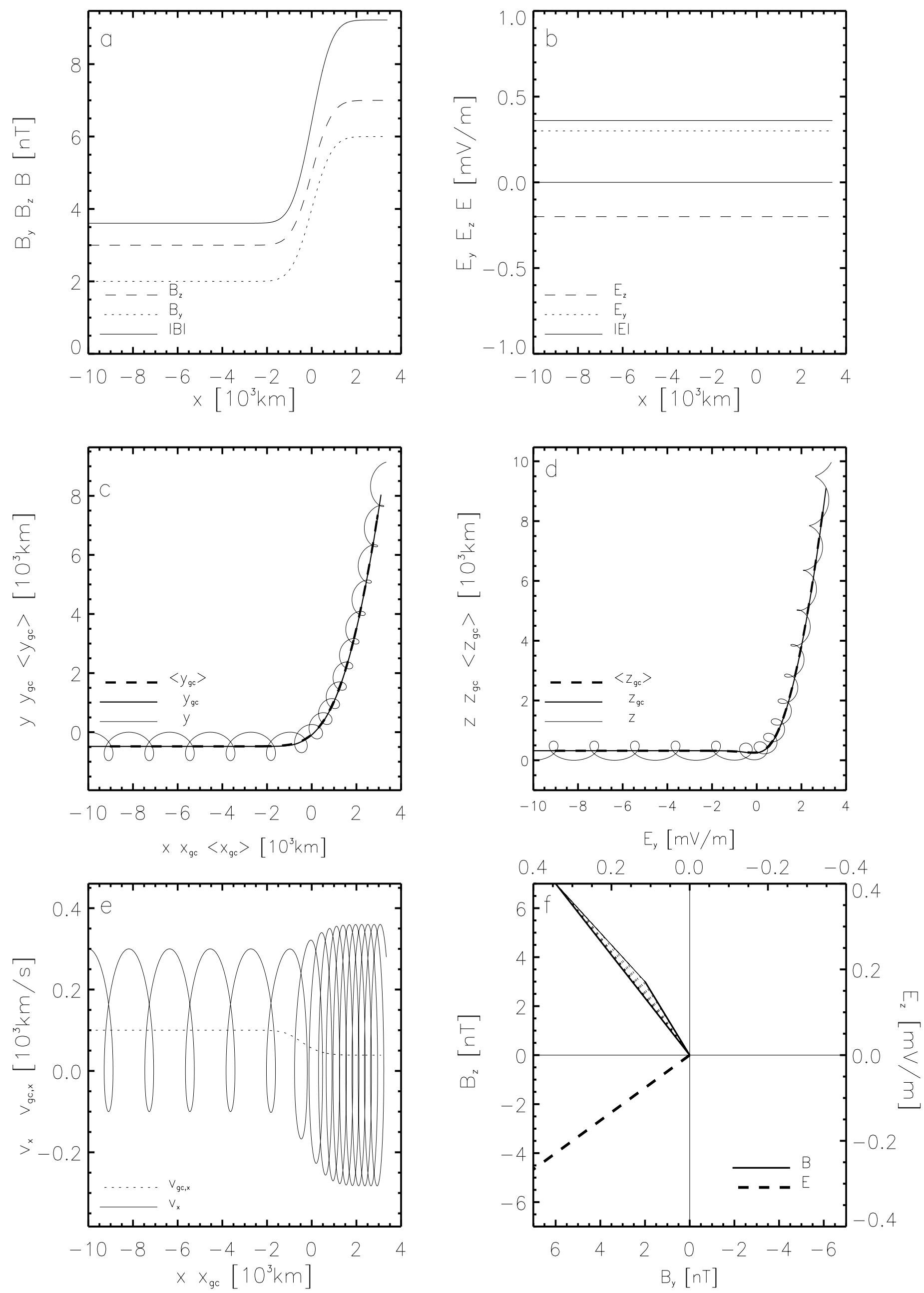

Figure 2.4: *Case A:* same panel distribution as in figure **2.1** but for a small magnetic shear angle α.

The orbits of three pairs of ions and electrons with different initial energies are plotted in figure **2.3**. The ions are deflected in the $-Oy$ direction, the electrons deviate in the $+Oy$ direction. A large number of such electrons and protons can carry the appropriate diamagnetic current density parallel to the surface of discontinuity such that $\mu_0 \boldsymbol{J} = \boldsymbol{\nabla} \times \boldsymbol{B}$.

When the magnetic field never becomes exactly parallel to the uniform electric field the particle moves in the Ox direction without being stopped. Such an example is given in figures **2.4 a-f** in the case of a small magnetic shear angle ($\alpha = 10^0$). The parallel component of the electric field is smaller than in the simulation shown in figure **2.2**; it accelerates moderately the particle. The perpendicular component of the electric field is everywhere different from zero; it drives the particle and the guiding center across $\boldsymbol{B}$-field lines. The particle penetrates all through the magnetic barrier and reach the right side of the transition region, as shown in figures **2.4 c-d**. Its average velocity is slowed down when traversing the discontinuity as shows the phase space plot given in fig. **2.4 e**. On the other hand its gyro velocity increases. In this case the guiding center path follows closer the averaged particle's position (see panels **2.4 c-d**).

In summary, the numerical integration of equations (2.1-a)-(2.1-c) with a constant electric field illustrate the divergence of the first order drift in the case of an antiparallel distribution of $\boldsymbol{B}$. Equations (2.1-b) and (2.1-c) for the motion of the guiding center, have a point of singularity at $x = 0$ where $B = 0$; $r_L \rightarrow \infty$ and therefore the first Alfven condition is violated since $r_L \div L \gg 1$. Both the guiding center and the ideal MHD approximations break down where $B = 0$. None of these approximations of plasma physics can be then used to describe the actual trajectory of a particle as the superposition of a Larmor gyromotion plus a first order drift.

The equation of motion of the particle (2.1-a) has no mathematical singularity and can be numerically integrated — the result is a classical oscillatory motion about the surface of discontinuity. The velocity of the particle itself does not experience any anomalous/explosive energization at $x = 0$ where $B = 0$. The motion in the direction perpendicular to $\boldsymbol{B}$ stops at a "maximum penetration" distance where $\boldsymbol{B} \parallel \boldsymbol{E}$ and $\boldsymbol{E} \times \boldsymbol{B}/B^2 = 0$.

In the case of B-field distributions having a small angle of rotation (or magnetic shear) there is a constant acceleration of the particle parallel to the B-field lines, but the motion across magnetic field is stopped nowhere. The test-particle drifts then all across the TD or the "magnetic barrier", e.g. the magnetopause. Test-electrons and test-protons injected simultaneously with different energies are diverted in opposite directions, parallel to the TD surface which corresponds to a kind of magnetopause Chapman-Ferraro layer (*Chapman and Ferraro*, 1931).

These examples of magnetic and electric fields show that in the case of a uniform electric field, the relative orientation of $\boldsymbol{B}$ with respect to $\boldsymbol{E}$ and the overall magnetic shear angle determine the distance a particle can move across a region of sheared magnetic field.

2.2 Case B : Non-uniform E-field conserving the zero order drift

This subsection discusses the results obtained by integrating numerically the trajectory of the test-particle injected into a non-uniform sheared distribution of the magnetic field given by (1.17) and the E-field described by (1.20).

2.2.1 Antiparallel B-field distribution

First we will inject the particle into the antiparallel B-field distribution with $B = 0$ and B_z changing sign in $x = 0$. The results, further referred to as *case B'*, are shown in figures **2.5**. The first two panels (figures **2.5 a-b**) show that when the B_z component changes sign, E_y changes sign also. B_y and E_z are equal to zero everywhere.

According to (1.20), although B takes zero value at $x = 0$, the zero order drift remains finite in the vicinity of $x = 0$ plane:

$$\lim_{x \to 0} \frac{E_B(x)}{B(x)} = U_{E1} \tag{2.5}$$

Figure **2.5 e** shows indeed that the average of the particle velocity has a constant value in the simulation domain and does not diverge at $x = 0$. Nevertheless, the first order guiding center velocity, v_{gc}, diverges (see the insert of figure **2.5 e**). Indeed, the gradient-B drift velocity diverges at that point because it is proportional to $|\boldsymbol{\nabla} B|/B^3$. The integration for the *gc* orbit then stops at $x = 0$ where, as in the case A', a mathematical singularity occurs in the first order drift approximation.

The integration continues, however, for the exact equation of motion of the particle since there is no singularity in this equation where $B = 0$. Unlike in the previous case A', in case B' both B_z and E_y reverse sign at $x = 0$. Thus the particle can now cross the point of fields reversal as show figures **2.5 c-d**. In the region around the discontinuity the average of the particle's velocity varies but retrieves its initial value when the particle drifts across the TD into the region of asymptotically uniform fields (figure **2.5 e**). The difference between the two antiparallel distributions is evident: while in case

A' the non-divergent trajectory of the particle oscillates around the neutral plane, in the case B' the actual trajectory of the particle proceeds beyond the plane where $B = 0$.

2.2.2 Sheared B-field distribution

In figures **2.6**-**2.10** are given the numerical trajectories corresponding to magnetic field distributions that have a non-zero B_y component. All these numerical integrations have in common the fact that, like in case B', the test-particle penetrates all the way through, into the region beyond the discontinuity. Since there is no null point in the B-field distribution, the trajectory of the guiding center does not diverge; it traces the average orbit of the particle better than in case B'.

Figures **2.6 c** and **d** show the orbit of the test-proton injected into a B-field distribution that has a total magnetic shear angle of 95^0. The transition region has here a scale length of the same order as the Larmor radius of the test-particle thus violating Alfven's condition **1.4**. As a matter of consequence the guiding center path departs more and more from the actual trajectory of the particle as one can observe in figures **2.6 c** and **d** at $x > 3000\ km$. The gyration energy of the particle decreases slightly at the traversal of the discontinuity surface (see, figure **2.6 e**). The magnetic moment decreases also. Nevertheless, the zero order (electric) drift velocity remains uniform and is a good approximation of the actual average of the particle velocity.

A test-proton with the same initial energy has been injected into a magnetic field distribution with a smaller magnetic shear angle, $\alpha \leq 6^0$. Figures **2.7 a-f** give the results of the numerical integration. The value of B increases from 4 nT at the left side to 9 nT at the right hand side of the discontinuity. The electric vector rotates by the same angle α as the $\boldsymbol{B}$ vector. Although the characteristic scale length of the discontinuity is the same as in the case A figures **2.7c-d** show that here the gc path follows more closely the actual trajectory of the particle.

The scale length of the discontinuity can increase such that it becomes much larger than the Larmor radius of the test-particle. This is the case for the results given in figures **2.8 a-f**. They illustrate an example of adiabatic motion satisfying the Alfven condition (1.4). Figures **2.8 c-d** shows that the guiding center path and mean trajectory coincide fairly well.

In order to illustrate the effects of mass and charge of the injected particle, we have injected simultaneously three test-electrons and three test-protons. In a first numerical experiment the electron and proton of each pair have the same initial thermal energy: $\mathcal{K}T_{e0} = \mathcal{K}T_{i0}$ ($\mathcal{K}$ - Boltzmann constant).

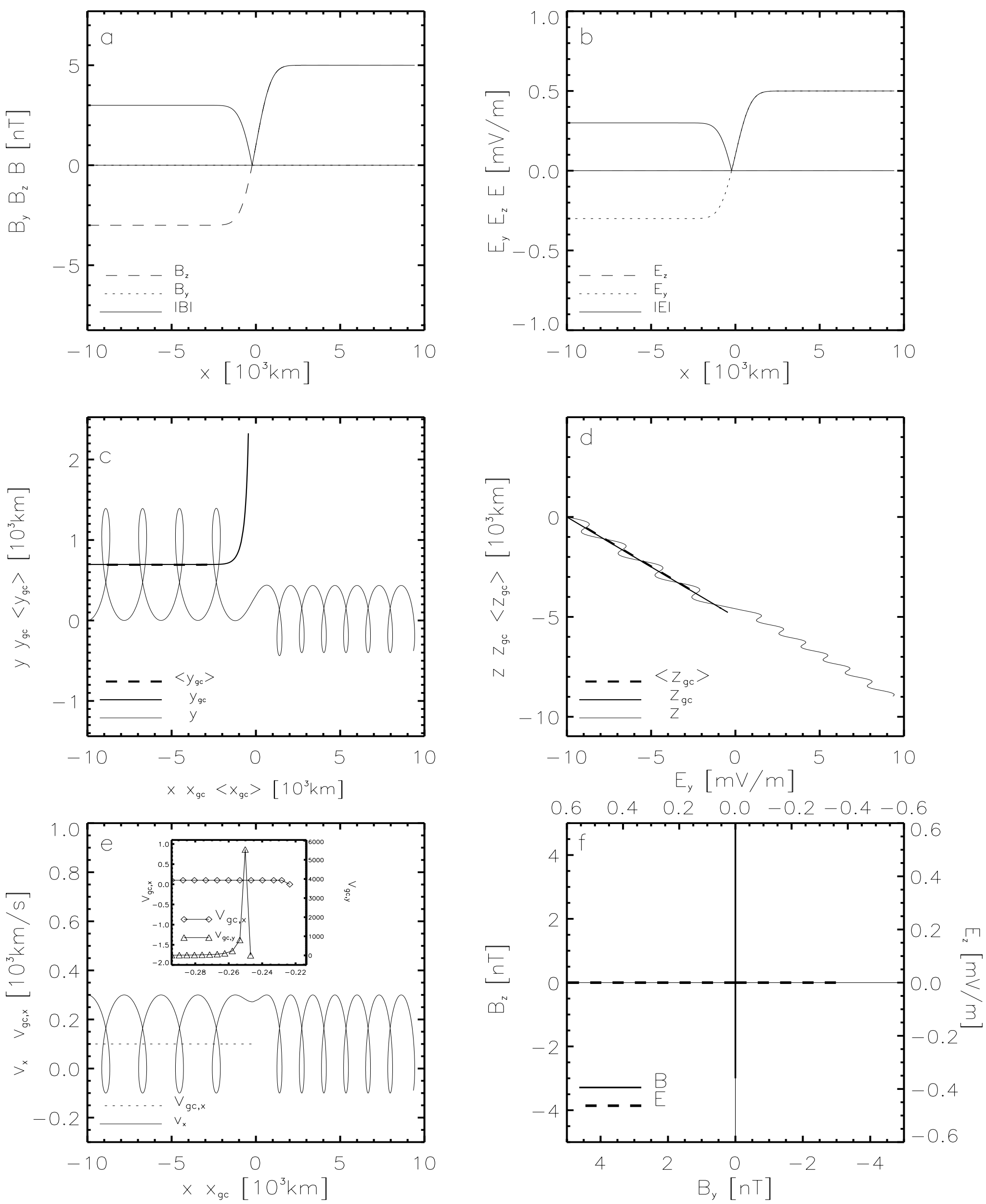

Figure 2.5: *Case B′*: the first two panels show ***a***) Magnetic field distribution; ***b***) Electric field distribution; panel ***c***) gives the xOy projection of trajectories: particle (y), guiding center (y_{gc}), and averaged gc ($< y_{gc} >$); panel ***d***) gives xOz projections; in panel ***e***) is given the phase space plot for particle and gc; panel ***f***) shows the B and E fields as "seen" by the drifting particle.

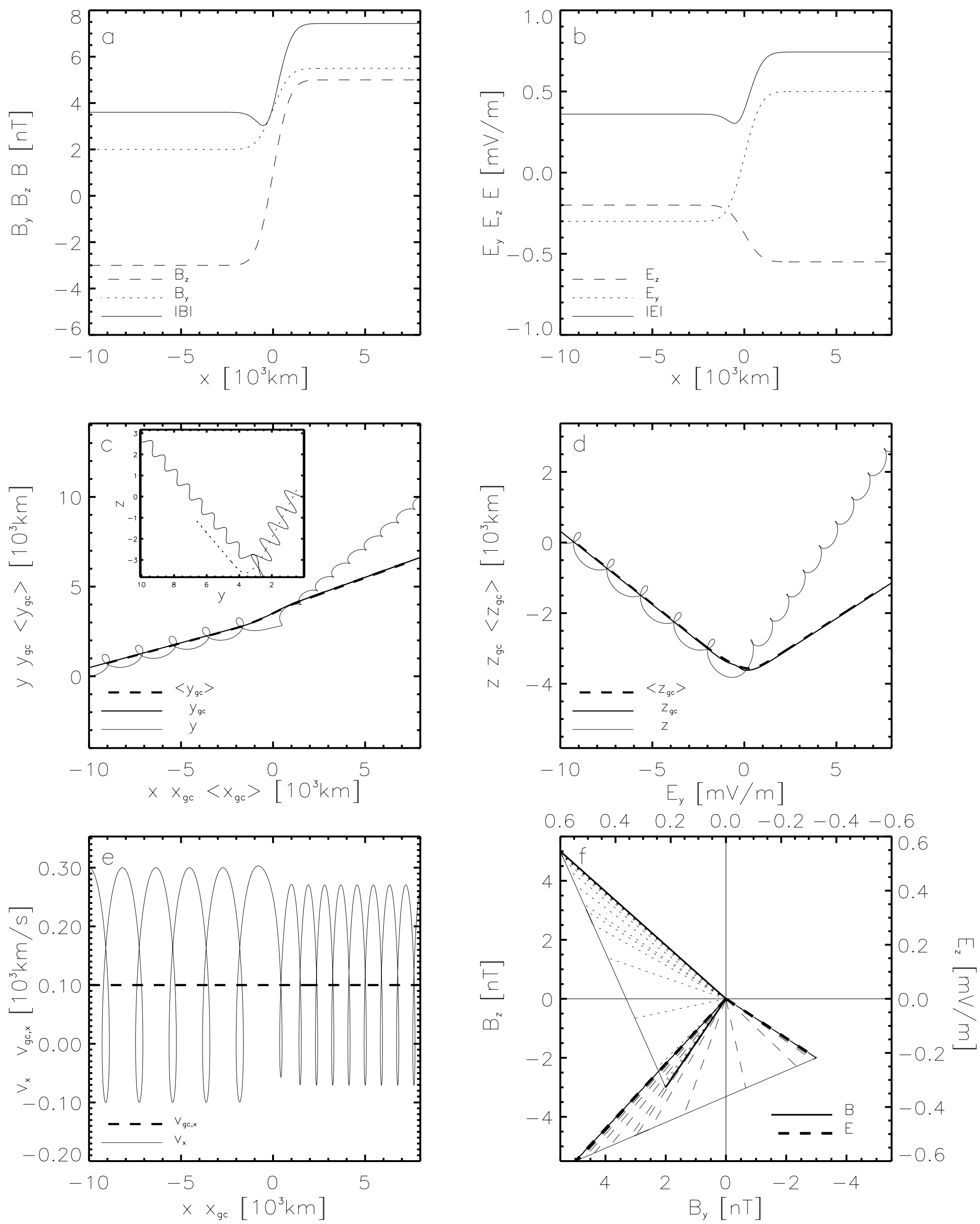

Figure 2.6: *Case B* - large magnetic shear angle , $\alpha \approx 95^0$. The distribution of the graphs in the six panels is the same as in figure **2.5**. The initial energy of the test-proton is equal to 15 eV.

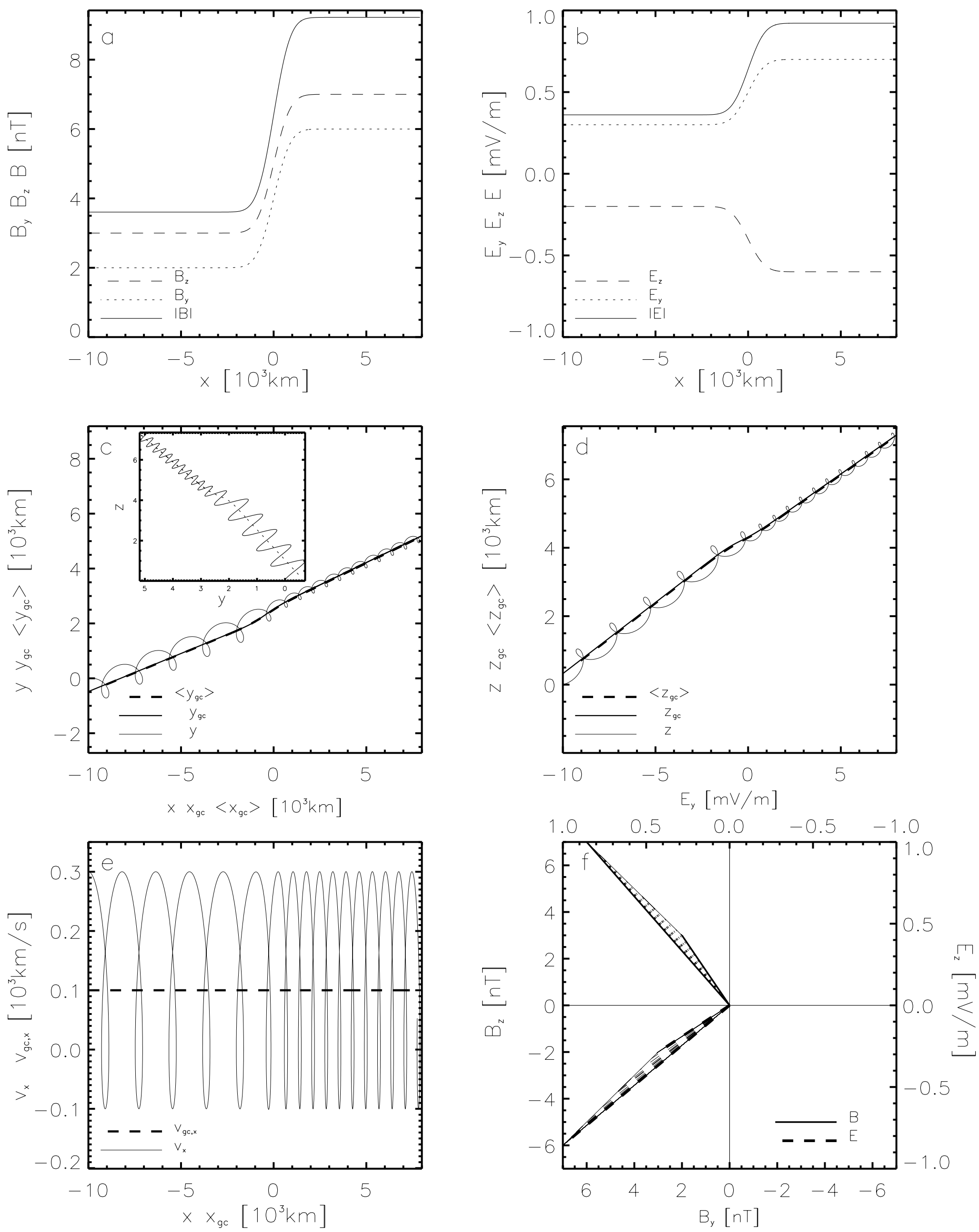

Figure 2.7: *Case B* - small magnetic shear angle ($\alpha \leq 6^0$); the distribution of the plots in the six panels is the same as that of figure **2.6**

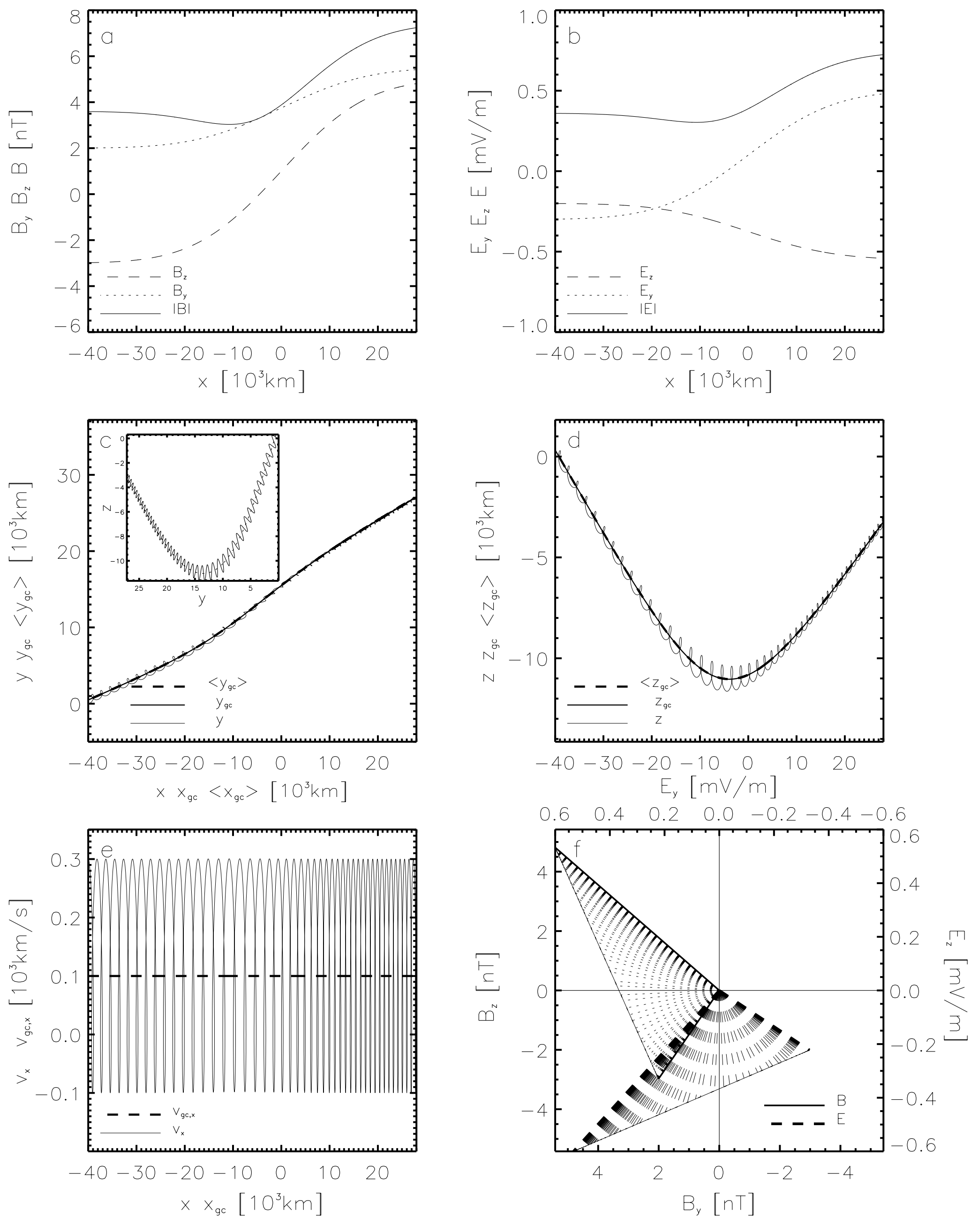

Figure 2.8: *Case B* - moderate magnetic shear angle and *adiabatic* motion of a 15 eV proton; the distribution of graphs in the six panels is the same as in figure **2.6**

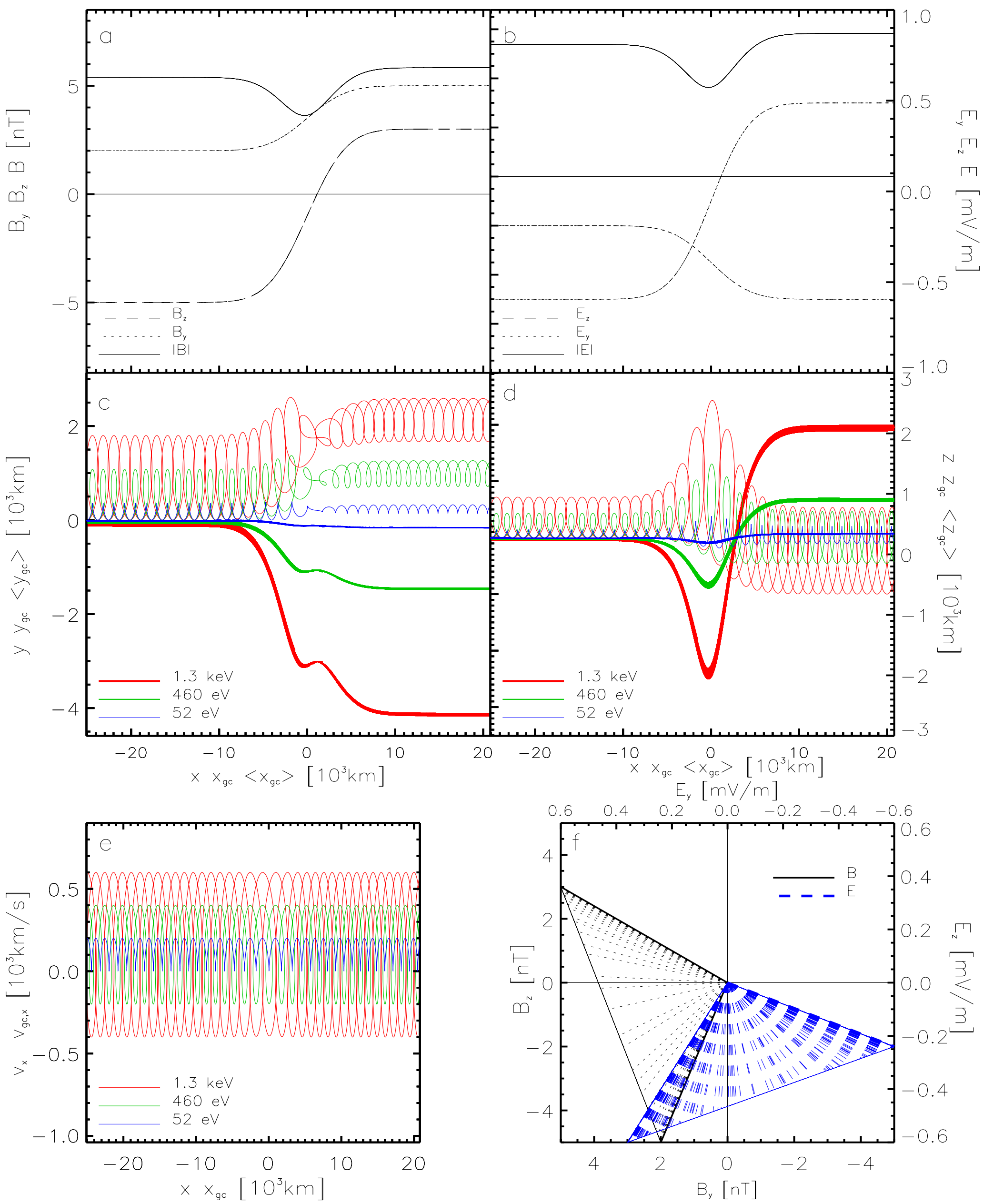

Figure 2.9: *Case B*: orbits of three protons and three electron. The panels shows the same graphs as in fig. **2.5**; *gc* path is not shown. Each pair ion-electron is injected in the same point with the same initial "thermal" energy, $\mathcal{K}T_{e0} = \mathcal{K}T_{i0}$. The initial velocity of the guiding center of all particles: $v_{gc} = U_E = 100\ km/s$.

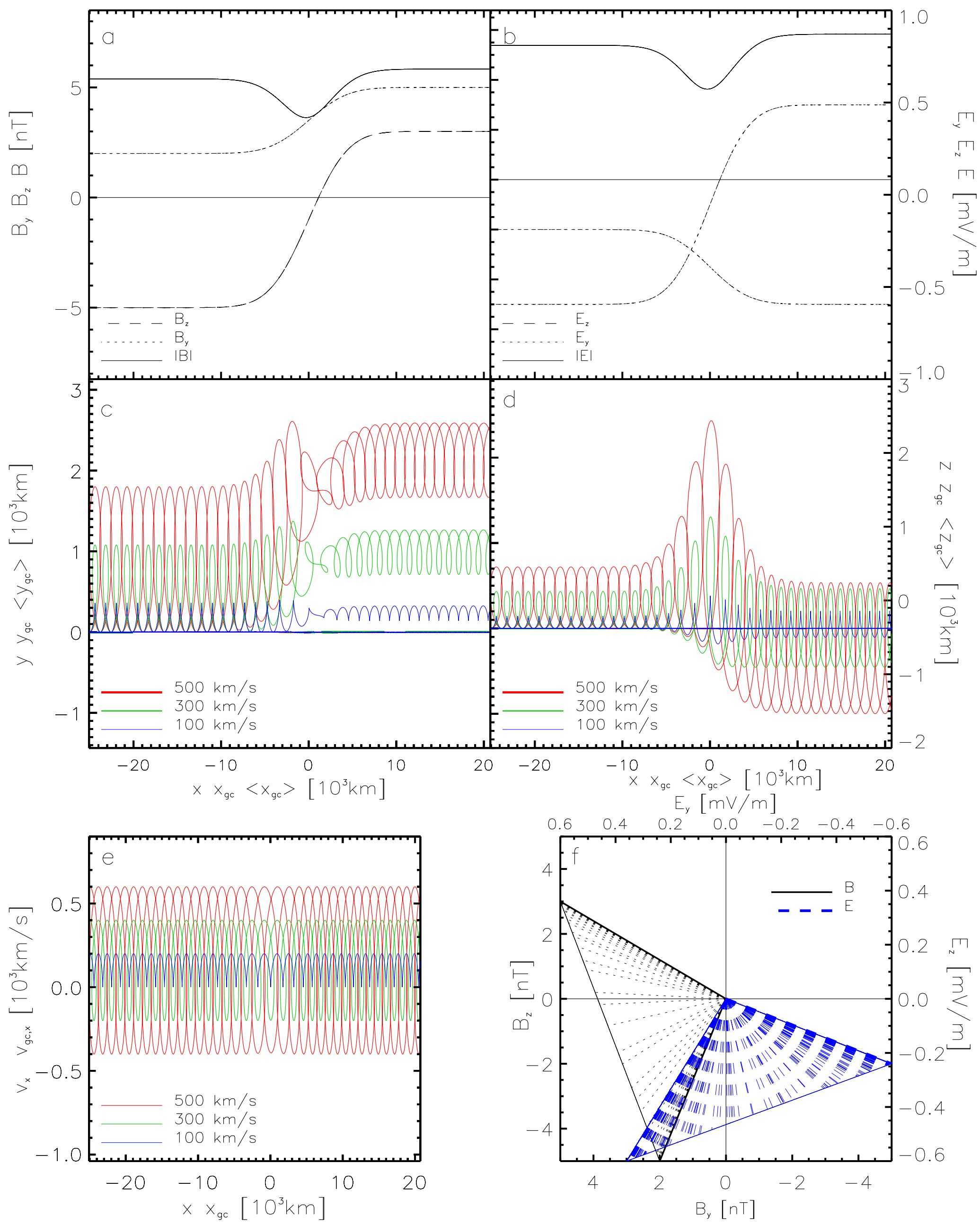

Figure 2.10: *Case B*: orbits of three protons and three electrons of different energies. In this case each pair electron-ion is injected with the same "thermal" velocity, $v_{p0} = v_{e0}$. The initial velocity of the guiding center for the six particles is equal to $v_{gc} = U_E = 100\ km/s$.

In the example given in figures **2.9 a-f** the initial velocity of the guiding center has a value of $v_{gc} = 100\ km/sec$ in the direction perpendicular to the magnetic field. The ensemble of three electron-proton pairs simulates then a non-diamagnetic, collisionless, rarefied plasma moving across B-field lines with the convection velocity $U_E = v_{gc}$.

The initial energy of the three electron-proton pairs is equal to $52\ eV$, $460\ eV$ and $1.3\ keV$ respectively. The magnetic and electric field distribution given in figures **2.9 a-b** produces a separation of test-particles according to their energy and charge. Indeed, figures **2.9 c-d** illustrates how the electrons deviate in the negative sense of the Oy axis. The test protons deviate in the opposite direction. This charge separation depends of course on the energy : the largest deflection is observed for the particles with the larger initial energy.

Figures **2.10 a-f** show the results of another numerical integration of the orbits of three electron-proton pairs. As in the previous case the guiding center velocity of each particle is $v_{gc} = 100\ km/s$ in the Ox direction. Instead of having the same initial energy, the electron and proton of each pair have the same initial injection velocity, $v_{e0} = v_{p0}$. The three values of the initial velocity are 100, 300 and 500 km/s respectively. Thus the electrons have smaller gyration energies $(m_e w_\perp^2/2)$ than in the previous simulation. Indeed one can observe a smaller deviation of the electrons in the negative direction of Oy and a larger deviation of protons in the positive direction. A charge separation is produced during propagation across the sheared B-field and E-field distributions but it is reduced compared to the previous simulation. All the test-particles drift forward across the TD and penetrate all together inside the right hand side where the fields are uniform.

These results may be extrapolated to a collisionless, diamagnetic plasma drifting across a sheared B-field distribution with a uniform velocity U_E. The simulations discussed above indicate that an electromagnetic field distribution can be imagined such that plasma particles drift all together with uniform velocity normal to a sheared B-field distribution. The particles penetrate inside the magnetosphere without the process of reconnection often invoked to describe the physical processes operating at the magnetopause.

The numerical integrations performed with the sheared B-field distribution and the E-field distribution of the case B can be summarized as below. In the case of an antiparallel B-field distribution with a neutral plane where $B = 0$ the value of the guiding center drift velocity diverges at the neutral plane, although the zero order drift velocity remains finite. Although this constitutes a mathematical singularity for the first order drift approximation the actual trajectory of the particle can be integrated all the way through. The particles drift across TD for a large range of the magnetic shear angles when the Alfven conditions are satisfied or not.

The E-field distribution tested in case B produces a charge separation inside the discontinuity; the guiding center velocity of the electron drift is opposite to that of the positively charged ions. This combination of electric and magnetic field enables plasma transport across magnetic field with a uniform and constant convection velocity, U_E.

2.3 Case C : Non-uniform E-field conserving the average magnetic moment

The next electric field distribution that is tested by numerical integration of test-particle orbits is that described in subsection **1.2.2** as *case C*. We remind that this E-field distribution is defined such that $\boldsymbol{E}$ is perpendicular to $\boldsymbol{B}$ everywhere. The intensity of the electric field is computed at each point along the trajectory such that the magnetic moment of the test-particle is conserved and the following relation holds true for each value of x:

$$\frac{m^+ + m^-}{2}\left(\frac{E_{1y}B_{1y} + E_{1z}B_{1z}}{B_{1y}^2 + B_{1z}^2}\right)^2 + \left(\overline{\mu^+} + \overline{\mu^-}\right)\sqrt{B_{1y}^2 + B_{1z}^2} =$$
$$\frac{m^+ + m^-}{2}\left(\frac{E_yB_y + E_zB_z}{B_y^2 + B_z^2}\right)^2 + \left(\overline{\mu^+} + \overline{\mu^-}\right)\sqrt{B_y^2 + B_z^2} \qquad (2.6)$$

where $E_{1y}, E_{1z}, B_{1y}B_{1z}$ are the asymptotic values of the E and B fields on the left side (i.e. initial values for the numerical integration) and E_y, E_z, B_y, B_z are the values of the fields all along the orbit. The electric field at the starting point is determined by:

$$\boldsymbol{E}_1 = -\boldsymbol{v}_{gc1} \times \boldsymbol{B}_1 \qquad (2.7)$$

where $\boldsymbol{v}_{gc1}$ is the initial velocity of the guiding center.

The first term in both sides of (2.6) is related to the energy associated with the drift velocity of the particle while the second term corresponds to the gyration energy. The equation (2.6) determines how the translational energy is transformed into gyration energy when the particle penetrates into the TD while conserving its magnetic moment invariant. *Demidenko et al.* (1967,1969) explained their laboratory experiments by this mechanism which later on was generalized by *Lemaire* (1985) for sheared B-field distribution.

If the magnetic field intensity increases with x, equation (2.6) implies that the electric field intensity necessarily decreases. When the value B_y and/or B_z of the right hand side of equation (2.6) are large enough such that $\left(\overline{\mu^+} + \overline{\mu^-}\right)\sqrt{B_y^2 + B_z^2}$ can become equal to the value of the left hand side, the electric components, E_y, E_z will necessarily become equal to zero such that (2.6) is satisfied. In this case the particle will not be able to penetrate all the way through across the TD and magnetic barrier.

2.3.1 Antiparallel B-field distribution

The first numerical integration corresponds to case C'. The antiparallel magnetic field distribution satisfies the condition: $B_y = 0$. The B-field distribution has a null point, $B = 0$, at $x = 0$ when B_z changes sign from negative ("Southward") to positive ("Northward") values. This is a magnetic field topology similar to those already used in the cases A' and B'.

Figures **2.11 a-f** illustrate the results obtained for a proton having an initial energy equal to $\approx 430\ eV$. The magnetic field increase from $B_1 = 3\ nT$ on the left hand side to $B_2 = 5\ nT$ at the right side; the only one non-vanishing component, B_z, changes sign at $x = 0$. The initial velocity of the guiding center is $v_{gc1} = 100\ km/s$ and the initial electric field intensity is equal to $E_1 = \sqrt{E_{1y}^2} = \sqrt{(v_{gc1}B_1)^2} = 0.3\ mV/m$.

At $x \approx 500\ km$ the magnetic field intensity increases enough such that the gyration energy equals the initial total energy of the particle. When this occurs the electric field intensity computed from (2.6) is equal to zero as figure **2.11 b** shows. This is also the location where the forward motion of the particle is stopped.

The zero order (electric) drift velocity goes to zero at $x \approx 500\ km$ where the energy of the drift motion has been completely converted into gyroenergy. The velocity of the guiding center diverges in $x = 0$ where $B = 0$ and the gradient-B drift velocity increases to infinity. The integration of the first order drift equations stops. Therefore, the applicability of the first order guiding center theory breaks down again at $x = 0$. As in the previous two cases, A' and B', this is only a mathematical singularity where the gc approximation breaks down but. The exact equation of motion of the test-particle is not singular and can be integrated.

The test-particle advancement in the Ox direction is stopped at the "maximum penetration distance", $x_M = 500\ km$. The projections of the trajectory illustrated in figures **2.11 c-d** show that its final gyration is centered on the magnetic field line localized at x_M. The particle gets trapped within a sheath of one Larmor radius width and oscillates about the plane $x = x_M$.

Though the orbit looks similar to that illustrated in case A', the mechanism which produces it is different. Since in case A' the electric field was uniform and non-vanishing, there was a non-vanishing electric force at $x = 0$ (where $B = 0$) that accelerated the test-particle in the Oy direction. In section **2.2** we argued that this acceleration would produce thin current sheets of accelerated particles or *jetting*. In case C' at $x = x_M$ where the electric field vanishes, the electric force acting on the particle tends to zero, but the magnetic field intensity B_M is not equal to zero. In the absence of the electric force, the Lorentz force acting on the right hand side of the B_z reversal point drives the particle back towards the discontinuity. No acceleration (or *jetting*) is expected in this case (see **2.11 e**).

The particle can penetrate the discontinuity when the gyration energy, μB_2, at the right hand side of the discontinuity is smaller than the initial total energy of the particle at the left side. This condition can be accomplished by increasing the left hand side term of eq.(2.6). This is precisely what has been done to obtain the results shown in figures **2.12 a-f**. The initial convection energy has been increased by increasing the initial velocity of the guiding center from 100 km/s to 250 km/s. Thus the initial value of the electric field has also been increased to $E_1 = 0.75\ mV/m$.

The test-particle penetrates through the discontinuity as illustrated in figures **2.12 c-d**. The electric field decreases across the discontinuity but keeps a finite value as shown by figure **2.12 b**. Figure **2.12 e** shows that the particle is decelerated during the traversal of the discontinuity.

The guiding center velocity diverges again at $x = 0$ where $B = 0$, i.e. where the gyroradius becomes infinitely large and where the Alfven conditions are violated. This is illustrated by the insert of figure **2.12 e**. As in all previous simulations with antiparallel distributions of B, the mathematical singularity of the first order drift approximation does not correspond to a physical singularity of the actual motion of the test-particle.

2.3.2 Sheared B-field distribution

When one adds a non-zero component, $B_{y_1} = 2\ nT$, the minimum value of the initial convection energy needed for the particle to move across the magnetic barrier is increased.

Figures **2.13 a-f** show an example. The magnetic field intensity increases from $B_1 = 3.5\ nT$ to $B_2 = 7.5\ nT$. The initial value of the *gc* velocity is equal to 300 km/s; the initial value of the electric field is equal to $E_1 = 1.1\ mV/m$. The trajectory of a *"penetrating"* particle is shown in figures **2.13 c-d**.

Prior to the interaction with the discontinuity, the electric field is so intense that the projections of the particle's orbit in xOy and xOz planes are prolate cycloids. However at $x = 0$ the guiding center velocity in the direction normal to the TD is slowed down.

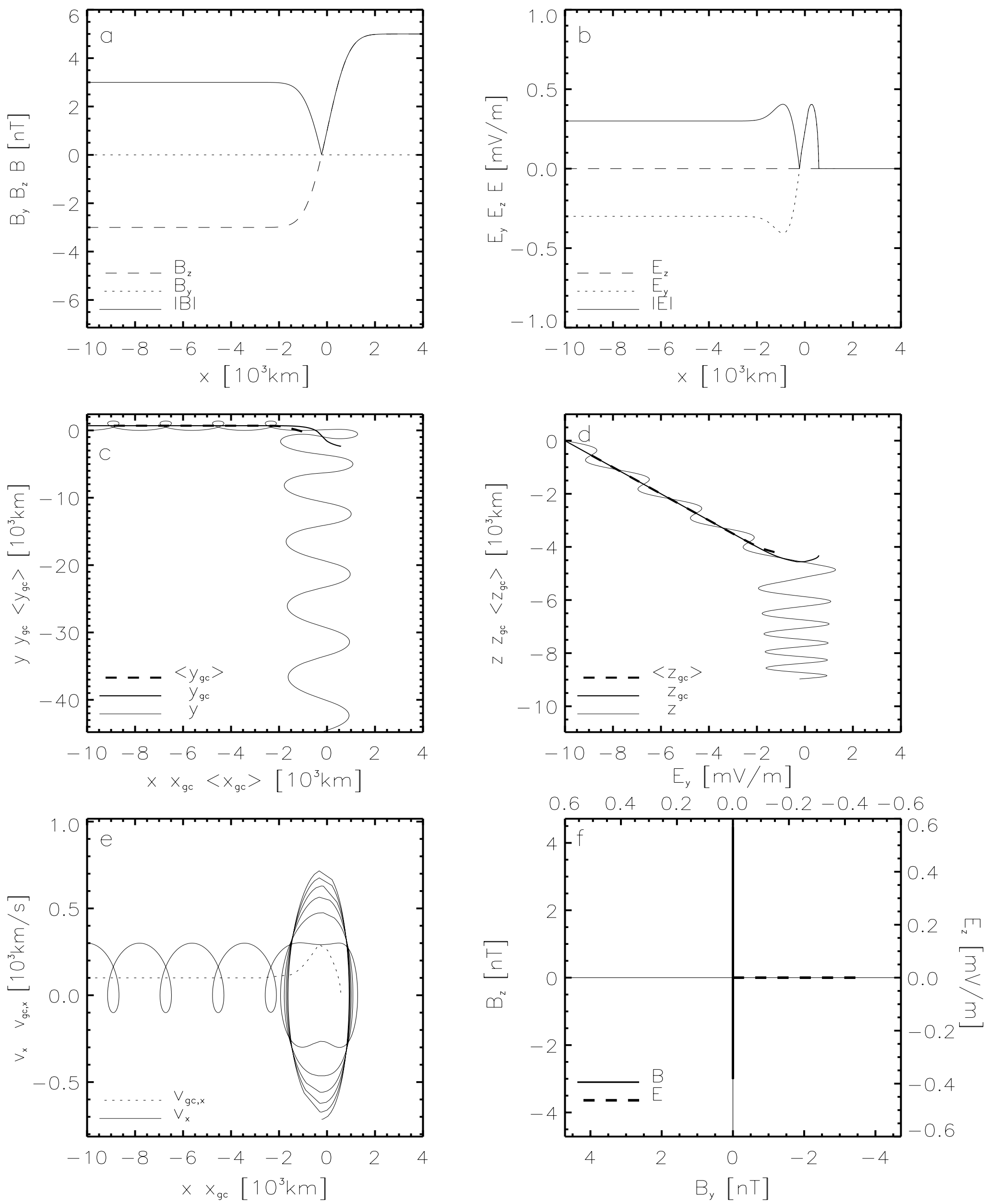

Figure 2.11: *Case C'* - non-penetrating proton trajectory : panel ***a***) gives the B-field distribution; panel ***b***) gives the E-field distribution; panel ***c***) shows the xOy projection of particle, guiding center, and averaged gc trajectories; panel ***d***) shows the xOz projections; panel ***e***) gives the (x, v_x) phase space plot for particle and guiding center; panel ***f***) shows the B and E fields as "seen" by the drifting proton of 430 eV.

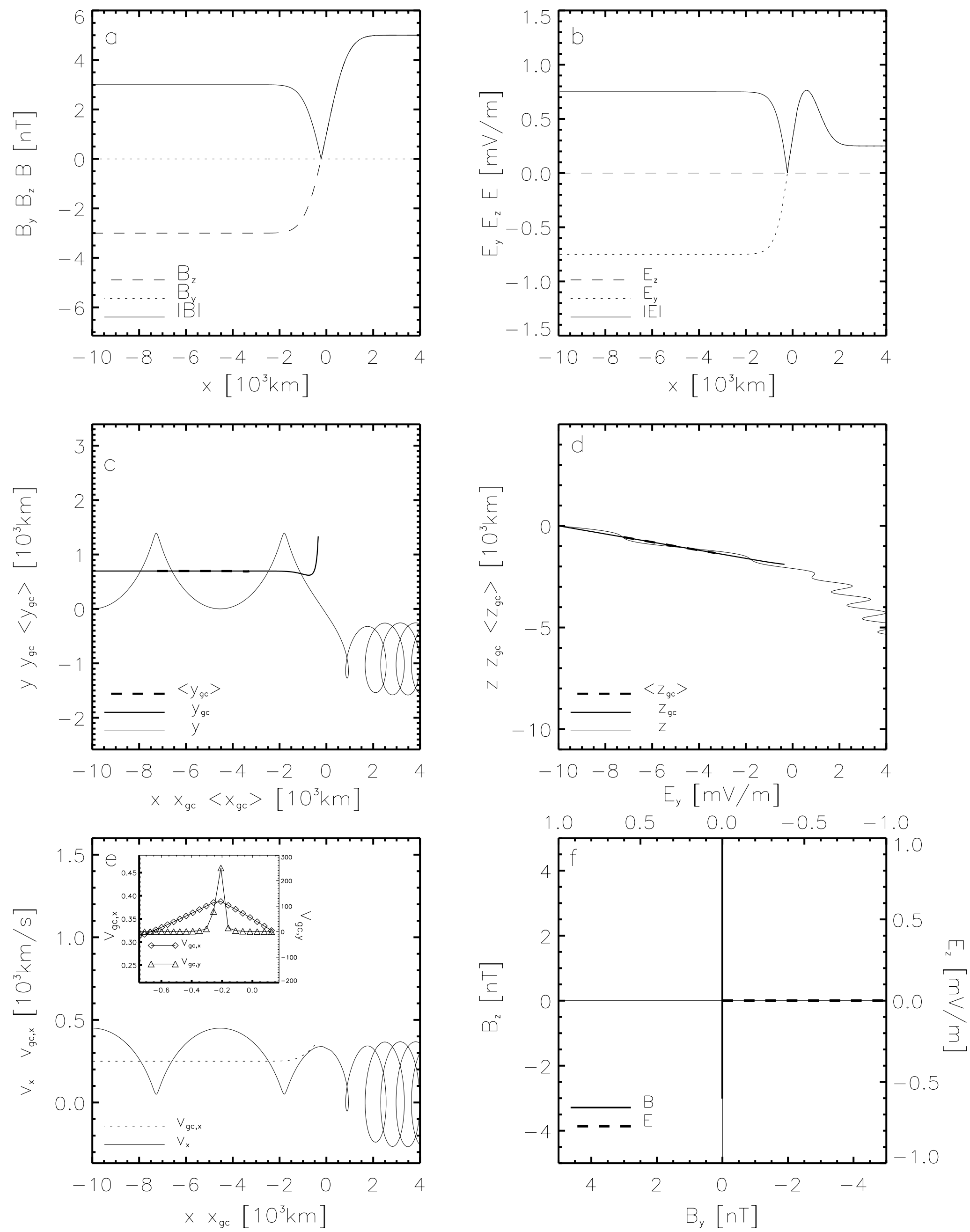

Figure 2.12: *case C′* - penetrating proton trajectory; the distribution of the plots in the six panels is similar to figure **2.11**

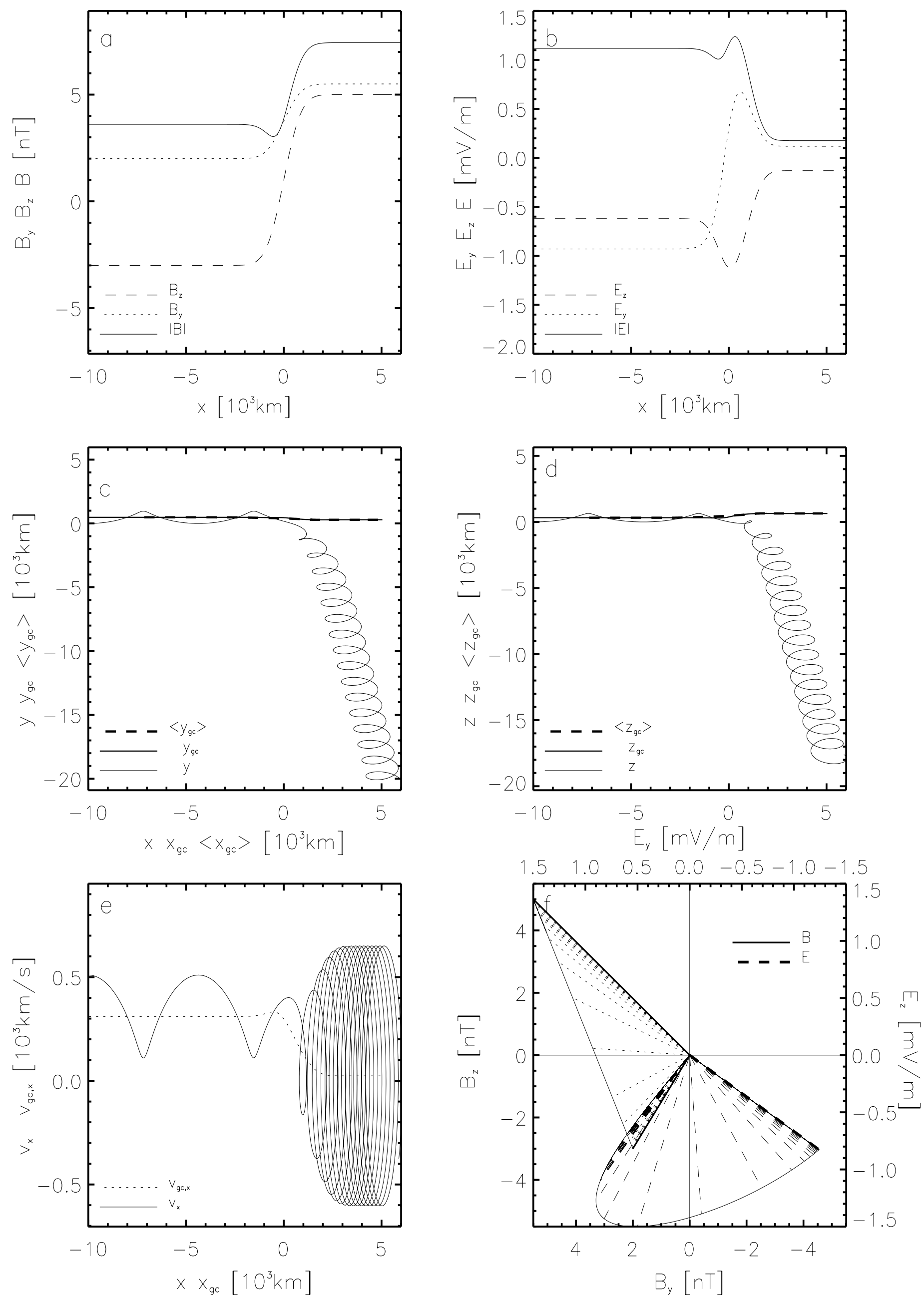

Figure 2.13: *case C* - penetrating proton trajectory injected into a B-field distribution having a large angle of shear; the six panels show the plots of the same variables as figure **2.11**

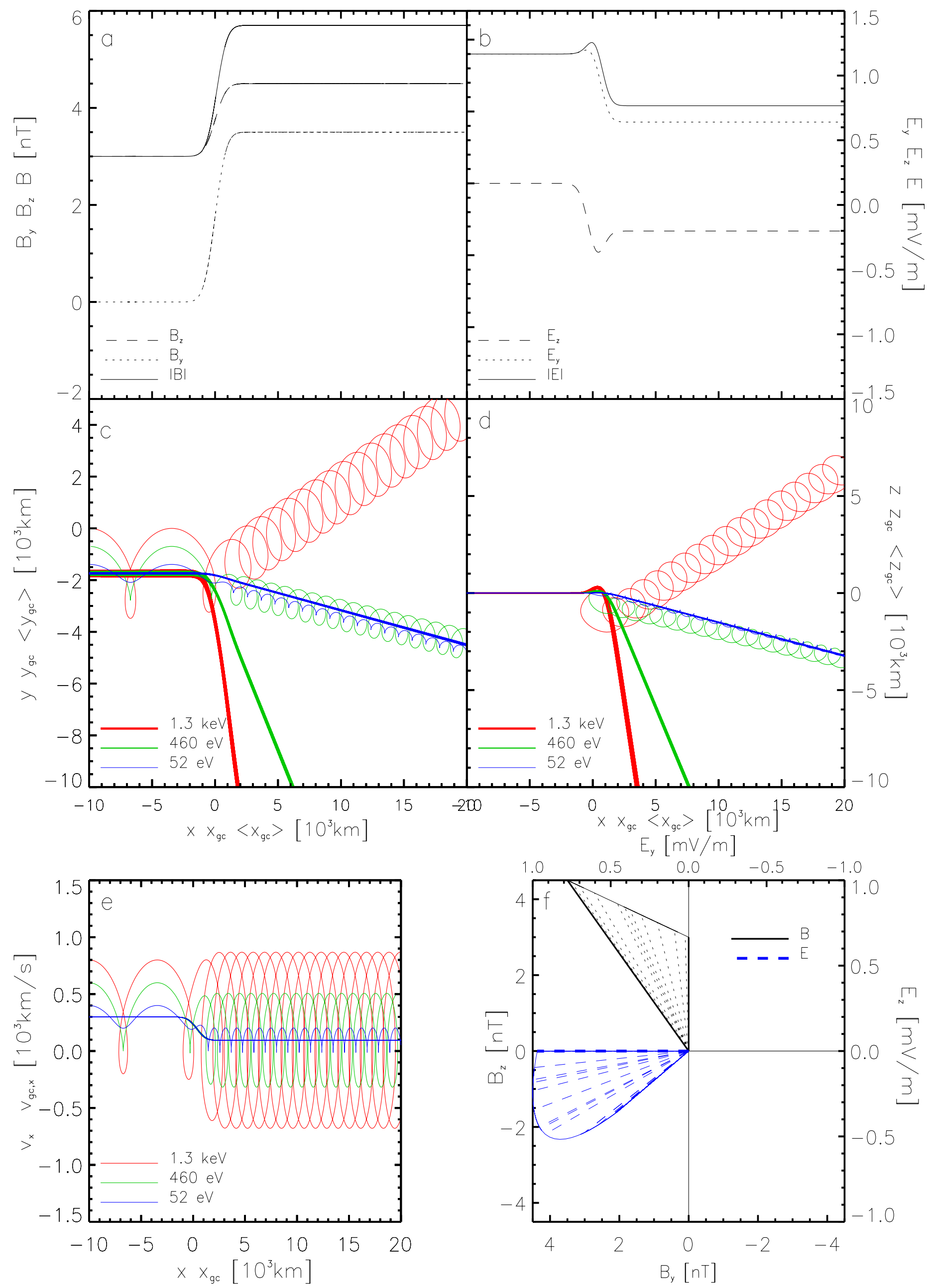

Figure 2.14: *case C* - three penetrating protons and electrons across a *sheared* B-field distribution; the six panels give the distribution of the same variables as in figure **2.11**

Figure **2.13 e** shows clearly that when the particle enters the region of increased B-field it experiences an increase of the gyration (kinetic) energy. At the same time the convection energy and consequently the velocity of advancement in the Ox direction decrease. The calculated guiding center path does not track the average of the actual orbit of the particle as shown in figures **2.13 c-d**. The reason for this mismatch is that the scale length of the discontinuity, L, is comparable to the Larmor radius of the test-proton and as a matter of consequence the Alfven condition (1.4) is not satisfied.

Additional particle simulations for magnetic field gradients whose characteristic scale length, L, is much larger than the local Larmor radius demonstrate that the particle cannot penetrate beyond the point where the gyration energy becomes equal to the initial total energy even when the Alfven conditions are strictly satisfied (*Echim*, 2002b; *Echim and Lemaire*, 2003).

Assuming that the electric field distribution of case C is produced inside a moving non-diamagnetic plasma irregularity the results discussed here can be used to understand the interaction of the solar wind with the magnetosphere. They illustrate at a kinetic scale the mechanism of plasma penetration across magnetic field barriers proposed by *Lemaire* (1985). In order to penetrate into the magnetosphere a plasmoid needs to have a sufficiently large momentum density to pass through the magnetic barrier at the magnetopause. The results of case C indicate that the penetration takes place for any magnetic shear angle and/or relative orientation of $\boldsymbol{B}$ on both sides of the magnetopause, provided that the plasmoid has enough initial momentum.

In order to illustrate the mass and charge effects figures **2.14 a-f** show the results obtained for three pairs of electrons and protons having different initial energies and momentum. The magnetic field is sheared and its intensity increases from 3 nT to 5 nT over a distance equal to 5000 km. The initial velocity of the guiding center is equal to 300 km/s. The electric field intensity decreases from an initial value $E_1 = 1.3$ mV/m to 0.75 mV/m. All the protons and ions have enough initial energy to pass through the discontinuity and to enter the right hand side of the TD. Tracing the numerical trajectories of particles shows that the deflection of the particles from their initial drift direction depends on their energy: the particle with the highest energy is deflected most.

The deflection in the y-direction, perpendicular to $\boldsymbol{B}$ is due to the gradients of the magnetic and electric fields and depends on the charge and velocity of the particle in the gc frame. This deflection contributes an electric current in the Oy direction. In case of a moving plasma element the J_y current evidenced above is called a displacement current. At the front edges of the penetrating plasma element it this current that carries continuously charges to the lateral edges of the moving plasma element. The displacement current sustains the polarization electric field that drives the forward motion of plasma. The role of the displacement current has been theoretically outlined by *Schmidt* (1960) and *Lemaire* (1985) in their kinetic theories of plasma motion across magnetic field.

To summarize this subsection, we point out that the electric field distribution described by equations (2.6) and (2.7) simulates the polarization field produced by charge separation at the edges of solar-wind plasmoids. It is based on the theoretical models proposed by *Demidenko et al.* (1967, 1969) and generalized by *Lemaire* (1985) for sheared magnetic fields. The numerical results discussed in the subsection devoted to case C are relevant for the plasma particles forming the "core" of the impulsively penetrating plasmoid. Indeed, test-particles considered here are assumed not to contribute to the space charge and current density.

The numerical results illustrate both quantitatively and qualitatively the mechanism of adiabatic breaking of the particle injected into B-field distribution having a positive gradient ($dB/dx > 0$). This mechanism is based on the conservation of the first adiabatic invariant imposing that the convection energy of the particle is transformed into gyration energy. Provided the particle has enough initial total energy, it is braked in regions of increasing total magnetic field but can penetrate all the way through the region of non-uniform B-field.

In the case of an antiparallel distribution of the magnetic field, there is a neutral plane, $x = 0$, where the magnetic field intensity is equal to zero. As in the previous two cases the exact equation of motion of the particle has no singularity at the neutral plane. It is only the first order drift approximation that is (mathematically not physically) singular at $x = 0$. In case C' no jetting of particles is observed on the contrary to the case A'.

2.4 Summary and conclusions

We have performed a set of numerical simulations by integrating numerically the trajectory of test-particles injected into the magnetic field distribution of a one-dimensional tangential discontinuity. The main feature of this distribution is that the magnetic field vector is confined into the yOz plane and $B_x = 0$ everywhere. The particles are "test-particles" in the sense that their motion does not perturb the electromagnetic field.

Previous studies of test-particles trajectories injected into non-uniform B-field distributions have pointed out the role of B_n, the normal component of $\boldsymbol{B}$, in driving the particles across rotational discontinuities. When B_n is different from zero the particle dynamics is non-integrable from the point of view of fundamental dynamics, i.e. there are only two independent constants of motion (*Chen and Palmadesso*, 1986; *Büchner and Zelenyi, 1989*).

In our work we emphasize the role of the electric field superimposed onto a B-field distribution when $B_n = 0$. Indeed, we have tested three different distributions of the electric field: (A) uniform, (B) conserving the zero order drift, and (C) conserving the magnetic moment.

The main objective of this part was to show that at the location where $B = 0$ (or at an X-line in reconnection models) drifting particles do not necessarily experience anomalous acceleration or 90^0 deflections as assumed to be the case in the diffusion region around the X-line. As our results demonstrate, the exact equations of motion of charged particles are not singular at an X-line or in a plane where $B = 0$. It is only the MHD convection velocity, $\boldsymbol{U}_E = \boldsymbol{E} \times \boldsymbol{B}/B^2$ that diverges as well as the Larmor radius of the particles. The actual velocity does not diverge. The drift path of the guiding center is not necessarily deflected at right angles.

True acceleration of particles occurs in a steady B-field distribution when and where the electric field intensity has non-zero component parallel to the magnetic field lines. True reconnection occurs also when the electric field intensity has a non-zero component parallel to the X-line. From the six case studies simulated here only one (case A') reproduce the particle dynamics predicted by the steady-state reconnection model. Indeed in case A' we have retrieved an acceleration of the particles in the direction normal to the neutral plane. This corresponds to the formation of thin current sheets and jetting at the reconnection site where $B = 0$ and $E \neq 0$.

In the other five cases the test-particle simply moved across the field reversal region and penetrated inside the right hand side of the TD along a distance that depends on the initial energy of the particle and the electric and magnetic field distribution. In case A the electric field had a finite parallel component throughout the simulation domain, not only in the neutral plane as in the reconnection models. The particle experiences a true acceleration in the direction of the magnetic field. In cases B', B, C' and C the electric field was everywhere perpendicular to the magnetic field. In all these cases we found electric field distributions that enable mass transport across a sheared B-field distribution.

These results demonstrates that the topology of the electromagnetic field prescribed by the steady-state reconnection models is by no means necessary to transport plasma from the magnetosheath into the magnetosphere. We give here five alternatives that may also exist at the magnetopause. It remains for some of them to be tested using comprehensive experimental data collected in the magnetopause region.

Part II

The kinetic treatment of steady sheared two-dimensional flows in collisionless magnetized plasma

Chapter 3

Kinetic model of a two-dimensional sheared plasma flow

In the previous chapter it has been investigated the dynamics of test-particles injected into a non-uniform electromagnetic field, like that existing in the magnetopause when this surface can be approximated by a tangential discontinuity. The one-dimensional distributions of $\boldsymbol{E}$ and $\boldsymbol{B}$ fields used for numerical integration were prescribed. It has also been assumed that the test-particles do not perturb the background fields. In the following chapters some of these limitations/approximations will be relaxed. Electric and magnetic field distributions will be determined as a solution for the system of equations that couples the plasma velocity distribution functions (Vlasov equation) and the electromagnetic field (Poisson-Ampere equations).

Instead of integrating individual trajectories we will study an "ensemble" of positive ions (protons) and electrons. Each species is described by its own velocity distribution function (VDF). In the MHD (or zero order) approximation of plasma physics it is considered that this ensemble of charged particles –the *plasma*– is drifting across magnetic field lines with an average velocity equal to the *convection velocity*:

$$\boldsymbol{U}_E = \frac{\boldsymbol{E} \times \boldsymbol{B}}{B^2}$$

where $\boldsymbol{E}$ and $\boldsymbol{B}$ are the total electric and magnetic field, including the external as well as the internal (plasma) contribution.

In the kinetic approximation the average velocity –or *bulk velocity*– of plasma is computed from the partial average velocities ,$< \boldsymbol{v}_\alpha >$, of each component ion species and electrons respectively :

$$\boldsymbol{V} = \frac{\sum_\alpha m_\alpha n_\alpha < \boldsymbol{v}_\alpha >}{\sum_\alpha m_\alpha n_\alpha}$$

$\boldsymbol{U}_E$ can be considered an approximation of $\boldsymbol{V}$ only when the electric and magnetic field distributions are uniform and steady state. Whenever the electromagnetic fields have gradients and/or shears, this approximation is not valid anymore.

In the following we will study the problem of a two-dimensional non-uniform streaming of a plasma across the magnetic field. Both $\boldsymbol{E}$ and $\boldsymbol{B}$ field can be non-uniform. An external magnetic field, $\boldsymbol{B} \equiv (0, 0, B_0)$ is assumed but the perturbation produced by internal plasma currents will be also calculated. In the discussion that follows below "perpendicular" and "parallel" refer to the direction of the total magnetic field (including the plasma internal contribution).

The case of plasma flow across magnetic field with the *perpendicular bulk velocity varying in the direction* <u>*perpendicular*</u> *to* $\boldsymbol{B}$ *and* $\boldsymbol{V}$ has been studied by the one-dimensional kinetic models of tangential discontinuities (*Sestero* 1966; *Roth*, 1984; *Roth et al.*, 1996). We will call this type of variation of the bulk velocity a *perpendicular shear* since the perpendicular velocity varies only in the direction perpendicular to the magnetic field. Experimental data from laboratory and space show that the perpendicular component of the plasma bulk velocity can vary also in the direction <u>parallel</u> to the magnetic field. This type of variation of the plasma bulk velocity will be called then a *parallel shear*. In the general case both types of shear can be present. This situation will be called a *mixed shear*.

In this study we consider a two dimensional plasma flow. The bulk velocity is oriented in the Ox direction, $\boldsymbol{V} = (V_x(y, z), 0, 0)$. We will look for a kinetic solution that gives a non-uniform bulk velocity that is sheared in both directions: perpendicular and parallel to the magnetic field. Kinetic solution for the parallel shears of velocity were not reported yet in the literature. The self-sustained electromagnetic field, including the electric parallel component, will be computed starting from Vlasov and Maxwell equation. The geometry of the problem is inherently two-dimensional.

This chapter is organized as follows: section **3.1** introduces briefly the main concepts used by the plasma kinetic theory; section **3.2** describes the geometry and the $2D$ boundary conditions to be fulfilled by the fields; section **3.3** gives the velocity distribution function that is solution of the Vlasov equation; in section **3.4** the moments of the VDF are computed analytically by integrating the Vlasov solution in the velocity space.

3.1 The Vlasov-Poisson-Ampere system of equations

The global plasma dynamics may be described in terms of macroscopic quantities like mass and particle density, bulk velocity and momentum, energy, etc., that are "observable" by physical instruments like detectors, probes, magnetometers, etc. It is important to keep in mind however that the generally called "global/macroscopic/fluid" behavior of plasma is intrinsically related to its microstructure or kinetics, i.e. the velocity distribution function (VDF) of the electrons and each ion species.

The equation describing the evolution of the VDF (f) in a collisionless plasma has been given by *Vlasov* (see *Vlasov*, 1961) by applying the general Liouville theorem for a collisionless plasma :

$$\frac{\partial f}{\partial t} + \boldsymbol{v} \cdot \frac{\partial f}{\partial \boldsymbol{r}} + \frac{q}{m} \left(\boldsymbol{E} + \boldsymbol{v} \times \boldsymbol{B} \right) \cdot \frac{\partial f}{\partial \boldsymbol{v}} = 0 \tag{3.1}$$

where the $\boldsymbol{E}$ and $\boldsymbol{B}$ fields include both the external component and the internal component produced by the electric charge density and electric currents of the plasma itself. For a mixture of positive ion species and electrons, each component species, α, will be described by its own velocity distribution, f_α, that satisfies equation (3.1).

The Vlasov equation (3.1) is a nonlinear partial derivative equation. The charge and current density are nonlinear functions of f_α; they are determined by the moments of the velocity distribution functions. Once the velocity distribution function is determined from (3.1), one can compute the spatial distribution of the charge and current density by integrating over the entire velocity space:

$$\rho(\boldsymbol{r}, t) = \sum_\alpha q_\alpha \int\int\int f_\alpha d^3\boldsymbol{v} \tag{3.2}$$

$$\boldsymbol{j}(\boldsymbol{r}, t) = \sum_\alpha q_\alpha \int\int\int \boldsymbol{v} f_\alpha d^3\boldsymbol{v} \tag{3.3}$$

where $d^3\boldsymbol{v} = dv_x dv_y dv_z$ is the infinitesimal volume element of the velocity space.

The electromagnetic field satisfies Maxwell equations: the electric potential distribution satisfies Poisson's equation and the magnetic vector potential distribution satisfies Ampere equation:

$$\nabla^2 \Phi = -\frac{1}{\epsilon_0}\rho \tag{3.4}$$

$$\nabla^2 \boldsymbol{A} = -\mu_0 \boldsymbol{j} - \epsilon_0 \frac{\partial \boldsymbol{E}}{\partial t} \tag{3.5}$$

where ρ and $\boldsymbol{j}$ are the charge density and current density of the plasma itself.

In a steady state situation, $\partial/\partial t = 0$, the electric and the magnetic intensities are defined as:

$$\boldsymbol{E} = -\boldsymbol{\nabla}\Phi \tag{3.6}$$

$$\boldsymbol{B} = \boldsymbol{\nabla} \times \boldsymbol{A} \tag{3.7}$$

Of course the other two Maxwell equations must also be satisfied:

$$\boldsymbol{\nabla} \times \boldsymbol{E} = 0 \tag{3.8}$$

$$\boldsymbol{\nabla} \cdot \boldsymbol{B} = 0 \tag{3.9}$$

(3.8) is automatically satisfied due to (3.6). Equation (3.9) is also satisfied due to eq. (3.7).

In the remainder of this thesis we will search for a steady-state solution of the system of equations (3.1) and (3.4)-(3.5) with the plasma charge and current densities calculated from (3.2)-(3.3).

3.2 Equations and two-dimensional boundary conditions for the electromagnetic fields

Let us briefly state the problem we want to solve in this chapter: we assume that a driving force sustains a stationary plasma flow in the direction Ox, normal to the magnetic field (see figure **3.1**). The bulk velocity of the plasma is non-uniform: it varies along the direction of the magnetic field (z-direction in figure **3.1**) generating a *parallel shear*. The plasma bulk velocity may also vary in the direction perpendicular to the magnetic field (y-direction in fig. **3.1**) generating a *perpendicular shear*.

3.2.1 Flow and field geometry

The main (external) magnetic field is parallel to Oz, $\boldsymbol{B}_0 = (0, 0, B_0)$. The internal plasma currents may produce an additional component, B_y. There is an additional condition, $B_x = 0$ that is satisfied everywhere.

We search the velocity distribution functions of each species (H^+ and electrons in this study) – solutions of the Vlasov equation– and the electric and magnetic field distributions –solutions of the Maxwell equations– that satisfy the flow and field pattern described above. The front edge interaction

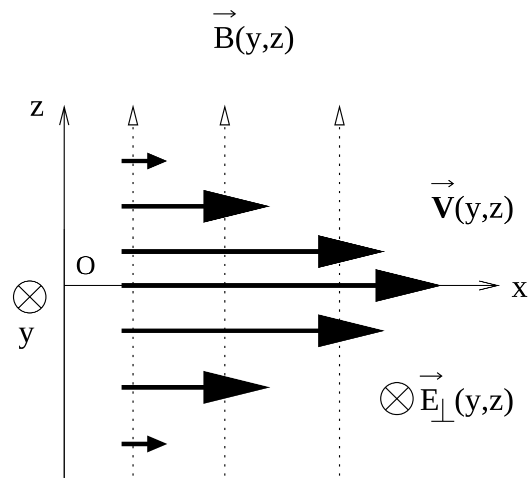

Figure 3.1: Field and flow distribution with parallel shear ($\partial V_x/\partial z \neq 0$) illustrated in the case when the plasma magnetic perturbation is very small with respect to the external magnetic field ($B_y \ll B_0$). Dotted lines illustrate the magnetic field distribution, solid arrows illustrate the plasma bulk velocity profile that has a maximum in the plane $z = 0$.

of the flow with the ambient plasma and field is not treated here. As a matter of consequence the spatial coordinate x is ignorable.

The cross-B propagation of a plasma element sets-up a polarization electric field which is perpendicular to both $\boldsymbol{B}$ and $\boldsymbol{V}$. The polarization component of the electric field that sustains the plasma advancement in the direction normal to the magnetic field has been discussed by *Schmidt* (1960) and *Lemaire* (1985) from a microscopic/kinetic point of view. Two-fluid, non-MHD, models have also treated the polarization electric produced by the plasma motion across B-field lines (*Dolique*, 1963; *Peter and Rostoker*, 1982; *Buneman*, 1992). Recently the problem of "what drives what" has been investigated by *Vasyliunas* (2001) in the framework of magnetohydrodynamics. He reaches the same result as put forward by kinetic theory: the cross-B flow drives a polarization electric field and not the reverse as postulated in the ideal MHD where the displacement current is neglected in Maxwell's equation (3.5).

The two independent spatial variables considered in this chapter are z and y. We assume that there is an external magnetic field aligned with z. We also assume that $\boldsymbol{V}$, the plasma bulk flow is parallel to Ox but non-uniform; $\boldsymbol{V}$ is sheared, i.e. it depends on z and y. When the internal contribution of the plasma currents is taken into account a B_y component may also exist. There are two privileged directions in this sheared magnetized plasma flow:

Oz - the direction of the main magnetic field $\boldsymbol{B}_0$ and Ox - the direction of the main plasma bulk velocity $\boldsymbol{V}$. A schematic picture of the geometry of the flow described above is given in figure **3.1** for the case when the diamagnetic currents do not modify the external magnetic field.

3.2.2 Maxwell's equations

Since x is an ignorable coordinate of the problem we can introduce $\partial/\partial x = 0$ in Maxwell's equations (3.4) - (3.9). For the electric field we obtain :

$$\boldsymbol{E}(y,z) = (E_0, E_y(y,z), E_z(y,z)) \tag{3.10}$$

where E_0 is a constant that necessarily is equal to zero in order to satisfy the requirement that the plasma flow is aligned with Ox-direction. The only non-vanishing components of the electric field are $E_y(y,z)$ and $E_z(y,z)$. The magnetic field distribution is given by

$$\boldsymbol{B}(y,z) = \boldsymbol{\nabla} \times \boldsymbol{A}(y,z)$$

For the sake of simplification and without loss of generality we assume that $A_y = A_z = 0$. implying that:

$$\boldsymbol{B}(y,z) \equiv \left(0, \frac{\partial A_x(y,z)}{\partial z}, -\frac{\partial A_x(y,z)}{\partial y}\right) \tag{3.11}$$

Under steady-state conditions ($\epsilon_0 \partial \boldsymbol{E}/\partial t$=0) one can write:

$$\mu_0 \boldsymbol{J} = \left(-\frac{\partial^2 A_x}{\partial y^2} - \frac{\partial^2 A_x}{\partial z^2}, 0, 0\right) \tag{3.12}$$

From equation (3.11) above one can note that

$$\boldsymbol{\nabla} \cdot \boldsymbol{B} = 0$$

is automatically satisfied. In a steady-state electromagnetic field the equation (3.8) becomes:

$$\frac{\partial E_z}{\partial y} - \frac{\partial E_y}{\partial z} = 0$$

and is satisfied due to (3.6). The equations above define the general configuration of the fields under the assumptions that $\partial/\partial x = 0$ and $\partial/\partial t = 0$.

The distribution of the electric, $\Phi(y, z)$, and magnetic vector potentials, $\boldsymbol{A}(y, z)$, are solution of the Maxwell's equations (3.4) - (3.9) that in $2D$ read as below:

$$\frac{\partial^2 \Phi}{\partial y^2} + \frac{\partial^2 \Phi}{\partial z^2} = -\frac{1}{\epsilon_0}\rho(y, z) \tag{3.13}$$

$$\frac{\partial^2 A_x}{\partial y^2} + \frac{\partial^2 A_x}{\partial z^2} = -\mu_0 j_x(y, z) \tag{3.14}$$

with

$$E_y = -\frac{\partial \Phi}{\partial y} \quad , \quad E_z = -\frac{\partial \Phi}{\partial z} \tag{3.15}$$

$$B_y = \frac{\partial A_x}{\partial z} \quad , \quad B_z = -\frac{\partial A_x}{\partial y} \tag{3.16}$$

The solutions of the system (3.13)-(3.14) will be computed in a rectangular domain of the yOz plane. The boundaries of the two-dimensional simulation domain are determined by $y \in [-y_\infty, +y_\infty]$ and $z \in [-z_\infty, +z_\infty]$ respectively. Recall that all physical quantities are independent of the x-coordinate which is ignorable in the rest of this text.

3.2.3 Asymptotic values of fields and potentials. Boundary conditions

Since in Chapter 4 we will test the $2D$ kinetic solution by simulating a one-dimensional case, let us discuss first the asymptotic conditions for a plasma flow and field depending only on y.

Sestero Tangential Discontinuity

In Sestero one-dimensional model of a tangential discontinuity (TD) all the quantities vary only with the coordinate normal to the discontinuity surface (*Sestero*, 1966). The plasma flow is everywhere perpendicular to $\boldsymbol{B}$. A graphical illustration of the flow pattern is given in figure **3.2**.

The plasma bulk velocity takes a non-zero value (V_L) at the left hand side of the discontinuity ($y = -y_\infty$). The bulk velocity decreases and takes the zero value at the right hand side ($y = +y_\infty$). The transition between these two asymptotic values is computed self-consistently. In a Sestero TD the magnetic field is everywhere parallel to the Oz-axis. The intensity of $\boldsymbol{B}$ is fixed at the two lateral edges: $B_L = B_R = B_0$.

This asymptotic behavior is also described by the general boundary conditions given in table 3.1. They correspond to a TD that is parallel to the plane

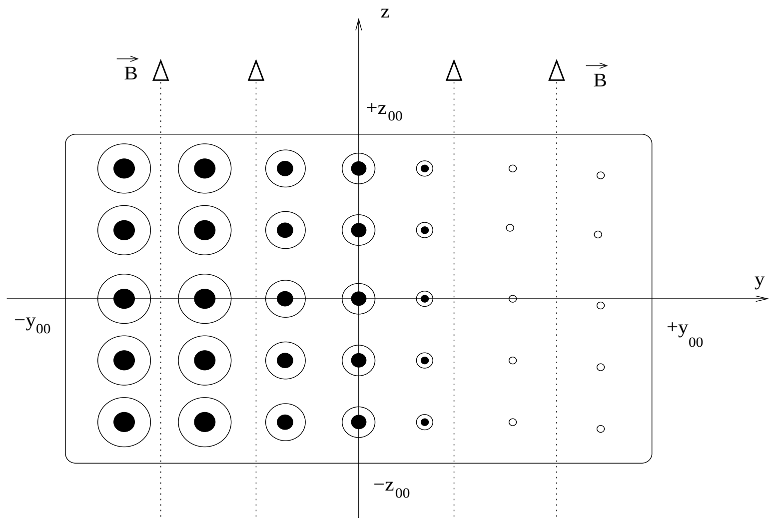

Figure 3.2: Flow configuration of the Sestero Tangential Discontinuity. Plasma flows in the positive x-direction, out of the page. Plasma bulk velocity is represented by circles whose diameter is proportional to $V(y)$. The bulk velocity has a maximum at the left hand side ($y \to -y_\infty$) and decreases with increasing y, taking zero value at the right side ($y \to +y_\infty$). Dotted lines illustrate the B-field distribution. The TD is centered in $y = 0$.

xOz; the electromagnetic potentials and fields as well as plasma parameters depend only on y - the coordinate normal to the TD plane.

Not all the boundary values specified in table 3.1 are independent. Indeed, the boundary values of the convection velocity and magnetic field intensity determine the boundary values of the convection electric field. Thus at the left hand side the electric field is oriented parallel to Oy-axis and takes the value: $E_L = V_0 B_0$. At the right hand side the electric field is equal to zero since the convection velocity is equal to zero. The parallel component of $\boldsymbol{E}$ is everywhere equal to zero in a Sestero TD. The profiles of variation for $A_x^B(y)$, $A_x^T(y)$, $B(y)$, $\Phi^B(y)$, $\Phi^T(y)$, $E_y^B(y)$, $E_y^T(y)$ and $V_x(y)$ are computed self-consistently as will be described in the next chapter. The free input parameters of the boundary conditions are V_0 and B_0.

In the Sestero TD the electric potential, $\Phi(y)$, is computed from the plasma quasineutrality equation. The non vanishing component of the magnetic vector potential is computed from the Ampere equation (3.14) with the boundary conditions of Robin-type specified in table 3.2. The values of A_x are specified on the $z = \pm z_\infty$ boundaries while the derivatives $\partial A_x/\partial z$ are specified on the $y = \pm y_\infty$ borders. The latter condition is equivalent to imposing $B_y = 0$ but letting B_z to vary with y. The Sestero TD will be simulated in Chapter 4 as a test case for our $2D$ kinetic model.

Table 3.1: Two-dimensional boundary/asymptotic values of the electromagnetic potentials and fields and of the plasma bulk velocity characterizing a Sestero-type tangential discontinuity

	$y = -y_\infty$	$y = +y_\infty$	$z = -z_\infty$	$z + z_\infty$
Φ	$E_L y_\infty + \phi^L$	ϕ^R	$\Phi^B(y)$	$\Phi^T(y)$
A_x	$B_0 y_\infty + A_x^L$	$-B_0 y_\infty + A_x^R$	$A_x^B(y)$	$A_x^T(y)$
$\boldsymbol{B}$	$(0, 0, B_0)$	$(0, 0, B_0)$	$(0, 0, B(y))$	$(0, 0, B(y))$
$\boldsymbol{E}$	$(0, E_y^L, 0)$	$(0, 0, 0)$	$(0, E_y^B(y), 0)$	$(0, E_y^T(y), 0)$
$\boldsymbol{V}$	$(V_0, 0, 0)$	$(0, 0, 0)$	$(V_x(y), 0, 0)$	$(V_x(y), 0, 0)$

Table 3.2: Robin-type boundary conditions used in the Sestero TD model to solve the Ampere equation (3.14) in the $2-D$ domain $[-y_\infty, +y_\infty] \times [-z_\infty, +z_\infty]$.

	$y = -y_\infty$	$y = +y_\infty$	$z = -z_\infty$	$z = +z_\infty$
A_x	$B_0 y_\infty$	$-B_0 y_\infty$	-	-
$\frac{\partial A_x}{\partial y}$	-	-	-	-
$\frac{\partial A_x}{\partial z}$	-	-	0	0

Two-dimensional sheared plasma flow

The asymptotic values and boundary conditions defined in the previous subsection will be modified to describe the more general case of a two-dimensional plasma flow.

An illustration of the $2D$ flow is given in figure **3.3**. The asymptotic values of the electromagnetic fields and velocity for a $2D$ plasma flow are given in table 3.3. The boundary value of the plasma bulk velocity at the left hand side of the simulation domain ($y = -y_\infty$) depends on z. In the computations of chapter 4 the profile of $V_L(z)$ is computed self-consistently; the only constraint is that it takes a maximum value in $z = 0$. The bulk velocity decreases and takes the zero value at the right hand side ($y = +y_\infty$).

The transition between the two asymptotic plasma flowing regimes will be computed self-consistently.

The asymptotic magnetic field is assumed to be parallel to the Oz-axis except for the left boundary, $y = -y_\infty$, where an additional $B_{yL}(z)$ component is added. Not all the asymptotic values described in table 3.3 are independent. The asymptotic values of the electric field satisfies: $\boldsymbol{E}^L_\perp = \boldsymbol{V}^L \times \boldsymbol{B}^L$, $E^B_y = V^B_x(y)B_0$ and $E^T_y = V^T_x(y)B_0$. We impose also that the parallel electric component tends to zero at $z = \pm z_\infty$.

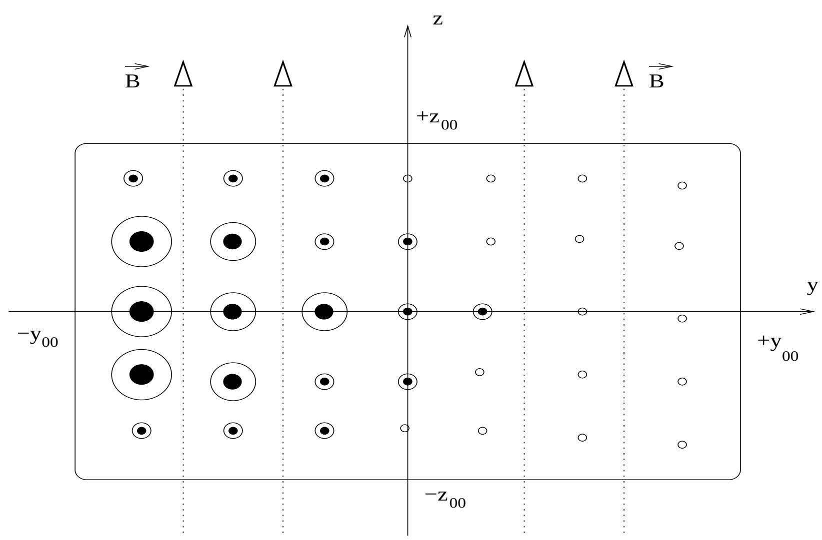

Figure 3.3: $2D$ plasma flow across B-field - plasma bulk velocity is everywhere parallel to the positive x-direction, out of the page; it is illustrated by circles having the diameter proportional to $V(y, z)$. Dotted lines illustrate the distribution of the external magnetic field. Plasma internal perturbation of $\boldsymbol{B}$ is not shown but it is self-consistent computed.

The asymptotic conditions for plasma and fields given in table 3.3 define the mathematical boundary conditions used in Maxwell's equations. The electric potential, $\Phi(y, z)$ will be determined from the equation of plasma neutrality. The non vanishing component of magnetic vector potential will be found from the Ampere equation (3.14) with Dirichlet boundary conditions specified in table 3.4.

So far we specified the values of the potentials and fields on the boundaries of the two-dimensional domain. We will now define the charge density and current density that are the "sources" of the potentials inside the domain.

Table 3.3: Two-dimensional boundary/asymptotic values of the electromagnetic potentials and fields and of the plasma bulk velocity characterizing a $2D$ sheared plasma flow.

	$y = -y_\infty$	$y = +y_\infty$	$z = -z_\infty$	$z + z_\infty$
Φ	$-E_L(z)y + \phi_L$	ϕ_R	$\Phi_B(y)$	$\Phi_T(y)$
A_x	$B_0 y_\infty + \zeta(z)$	$-B_0 y_\infty$	$-B_0 y$	$-B_0 y$
$\boldsymbol{B}$	$(0, B_y^L(z), B_z^L(z))$	$(0, 0, B_0)$	$(0, 0, B_0)$	$(0, 0, B_0)$
$\boldsymbol{E}$	$(0, E_y^L(z), E_z^L)$	$(0, 0, 0)$	$(0, E_y^B(y), 0)$	$(0, E_y^T(y), 0)$
$\boldsymbol{V}$	$(V_x^L(z), 0, 0)$	$(0, 0, 0)$	$(V_{xB}(y), 0, 0)$	$(V_{xT}(y), 0, 0)$

Table 3.4: Dirichlet-type boundary conditions used in the 2D sheared model to solve the Ampere equation (3.14) in the $2D$ domain $[-y_\infty, +y_\infty] \times [-z_\infty, +z_\infty]$.

	$y = -y_\infty$	$y = +y_\infty$	$z = -z_\infty$	$z = +z_\infty$
A_x	$B_0 y_\infty$	$-B_0 y_\infty$	$-B_0 y$	$-B_0 y$
$\frac{\partial A_x}{\partial y}$	-	-	-	-
$\frac{\partial A_x}{\partial z}$	-	-	-	-

3.3 Steady-state kinetic solution of the 2D sheared flow

The velocity distribution function , f_α is generally considered to be the probable number of particles of the species α that are confined in space in a sphere centered in $\boldsymbol{r}$ having the radius $d\boldsymbol{r}$ and with velocities in the range $(\boldsymbol{v}, \boldsymbol{v}+\mathrm{d}\boldsymbol{v})$, at time t. In the case of a steady-state two-dimensional problem, with x being ignorable, the Vlasov equation (3.1) reads as follows :

$$\begin{aligned} & v_y \frac{\partial f_\alpha}{\partial y} + v_z \frac{\partial f_\alpha}{\partial z} - \frac{q_\alpha}{m_\alpha}\left[v_y \frac{\partial A_x}{\partial y} + v_z \frac{\partial A_x}{\partial z}\right]\frac{\partial f_\alpha}{\partial v_x} \\ & -\frac{q_\alpha}{m_\alpha}\left[\frac{\partial \Phi}{\partial y} - v_x \frac{\partial A_x}{\partial y}\right]\frac{\partial f_\alpha}{\partial v_y} - \frac{q_\alpha}{m_\alpha}\left[\frac{\partial \Phi}{\partial z} - v_z \frac{\partial A_x}{\partial z}\right]\frac{\partial f_\alpha}{\partial v_z} = 0 \end{aligned} \quad (3.17)$$

where $\Phi(y, z)$ and $A_x(y, z)$ are the electromagnetic potentials.

Equation (3.17) shows that the symmetry of the problem does not eliminate the variation of the VDF with any of the velocity components, v_x, v_y, v_z. Thus the solution of (3.17) shall depend on the three velocity components. Indeed, the velocity distribution function of a plasma streaming in the Ox direction, across the main magnetic field parallel to Oz-axis, is not gyrotropic (*Mahajan and Hazeltine*, 2000).

3.3.1 Constants of motion and adiabatic invariant

It is known that the general solution of the steady-state Vlasov equation is any function of the constants of motion (see, *Holt and Haskell*, 1965; *Delcroix and Bers*, 1994).

In the geometry chosen here rectangular coordinates are appropriate. The Lagrangian of the charged particle is equal to :

$$\mathcal{L} = \frac{m_\alpha}{2}\left({v_x}^2 + {v_y}^2 + {v_z}^2\right) - q_\alpha \phi(y,z) + q_\alpha v_x A_x(y,z) \tag{3.18}$$

In the case of stationary fields the Hamiltonian $\mathcal{H}$ of the charged particle is a constant of motion:

$$\mathcal{H} = \frac{m_\alpha}{2}\left({v_x}^2 + {v_y}^2 + {v_z}^2\right) + q_\alpha \phi(y,z) \tag{3.19}$$

Because x is ignorable, the corresponding component of the canonical momentum, p_x, is also a constant of motion:

$$p_x = m_\alpha v_x + q_\alpha A_x(y,z) \tag{3.20}$$

A thorough analysis of the Hamiltonian dynamics of the charged particle can be found, for instance, in *Lehnert* (1964).

As the solution of the Vlasov equation shall depend on all three velocity components, a third constant of motion is needed to write the solution in the velocity space and to compute its moments. We therefore introduce the magnetic moment as an adiabatic invariant that approximates well a constant of motion when the Alfven conditions (see eqs. 1.4-1.7) are fulfilled. Considering that the zero order drift velocity has only one non-vanishing component, U_{Ex}, and that $\boldsymbol{B}$ is mainly parallel to Oz-direction, the third constant of motion is approximated by:

$$\mu_\alpha = \frac{m_\alpha\left[(v_x - U_{Ex})^2 + v_y^2\right]}{2B} \tag{3.21}$$

Any function of the 3 constants of motion, $\mathcal{H}$, p_x and μ, is a solution of the Vlasov equation (3.17). In the following we will define the asymptotic conditions that must be satisfied by the solution.

3.3.2 Asymptotic values of the velocity distribution function

In section **3.2** we discussed the boundary values to be imposed onto the electromagnetic potentials. Additional assumptions must be imposed onto the asymptotic values of the velocity distribution function in order to remain consistent with the asymptotic values given in tables 3.1-3.4.

We assume that the plasma is non-moving and in thermal equilibrium at the right hand side ($y = +y_\infty$); thus each component species, α, can be described by an exponential function of the total energy, $f_{\alpha 1} = e^{-\frac{m_\alpha (v_x^2+v_y^2+v_z^2)}{2\mathcal{K}T_{\alpha 1}}}$ whose first order moments (see section 3.4) are all equal to zero ($\mathcal{K}$ is the Boltzmann constant, $T_{\alpha 1}$ the equilibrium temperature). This type of equilibrium VDF is known as the isotropic *Maxwellian* distribution function. At the left hand side boundary the plasma is moving and each species can be described by an exponential function of the energy that gives a uniform average velocity in the Ox-direction equal to V_0, $f_{\alpha 2} = e^{-\frac{m_\alpha \left[(v_x - V_0)^2+v_y^2+v_z^2\right]}{2\mathcal{K}T_{\alpha 2}}}$. This type of VDF is known as the *displaced Maxwellian* distribution function. If the bulk velocity of the plasma is non-uniform, the displaced Maxwellian does not satisfy the Vlasov equation and cannot be used to describe the moving plasma. A more general solution must be found.

Before giving the solution in the whole spatial domain we must define first the desired asymptotic values of the VDF at the borders of the $2D$ domain.

Asymptotic values of the VDF for $y = \pm y_\infty$

The boundary values of the VDF must be consistent with the boundary values chosen for the electromagnetic potentials and fields. Therefore in the left side ($y = -y_\infty$) the first order moment of the VDF must give a non-zero plasma bulk velocity in the Ox direction, V_x^L, for any z. Note that the solution given at the reference level (see sect. 3.3.3) fixes the bulk velocity in $y = -y_\infty$ for only one z value, i.e. $V_x^L(z=0) = V_0$.

In the case of a $2D$ flow, V_x^L is a function of z described by the profile $\boldsymbol{V}^L \equiv (V_x^L(z), 0, 0)$. For $y = +y_\infty$ the plasma must be at rest and the average velocity equal to zero. The asymptotic behavior on $y = -y_\infty$ and $y = +y_\infty$ can be expressed in the integral form as below:

$$\lim_{y \to -y_\infty} \left[\int_{-\infty}^{+\infty} \int_{-\infty}^{+\infty} \int_{-\infty}^{+\infty} v_x f_\alpha(y, z, v_x, v_y, v_z) dv_x dv_y dv_z \right] = V_x^L \quad (3.22)$$

$$\lim_{y \to +y_\infty} \left[\int_{-\infty}^{+\infty} \int_{-\infty}^{+\infty} \int_{-\infty}^{+\infty} v_x f_\alpha(y, z, v_x, v_y, v_z) dv_x dv_y dv_z \right] = 0 \quad (3.23)$$

where V_x^L can be a function of z.

Asymptotic values of the VDF for $z = \pm z_\infty$

The asymptotic values of the VDF in the z direction must be consistent with the condition that the plasma bulk velocity is sheared in the direction parallel to $\boldsymbol{B}$. The plasma bulk velocity must vary asymptotically to $\boldsymbol{V}^B \equiv (V_x^B, 0, 0)$ for $z = -z_\infty$ and to $\boldsymbol{V}_T \equiv (V_x^T, 0, 0)$ for $z = +y_\infty$. Since the asymptotic average velocities $\boldsymbol{V}^B$ and $\boldsymbol{V}^T$ may depend on y one can specify the asymptotic behavior of the VDF in the z-direction in terms of first order moment :

$$\lim_{z \to -z_\infty} \left[\int_{-\infty}^{+\infty} \int_{-\infty}^{+\infty} \int_{-\infty}^{+\infty} v_x f_\alpha(y, z, v_x, v_y, v_z) dv_x dv_y dv_z \right] = V_x^B \quad (3.24)$$

$$\lim_{z \to +z_\infty} \left[\int_{-\infty}^{+\infty} \int_{-\infty}^{+\infty} \int_{-\infty}^{+\infty} v_x f_\alpha(y, z, v_x, v_y, v_z) dv_x dv_y dv_z \right] = V_x^T \quad (3.25)$$

V_B and V_T are functions that can depend on y. Thus we have defined the asymptotic behavior of the Vlasov solution at the borders of the $2D$ domain. We will know give the solution in the entire domain.

3.3.3 Solution of the Vlasov equation

In order to give the Vlasov solution in the entire $3D$ space[1] we need to specify it on a reference plane.

Velocity distribution function in the $z = 0$ plane

We take the plane xOy as a reference level where we will write the solution of the Vlasov equation as a function of $\mathcal{H}$, p_x and μ. In the plane xOy we define a velocity distribution whose first oder moment gives a plasma velocity similar to that described in subsection (3.3.2) and the asymptotic conditions (3.22)-(3.23). Thus we look for a solution of the Vlasov equation that satisfies in the xOy plane the following conditions:

$$\lim_{y \to +y_\infty} f_\alpha(y, v_x, v_y, v_z) = f_{\alpha 1}(v_x, v_y, v_z) \quad (3.26)$$

$$\lim_{y \to -y_\infty} f_\alpha(y, v_x, v_y, v_z) = f_{\alpha 2}(v_x, v_y, v_z) \quad (3.27)$$

with :

$$f_{\alpha 1}(v_x, v_y, v_z) = N_{\alpha 1} \left(\frac{m_\alpha}{2\pi \mathcal{K} T_{\alpha 1}} \right)^{\frac{3}{2}} e^{-\frac{m_\alpha \left(v_x^2 + v_y^2 + v_z^2 \right)}{2\mathcal{K} T_{\alpha 1}}} \quad (3.28)$$

[1] in the $3D$ space there is no variation with the x-coordinate

$$f_{\alpha 2}\left(v_x, v_y, v_z\right) = N_{\alpha 2}\left(\frac{m_\alpha}{2\pi\mathcal{K}T_{\alpha 2}}\right)^{\frac{3}{2}} e^{-\frac{m_\alpha\left[(v_x-V_0)^2+v_y^2+v_z^2\right]}{2\mathcal{K}T_{\alpha 2}}} \quad (3.29)$$

where $N_{\alpha 1}$, $T_{\alpha 1}$ are the equilibrium density and temperature of the corresponding species of the asymptotic stagnant plasma; $N_{\alpha 2}$, $T_{\alpha 2}$ are the equilibrium density and temperature of the corresponding species of the asymptotic moving plasma. Equations (3.26)-(3.29) describe that in the plane $z = 0$ the solution of the Vlasov equation goes asymptotically to a displaced Maxwellian for $y = -y_\infty$ and to an isotropic Maxwellian for $y = +y_\infty$. As in the plane $z = 0$ the solution depends only on y it is similar to that given in the $1D$ kinetic models of the tangential discontinuities of *Sestero* (1966) and *Roth et al.* (1996).

The two asymptotic boundary VDF described by eqs. (3.28)-(3.29) can be rewritten in terms of the constants of motion:

$$f_{\alpha 1}(\mathcal{H}, p_x) = N_{\alpha 1}\left(\frac{m_\alpha}{2\pi\mathcal{K}T_{\alpha 1}}\right)^{\frac{3}{2}} e^{-\frac{\mathcal{H}}{\mathcal{K}T_{\alpha 1}}} \quad (3.30)$$

$$f_{\alpha 2}(\mathcal{H}, p_x) = N_{\alpha 2}\left(\frac{m_\alpha}{2\pi\mathcal{K}T_{\alpha 2}}\right)^{\frac{3}{2}} e^{-\frac{\mathcal{H}-p_x V_0+\frac{1}{2}m_\alpha {V_0}^2}{kT_{\alpha 2}}} \quad (3.31)$$

A function $f_\alpha(\mathcal{H}, p_x)$ that goes asymptotically to (3.30) when $y \to -y_\infty$ and to (3.31) when $y \to +y_\infty$ is given by:

$$f_\alpha(\mathcal{H}, \mu, p_x) = g_1(\mathcal{H}, p_x) f_{\alpha 1} + g_2(\mathcal{H}, p_x) f_{\alpha 2} \quad (3.32)$$

with the functions $g_i, i = \overline{1, 2}$ satisfying:

$$\lim_{y\to -y_\infty} g_1(p_x) = 0 \quad , \quad \lim_{y\to +y_\infty} g_1(p_x) = 1$$
$$\lim_{y\to -y_\infty} g_2(p_x) = 1 \quad , \quad \lim_{y\to +y_\infty} g_2(p_x) = 0$$

Since $f_{\alpha 1}$, $f_{\alpha 2}$ and g_1, g_2 are functions of $\mathcal{H}$ and p_x only, the functions (3.32) are solutions of the Vlasov equation. These functions need not necessarily to be continuous functions but can be Heaviside step functions like those used by *Sestero* (1964,1966) and *Lemaire and Burlaga* (1976) in their kinetic models of tangential discontinuities. *Lee and Kan* (1979) and *Roth et al.*(1996) have used complementary error function to define the g_i in more elaborated kinetic models of tangential discontinuities.

In order to keep the system as simple as possible from the mathematical point of view, in the following we will use Heaviside step functions to describe the transition of the velocity distribution function from a displaced Maxwellian to an isotropic Maxwellian.

Without loss of generality one can also choose the system of reference such that $B_0 > 0$. In this case, from the boundary conditions given for A_x in Table 3.1 and Table 3.3, it follows that

$$\lim_{y \to y_\infty} A_x = -\infty$$

$$\lim_{y \to -y_\infty} A_x = +\infty$$

From eq. (3.20) it follows:

$$\lim_{y \to y_\infty} p_x = \lim_{y \to y_\infty} q_\alpha A_x = -sign(q_\alpha) \cdot \infty \tag{3.33}$$

$$\lim_{y \to -y_\infty} p_x = \lim_{y \to -y_\infty} q_\alpha A_x = +sign(q_\alpha) \cdot \infty \tag{3.34}$$

the signum function being defined as:

$$sign(t) = \begin{cases} -1 & if \quad t < 0 \\ +1 & if \quad t > 0 \end{cases} \tag{3.35}$$

The asymptotic behavior of $p_x(y)$ suggests that the functions g_i can be written as Heaviside step functions of p_x. The discontinuous step function, $\eta(t)$, is defined as:

$$\eta(t) = \begin{cases} 0 & if \quad t < 0 \\ 1 & if \quad t > 0 \end{cases} \tag{3.36}$$

Thus we can write the solution of the Vlasov equation in the plane $z = 0$ as below:

$$f_\alpha|_{z=0} = \eta\left(-b_\alpha \frac{p_x}{\sqrt{m_\alpha \mathcal{K} T_{\alpha 1}}}\right) f_{\alpha 1} + \eta\left(b_\alpha \frac{p_x - m_\alpha V_0}{\sqrt{m_\alpha \mathcal{K} T_{\alpha 2}}}\right) f_{\alpha 2} \tag{3.37}$$

where $b_\alpha = sign(q_\alpha)$. With (3.33) and (3.34) one can see that indeed:

$$\lim_{y \to -\infty} f_\alpha|_{z=0} = f_{\alpha 2}$$

$$\lim_{y \to +\infty} f_\alpha|_{z=0} = f_{\alpha 1}$$

thus (3.37) really satisfies the boundary conditions (3.28)-(3.29) or (3.30)-(3.31).

General solution

The function given by equation (3.37) is a solution of the steady-state Vlasov equation in the plane $z = 0$. It has the remarkable property that it depends only on the constants of motion $\mathcal{H}$ and p_x plus the parameters V_0, $T_{\alpha 1}$, $T_{\alpha 2}$, $N_{\alpha 1}$, $N_{\alpha 2}$. Thus the function $f_\alpha|_{z=0}$ defined in the reference plane $z = 0$ can be mapped to any other point (x, y, z) along particle trajectories that are characteristics of the Vlasov equation (*Delcroix and Bers*, 1994). We can therefore consider that the solution of the Vlasov equation in any point (x, y, z) is equal to the solution given in (3.37):

$$f_\alpha(\mathcal{H}, \mu, p_x) = f_\alpha|_{z=0}(\mathcal{H}, \mu, p_x) \tag{3.38}$$

Mapping of the VDF from a reference level in the whole spatial domain has been successfully used before in the kinetic theory to develop exospheric models of the solar and polar wind (e.g. *Lemaire and Scherer*, 1971, *Pierrard*, 1997).

In the remainder of this study we will consider a plasma consisting on electrons and protons with the velocity distributions:

- for electrons:

$$\begin{aligned} f_e(\mathcal{H}, p_x) \;\; &= \;\; \eta\left(\frac{p_x}{\sqrt{m_e \mathcal{K} T_{e1}}}\right) N_{e1} \left(\frac{m_e}{2\pi \mathcal{K} T_{e1}}\right)^{\frac{3}{2}} e^{-\frac{\mathcal{H}}{\mathcal{K} T_{e1}}} \\ &+\eta\left(-\frac{p_x - m_e V_0}{\sqrt{m_e \mathcal{K} T_{e2}}}\right) N_{e2} \left(\frac{m_e}{2\pi \mathcal{K} T_{e2}}\right)^{\frac{3}{2}} e^{-\frac{\mathcal{H} - p_x V_0 + \frac{1}{2} m_e V_0{}^2}{k T_{e2}}} \end{aligned} \tag{3.39}$$

- for protons:

$$\begin{aligned} f_i(\mathcal{H}, p_x) \;\; &= \;\; \eta\left(-\frac{p_x}{\sqrt{m_i \mathcal{K} T_{i1}}}\right) N_{i1} \left(\frac{m_i}{2\pi \mathcal{K} T_{i1}}\right)^{\frac{3}{2}} e^{-\frac{\mathcal{H}}{\mathcal{K} T_{i1}}} \\ &+\eta\left(\frac{p_x - m_i V_0}{\sqrt{m_i \mathcal{K} T_{i2}}}\right) N_{i2} \left(\frac{m_i}{2\pi \mathcal{K} T_{i2}}\right)^{\frac{3}{2}} e^{-\frac{\mathcal{H} - p_x V_0 + \frac{1}{2} m_i V_0{}^2}{k T_{i2}}} \end{aligned} \tag{3.40}$$

The conversion from Cartesian velocity space (v_x, v_y, v_z) to the space of the constants of motion $(\mathcal{H}, \mu, p_x)$ removes the spatial dependence of f_α. The VDF depends now only on the new variables $(\mathcal{H},\ p_x)$. Nevertheless in the space $(\mathcal{H}, p_x, \mu)$ the regions effectively "filled" with particles varies with Φ and A_x thus with y and z. The boundaries of the regions accessible for the particles are determined from the conservation laws written for the three constants of motion (3.19)-(3.21). The problem of accessibility will be treated in section **3.4**.

The general solution (3.38) satisfies also the boundary conditions (3.22)-(3.23) and (3.24)-(3.25). Indeed, as will become more clear in the next section, the V_x component of the plasma average velocity computed by integrating (3.38) in the velocity space gives a non-zero value. In other words the general solution describes a plasma having a non-uniform average velocity in the direction normal to the main magnetic field. This velocity is found self-consistently from $2D$ boundary conditions imposed on the magnetic potential, A_x. Note that in case of a $2D$ flow the plasma bulk velocity component $V_x(y,z)$ will be different from V_0 everywhere except for the center ($z=0$) of the left border of our $2D$ integration domain, where we have: $\lim_{y\to -y_\infty} V_x = V_0$.

The solution (3.38) is *general* in the sense that it describes the plasma in each point (x,y,z). It is not unique however. From the infinite number of possibilities to define positive functions of the constants of motion (all being solutions of the Vlasov equation) we choose (3.38) because it conveniently satisfies the criterion of mathematical simplicity. Although given in terms of simple functions it still satisfies our rather complex asymptotic boundary conditions required for the electromagnetic field as well as for the plasma bulk velocity. In the following section we will compute analytically its zero and first order moments.

3.4 Moments of the velocity distribution function

Having defined the velocity distribution function (3.38), we can now compute its moments. When the velocity distributions function is given in the (y,z,v_x,v_y,v_z) variables, the moments of the VDF are defined as below:

$$Q_\alpha^{rst}(y,z) = \int_{-\infty}^{+\infty}\int_{-\infty}^{+\infty}\int_{-\infty}^{+\infty} {v_x}^r {v_y}^s {v_z}^t f_\alpha(v_x,v_y,v_z)dv_x dv_y dv_z \tag{3.41}$$

When the VDF is given in terms of $(\mathcal{H},\mu)$ as was shown above, the moments are computed alternatively as below:

$$\begin{aligned} Q_\alpha^{rst}(y,z) &= \int_{-\infty}^{+\infty}\int_{0}^{+\infty}\int_{0}^{+\infty} \Big[[v_x(\mathcal{H},\mu,p_x)]^r[v_y(\mathcal{H},\mu,p_x)]^s[v_z(\mathcal{H},\mu,p_x)]^t \times \\ &\quad \times f_\alpha(\mathcal{H},p_x)\left|\frac{D(v_x,v_y,v_z)}{D(\mathcal{H},\mu,p_x)}\right|\Big] dp_x d\mathcal{H} d\mu \end{aligned} \tag{3.42}$$

where $\left|\frac{D(v_x,v_y,v_z)}{D(\mathcal{H},\mu,p_x)}\right|$ is the Jacobian of the transformation from the (v_x,v_y,v_z) space to the $(\mathcal{H},\mu,p_x)$ space. In (3.42) v_x, v_y v_z must be given in terms of $\mathcal{H}$,

μ and p_x from the definitions of the constants of motion (3.19)-(3.21). The following equations hold true :

$$v_x = \frac{p_x - q_\alpha A_x}{m_\alpha} \tag{3.43-a}$$

$$v_y = \pm\sqrt{\frac{2\mu B}{m_\alpha} - \left(\frac{p_x - q_\alpha A_x}{m_\alpha} - U_E\right)^2} \tag{3.43-b}$$

$$v_z = \pm\sqrt{\frac{2\mathcal{H}}{m_\alpha} - \frac{2\mu B}{m_\alpha} - \frac{2U_E}{m}(p_x - q_\alpha A_x) + U_E^2 - \frac{2q_\alpha\phi}{m_\alpha}} \tag{3.43-c}$$

where U_E is the zero order (electric) drift velocity. The $\pm$ sign in (3.43-b) and (3.43-c) indicate the sign to be introduced in the integrals that give the moments of $f_\alpha(\mathcal{H}, p_x)$ when v_y and/or v_z take negative and positive values respectively (see section 3.4.2 and 3.4.3). The Jacobian of the transformation from the variables (v_x, v_y, v_z) to $(\mathcal{H}, p_x, \mu)$ is equal to:

$$\mathcal{J}_\alpha = \left|\frac{D(v_x, v_y, v_z)}{D(\mathcal{H}, \mu, p_x)}\right| = \frac{B}{m_\alpha^3 v_y(\mathcal{H}, \mu, p_x) v_z(\mathcal{H}, \mu, p_x)}$$

$$\mathcal{J}_\alpha = \frac{B}{m_\alpha^3\sqrt{\left[\frac{2\mu B}{m_\alpha} - \left(\frac{p_x - q_\alpha A_x}{m_\alpha} - U_E\right)^2\right]\left[\frac{2\mathcal{H}}{m_\alpha} - \frac{2\mu B}{m_\alpha} - \frac{2U_E}{m}(p_x - q_\alpha A_x) + U_E^2 - \frac{2q_\alpha\phi}{m_\alpha}\right]}}$$

In the next chapter the distribution of the electric potential $\Phi(y, z)$ is found from the quasi-neutrality equation which is a good approximation of equation (3.13). To solve this equation in terms of Φ one needs to determine analytical expressions of the density of electrons and protons by computing the zero order moment (Q_α^{000}) of f_e and f_i respectively.

Furthermore the magnetic potential $A_x(y, z)$ is a solution of (3.14). To solve this partial differential equation one needs to determine the analytical expression of the partial current density j_{xe} and j_{xi} of the electrons and ions. The current densities are obtained from the first order moments (Q_α^{100}) of the two velocity distribution functions, f_e and f_i respectively.

3.4.1 Accessibility condition

The conservation of the three constants of motion in the case of non-uniform fields, $\Phi(y, z)$, $A_x(y, z)$, defines a range of accessible regions in the physical space for the particles with a given initial energy. In other words, not all the particles starting from a "source" region can reach any point (x, y, z). The phase space is non-uniformly populated. The regions accessible to the particles must first be defined. Their boundaries depend on $\mathcal{H}$, the particle total energy, p_x, the canonical momentum component and μ, the magnetic moment at the reference level, where the VDF is specified. In our case the reference level is the plane $z = 0$ where the VDF is given by (3.37).

Accessibility condition in (v_x, v_y, v_z) space

Since the total energy of the particle must be the same at level $z = 0$ and at any other point (x, y, z) the following relationship holds:

$$v_x{}^2|_{z=0} + v_y{}^2|_{z=0} + v_z{}^2|_{z=0} + \frac{2q_\alpha}{m_\alpha}\phi_0(y) = v_x{}^2|_{y,z} + v_y{}^2|_{y,z} + v_z{}^2|_{y,z} + \frac{2q_\alpha}{m_\alpha}\Phi(y,z) \tag{3.44}$$

where $v_x|_{z=0}$, $v_y|_{z=0}$, $v_z|_{z=0}$ and $\phi_0(y)$ are the particle's velocity components and the electric potential in a point $(y, 0)$ in the plane $z = 0$; the notations $v_x|_{y,z} = v_x(y, z)$, $v_y|_{y,z} = v_y(y, z)$, $v_z|_{y,z} = v_z(y, z)$ have been used for the velocity components in a point outside the plane $z = 0$.

From the conservation of the canonical momentum p_x and of the magnetic moment, μ, we obtain two additional relationships between the particle's velocity components at level $z = 0$ and their corresponding values at any "off-plane" point (y, z) :

$$v_x|_{z=0} + \frac{q_\alpha}{m_\alpha}A_{x0}(y) = v_x|_{y,z} + \frac{q_\alpha}{m_\alpha}A_x(y,z) \tag{3.45}$$

$$\frac{\left[v_x|_{z=0} - U_{E0}(y)\right]^2 + v_y^2|_{z=0}}{2B_0} = \frac{\left[v_x|_{y,z} - U_E(y,z)\right]^2 + v_y^2|_{y,z}}{2B(y,z)} \tag{3.46}$$

where $A_{x0}(y)$ and $A_x(y, z)$ give the magnetic potential in the $z = 0$ plane and in the point (y, z) respectively. $U_{E0}(y)$ and $U_E(y, z)$ are the zero order drift (or *convection velocity*). $U_{E0}(y)$ satisfies $\lim_{y\to -y_\infty} U_{E0} = V_0$. The convection velocity, $U_E(y, z) = |\boldsymbol{E}(y, z) \times \boldsymbol{B}(y, z)| / B^2(y, z)$, depends on the local value of the electric and magnetic field intensities.

From eqs. (3.44)-(3.46) one can determine $v_y^2|_{y,z}$ and $v_z^2|_{y,z}$ as functions of $v_x{}^2|_{z=0}$, $v_y{}^2|_{z=0}$, $v_z{}^2|_{z=0}$, $\phi_0(y)$, $\Phi(y, z)$, $A_{x0}(y)$, $A_x(y, z)$. Thus it is possible to determine the conditions that must be satisfied by the initial velocity components of the particle in $z = 0$ such that the particle reach a point where the electromagnetic potentials are equal to $\Phi(y, z)$ and $A_x(y, z)$. These conditions are that the functions $v_y^2|_{y,z}$ and $v_z^2|_{y,z}$ obtained from (3.44)-(3.46) to take values greater than zero in (y, z):

$$v_y^2|_{y,z}\left(v_x{}^2|_{z=0}, v_y{}^2|_{z=0}, v_z{}^2|_{z=0}, \phi_0, \Phi, A_{x0}, A_x\right) \geq 0 \tag{3.47}$$

$$v_z^2|_{y,z}\left(v_x{}^2|_{z=0}, v_y{}^2|_{z=0}, v_z{}^2|_{z=0}, \phi_0, \Phi, A_{x0}, A_x\right) \geq 0 \tag{3.48}$$

The reader should not be confused about the square appearing in $v_y^2|_{y,z}$ and $v_z^2|_{y,z}$. These functions are not necessarily positive. Indeed, depending on the values of the velocity components in $z = 0$ and on the values of the electromagnetic potentials in $z = 0$ and (y, z), the functions $v_y^2|_{y,z}$ and $v_z^2|_{y,z}$ found from (3.44)-(3.46) can take negative values as well. In that case the point (y, z) is not accessible.

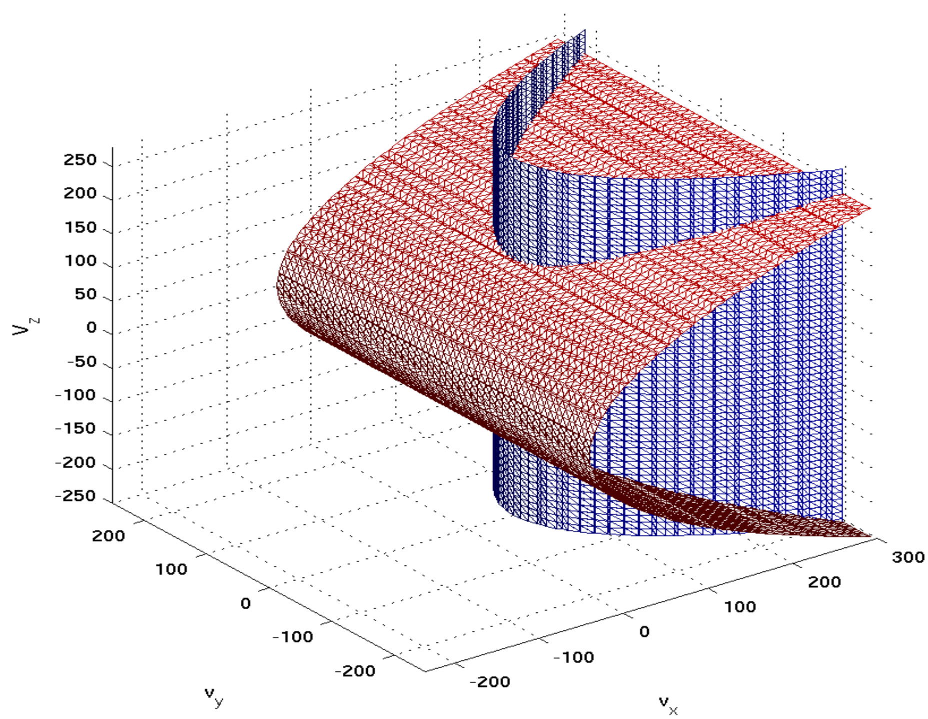

Figure 3.4: Illustration of the integration subspace at $z = 0$; the particles whose velocity components are contained within the *intersection* of the interior of the two parabolic surfaces reach the point (x, y, z). The two surfaces are solutions of (3.49)-(3.50) for arbitrary values of potentials.

After finding explicitly the functions $v_y^2|_{y,z}$ and $v_z^2|_{y,z}$ the accessibility conditions (3.47)-(3.48) can be written as below:

$$v_y^2|_{z=0} - 2\left[\Delta U(y,z) + \frac{q_\alpha}{m_\alpha}\Delta A_x(y,z)\right] v_x|_{z=0} + \Delta_1(y,z) \geq 0 \quad (3.49)$$

$$v_z^2|_{z=0} + 2\Delta U v_x|_{z=0} - \Delta_2(y,z) \geq 0 \quad (3.50)$$

where the functions $\Delta_1(y, z)$ and $\Delta_2(y, z)$ were defined as :

$$\Delta_1 = [U_{E0}(y) + U_E(y,z)]\,\Delta U + \frac{2q_\alpha}{m_\alpha} U_E(y,z)\Delta A_x - \left[\frac{q_\alpha}{m_\alpha}\Delta A_x\right]^2$$

$$\Delta_2 = \frac{2q_\alpha}{m_\alpha} U_E(y,z)\Delta A_x - \frac{2q_\alpha}{m_\alpha}\Delta\Phi + \left[U_{E0}(y) + U_E(y,z)\right]\Delta U$$

with

$$\begin{aligned} \Delta U(y,z) &= U_{E0}(y) - U_E(y,z) \\ \Delta A_x(y,y) &= A_{x0}(y) - A_x(y,z) \\ \Delta\Phi(y,z) &= \Phi_0(y) - \Phi(y,z) \end{aligned}$$

$U_{E0}(y)$, $A_{x0}(y)$ and $\Phi_0(y)$ are parametric functions of the model implementing the boundary values we impose in the plane $z = 0$ where the VDF was defined. $U_E(y,z)$ is a parametric function providing an initial estimate of *convection velocity* that varies monotonically with the perpendicular component of the electric field. $A_x(y,z)$ and $\Phi(y,z)$ are the unknown distributions of the magnetic and electric potentials that have to be computed from the Maxwell equations and/or quasi-neutrality equation as outlined in Chapter **4**.

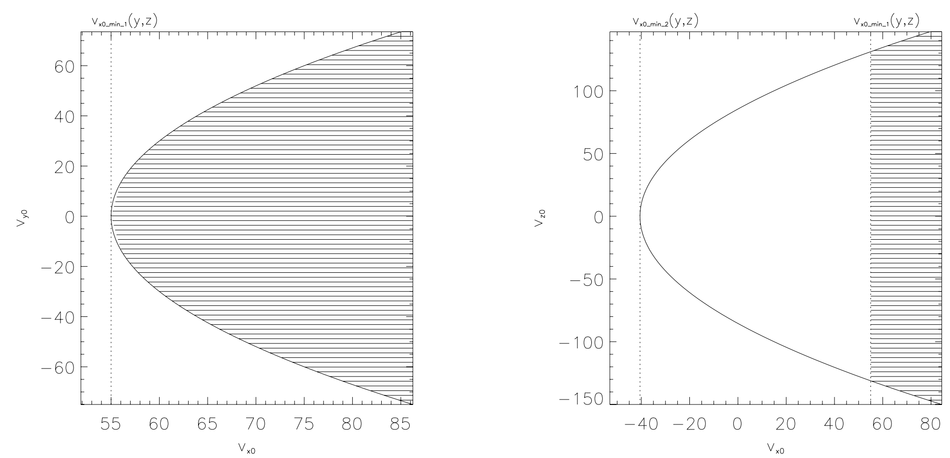

(a) Integration region in the $v_{x_0}Ov_{y_0}$ plane (for $v_{z_0} = 0$).

(b) Integration region in the $v_{x_0}Ov_{z_0}$ plane (for $v_{y_0} = 0$).

Figure 3.5: Intersections of the parabolic surfaces plotted in figure **3.4** with the $v_{x_0}Ov_{y_0}$ and $v_{x_0}Ov_{z_0}$ planes at level $z = 0$. The hatched regions are the domain of integration to calculate the number of particles originating from the plane $z = 0$ that can reach the point (x, y, z).

The two inequalities (3.49)-(3.50) define in the velocity space (v_x, v_y, v_z) the subspace containing the velocity components of all the particles that can reach the point (x, y, z) where the fields take the values $\Phi(y,z)$ and

$A_x(y,z)$. These subspaces of the velocity space are visualized in figures **3.4** and **3.5(a)-3.5(a)**. The graphics illustrates the situation when the parabolic hypersurface given by (3.49) is "interior" to the one determined by (3.50).

In order to find the number of particles that indeed reach this point one has to compute the zero order moment of the VDF by integrating only over this subspace. Similar relationships can be found between velocity components at any other level (z). A thorough analysis of the classes of particles determined by the conservation of the total energy and of the magnetic moment in a convergent geometry of the magnetic field has been done by *Lemaire and Scherer*(1970, 1971a, 1971b) and *Pierrard and Lemaire* (1996) in their exospheric models of the polar and solar wind.

An alternative to defining the classes of particles of the system as in the exospheric models, is to find the accesibility conditions in terms of the constants of motion. The two methods are completely equivalent as was shown by *Liehmohn and Kazhanov* (1998) and *Kazhanov et al.* (1998).

Accessibility condition in the (E, p_x, μ) space

The condition for the particles to be locally reflected at level z given by equations (3.48) and (3.50) can be rewritten with the aid of equation (3.43-c) in terms of the constants of motion as:

$$\mathcal{H} \geq \mathcal{H}_{c\alpha} \tag{3.51}$$

where the function $\mathcal{H}_{c\alpha}(p_x, \mu, \Phi, A_x)$ is defined as:

$$\mathcal{H}_{c\alpha} = \mu B + [p_x - q_\alpha A_x(y,z)]\, U_E(y,z) + +q_\alpha \Phi(y,z) - \frac{m_\alpha U_E^2(y,z)}{2} \tag{3.52}$$

From (3.43-b) the conditions of accesibility of particles in the Oy direction given in (3.47) and (3.49) can be rewritten as below:

$$\mu \geq \mu_{c\alpha} \tag{3.53}$$

where the function $\mu_{c\alpha}(p_x, \Phi, A_x)$ is defined as below:

$$\mu_{c\alpha} \quad = \quad \frac{m_\alpha}{2B}\left[\frac{p_x - q_\alpha A_x(y,z)}{m_\alpha} - U_E(y,z)\right]^2 \tag{3.54}$$

The last two equations define the regions "populated" with particles in the $(\mathcal{H}, p_x, \mu)$ space. In other words they define the limits of integration, $E_{c\alpha}$, $\mu_{c\alpha}$, that must be used to compute the moments of the VDF.

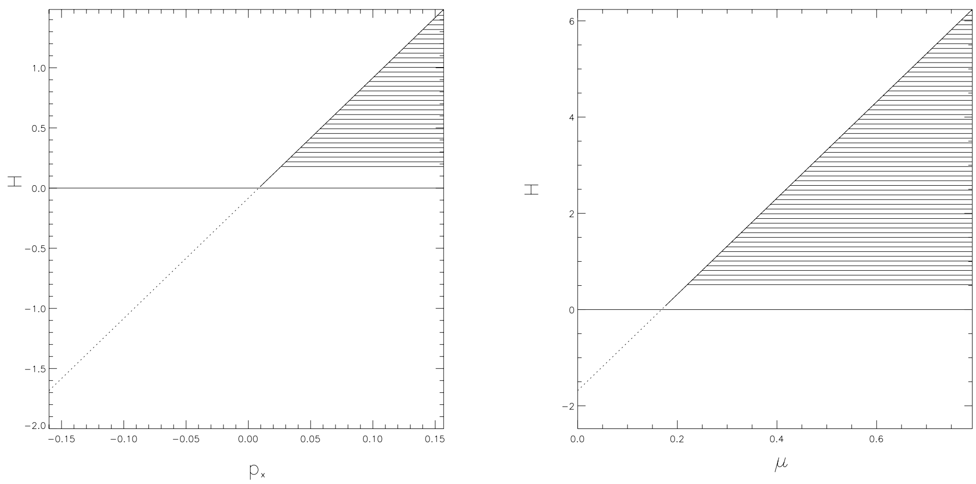

(a) section in the Hp_x plane for $\mu = 0$ (b) section in the $H\mu$ plane for $p_x = 0$.

Figure 3.6: Illustration of a possible shape of the integration region defined by (3.51); arbitrary units and potentials.

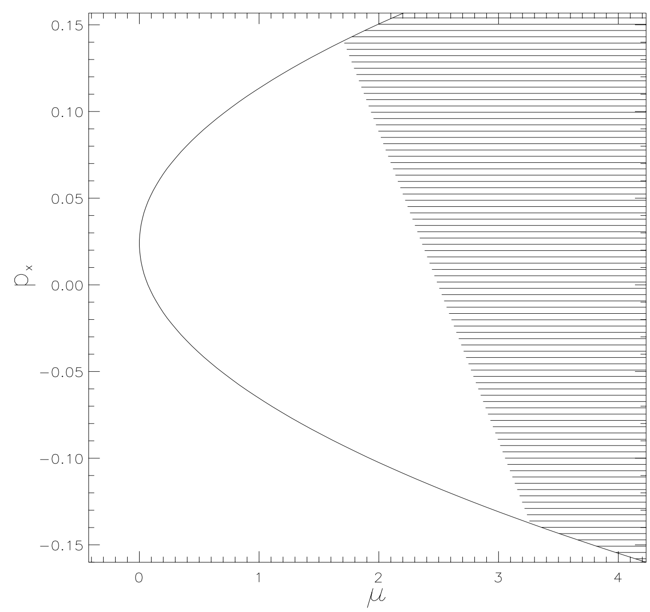

Figure 3.7: Illustration of a possible shape of the integration region defined by (3.51) at level $z = 0$: intersection with $H = 0$, arbitrary units and potentials.

The moments $Q_\alpha^{rst}(A_x, \Phi)$ will be computed by integration in the $(\mathcal{H}, p_x, \mu)$ space as below:

$$Q_\alpha^{rst} = \begin{cases} 4\int_{-\infty}^{+\infty}\int_{\mathcal{H}_{c\alpha}}^{+\infty}\int_{\mu_{c\alpha}}^{+\infty}\left[(\mathcal{V}_x)^r(\mathcal{V}_y)^s(\mathcal{V}_z)^t\frac{\sqrt{B}f_\alpha(\mathcal{H},\mu,p_x)}{2m_\alpha^2\sqrt{\mathcal{H}-\mathcal{H}_{c\alpha}}\sqrt{\mu-\mu_{c\alpha}}}\right]d\mathcal{H}d\mu dp_x & , \\ 0 & \end{cases} \tag{3.55}$$

where $\mathcal{V}_x(\mathcal{H}, p_x, \mu)$, $\mathcal{V}_y(\mathcal{H}, p_x, \mu)$ and $\mathcal{V}_z(\mathcal{H}, p_x, \mu)$ are the functions (3.43-a)-(3.43-c) defined by the transformations from the (v_x, v_y, v_y) space into the $(\mathcal{H}, p_x, \mu)$ space. Note the change of the lower bound of the integrals over $\mathcal{H}$ and μ.

Q_α^{rst} is equal to zero whenever at least one of the exponents "s" or "t" is odd. Indeed, in (3.42) we have obscured the dependence of the velocity distribution function on the sign of v_y and v_z as these velocity components appeared squared in (3.19) and (3.21). Therefore we have to integrate separately for each of the four quadrants defined in the v_yOv_z subspace: $I \equiv (v_y > 0, v_z < 0)$, $II \equiv (v_y > 0, v_z > 0)$, $III \equiv (v_y < 0, v_z < 0)$, $IV \equiv (v_y < 0, v_z > 0)$.

In the integral (3.55), corresponding to each quadrant, the functions $\mathcal{V}_y$ and $\mathcal{V}_z$ will take the correct sign given in (3.43-b)-(3.43-c). Thus whenever the VDF moment implies an integration of an odd power of $\mathcal{V}_y$ the integral corresponding to the quadrants I and II and the integral corresponding the quadrants III and IV have the same modulus but different signs. Their sum is equal to zero. Similarly, in case of an integration of an odd power of $\mathcal{V}_z$ then the integral corresponding to the quadrants I and III cancels the integral over quadrant II and IV. It is only when both powers, s and t, appearing in the moment Q^{rst} are even that the contributions from all quadrants add and give the factor 4 in front of the integral in (3.55).

3.4.2 Densities

The number density of the species α is given by the moment Q_α^{000} :

$$Q_\alpha^{000} = 4\int_{-\infty}^{+\infty}\int_{\mathcal{H}_{c\alpha}}^{+\infty}\int_{\mu_{c\alpha}}^{+\infty}\frac{\sqrt{B}f_\alpha(\mathcal{H},\mu,p_x)}{2m_\alpha^2\sqrt{\mathcal{H}-\mathcal{H}_{c\alpha}}\sqrt{\mu-\mu_{c\alpha}}}d\mathcal{H}d\mu dp_x \tag{3.56}$$

The following expressions for the electron and ion density are then found:

$$\begin{aligned} n_i(y,z) \quad = \quad & \frac{N_{i1}}{2}e^{-\frac{e\Phi(y,z)}{\mathcal{K}T_{i1}}}erfc\left(\frac{eA_x(y,z)}{\sqrt{2m_i\mathcal{K}T_{i1}}}\right) + \\ & \frac{N_{i2}}{2}e^{-\frac{e\Phi(y,z)}{\mathcal{K}T_{i2}}}e^{\frac{eA_x(y,z)V_0}{\mathcal{K}T_{i2}}}erfc\left(-\frac{eA_x(y,z)}{\sqrt{2m_i\mathcal{K}T_{i2}}}\right) \end{aligned} \tag{3.57}$$

$$\begin{aligned} n_e(y,z) &= \frac{N_{e1}}{2} e^{\frac{e\Phi(y,z)}{\mathcal{K}T_{e1}}} erfc\left(\frac{eA_x(y,z)}{\sqrt{2m_e\mathcal{K}T_{e1}}}\right) + \\ & \frac{N_{e2}}{2} e^{\frac{e\Phi(y,z)}{\mathcal{K}T_{e2}}} e^{-\frac{eA_x(y,z)V_0}{\mathcal{K}T_{e2}}} erfc\left(-\frac{eA_x(y,z)}{\sqrt{2m_e\mathcal{K}T_{e2}}}\right) \end{aligned} \tag{3.58}$$

where N_{i1}, N_{i2}, N_{e1}, N_{e2} are constant values that can be adjusted such that (3.57)-(3.58) give the correct asymptotic densities in $z = 0$, $z \to +z_\infty$, $y \to -y_\infty$, $y \to +y_\infty$, for ions respectively for electrons. The integrals computed in order to obtain the densities written above are given in the Appendix.

It can be verified that the analytical moments given above give the correct particle density for a uniform, stagnant plasma, immersed in a uniform magnetic field. Indeed, taking $V_0 = 0$ (plasma stagnant everywhere), and a uniform magnetic field, $A_x(y,z) = -B_0 y$, with $\Phi(y,z) = \Phi_L = \Phi_R = 0$ (no electric field), $T_{i1} = T_{i2} = T_i$, $N_{i1} = N_{i2} = N_i$ and $T_{e1} = T_{e2} = T_e$, $N_{e1} = N_{e2} = N_e$, equations (3.57)-(3.58) give:

$$\begin{aligned} n_i(y,z) &= N_i \\ n_e(y,z) &= N_e \end{aligned}$$

since $erfc(-x) = 2 - erfc(x)$. Thus the solutions correctly describe the plasma in a thermal equilibrium state: the density is uniform throughout the $3D$ space.

It is useful to use normalized densities, thus n_i and n_e can be scaled as below:

$$\begin{aligned} n_{i1}^* &= \frac{N_{i1}^*}{2} e^{-\tau_i\Phi^*} erfc\,(\sqrt{\gamma\tau_i}A_x^*) + \frac{N_{i2}^*}{2} e^{-\tau_{i2}\Phi^*} e^{2\tau_{i2}A_x^*V_0^*} erfc\,(-\sqrt{\gamma\tau_{i2}}A_x^*) \\ n_{e1}^* &= \frac{N_{e1}^*}{2} e^{\tau_e\Phi^*} erfc\,(\sqrt{\gamma\tau_e}A_x^*) + \frac{N_{e2}^*}{2} e^{\tau_{e2}\Phi^*} e^{-2\tau_{e2}A_x^*V_0^*} erfc\,(-\sqrt{\gamma\tau_{e2}}A_x^*) \end{aligned} \tag{3.59}$$

The scaling factors for electric and magnetic potential, velocity and the coefficients γ, τ_e, τ_{e2}, τ_i, τ_{i2} are defined below:

$$\begin{aligned} \Phi &= \lambda_\Phi \Phi^*, \quad \lambda_\Phi = \frac{\mathcal{K}T_e}{e} \\ A_x &= \lambda_{A_x} A_x^*, \quad \lambda_{A_x} = \frac{\sqrt{2m_e\mathcal{K}T_{re}}}{e} \\ V_0 &= \lambda_V V_0^*, \quad \lambda_V = \sqrt{\frac{2\mathcal{K}T_{re}}{m_e}} \\ \gamma &= \frac{m_e}{m_i}, \quad \tau_e = \frac{T_{re}}{T_{e1}}, \quad \tau_{e2} = \frac{T_{re}}{T_{e2}} \\ \tau_i &= \frac{T_{re}}{T_{i1}}, \quad \tau_{i2} = \frac{T_{re}}{T_{i2}} \end{aligned} \tag{3.60}$$

3.4.3 Currents

The partial currents density $j_{x\alpha}$ of the species α is defined as:

$$j_{x\alpha} = q_\alpha n_\alpha < v_x >_\alpha = q_\alpha Q_\alpha^{100} \tag{3.61}$$

where $< v_x >_\alpha$ is the average velocity of the species α and q_α its charge with algebraic sign. The moment Q_α^{100} is equal to:

$$Q_\alpha^{100} = 4\int_{-\infty}^{+\infty}\int_{\mathcal{H}_{c\alpha}}^{+\infty}\int_{\mu_{c\alpha}}^{+\infty}\left(\frac{p_x - q_\alpha A_x}{m_\alpha}\right)\frac{\sqrt{B} f_\alpha(\mathcal{H},\mu,p_x)}{2m_\alpha^2\sqrt{\mathcal{H}-\mathcal{H}_{c\alpha}}\sqrt{\mu-\mu_{c\alpha}}} d\mathcal{H} d\mu dp_x \tag{3.62}$$

The contribution of the four quadrants corresponding to the positive and negative values of v_y and v_z are added in this case as discussed in section 3.4.1. After calculating the integrals occuring in (3.62) one finds the following expression for Q_i^{100} and Q_e^{100}:

$$\begin{aligned} Q_i^{100} &= N_{i2}\sqrt{\frac{\mathcal{K}T_{i2}}{2\pi m_i}} e^{-\frac{e\Phi(y,z)}{\mathcal{K}T_{i2}}} e^{\frac{eA_x(y,z)V_0}{\mathcal{K}T_{i2}}}\left[V_{0i}^* erfc\left(-\frac{eA_x(y,z)}{\sqrt{2m_i\mathcal{K}T_{i2}}}\right) + e^{-\frac{(eA_x)^2}{2m_i\mathcal{K}T_{i2}}}\right] \\ &\quad - N_{i1}\sqrt{\frac{\mathcal{K}T_{i1}}{2\pi m_i}} e^{-\frac{e\Phi(y,z)}{\mathcal{K}T_{i1}}} e^{-\frac{(eA_x(y,z))^2}{2m_i\mathcal{K}T_{i1}}} \end{aligned} \tag{3.63}$$

$$\begin{aligned} Q_e^{100} &= N_{e2}\sqrt{\frac{\mathcal{K}T_{e2}}{2\pi m_e}} e^{\frac{e\Phi(y,z)}{\mathcal{K}T_{e2}}} e^{-\frac{eA_x(y,z)V_0}{\mathcal{K}T_{e2}}}\left[V_{0e}^* erfc\left(-\frac{eA_x(y,z)}{\sqrt{2m_e\mathcal{K}T_{e2}}}\right) - e^{-\frac{(eA_x)^2}{2m_e\mathcal{K}T_{i2}}}\right] \\ &\quad + N_{e1}\sqrt{\frac{\mathcal{K}T_{e1}}{2\pi m_e}} e^{\frac{e\Phi(y,z)}{\mathcal{K}T_{e1}}} e^{-\frac{(eA_x(y,z))^2}{2m_e\mathcal{K}T_{e1}}} \end{aligned} \tag{3.64}$$

By multiplying the moments Q_i^{100} and Q_e^{100} with the charge of the proton ($+e$) and electron ($-e$), one obtains the corresponding partial current:

$$\begin{aligned} j_{xi} &= eN_{i2}\sqrt{\frac{\mathcal{K}T_{i2}}{2\pi m_i}} e^{-\frac{e\Phi(y,z)}{\mathcal{K}T_{i2}}} e^{\frac{eA_x(y,z)V_0}{\mathcal{K}T_{i2}}}\left[V_{0i}^* erfc\left(-\frac{eA_x(y,z)}{\sqrt{2m_i\mathcal{K}T_{i2}}}\right) + e^{-\frac{(eA_x)^2}{2m_i\mathcal{K}T_{i2}}}\right] \\ &\quad - eN_{i1}\sqrt{\frac{\mathcal{K}T_{i1}}{2\pi m_i}} e^{-\frac{e\Phi(y,z)}{\mathcal{K}T_{i1}}} e^{-\frac{(eA_x(y,z))^2}{2m_i\mathcal{K}T_{i1}}} \end{aligned} \tag{3.65}$$

$$\begin{aligned} j_{xe} &= -eN_{e2}\sqrt{\frac{\mathcal{K}T_{e2}}{2\pi m_e}} e^{\frac{e\Phi(y,z)}{\mathcal{K}T_{e2}}} e^{-\frac{eA_x(y,z)V_0}{\mathcal{K}T_{e2}}}\left[V_{0e}^* erfc\left(-\frac{eA_x(y,z)}{\sqrt{2m_e\mathcal{K}T_{e2}}}\right) - e^{-\frac{(eA_x)^2}{2m_e\mathcal{K}T_{i2}}}\right] \\ &\quad - eN_{e1}\sqrt{\frac{\mathcal{K}T_{e1}}{2\pi m_e}} e^{\frac{e\Phi(y,z)}{\mathcal{K}T_{e1}}} e^{-\frac{(eA_x(y,z))^2}{2m_e\mathcal{K}T_{e1}}} \end{aligned} \tag{3.66}$$

where e is the magnitude (without sign) of the elementary charge ($1.626 \times 10^{-19}\ C$) and the following notations have been used:

$$V_{0i}^* = \sqrt{\frac{\pi m_i}{2\mathcal{K}T_{i2}}} V_0$$

$$V_{0e}^* = \sqrt{\frac{\pi m_e}{2\mathcal{K}T_{e2}}} V_0$$

The total current is then equal to :

$$j_x = j_{xi} + j_{xe} \tag{3.67}$$

A simple verification consists in considering the case of a plasma in thermal equilibrium, stagnant and immersed in a uniform magnetic field. Taking again $V_0 = 0$, $A_x(y,z) = -B_0 y$, $\Phi(y,z) = \Phi_L = \Phi_R = 0$, $T_{i1} = T_{i2} = T_i$, $N_{i1} = N_{i2} = N_i$, $T_{e1} = T_{e2} = T_e$ and $N_{e1} = N_{e2} = N_e$ one obtains from the formulas above the following values:

$$\begin{aligned} j_{xi} &= 0 \\ j_{xe} &= 0 \end{aligned}$$

These results are correct since inside the thermal plasma there should be no current.

The current density can be normalized and one obtains :

$$\begin{aligned} j_{xi}^* &= N_{i2}\sqrt{\frac{\gamma}{\pi\tau_{i2}}} e^{-\tau_{i2}\Phi^*} e^{2\tau_{i2}A_x^* U_{E0}^*} \left[\sqrt{\frac{\pi\tau_{i2}}{\gamma}} V_0^* erfc\,(-\sqrt{\gamma\tau_{i2}}A_x^*) + e^{-\gamma\tau_{i2}(A_x^*)^2}\right] - \\ &\quad -\sqrt{\frac{\gamma}{\pi\tau_i}} N_{i1}^* e^{-\tau_i\Phi^*} e^{-\gamma\tau_i(A_x^*)^2} \end{aligned} \tag{3.68}$$

$$\begin{aligned} j_{xe}^* &= -N_{e2}^*\sqrt{\frac{1}{\pi\tau_{e2}}} e^{\tau_{e2}\Phi^*} e^{-2\tau_{e2}A_x^* U_{E0}^*} \left[\sqrt{\pi\tau_{e2}} V_0^* erfc\,(-\sqrt{\gamma\tau_{e2}}A_x^*) - e^{-\gamma\tau_{e2}(A_x^*)^2}\right] + \\ &\quad -N_{e1}^*\sqrt{\frac{1}{\pi\tau_e}} e^{\tau_e\Phi^*} e^{-\tau_e(A_x^*)^2} \end{aligned} \tag{3.69}$$

where in addition to the scaling factors given in (3.60) we have introduced :

$$\boldsymbol{j} = \lambda_j \boldsymbol{j}^*, \qquad \lambda_j = (eN_0)\sqrt{\frac{2\mathcal{K}T_{re}}{m_e}} \tag{3.70}$$

The $j_{\alpha y}$ component of the partial current density is determined by computing the moment:

$$Q_\alpha^{010} = 4\int_{-\infty}^{+\infty}\int_{\mathcal{H}_{c\alpha}}^{+\infty}\int_{\mu_{c\alpha}}^{+\infty}\left\{\mathcal{V}_y \frac{\sqrt{B} f_\alpha(\mathcal{H},\mu,p_x)}{2m_\alpha^2\sqrt{\mathcal{H}-\mathcal{H}_{c\alpha}}\sqrt{\mu-\mu_{c\alpha}}}\right\} d\mathcal{H} d\mu dp_x \tag{3.71}$$

that is precisely equal to zero because the exponent of $\mathcal{V}_y$ is odd, $s = 1$. Thus the total protonic and electronic current is equal to :

$$\begin{aligned} j_{yi} &= 0 \\ j_{ye} &= 0 \end{aligned}$$

The j_z current is found by computing the moment:

$$Q_\alpha^{001} = 4\int_{-\infty}^{+\infty}\int_{\mathcal{H}_{c\alpha}}^{+\infty}\int_{\mu_{c\alpha}}^{+\infty}\mathcal{V}_z\frac{\sqrt{B}f_\alpha(\mathcal{H},\mu,p_x)}{m_\alpha^2\sqrt{\mathcal{H}-\mathcal{H}_{c\alpha}}\sqrt{\mu-\mu_{c\alpha}}}d\mathcal{H}d\mu dp_x \tag{3.72}$$

that is equal to zero according to 3.55 since it contains an odd power of $\mathcal{V}_z$, $t = 1$. Thus the protonic and electronic partial current densities in the Oz-direction are equal to :

$$\begin{aligned} j_{zi} &= 0 \\ j_{ze} &= 0 \end{aligned}$$

It this thus demonstrated that in the geometry of the flow defined above the only non-vanishing component of the current density is $j_x = j_{xi} + j_{xe}$.

3.4.4 Bulk velocity

In the fluid models of plasma dynamics one assigns to the plasma velocity the value of the zero order drift or convection velocity, $\boldsymbol{U}_E$. In these models it is assumed by default that all the ions and electrons move with the same velocity $\boldsymbol{U}_E$.

In our kinetic model however we consider that the plasma moves with a velocity determined by average velocity of ions, $<\boldsymbol{v}_i>$, and of electrons, $<\boldsymbol{v}_e>$. The partial average velocities are computed by integration in the velocity space of the corresponding VDF, i.e. by computing the zero and first order moments. We can then define $\boldsymbol{V}$, the plasma average or bulk velocity, as below:

$$\boldsymbol{V} = \frac{m_i n_i <\boldsymbol{v}_i> + m_e n_e <\boldsymbol{v}_e>}{m_i n_i + m_e n_e} \tag{3.73}$$

In the geometry of the flow chosen for this study the only non-vanishing component of $\boldsymbol{V}$ is V_x. With the definitions (3.57), (3.58), (3.63) and (3.64) the non-vanishing component of the plasma bulk velocity is equal to:

$$V_x = \frac{m_i Q_i^{100} + m_e Q_e^{100}}{m_i Q_i^{000} + m_e Q_e^{000}} \tag{3.74}$$

Chapter 4

Kinetic numerical models of sheared plasma flows

The charge and current densities computed in the previous chapter are now introduced in the right hand side terms of the Maxwell's equations (3.13)-(3.14) in order to determine the electromagnetic potentials satisfying the boundary conditions defined in tables 3.1 and 3.3.

The right landside term of equation (3.13) is equal to the *net charge density*. In plasma even a very small charge imbalance, $n_i - n_e$, produces important electric fields. Therefore plasmas in general and space plasmas in particular have the tendency to remain quasineutral with $n_e \approx n_i$. Furthermore, solving the Poisson equation for a plasma is a difficult numerical problem since the right landside term is several orders of magnitude smaller than the left landside, driving numerical instability of the algorithms.

Therefore instead of solving the Poisson equation to determine the electric potential we will solve the quasineutrality equation:

$$n_i(\Phi(y,z)) - n_e(\Phi(y,z)) \approx 0 \tag{4.1}$$

with $n_i(\Phi, A_x)$ and $n_e(\Phi, A_x)$ given by (3.57) and (3.58) respectively.

The non-vanishing component of the magnetic vector potential is determined from the Ampere equation:

$$\frac{\partial^2 A_x}{\partial y^2} + \frac{\partial^2 A_x}{\partial z^2} = -\mu_0[j_{xi}(y,z) + j_{xe}(y,z)] \tag{4.2}$$

where $j_{xi}(y,z)$, $j_{xe}(y,z)$ are given by (3.65)-(3.66). Equation (4.2) is subject to the boundary conditions specified in Tables 3.2 and 3.4

4.1 Numerical method to solve the coupled Ampére-quasineutrality equations

The solution of the system formed by equations (4.1)-(4.2) is determined numerically. An equidistant two-dimensional mesh, with $M_y \times N_z$ points is adopted in the yOz plane. The Ampere equation, which is of Poisson-type, is discretized using a standard finite difference method (*Morse and Feschbach*, 1953). With the 5-point Poisson method eq. (4.2) is discretized as below:

$$\begin{aligned}-(A_x)_{j+1,k} - (A_x)_{j-1,k} - (A_x)_{j,k+1} - (A_x)_{j,k-1} + 4(A_x)_{j,k} = \\ -\Delta^2 \mu_0 [j_{xi}(y_j, z_k) + j_{xe}(y_j, z_k)]\end{aligned} \tag{4.3}$$

where $\Phi_{j,l} = \Phi(y_j, z_l)$ and $(A_x)_{j,k} = A_x(y_j, z_l)$ are the discrete values of the non vanishing components of the electric and magnetic vector potentials; $\Delta = y_j - y_{j-1} = z_k - z_{k-1}$ is the step of spatial sampling (assumed equidistant).

The boundary conditions in $y = -y_\infty$ and $y = +y_\infty$ (labeled BCY) and respectively in $z = -z_\infty$ and $z = +z_\infty$ (labeled BCZ) are also discretized. The corresponding equations are given below in the general form of the Robin type boundary condition:

$$BCY = \begin{cases} y = -y_\infty \; : \; \gamma_{11}(A_x)_{1l} + \gamma_{21}\frac{(A_x)_{2l}-(A_x)_{1l}}{\Delta} + \gamma_{31}(A_x)_{Ml} + \\ \qquad + \gamma_{41}\frac{(A_x)_{Ml}-(A_x)_{M-1l}}{\Delta} = \gamma_{51}(l) \\ y = +y_\infty \; : \; \gamma_{12}(A_x)_{1l} + \gamma_{22}\frac{(A_x)_{2l}-(A_x)_{1l}}{\Delta} + \gamma_{32}(A_x)_{Ml} + \\ \qquad + \gamma_{42}\frac{(A_x)_{Ml}-(A_x)_{M-1l}}{\Delta} = \gamma_{52}(l) \end{cases} \tag{4.4}$$

with l spanning $l = \overline{1, N}$.

$$BCZ = \begin{cases} z = -z_\infty \; : \; \eta_{11}(A_x)_{j1} + \eta_{21}\frac{(A_x)_{j2}-(A_x)_{j1}}{\Delta} + \eta_{31}(A_x)_{jN} + \\ \qquad + \eta_{41}\frac{(A_x)_{jN}-(A_x)_{jN-1}}{\Delta} = \eta_{51}(l) \\ z = +z_\infty \; : \; \eta_{12}(A_x)_{j1} + \eta_{22}\frac{(A_x)_{j2}-(A_x)_{j1}}{\Delta} + \eta_{32}(A_x)_{jN} + \\ \qquad + \eta_{42}\frac{(A_x)_{jN}-(A_x)_{jN-1}}{\Delta} = \eta_{52}(l) \end{cases} \tag{4.5}$$

with j spanning $j = \overline{2, M-1}$. The Dirichlet and/or Neumann boundary conditions (*Morse and Feschbach*, 1953) can be obtained from the general form by appropriate choice of the parameters γ_{mn} and η_{mn}.

Replacing in (4.4)-(4.5) the Robin-type conditions defined in table 3.2 assign the following values to the coefficients:

$$\gamma_{21} = \gamma_{31} = \gamma_{12} = \gamma_{42} = \gamma_{41} = \gamma_{22} = 0$$

$$\begin{aligned}
&\gamma_{11} = \gamma_{32} = 1 \\
&\gamma_{51}(l) = B_0 y_\infty, \;\; \gamma_{52}(l) = -B_0 y_\infty \\
&\eta_{11} = \eta_{31} = \eta_{12} = \eta_{32} = \eta_{41} = \eta_{22} = 0 \\
&\eta_{21} = \eta_{42} = 1 \\
&\eta_{51}(l) = 0, \;\; \eta_{52}(l) = 0
\end{aligned} \tag{4.6}$$

with l spanning $l = \overline{1, N}$. On the other hand the Dirichlet conditions defined for the Ampere equation in table 3.4 correspond to the following values of the parameters:

$$\begin{aligned}
&\gamma_{21} = \gamma_{31} = \gamma_{12} = \gamma_{42} = \gamma_{41} = \gamma_{22} = 0 \\
&\gamma_{11} = \gamma_{32} = 1 \\
&\gamma_{51}(l) = B_0 y_\infty, \;\; \gamma_{52}(l) = -B_0 y_\infty \\
&\eta_{21} = \eta_{31} = \eta_{12} = \eta_{41} = \eta_{42} = \eta_{22} = 0 \\
&\eta_{11} = \eta_{32} = 1 \\
&\eta_{51}(l) = -B_0 y_l, \;\; \eta_{52}(l) = -B_0 y_l
\end{aligned} \tag{4.7}$$

with l spanning $l = \overline{1, N}$.

The two-dimensional array $A_x(j, l)$, $j = \overline{1, M}, l = \overline{1, N}$ is transformed into a one-dimensional array $\mathcal{A}_x$ having $M \times N$ elements. The same is done for the discretized current density which is written into the one-dimensional array $\mathcal{J}_x$.

The PDE given in (4.2) together with the boundary conditions given in table 3.2 or 3.4 can be written as a linear system whose unknowns are the discretized values of A_x on the $2-D$ mesh. The discretized Poisson operator in (4.3) is written in the matrix C by collecting the coefficients of $(A_x)_{j,k}$ from (4.3). The linear system we have to solve reads:

$$\mathrm{C}\mathcal{A}_x = \mathcal{J}_x \tag{4.8}$$

In the linear system (4.8) the lines corresponding to the point grids of the boundaries were replaced by the appropriate equations given by the boundary conditions (*Haidvogel and Zhang*, 1979).

The matrix C is a square matrix having $(M \times N)^2$ elements. Even for a moderate number of grid points (for instance $M = N = 40$ for the linear system) one has to solve a considerable number of equations and unknowns (1600) increasing significantly the computational effort. In that case the coefficients matrix C has 2560000 elements and is sparse since many of these elements are equal to zero. Thus solving the linear system (4.8) can be optimized by using some of the important properties of the *sparse* matrix systems

(*Golub and Van Loan*, 1989). In the calculus presented in this chapter we have used an iterative preconditioned Gauss-Seidel method (*Lu*, 1981; *Erisman*, 1986) that in general converged after a reasonable number of iterations. A short description of the method is given in the Appendix.

Insofar as the electric potential, $\Phi(y,z)$, is concerned, we do not have to solve a PDE but the nonlinear algebraic equation of plasma quasineutrality. The discretized quasineutrality equation will be solved in each point of the mesh, thus that $M \times N$ numerical solutions have to be found satisfying:

$$n_i\left(\Phi(y_j,z_l), A_x(y_j,z_l)\right) - n_e\left(\Phi(y_j,z_l), A_x(y_j,z_l)\right) = 0 \tag{4.9}$$

in each grid point (y_j, z_l). The equation will be solved by a bisection method (*Ortega and Rheinboldt*, 1970) that converges rapidly once a change of sign of the left landside of (4.9) is found. The method is briefly described in the Appendix.

It is convenient to work with non-dimensional quantities as already mentioned in chapter 3. Thus, using the scaling factors described in (3.60) the discretized non dimensional quasineutrality equation can be written:

$$n_i^*\left(\Phi^*(y_j^*,z_l^*), A_x^*(y_j^*,z_l^*)\right) - n_e^*\left(\Phi^*(y_j^*,z_l^*), A_x^*(y_j^*,z_l^*)\right) = 0 \tag{4.10}$$

The Ampere equation for the magnetic vector potential is also non-dimensional:

$$\frac{\partial^2 A_x^*}{\partial y^{*2}} + \frac{\partial^2 A_x^*}{\partial z^{*2}} = -\frac{\mu_0 N_0 \mathcal{K} T_{re}}{B_0^2}(j_{xi}^* + j_{xe}^*) \tag{4.11}$$

where μ_0 is the vacuum magnetic permeability and N_0, T_{re} and B_0 are constant parameters of the model. The spatial coordinate is normalized by the electron Larmor radius and the magnetic field by B_0 a physical free input of the model specified in Table 4.2:

$$y = \lambda_y y^*, \qquad \lambda_y = \frac{\sqrt{2 m_e \mathcal{K} T_e}}{eB} \tag{4.12}$$

$$B = \lambda_B Bj, \qquad \lambda_B = B_0 \tag{4.13}$$

The non-dimensional linear system that "discretizes" the Ampere equation for A_x is:

$$\mathrm{C}\mathcal{A}^*{}_x = \mathcal{J}^*{}_x \tag{4.14}$$

The normalized distributions of the electric and magnetic field, $\Phi^*(y_j^*, z_l)$, $A_x^*(y_j^*, z_l^*)$, are found by an iterative process. We start with an initial guess of the magnetic vector potential

$$(A_x^*)_{00}(y_j^*, z_l^*) = -B_0^* y_j^*$$

giving a uniform magnetic field for all j and l. $(A_x^*)_{00}(y_j^*, z_l^*)$ is introduced in (4.9) for finding $\Phi_{00}^*(y_j^*, z_l^*)$. This electric potential distribution is in turn introduced in the linear system (4.8). The solution of this equation gives a new distribution of the magnetic vector potential, $(A_x^*)_{01}(y_j^*, z_l^*)$. The procedure is repeated iteratively until two successive iterations give an improvement of the solution less than ϵ. In the calculations presented here we took $\epsilon = 10^{-7}$ and we used non-dimensional values of all the variables. When the procedure converges, one obtains the distribution of the electric and magnetic field consistent with the kinetic model and with the boundary conditions specified above.

4.2 Verification of the physical and numerical model: Sestero Tangential Discontinuity

In the previous sections a kinetic model for the two-dimensional sheared flows has been outlined as well as the numerical method used to solve the quasineutrality-Ampere system of nonlinear-PDE equations. The velocity distribution function of each component species (protons and electrons respectively) was given in terms of the constants of motion, $\mathcal{H}$ and p_x.

As a verification of our physical model and of the numerical method, we apply them to recover the results obtained by *Sestero* (1966) for a one-dimensional tangential discontinuity. All the quantities of the TD's model depend on only one spatial variable – the coordinate normal to the discontinuity surface.

We have defined in (3.39) and (3.40) the velocity distribution functions of ions and electrons satisfying the desired boundary conditions. In order to obtain a configuration consistent with the plasma state and fields similar to the early Sestero model of the TD we introduce in our $2D$ model the following approximations: **(a)** the magnetic field is everywhere parallel to Oz and **(b)** there is no variation with z of A_x and Φ (and implicitly of $H_{c\alpha}$ and $\mu_{c\alpha}$ in 3.56 and 3.62).

With these assumptions one recovers indeed the one-dimensional TD model of Sestero as summarized below:

- a transition from a plasma at the left side ($y = -y_\infty$) drifting with a convection velocity V_0, to a stagnant ($V = 0$) plasma state at the right side ($y = +y_\infty$);

- the *tangential discontinuity* is parallel to the xOz plane;

- all the quantities vary only with y – i.e. the coordinate *perpendicular* to the the surface of the discontinuity
- no shear of the magnetic field is considered; only the perpendicular shear of the perpendicular plasma velocity is taken into account.

The boundary conditions assumed for the Maxwell-Ampère equation are given in table 4.1. There are no boundary conditions to be imposed on the electric potential as we solve the algebraic quasineutrality equation and not the partial derivative Poisson equation.

Table 4.1: Robin-type boundary conditions used in the Sestero TD model to solve the non-dimensional Ampere equation (3.14) in the $2D$ domain $[-y^*_\infty, +y^*_\infty] \times [-z^*_\infty, +z^*_\infty]$.

	$y^* = -y^*_\infty$	$y^* = +y^*_\infty$	$z^* = -z^*_\infty$	$z^* = +z^*_\infty$
A^*_x	$B^*_0 y^*_\infty$	$-B^*_0 y^*_\infty$	-	-
$\frac{\partial A^*_x}{\partial y^*}$	-	-	-	-
$\frac{\partial A^*_x}{\partial z^*}$	-	-	0	0

The discretized forms of the equations are given in eqs. (4.10) and (4.14). An initial guess for A^*_x is introduced in equation (4.10) and the electric potential, Φ^*_{jl}, satisfying the quasi-neutrality is found in each node of the $2D$ mesh. The electric potential is back introduced into (4.14) and the magnetic vector potential is found subject to the boundary conditions given in Table (4.1). The iteration procedure converged after in 15 iterations in case of the electron profile and after 5 iterations in case of the proton profile.

4.2.1 Sestero Electron Tangential Discontinuity - SETD

Before starting the discussion on the numerical results we indicate that the figures illustrating the results were collected at the end of each subsection. Indeed, since there are numerous figures, inserting them throughout the text of Chapter 4 might confuse the reader. A list of tables and figures is inserted at the end of the thesis.

In *Sestero* (1966) the sign of the shear flow, i.e. the sign of V_0, determines the nature of the transition. For $B_z(y) > 0$ Sestero obtained an ion-dominated layer when $V_0 < 0$ and an electron-dominated one when $V_0 > 0$, an effect due to the electric field inside the layer (see *DeKeyzer and Roth*, 1997a, 1997b, 1998 for additional details). In an electron-dominated layer ($V_0 > 0$) the ions do not contribute to the electrical current. This is achieved when the ion VDF is a sum of two Maxwellian distributions: the first describes the plasma at rest at $y = +y_\infty$ and the other one is a displaced Maxwellian describing the drifting plasma at $y = -y_\infty$:

$$\begin{aligned} f_i(\mathcal{H}, \mu, p_x) &= N_{i1}\left(\frac{m_i}{2\pi\mathcal{K}T_{i1}}\right)^{\frac{3}{2}} e^{-\frac{\mathcal{H}}{\mathcal{K}T_{i1}}} + \\ & N_{i2}\left(\frac{m_i}{2\pi\mathcal{K}T_{i2}}\right)^{\frac{3}{2}} e^{-\frac{\mathcal{H}}{kT_{i2}}+\frac{p_xV_0}{kT_{i2}}-\frac{1}{2}\frac{m_iV_0{}^2}{kT_{i2}}} \end{aligned} \tag{4.15}$$

Since $V_0 > 0$ this composite VDF satisfies indeed the boundary conditions: $\lim_{y\to -y_\infty} f_i = f_{i2}$ (i.e. a displaced Maxwellian) and $\lim_{y\to +y_\infty} f_i = f_{i1}$ (i.e. an isotropic Maxwellian). The density and current obtained for f_i above are equal to:

- number density:

$$n_i = N_{i1}e^{-\frac{e\Phi(y,z)}{\mathcal{K}T_{i1}}} + N_{i2}e^{-\frac{e\Phi(y,z)}{\mathcal{K}T_{i1}}} e^{\frac{eV_0A_x(y,z)}{\mathcal{K}T_{i2}}} \tag{4.16}$$

- j_x current density:

$$j_{xi} = N_{i2}V_0e^{-\frac{e\Phi(y,z)}{\mathcal{K}T_{i2}}} e^{\frac{eV_0A_x(y,z)}{\mathcal{K}T_{i2}}} \tag{4.17}$$

The corresponding non-dimensional density and current distributions are given in the Appendix. The VDF of electrons is given by the Vlasov solution written in Chapter 3:

$$\begin{aligned} f_e(\mathcal{H}, \mu, p_x) &= \eta\left(\frac{p_x}{\sqrt{m_e\mathcal{K}T_{e1}}}\right) N_{e1}\left(\frac{m_e}{2\pi\mathcal{K}T_{e1}}\right)^{\frac{3}{2}} e^{-\frac{\mathcal{H}}{\mathcal{K}T_{e1}}} \\ & +\eta\left(-\frac{p_x - m_eV_0}{\sqrt{m_e\mathcal{K}T_{e2}}}\right) N_{e2}\left(\frac{m_e}{2\pi\mathcal{K}T_{e2}}\right)^{\frac{3}{2}} e^{-\frac{\mathcal{H}-p_xV_0+\frac{1}{2}m_eV_0{}^2}{kT_{e2}}} \end{aligned} \tag{4.18}$$

The parameters used to compute the Sestero electron TD are given in Tabel 4.2. The distribution of the magnetic vector potential is illustrated in figure **4.1(a)**. In order to single out the effects of the velocity shear the asymptotic densities and temperatures were all chosen to be equal to 3 cm^{-3} and 15 eV respectively. The asymptotic value of the magnetic field is equal to 10 nT. The asymptotic value of the bulk velocity at the left side ($y = -y_\infty$) is equal to 114 km/sec.

The total magnetic field is shown in figure **4.1(b)**. It can be seen that $|\boldsymbol{B}|$ has a dip inside the discontinuity as in the original model of Sestero.

The current j_x is small and the magnetic field B_0 is not perturbed more than 15%. The characteristic scale length of the variation of B is of the order of the electron Larmor radius.

The electric potential found from the quasineutrality equation is shown in figure **4.2(a)**. The potential has a maximum value at the left hand side boundary ($y = -y_\infty$) where the plasma velocity V_x is maximum. Φ decreases with increasing y towards the right hand side boundary of the $2-D$ domain where the plasma velocity V_x tends to zero. The electric potential Φ varies with y as in the original figures of *Sestero* (1966). The spatial coordinates y and z are given in units of the electron Larmor radius (as in *Roth et al.*, 1996) and not the electron skin depth as in the original paper of *Sestero* (1966).

The perpendicular component, E_y, of the electric field is shown in figure **4.2(b)**. E_y is everywhere perpendicular to the discontinuity as in the work of *Sestero* (1966). It has a sharp gradient inside the transition region whose scale length is of the order of the electron Larmor radius. The maximal value, in physical units, at the left hand side edge is about $3\ mV/m$. The perpendicular component of the E-field sustains a zero order drift in the direction normal to both $\boldsymbol{E}$ and $\boldsymbol{B}$.

The parallel component of the electric field is equal to zero within the limits of numerical errors. Indeed, in this case the density and temperatures are uniform along the B-field.

The electric and magnetic potential determined above have been introduced in the analytical moments described in the previous chapter. The plasma bulk velocity found from equation (3.74) is shown in figure **4.3**. The V_x component has a maximum at the left boundary ($y = -y_\infty$) and tends to zero at the right boundary ($y = +y_\infty$) of the discontinuity. It reproduce exactly the profile of the bulk velocity obtained by Sestero (1966).

The density of ions is shown in figure **4.4(a)**. The asymptotic value of density, in physical units, is equal to $3\ cm^{-3}$. It shows that the density has a maximum exactly in the middle of the sheath. The gradient of the density in the direction normal to the sheath is symmetric with respect to $y = 0$, the center of the region of TD. The characteristic scale length of density variation is of the order of the electron Larmor radius. The transition region extends over approx 100 kilometers. It is a density distribution that recovers the results obtained by *Sestero* (1966), *Roth* (1984) and *Roth et al.* (1996). Figure **4.4(b)** shows the distribution of the net charge. The latter was found by computing the second order derivative of the electric potential, $d^2\Phi/dy^2$. It takes indeed very small values such that the assumption of quasineutrality is a-posteriori verified.

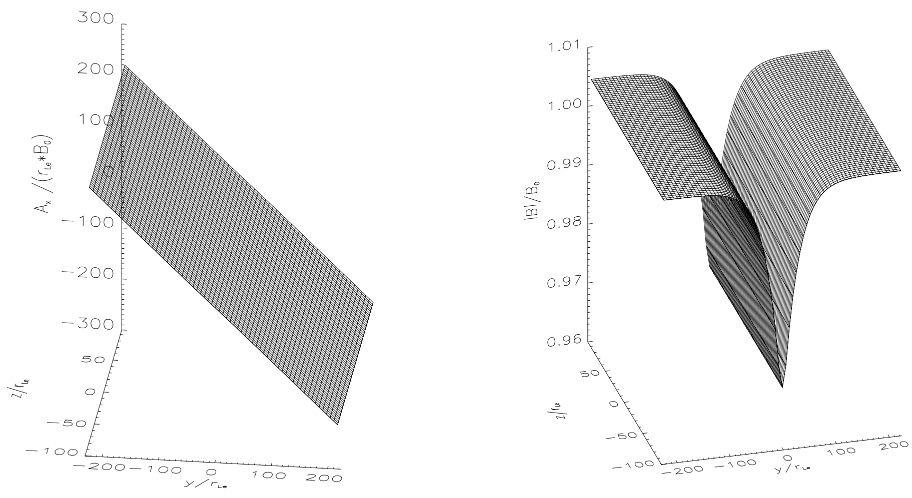

(a) Magnetic potential. (b) Total magnetic field.

Figure 4.1: SETD - distribution of the magnetic vector potential and total magnetic field given by eq. (4.14).

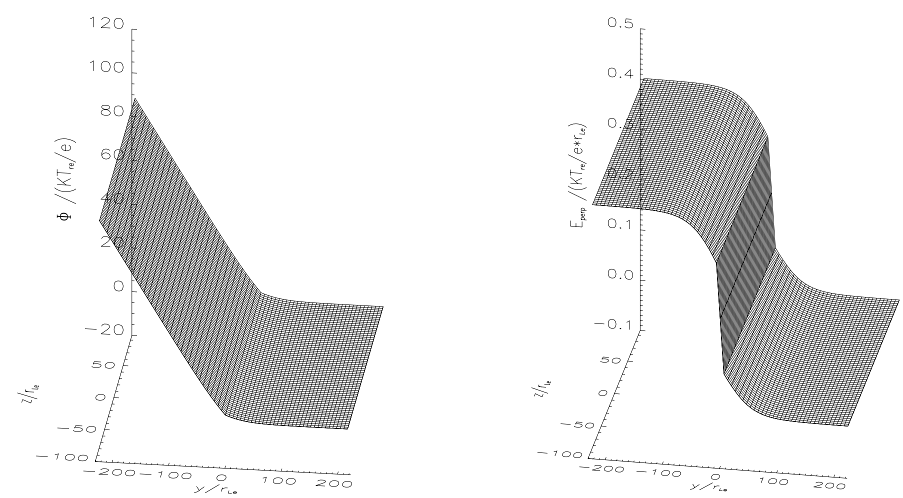

(a) Electric potential. (b) Perpendicular electric field.

Figure 4.2: SETD - Electric field potential given by the quasineutrality equation (4.10) and the perpendicular component of $\boldsymbol{B}$.

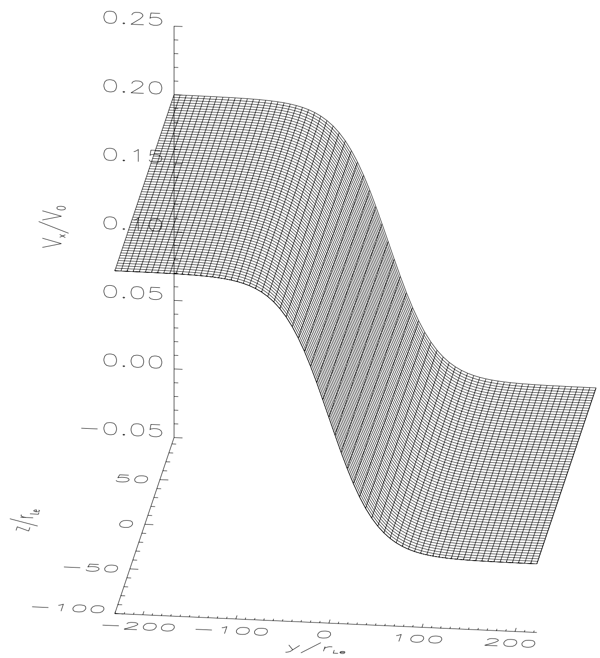

Figure 4.3: SETD - 2D profile of the plasma bulk velocity.

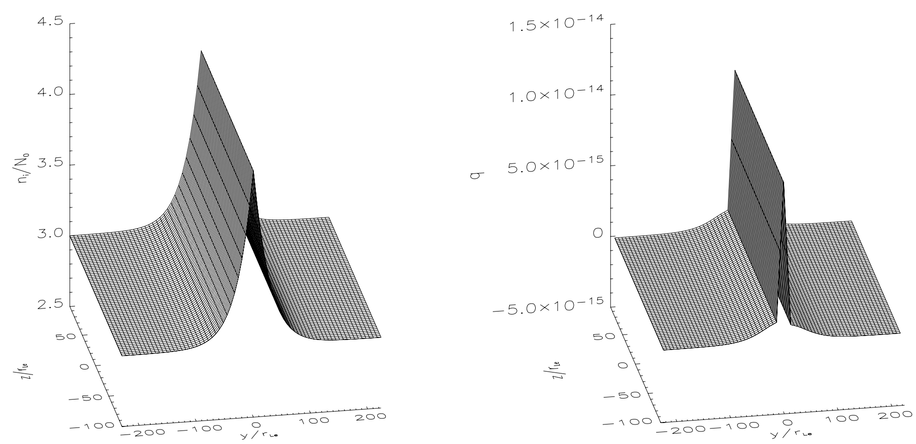

(a) Total density

(b) Total net charge

Figure 4.4: SETD - Total density and net charge.

4.2.2 Sestero Proton Tangential Discontinuity - SPTD

If $V_0 < 0$, the step functions introduced into the electron velocity distribution function can be eliminated without changing the asymptotic behavior of f_e at $y \to \pm\infty$. Thus the electrons can be described by the sum of two Maxwellians:

$$\begin{aligned} f_e(\mathcal{H}, \mu, p_x) &= N_{e1}\left(\frac{m_e}{2\pi\mathcal{K}T_{e1}}\right)^{\frac{3}{2}} e^{-\frac{\mathcal{H}}{\mathcal{K}T_{e1}}} + \\ & N_{e2}\left(\frac{m_e}{2\pi\mathcal{K}T_{e2}}\right)^{\frac{3}{2}} e^{-\frac{\mathcal{H}}{kT_{e2}}+\frac{p_x V_0}{kT_{e2}}-\frac{1}{2}\frac{m_e V_0{}^2}{kT_{e2}}} \end{aligned} \tag{4.19}$$

This VDF satisfies the boundary conditions: $\lim_{y\to -y_\infty} f_e = f_{e2}$ (i.e. a displaced Maxwellian) and $\lim_{y\to +y_\infty} f_e = f_{e1}$ (i.e. an isotropic Maxwellian). The number density and current distributions given by f_e are equal to:

- number density:

$$n_e = N_{e1} e^{\frac{e\Phi(y,z)}{\mathcal{K}T_{e1}}} + N_{e2} e^{\frac{e\Phi(y,z)}{\mathcal{K}T_{e1}}} e^{-\frac{eV_0 A_x(y,z)}{\mathcal{K}T_{e2}}} \tag{4.20}$$

- j_x current density:

$$j_{xe} = -N_{e2} V_0 e^{\frac{e\Phi(y,z)}{\mathcal{K}T_{e2}}} e^{-\frac{eV_0 A_x(y,z)}{\mathcal{K}T_{e2}}} \tag{4.21}$$

The corresponding non-dimensional charge and current densities are given in the Appendix.

The VDF of ions is given by:

$$\begin{aligned} f_i(\mathcal{H}, \mu, p_x) &= \eta\left(-\frac{p_x}{\sqrt{m_i\mathcal{K}T_{i1}}}\right) N_{i1}\left(\frac{m_i}{2\pi\mathcal{K}T_{i1}}\right)^{\frac{3}{2}} e^{-\frac{\mathcal{H}}{\mathcal{K}T_{i1}}} \\ & +\eta\left(\frac{p_x - m_i V_0}{\sqrt{m_i\mathcal{K}T_{i2}}}\right) N_{i2}\left(\frac{m_i}{2\pi\mathcal{K}T_{i2}}\right)^{\frac{3}{2}} e^{-\frac{\mathcal{H}-p_x V_0+\frac{1}{2}m_i V_0{}^2}{kT_{i2}}} \end{aligned} \tag{4.22}$$

The input parameters used in this model are given in Table 4.2. We keep the same asymptotic value of the magnetic field and of the reference energy, $\mathcal{K}T_{ref}$. The asymptotic value of the plasma velocity is negative and one order of magnitude smaller than in the SETD model. In figure **4.5(a)** we show the solution of the Ampere equation subject to the boundary conditions specified in table 4.1. Figure **4.5(b)** illustrates the corresponding total B-field. The perturbation of the magnetic field is small and extended over a much broader region than in the previous case. It retrieves the same value and orientation at the two lateral borders $y = \pm y_\infty$.

Figure **4.6(a)** shows the distribution of the electric potential found from the quasineutrality equation. The perpendicular component of the electric field, shown in figure **4.6(b)**, is everywhere perpendicular to the sheath. At the left hand side, where the plasma is moving, the values of the perpendicular electric field component, in physical units, is equal to 0.9 mV/m. The parallel component of E-field is equal to zero in the limit of the numerical errors. The velocity shear in the direction perpendicular to B does not produce a parallel electric field.

The plasma bulk velocity, computed by replacing the moments of the VDFs in (3.74), is shown in figure **4.7**. It has a transition from a maximum value ($V_0 = -0.05\sqrt{\frac{2\mathcal{K}T_e}{m_e}}$) at the left side ($y = -y_\infty$) to a minimum one ($V_0 = 0$) at the right edge. In physical units, the velocity at the left hand side is equal to 28.5 km/s. In the case presented here we have "forced" a total amount of shear across the transition region of about 10% of the electron thermal velocity. That is the reason why a slight oscillation of the bulk velocity values occurs inside the TD. Oscillations of the plasma velocity and density were reported by Sestero for values of the velocity shear exceeding 2% of the electron thermal velocity. The results (not shown here) obtained for cases with smaller perpendicular shears of velocity show that the solution is smooth and reproduce the asymptotic behavior at $y \to \pm\infty$.

The number density of protons, is shown in figure **4.8(a)**. The density increases inside the transition region by 10%. A symmetry with respect to the middle of the sheath can be also noticed. The characteristic scale length of the transition is of the order of the proton Larmor radius (about 40 km in this case). The transition layer extends over approx. 1000 kilometers. The net total charge is illustrated in figure **4.8(b)** and takes again very small values. These results reproduce well the ones obtained by *Sestero* (1966) and later on by *Roth et al.* (1996).

It can therefore be concluded that our $2D$ kinetic model and the numerical method used to solve the coupled system of PDE-nonlinear equations have passed the consistency check test. Indeed we have reproduce the results obtained previously by the $1D$ models of the tangential discontinuities. Our profiles are consistent with what Sestero called "ion dominated layer" and "electron dominated layer" respectively, depending on the sign of the asymptotic velocity V_0. The model produces profiles of the electric and magnetic potential, velocity and particle density that are consistent with the results obtained previously by $1D$ models of *Sestero* (1966) and *Roth et al.* (1981, 1996). In the next section we will add to the Sestero's sheath an additional shear of the plasma velocity in the Oz direction such that we will develop fully our two-dimensional kinetic model.

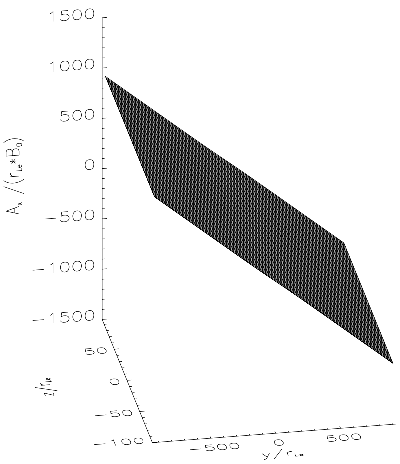

(a) Magnetic vector potential.

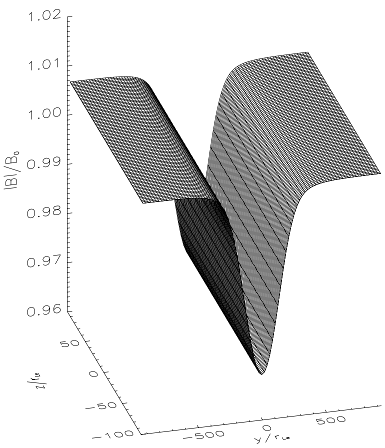

(b) Total magnetic field.

Figure 4.5: SPTD - magnetic vector potential and total magnetic field given by (4.14) with boundary conditions specified in table 4.1.

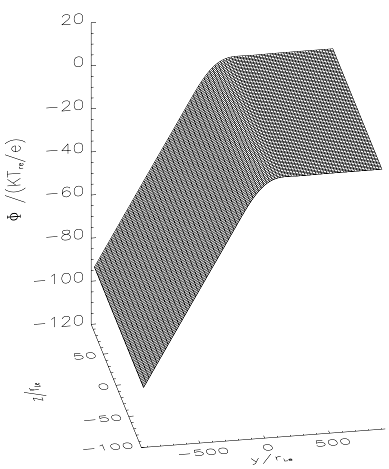

(a) Electric potential.

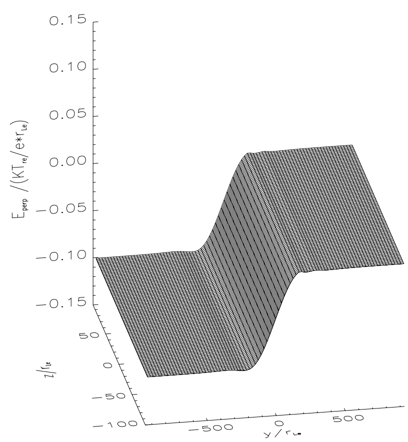

(b) Perpendicular electric field.

Figure 4.6: SPTD - Electric field potential given by the quasineutrality equation (4.10) and the perpendicular component of $\boldsymbol{B}$.

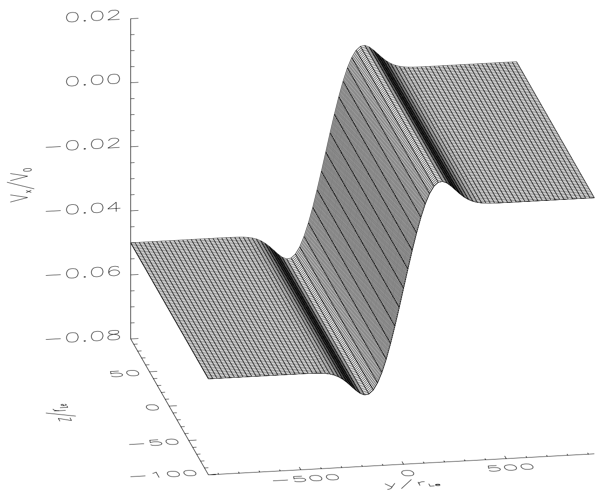

Figure 4.7: SPTD - 2D profile of the plasma bulk velocity.

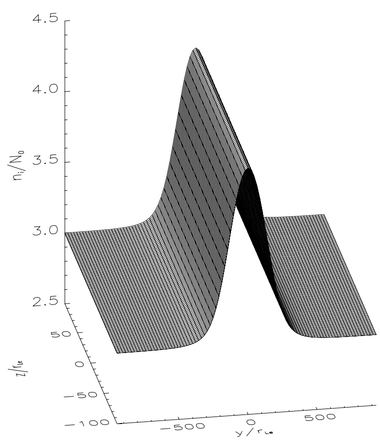

(a) Total density.

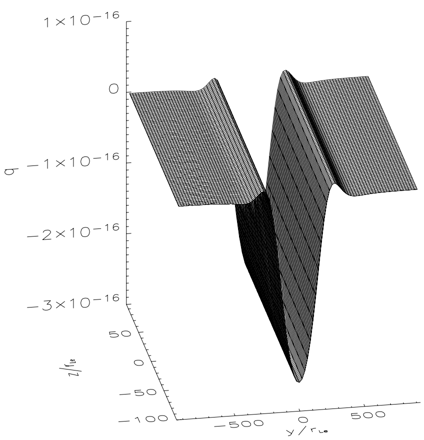

(b) Total net charge.

Figure 4.8: SPTD - total density and total net charge.

4.3 Solution for a $2D$ plasma flow with mixed shear of the velocity : perpendicular and parallel to the B-field

In this section a parallel shear of the plasma bulk velocity is added to the perpendicular one studied in the case of the Sestero-type plasma sheath. Since the VDF is given in terms of the constants of motion $\mathcal{H}$ and p_x the dependence of the VDF on the spatial coordinates y and z is determined by the spatial variation of the electromagnetic potentials. We will extend the Sestero TD model, by adding a variation with z in addition to the variation with the coordinate y discussed in the previous section.

The variation with z is introduced by modifying the boundary conditions of the Ampere equation. The Poisson equation is approximated by the quasineutrality equation. Thus the electric potential will be adjusted such that the number of plasma positive charges is approximately equal to the number of negative charges. The boundary conditions for the non-dimensional Maxwell-Ampere equation are given in Table 4.3. They are obtained by non-dimensionalizing the boundary conditions given in table 3.4.

The asterisk will be dropped from now on but will keep in mind that we work with non-dimensional quantities if not mentioned otherwise. The function $\zeta(z)$ introduces the variation of A_x with z on the left boundary. It is chosen thus that the asymptotic behavior of the plasma, described in section **3.3.3** is achieved, i.e. the bulk velocity defined in (3.74) satisfies the boundary conditions mentioned in table 3.3. In the numerical models developed in the next subsection $\zeta(z)$ will be defined on grounds of mathematical simplicity as:

$$\zeta(z) = \Theta_1 erfc\left(\frac{z^2 - z_{lim}^2}{z_c}\right)$$

with Θ_1 a constant defining the amplitude of the perturbation, $\pm z_{lim}$ the z-limits of the perturbed region z_c a constant defining the scale length of the boundary separating the perturbation region from the rest of the plasma. The choice of $erfc$ function does not restrict in any way the generality of the models. Indeed, any other function, symmetric or not with respect to $z = 0$ plane, can be adopted.

We use an iterative method to find the solutions for A_x and Φ: the first guess for the magnetic potential, $A^*_{x00} = -B^*_0 y^*$, giving a uniform magnetic field is introduced into the quasineutrality equation. A first estimation of the electric potential, $\Phi(y_j, z_l)$ is found from the quasineutrality. This solu-

Table 4.2: Boundary/asymptotic values of the plasma density and temperature used as input parameters to solve the Vlasov-Ampère-quasineutrality equations

Model	N_{i1}^*	N_{e1}^*	N_{e2}^*	N_{i2}^*	τ_i	τ_e	τ_{i2}	τ_{e2}	T_{ref}	V_0^*	B_0
SETD	3	3	3	3	10	10	10	10	1.5	0.2	10
SPTD	3	3	3	3	10	10	10	10	1.5	-0.05	10
PSEL1	1	1	1	1	55	55	55	55	1	1	10
PSEL2	1	1	10	10	55	55	55	55	1	1	10
PSEL3	1	1	10	10	55	55	25	25	1	1	10
PSPL1	1	1	1	1	55	55	55	55	1	-0.01	10
PSPL2	1	1	10	10	5	5	5	5	1	-0.01	10
PSPL3	1	1	10	10	5	5	51	51	1	-0.01	10

N_{i1}^*, N_{e1}^*, N_{i2}^*, N_{e2}^* = non-dimensional asymptotic number densities;
T_{ref} = reference energy (in eV); $\tau_i = \frac{T_{i1}}{T_{ref}}$, $\tau_e = \frac{T_{e1}}{T_{ref}}$, $\tau_{i2} = \frac{T_{i2}}{T_{ref}}$, $\tau_{e2} = \frac{T_{e2}}{T_{ref}}$
T_{i1}, T_{e1}, T_{i2}, T_{e2} = asymptotic temperatures in eV
V_0^* = non-dimensional parameter in the displaced Maxwellian VDF
$V_0^* = V_0/\sqrt{\frac{2\mathcal{K}T_{ref}}{m_e}}$, B_0 reference magnetic field, in nT

tion is back introduced into the Ampere equation subject to the boundary conditions given in Table 4.3.

4.3.1 Parallel Sheared Electron Layer - PSEL1

In this subsection we derive a numerical model, the *Parallel Sheared Electron Layer* (PSEL1) model, that describes the plasma parameters and fields in the case of a $2D$ flow. The model is defined for a positive value of the boundary magnetic field, $B_0 > 0$ and a positive value of the boundary velocity on the left hand side , $V_0 > 0$. In this case the protons and electrons are described by the velocity distribution functions given by eqs. (4.15) and (4.18).

The input parameters introduced into the model are given in Table **4.2**. The non-dimensional amplitude of the perturbation imposed at the left hand side boundary is equal to the non-dimensional asymptotic velocity, $\Theta_1 = V_0^*$. V_0^* is a free input parameter of the model.

The results shown in figures **4.9-4.20** correspond to the propagation of a plasma beam having a thermal energy of 55 eV and a bulk velocity of approximately +590 km/sec through a background plasma with the same temperature but which is stagnant. Both plasma populations have the same

Table 4.3: Dirichlet-type boundary conditions used in the $2D$ sheared models to solve the non-dimensional Ampere equation (3.14) in the $2D$ domain $[-y^*_\infty, +y^*_\infty] \times [-z^*_\infty, +z^*_\infty]$.

	$y^* = -y^*_\infty$	$y^* = +y^*_\infty$	$z^* = -z^*_\infty$	$z^* = +z^*_\infty$
A^*_x	$B^*_0 y^*_\infty + \zeta(z^*)$	$-B^*_0 y^*_\infty$	$-B^*_0 y$	$-B^*_0 y$
$\frac{\partial A^*_x}{\partial y^*}$	-	-	-	-
$\frac{\partial A^*_x}{\partial z^*}$	-	-	-	-

density ($1\ cm^{-3}$) at the boundaries. These asymptotic conditions define a situation that can be found at the magnetopause. The numerical procedure converges after 13 iterations. The dimension of the 2D domain was 60×60 points.

The $2D$ distribution of the magnetic potential is shown in figure **4.9**. $A_x(y, z)$ decreases from maximum values at the left boundary ($y = -y_\infty$) to minimum values at the right boundary of the integration box. The small perturbation imposed at the left boundary can be observed in the left half of the integration domain. It depends both on y and z The total magnetic field distribution computed from the potential $A_x(y, z)$ is illustrated in figure **4.10**. It shows two peaks in the region where the perturbation is imposed. It has been verified that the condition $\boldsymbol{\nabla} \cdot \boldsymbol{B} = 0$ is strictly satisfied everywhere.

The $2D$ distribution of the electric potential found from the quasineutrality equation is illustrated by figure **4.11**. One can note that the electric potential varies with y and z throughout the integration domain. It retrieves the general trend of the "Sestero-type" potential for $y/r_{Le} > 0$. The potential has a strong peak at the left hand side boundary where $A_x(y, z)$ has also a maximum.

The $2D$ distribution of the plasma bulk velocity is obtained by replacing in the moment equation (3.74) the distribution of $\Phi(y, z)$ and $A_x(y, z)$ found from quasi-neutrality equation and the Ampere equation. The result is displayed in figure **4.12**. A notable feature of the bulk velocity profile is the "hump" that corresponds to an excess of velocity with respect to the rest of the plasma flow. It occurs close to the left edge of the simulation box. This "hump" adds to the V_x profile already found for the one-dimensional Sestero sheath.

The observed excess of the bulk velocity is produced by: (1) an increased mass flux, $m_i n_i < v_{xi} > + m_e n_e < v_{xe} >$ (not shown) and (2) a decreased total mass density (see fig. **4.20(a)**). The 2D distribution of $V_x(y, z)$ has indeed the expected behavior: it decreases with increasing y and z. The maximum value of the bulk velocity is equal to 578 km/s. The scale of the transition region from $V_x = V_0$ to $V_x = 0$ is determined mainly by the ions and lesser by the electrons, due to the difference of mass between the two species.

It remains to be determined if the plasma bulk velocity has a gradient (or is sheared) in the direction parallel to the magnetic field. A contour plot of the plasma bulk velocity over the distribution of the magnetic field is shown in figure **4.13**. The picture gives an overall view of the variation of the modulus of velocity with respect to the direction of the magnetic field. One can note that in the regions close to the left hand side border the magnetic field is inclined with respect to z-direction. The plasma bulk velocity is everywhere directed parallel to the Ox direction, i.e. normal to the magnetic field. One can identify in figure **4.13** regions where the same magnetic field line is intersected by contours corresponding to different bulk velocities.

The magnetic field has only two non-zero components: B_y and B_z. Due to j_x currents, the external magnetic field is perturbed by the sheared plasma flow. Indeed, the diamagnetic current in the Ox direction produces a B_y component that adds to $\boldsymbol{B}_0$ as illustrated in figure **4.13**.

As suggested by figure **4.13** the variation or shear of the plasma bulk velocity has a perpendicular component as well as a parallel component in the 2D domain for $y/r_{Le} < 100$. This is a case of *mixed* shear. A more quantitative assessment of the parallel shear of velocity is given by figure **4.14**. The plasma bulk velocity has a non-vanishing parallel shear into a narrower region, close to the left boundary where the z-dependent boundary conditions were imposed for A_x. The existence of this parallel shear is a novel feature, not studied before by the kinetic models of TD's.

The electric field distribution is easily determined from the potential $\Phi(y, z)$. The parallel and perpendicular component with respect to $\boldsymbol{B}$ are computed as:

$$E_{parallel} = \frac{\boldsymbol{E} \cdot \boldsymbol{B}}{B}$$

and

$$\boldsymbol{E}_{perp} = \boldsymbol{E} - E_{parallel}\hat{\boldsymbol{b}}$$

where $\hat{\boldsymbol{b}}$ is the unit vector along the B-field direction. The results are shown in figure **4.15**.

The perpendicular component of the electric field (shown in figure **4.15**) has a maximum where the magnetic induction and plasma velocity are maximum. The maximum value of the E_{perp} is equal to 18 mV/m. This distribution of the perpendicular E-field shows similar features to the electric field distribution used in the numerical integration of orbits discussed in cases B and C of the Chapter 1 of this thesis.

The perpendicular electric field is sustaining the plasma advancement in the direction normal to the magnetic field. It is an electric field similar to the Schmidt convection electric field (*Schmidt*, 1960; *Lemaire*, 1985). The distribution of the perpendicular electric field exhibits a transition region, like in the Sestero sheath, within which the convection velocity ($U_E = E_{perp}/B$) decreases to zero. The sheath is no longer parallel to the yOz plane as for the Sestero TD, but is deformed and bent as can be seen in the figure **4.16**. Thus in the model PSEL the one-dimensional Sestero TD is "deformed" into a $2D$ boundary layer.

Even more notably is the existence of a parallel component of the electric field. Indeed the right panel of figure **4.15** shows two distinct regions where the parallel electric field is different from zero. In figure **4.16** the isocontours of $E_{parallel}(y, z)$ are superimposed over the vector plot of the magnetic field lines. The plot shows indeed that there are two regions where equipotential lines intersect the same magnetic field line. They are located in two distinct regions: **Region 1** around the zone of excess of momentum, where the velocity shear is maximum (delimited in the right panel of figure **4.15** by approx $z \in [-200, 200]$ and $y \in [-400, -250]$) and **Region 2** within the $2D$ layer mentioned before (delimited in the right hand side panel of figure **4.15** by $z \in [-400, 400]$ and $y \in [-150, 150]$). The maximum value of the parallel component of the electric field in the so-called Region 1 is approximately 18 $\mu V/m$ while in the Region 2 is much smaller: $E_{parallel} \approx 2\ \mu V/m$.

In order to have a better insight on the plasma and field configuration we plot the variation with the z-coordinate of the electric potential, electric current, parallel component of $\boldsymbol{E}$ and plasma bulk velocity at 4 different values of y. The results are shown in figure **4.18**. One can note that the parallel electric field has two peaks localized precisely in $z = z_{lim}$, where shear of the plasma velocity is maximum. The electric potential has also a maximum in that region.

The z-profile of the parallel component of $\boldsymbol{E}$ in the Region 1 has a "bipolar" signature, resembling the profile of parallel fields reported in weak double layers (see *Chiu and Schultz*, 1978; *Chiu and Cornwall*, 1980; *Raadu*, 1989; *Newman et al.*, 2002). These features of the electric potential and of the parallel electric field are centered in the **Region I** in $z = +100\ r_{lE}$ and $z = -100\ r_{lE}$ respectively. The centers of the field aligned weak double layers (WDL) are localized symmetric with respect to the $z = 0$ plane, in $z = \pm z_{lim}$. This symmetry is imposed by the function $\zeta(z)$. Any other, non-symmetric profile can be also adopted. The position of WDLs coincides with the maximum of the parallel gradient of the bulk velocity as shown by the low right panel of figure **4.18** and the right panel of figure **4.19**.

Thus in **Region 1** there is a parallel component of the electric field, with a bipolar distribution, produced by the parallel shear of the bulk velocity. The opposite polarization of the parallel component at both edges of the excess of momentum flow has a confining role. Indeed it can preclude the field-aligned spreading of the particles that are contained into the Region 1.

Since in Region 2 the parallel shear of velocity is very small, as can be seen from figure **4.14** and right panel of **4.19**, the existence of a non-zero parallel E-field may seem unexpected. Figure **4.17** explains why there is a parallel electric field in the **Region 2**. Indeed, a plasma density gradient is formed in the direction parallel to $\boldsymbol{B}$. This gradient has a component parallel to $\boldsymbol{B}$ in the Region 2. It is this parallel gradient of density that produces the second region of non-zero parallel electric field. This region is localized precisely inside the $2D$ layer formed at the interface between the convecting and stagnant regimes. In the PSEL1 model this sheath is a 2D structure not a 1D one as in the SETD model.

The difference between the two regions is that in Region I the parallel shear of the plasma velocity is stronger and localized within a narrower layer. This thesis presents for the first time a kinetic model for the parallel E-field produced by this type of shear. In Region II the parallel shear of the plasma velocity is absent but there is a parallel gradient of the density (or kinetic pressure) producing a parallel component of $\boldsymbol{E}$. The region where this parallel E-field exists extends over much longer distances in the direction of the magnetic field than in the case of **Region I** field. The distribution of the parallel electric field discussed in this section illustrates the situation when the two different mechanisms act together but their contribution can be clearly separated in the two regions discussed above.

The physical mechanism responsible for producing the double layers in both regions analyzed above is the anisotropy of the tensor of the momentum flux density. Indeed the latter is defined as (*Longmire, 1963*) :

$$P_{(\alpha)ij} = n_\alpha m_\alpha V_{\alpha i} V_{\alpha j} + p_{\alpha ij} \tag{4.23}$$

where $V_{\alpha i}$ is the i-th component of the average velocity of the species α and $p_{\alpha ij}$ is the partial pressure tensor. In the stationary case ($\partial/\partial t = 0$) and when there is an electromagnetic field the momentum conservation law for the ions ($\alpha = i$) and electrons ($\alpha = e$) read:

$$\boldsymbol{\nabla}_{||} \left(n_\alpha m_\alpha \overline{\overline{\boldsymbol{V}_\alpha \boldsymbol{V}_\alpha}} + \overline{\overline{p}}_\alpha \right) = n_\alpha q_\alpha E_{||} \tag{4.24}$$

$$\boldsymbol{\nabla}_{\perp} \left(n_\alpha m_\alpha \overline{\overline{\boldsymbol{V}_\alpha \boldsymbol{V}_\alpha}} + \overline{\overline{p}}_\alpha \right) = n_\alpha q_\alpha \left[E_\perp + (\boldsymbol{j}_\alpha \times \boldsymbol{B}) \right] \tag{4.25}$$

In model $PSEL1$ the **Region I** parallel electric field is mainly due to the first term (the shear of ion bulk velocity and ion momentum flux density of the ions) in the left hand side of equation (4.24), while **Region II** parallel E-field component is mainly due to the the second term (the gradient of the electron kinetic pressure).

The ion density distribution is shown in figure **4.20(a)**. It is equal to the density distribution of the electrons since the quasineutrality condition is satisfied. Close to $y/r_{Le} = 0$ the ion and electron densities have a maximum like that existing in the $1D$ Sestero sheath. Again one can note that the sheath is deformed and became a $2D$ structure. The quasineutrality is satisfied throughout the $2D$ layer. The net charge values $(n_i - n_e)/(n_i + n_e)$ (not shown) do not exceed 10^{-14}.

The distribution of the electric current, $J_x(y, z)$, shows also interesting features. There is a non-vanishing current density associated to the excess of velocity imposed at the left border of the $2D$ integration box. Otherwise the current is null except for the transition layer or sheath. Figure **4.20(b)** shows that within a layer with a width of 100-200 electron Larmor radii (corresponding to approx. 100-200 km) there are two sheets of antiparallel current flowing in the Ox direction. This is a striking feature as antiparallel current sheets are often encountered in the magnetosphere.

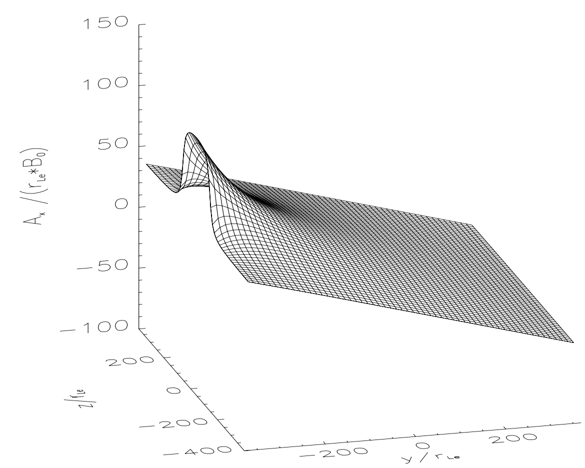

Figure 4.9: model PSEL1 - $2D$ distribution of the magnetic vector potential component, A_x. A small perturbation was introduced in the boundary condition for the left border $y = Y_1$.

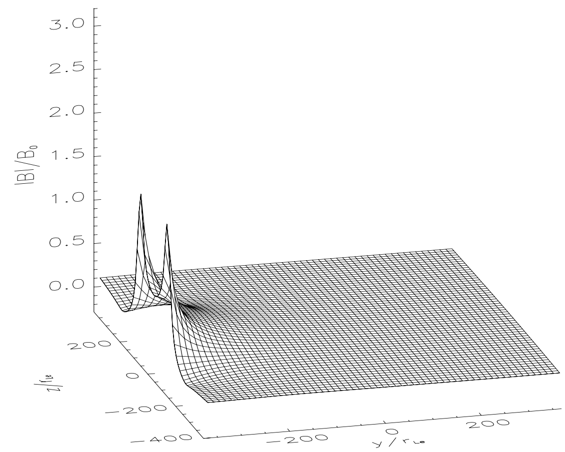

Figure 4.10: model PSEL1 - Total magnetic field given by the magnetic vector potential shown in figure **4.9**

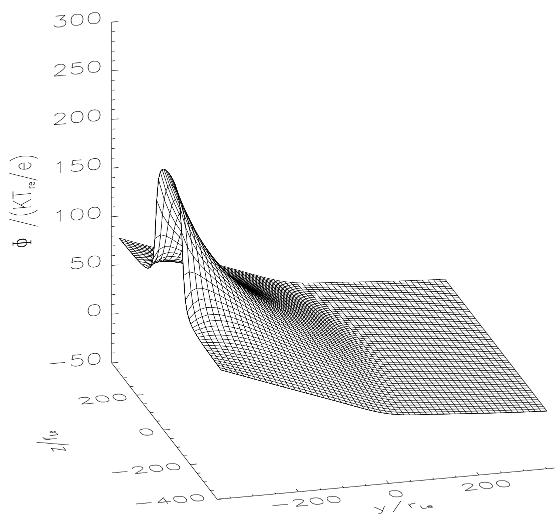

Figure 4.11: model PSEL1 - Solution of the quasineutrality for a $2D$ sheared plasma flow.

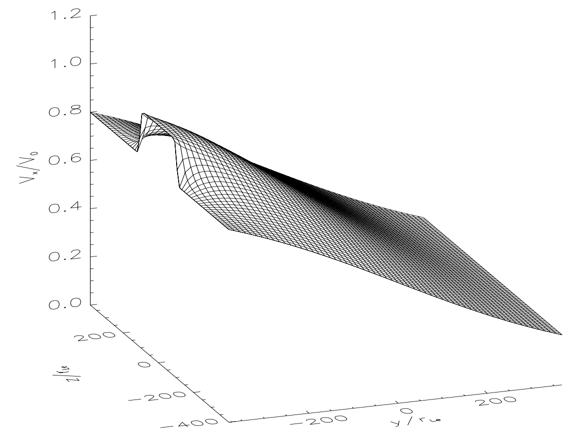

Figure 4.12: model PSEL1 - Non-uniform distribution of the plasma average velocity; Oz is the direction of the main magnetic field.

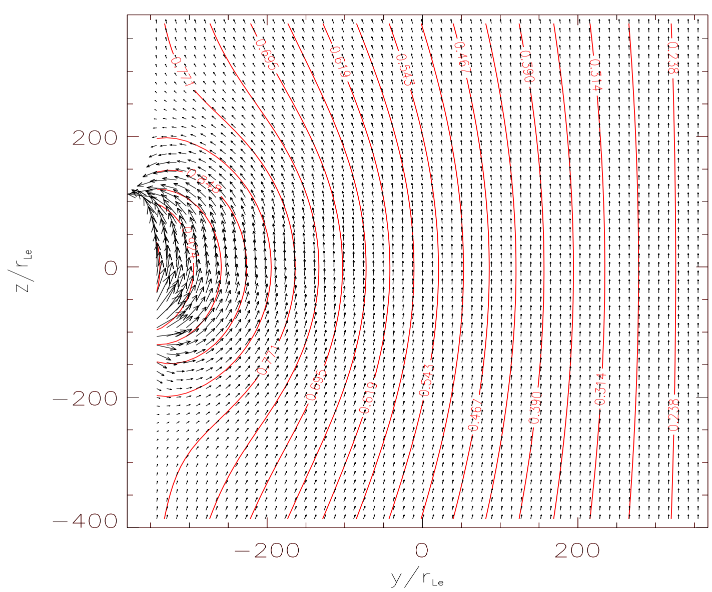

Figure 4.13: model PSEL1 - Illustration of the magnetic field distribution: arrows are plotted according to the local amplitude and inclination of the magnetic field. Contours of equal amplitude of the $2D$ velocity field were over plotted.

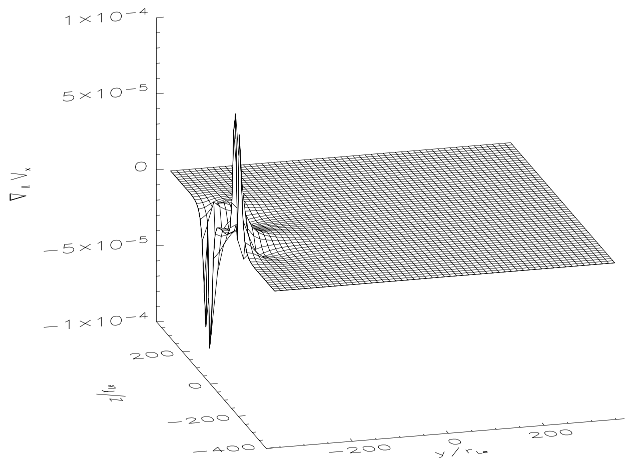

Figure 4.14: model PSEL1 - Distribution in the yOz plane of the parallel shear of the plasma bulk velocity.

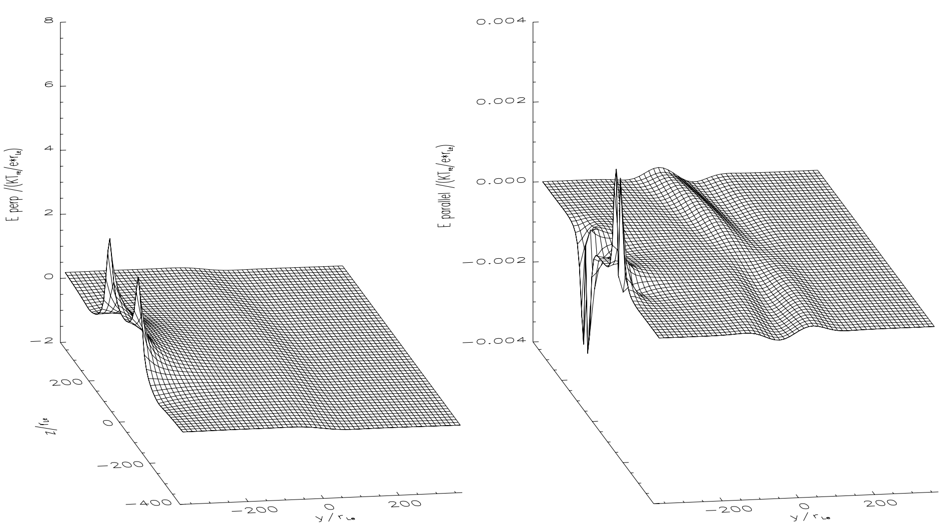

Figure 4.15: model PSEL1 - $2D$ distribution of the perpendicular component of the electric field (left panel) and of the parallel component (right panel).

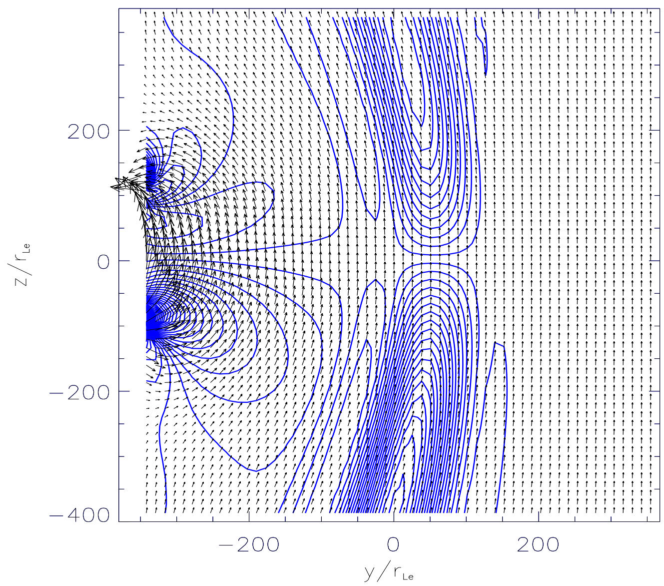

Figure 4.16: model PSEL1 - Isocontours of $E_{parallel}$(in blue); B-field is shown by black arrows.

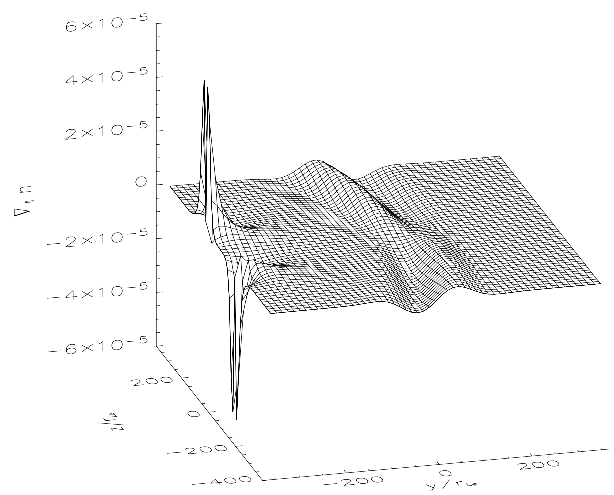

Figure 4.17: model PSEL1 - Gradient in the direction parallel to $\boldsymbol{B}$ of the density.

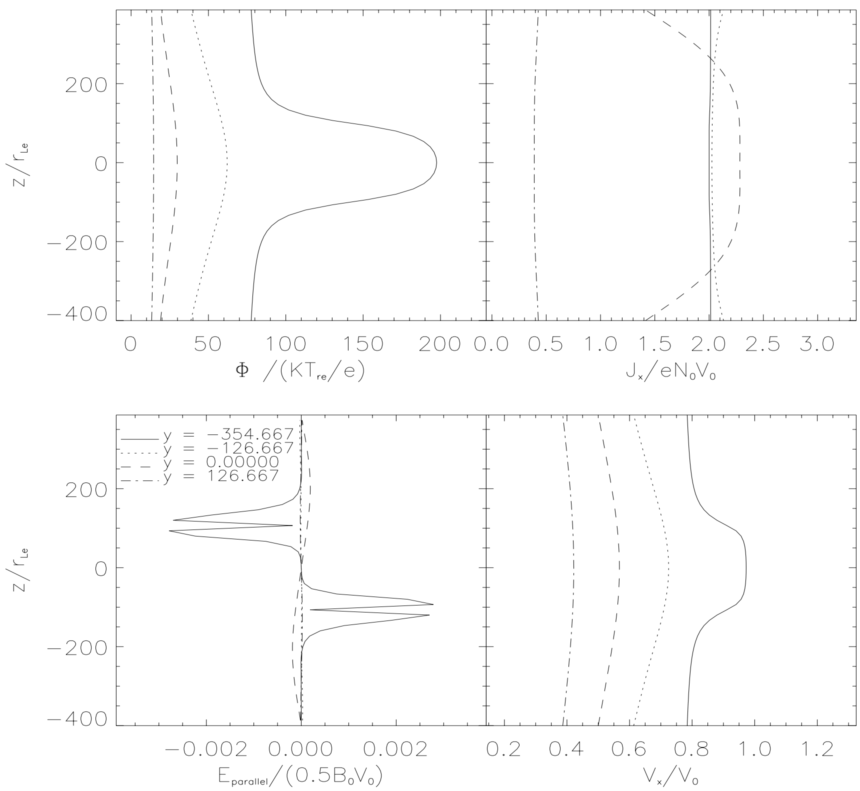

Figure 4.18: model PSEL1 - Electric potential (Φ), electric current (J_x), parallel E-field ($E_{parallel}$) and plasma bulk velocity (V_x) at 4 different y locations.

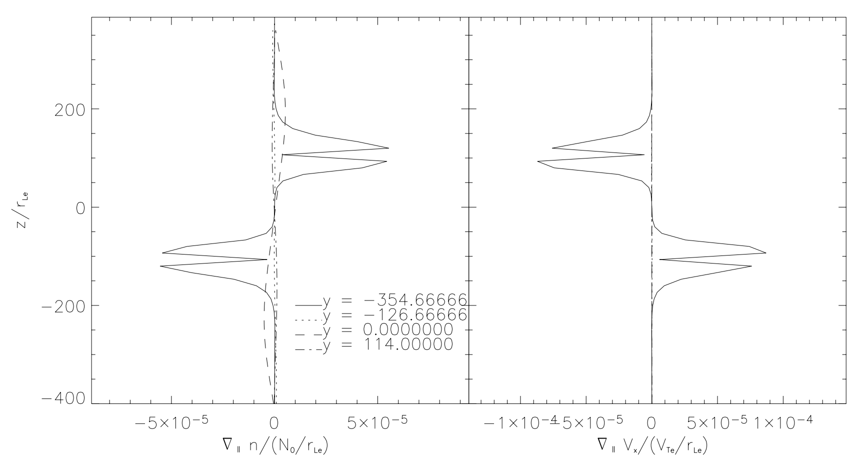

Figure 4.19: model PSEL1 - Gradient in the direction parallel to the magnetic field of the density (left panel) and bulk velocity (right panel) respectively.

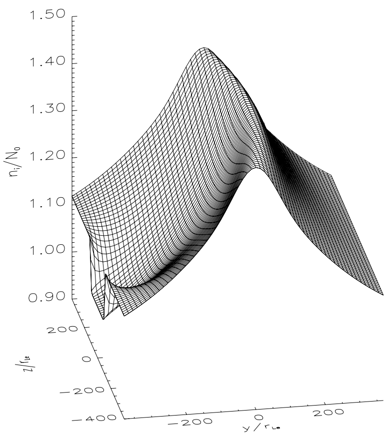

(a) Ion density

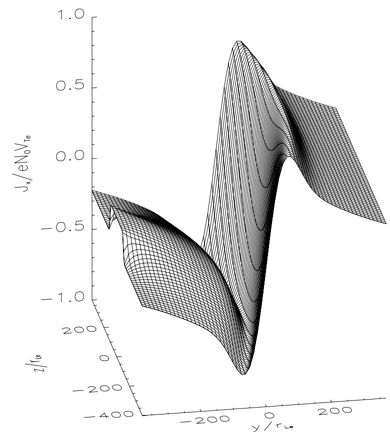

(b) Electric current

Figure 4.20: model PSEL1 - Ion density and electric current for the $2D$ sheared plasma flow.

4.3.2 Parallel Sheared Electron Layer - PSEL2

In the following we discuss the results obtained by modifying some or all of the model parameters: asymptotic densities of both species on both sides (N_{i1}, N_{e1}, N_{i2}, N_{e2}), asymptotic temperatures of both species on both sides (T_{i1}, T_{e1}, T_{i2}, T_{e2}), external magnetic field (B_0) and asymptotic maximum velocity (V_0).

First the asymptotic densities, N_{i2}, N_{e2}, of the convecting part of the VDFs (4.15)-(4.18) are increased. In this case, called *Parallel Sheared Electron Layer 2* ($PSEL2$), we compute the electromagnetic field and plasma parameters at the interface between a higher density plasma moving through a stagnant lower density plasma. Both plasmas have the same temperature, $\tau_i = \tau_e = \tau_{i2} = \tau_{e2} = 55$. The full set of parameters used for these computations is given in Table 4.2.

The increasing of the asymptotic density reduces the amplitude of the excess of velocity at the left boundary of the integration domain, as can be seen from figure **4.22**. To explain this, one has to remind that we compute the bulk velocity as the ratio between total mass flux and total mass density (see eq. 3.74). In the model $PSEL2$ the amplitude of the perturbation imposed on the left boundary, Θ_1, has the same value as in the model $PSEL1$. However, N_{i2} - the asymptotic density at the left hand side is 4 times greater in the $PSEL2$ model than in $PSEL1$. Thus the relative decreasing of the density in the sheared region observed in the model $PSEL1$ (see figure **4.20(a)**) has considerably reduced in the model $PSEL2$ (see fig. **4.22**). The mass density is then greater in case $PSEL2$ reducing the excess of velocity as can bee seen in figure **4.22**.

The width of the transition layer is of the order of the electron Larmor radius as can be seen from density data of the right panel of figure **4.22**. The denser plasma moves with a velocity close to V_0 at the left edge of the integration domain.

The distribution of the perpendicular and parallel components of the electric field are illustrated in figure **4.23**. The Region 1 feature found for the distribution of $E_{parallel}$ in the $PSEL1$ model is more reduced in the $PSEL2$ model. Still it has the same bi-polar signature revealed by the previous model. The velocity and density parallel gradients are also much more reduced in that region of the $2D$ domain. A more important component of the parallel electric field is found in what we have called the Region 2.

In low left panel of figure **4.21** the parallel component of the electric field is plotted at 4 different y-coordinates. The same figure shows the corresponding z-profiles for the electric potential (Φ), electric current density (j_x) and plasma bulk velocity (V_x). One can see that the peak value of Region 1 parallel component, given in non dimensional units in fig. **4.21**, corresponds to an intensity equal to 2.7 $\mu V/m$. In the Region 2 the maximum value of $E_{parallel}$ is equal to 18 $\mu V/m$.

The z-profiles of the parallel gradient of the density and of the bulk velocity at the same 4 different y locations were plotted in figure **4.24**. They show that in Region 1 two mechanisms producing parallel electric fields operate together: the parallel shear of the perpendicular bulk velocity and the parallel gradient of the electron density and electron kinetic pressure.

In Region 2 the parallel shear of bulk velocity is very small. There is a more important parallel gradient of density. As expected the enhancement of the total density of the moving plasma on the side 2 ($y = -y_\infty$) enhances the electron density and pressure gradient. Indeed, in Region 2 the effect of the parallel gradient of density, $\nabla_{||}n$, is more important in eqs.(4.24)-(4.25) than the parallel shear of the perpendicular velocity, $\nabla_{||}V_x$. Thus in Region 2, the distribution of $E_{parallel}$ (fig. 4.21 low left panel) closely follow the distribution of the parallel density gradient as shown in figure **4.24** (left). The signature of $E_{parallel}$ in Region 2 is bipolar.

One has to note also that whenever the parallel shear of velocity is non-negligible, this seems to be the dominant process producing the parallel electric field. Figures **4.21** (low left panel) and **4.24** show that in Region 1 the $E_{parallel}$ is correlated with $\nabla_{||}V_x$ and anti correlated with $\nabla_{||}n$, while in

Region 2 (where $\nabla_{||}V_x$ is negligible) $E_{parallel}$ is correlated with $\nabla_{||}n$. This is consistent with the momentum conservation law (4.24).

Finally, if one compares the parallel gradients calculated in the model $PSEL2$ (figs. 4.24) with those calculated in the model $PSEL1$ (figs. 4.19) one can note that: (i) $\nabla_{||}V_x$ in model $PSEL2$ is one order of magnitude smaller than in model $PSEL1$ and (ii) that $\nabla_{||}n$ in model $PSEL2$ is one order of magnitude greater than in model $PSEL2$. By comparing the parallel component of the E-field in model $PSEL2$ (figs. 4.23 right panel and 4.21 low left panel) with that of the model $PSEL1$ (figs. 4.15 right and 4.18 low left) one can see that parallel component of $\boldsymbol{E}$ in the Region 1 is one order of magnitude greater in the model $PSEL1$ while $E_{parallel}$ component in the Region 2 is one order of magnitude grater in model $PSEL2$.

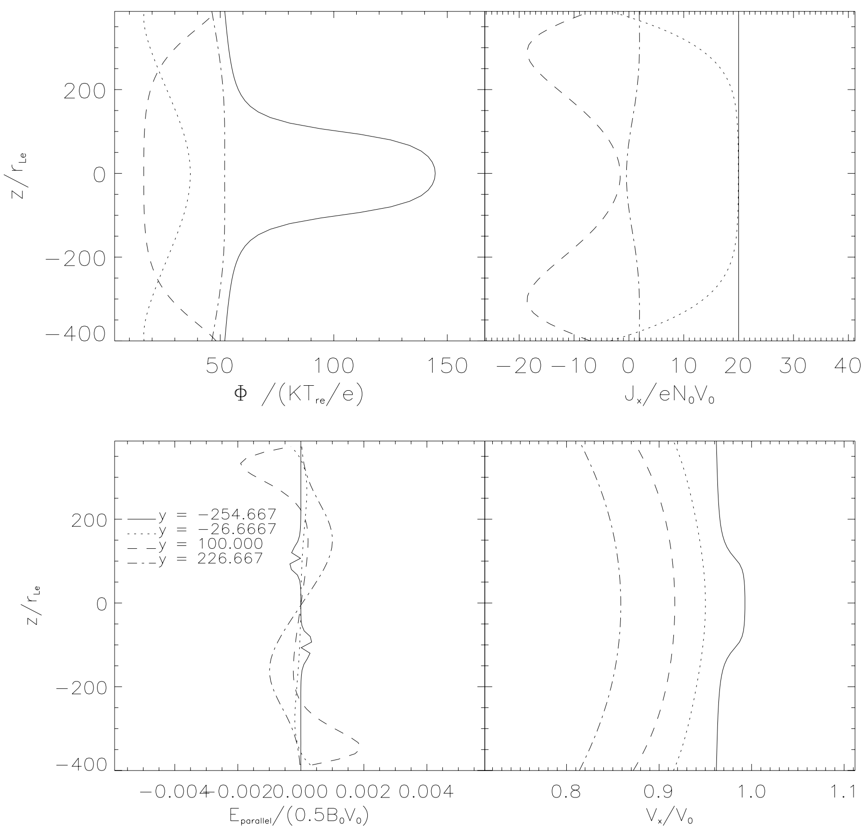

Figure 4.21: model PSEL2 - Electric potential (Φ), electric current (J_x), parallel E-field ($E_{parallel}$) and plasma bulk velocity (V_x) at 4 different y locations.

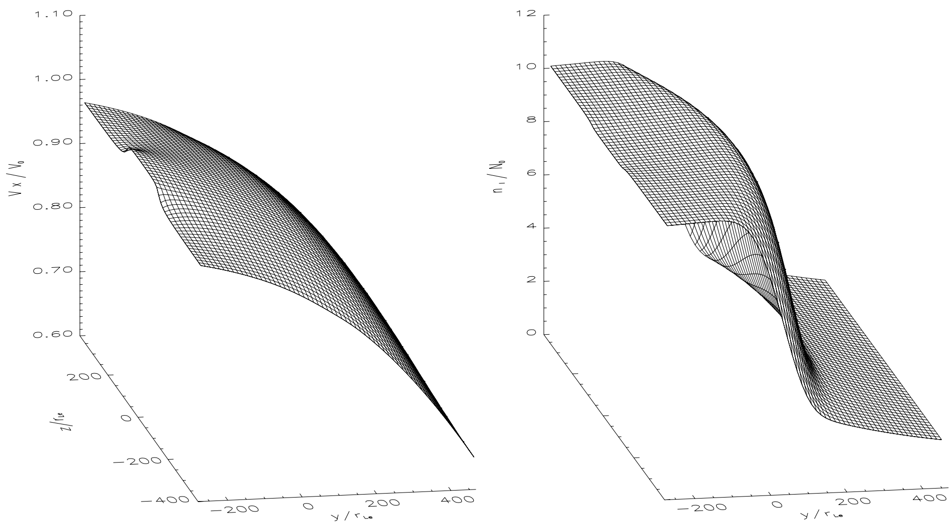

Figure 4.22: model PSEL2 - Plasma bulk velocity (left) and density (right).

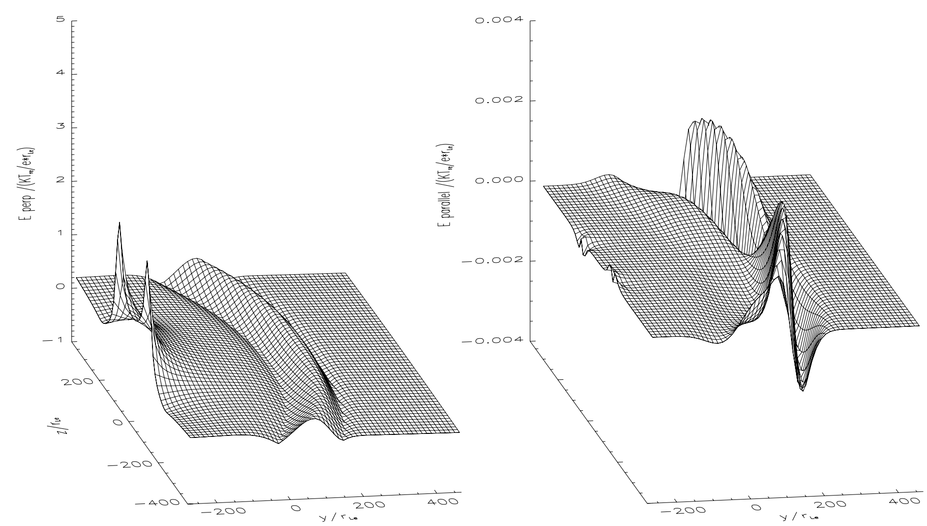

Figure 4.23: model PSEL2 - Parallel (left) and perpendicular (right) components of the electric field.

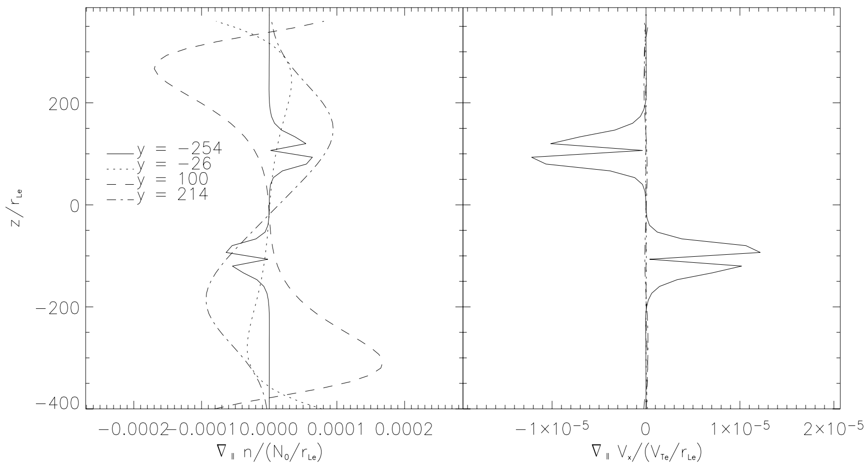

Figure 4.24: model PSEL2 - Parallel gradient of density (left) and bulk velocity (right).

4.3.3 Parallel Sheared Electron Layer - PSEL3

The model **Parallel Sheared Electron Layer 3** ($PSEL3$) describes a moving plasma having an excess of density but a lower temperature ($25\ eV$) with respect to the stagnant plasma population ($55\ eV$). In other words, the model $PSEL3$ simulates the stationary flow of a colder but denser plasma stream through a stagnant hotter but thinner background plasma. As in the previous models, the stream is moving parallel to the Ox-axis. The distribution of the bulk speed, $V_x(y, z)$, is given in the left panel of fig. **4.25**.

The distribution of the total density is shown in the right panel of the figure **4.25**. The bulk velocity is uniform at the left boundary where we have imposed non-uniform boundary condition for A_x. The decreasing of the parameters τ_{i2} and τ_{e2} produces a decreasing of the ion mass flux (see eq. 3.63) that is the dominant term in the expression of the bulk velocity (eq. 3.74). The effect of changing τ_{i2} and τ_{e2} is minor for the densities. Thus the mass flux in the model $PSEL3$ is less than in the model $PSEL2$ while the mass density is roughly the same in both models. Therefore the excess of velocity introduced by the function $\zeta(z)$ is reduced significantly. The parallel shear of velocity, $\nabla_{||}V_x$, almost vanishes at the left border where $\boldsymbol{E}$ is perpendicular to $\boldsymbol{B}$.

We retrieve a layer of transition from moving to stagnant regime which is a $2D$ structure. By decreasing the temperature of the moving plasma, the bulk velocity decreases more rapidly with y. It has a scale length larger than that of total density. Indeed, the model $PSEL3$ shows a sharp decreasing of the density within a layer of a few electron Larmor radii width.

In the model $PSEL3$ there is no significant parallel electric field in the Region 1 as can be seen from figure **4.28**. This is a consequence of the absence in Region 1 of the parallel shear of the perpendicular velocity ($\nabla_{||}V_x$) and/or of the parallel gradient of the density ($\nabla_{||}n$).

Figure **4.27** shows that in a layer extending a few electron radii width in the y-direction, there is a significant gradient of the density in what we called the Region 2. The parallel shear of the bulk velocity has also a significant value in Region 2, at the lower ($z \rightarrow -z_\infty$) and upper ($z \rightarrow +z_\infty$) edges of the region. The temperature difference between the two plasmas seems to enhance the parallel gradients inside the $2D$ layer.

Figure **4.26** shows that the parallel shear of velocity in Region 2 is one order of magnitude greater than its corresponding maximum in model $PSEL2$ and 3 times greater than its corresponding maximum in model $PSEL1$. The gradient of density also peaks at values one order of magnitude greater that in the previous two models. As a matter of consequence the parallel component of the electric field takes values greater than in the previous two models. Indeed, as one can see from figures **4.28** (right panel) **4.26** (low left panel) the maximum values of $E_{parallel}$ is equal to 0.45 mV/m, the maximum of all the three $PSEL$ models. Thus the model $PSEL3$ gives an example of concurrent action of both the parallel gradient of electronic pressure and of the parallel shear of ion bulk velocity producing an enhanced parallel component of the electric field.

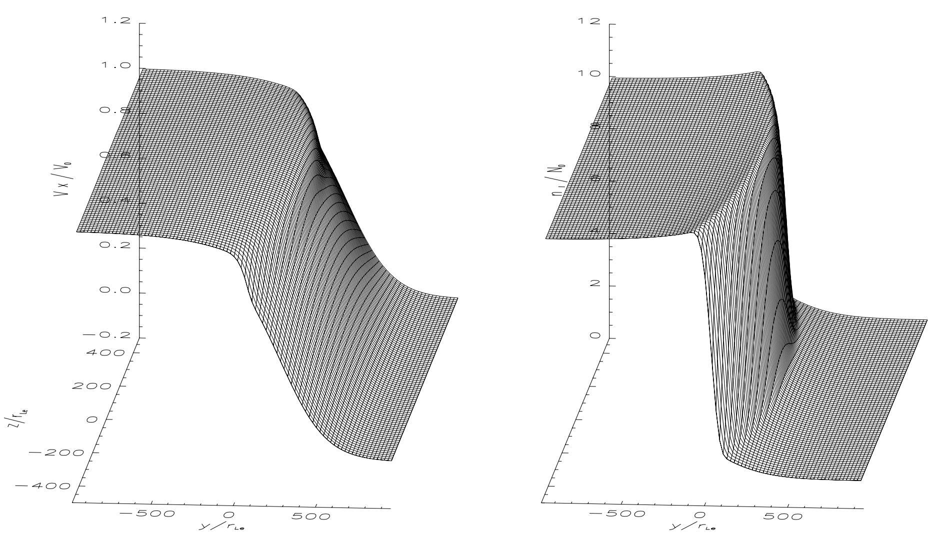

Figure 4.25: model PSEL3 - Plasma bulk velocity (left) and density (right).

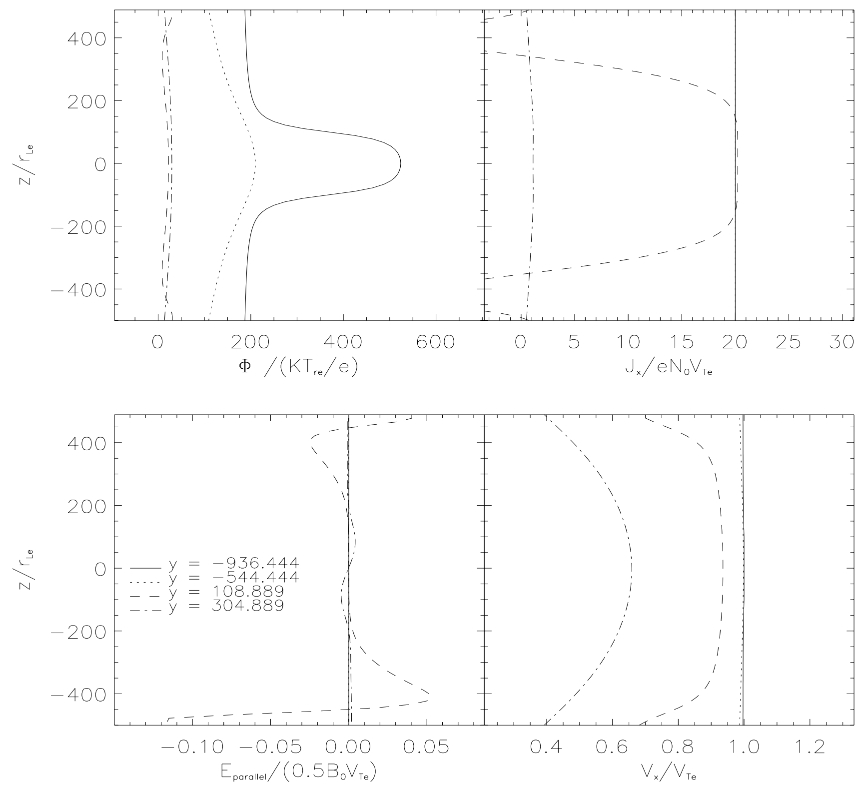

Figure 4.26: model PSEL3 - Electric potential (Φ), electric current (J_x), parallel E-field ($E_{parallel}$) and plasma bulk velocity (V_x) at 4 different y locations.

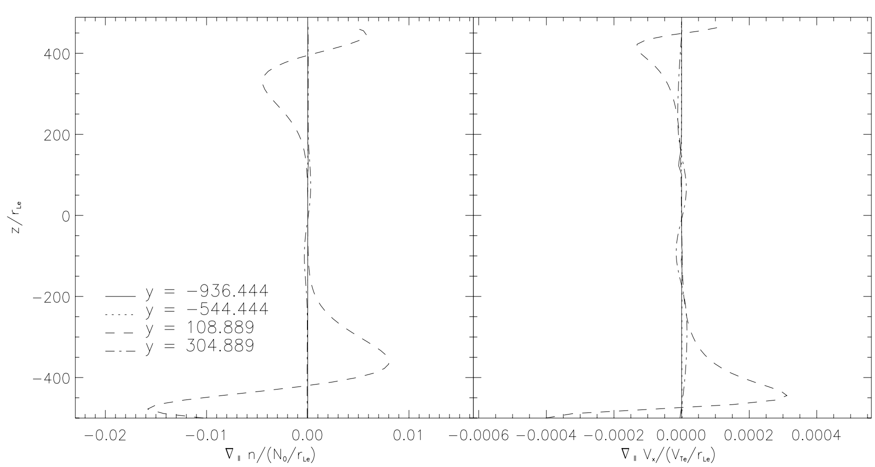

Figure 4.27: model PSEL3 - Parallel gradient of density (left) and bulk velocity (right).

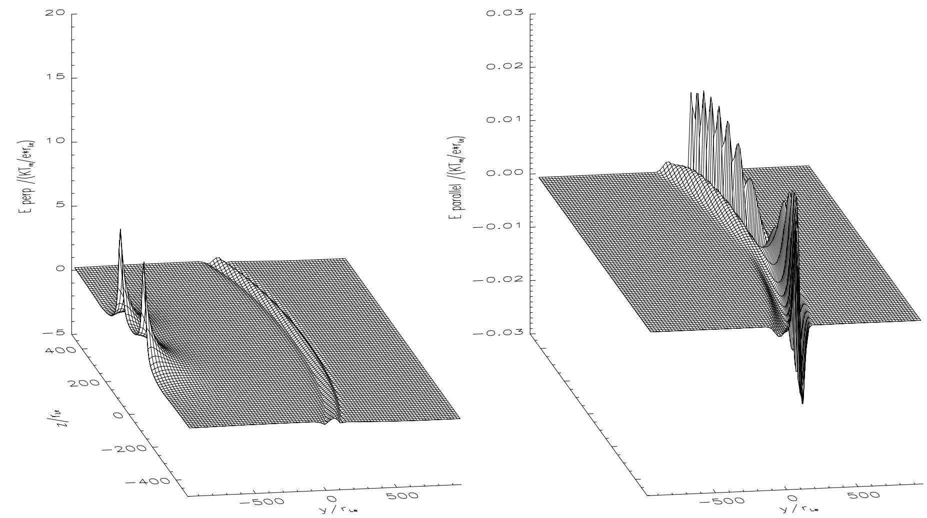

Figure 4.28: model PSEL3 - Parallel (left panel) and perpendicular (right panel) components of the electric field.

4.3.4 Parallel Sheared Proton Layer - PSPL1

This subsection treats the case of a plasma flowing in the negative direction of the Ox-axis ($V_0 < 0$) with the asymptotic magnetic field remaining parallel to Oz-axis ($B_0 > 0$). The velocity distribution functions of the protons and ions are given by eqs. (4.19) and (4.22) respectively. The partial charge and current density of the ions are given by eqs. (3.57), (3.65) while the partial charge and current density of the electrons are given by eqs. (4.20)-(4.21).

The results obtained for $V_0 = -0.01$ (in dimensional units a negative velocity of about -10 km/s) and the same asymptotic densities and temperatures as in the model $PSEL1$ are shown in figures **4.29**-**4.37**. The full set of parameters used to solve the quasineutrality and Ampere equations is specified in Table 4.2. This first model will be called **Parallel Sheared Proton Layer 1** ($PSPL1$).

The distribution of the magnetic potential, $A_x(y, z)$, and that of the total magnetic field are roughly the same as in the $PSEL1$ case, as one can see from figures **4.29** and **4.30**. In both models, $PSPL1$ and $PSEL1$, the diamagnetic currents are rather small such that the background magnetic field is perturbed only in the region close to the left boundary, where the z-dependent variation of $A_x(y, z)$, given in Tabel 4.3, has been imposed.

The distribution of the magnetic potential $A_x(y, z)$ found from the Ampere equation is introduced into the quasineutrality equation. The solution,

$\Phi(y,z)$, is shown in figure **4.31**. The electric potential takes negative values and decreases smoothly with y. The distribution of the bulk velocity computed by replacing $\Phi(y,z)$ and $A_x(y,z)$ into the zero and first order moments is shown in figure **4.32**. One can note immediately that the scale length of variation of V_x is much larger than in the previous case. In the y-direction the layer expands over the entire integration domain, approx. 800 km.

There is an excess of velocity at the left boundary of the integration domain, although both the asymptotic velocity and its perturbation are quite small, compared to that of $PSEL1$ (compare vertical scales of fig. 4.32 and fig. 4.12). The VDFs and the computed potentials give the expected macroscopic behavior of the plasma, when it moves in the negative direction of Ox-axis. Indeed, the bulk velocity decreases with y from the asymptotic boundary value $V_x = V_0$ to $V_x = 0$, but decreases also with z from the maximum value in $y = 0$, $z = 0$ to smaller values for $z \to \pm z_\infty$. The characteristic scale length of this transition exceeds the limits of the integration domain.

The modulus of the perpendicular electric field is shown in the left panel of figure **4.33**. There is an increase of the E_{perp} component in the region of increased magnetic field at the left border of the integration box. It peaks to a value that in physical units is equal to 90 $\mu V/m$. The corresponding convection velocity, $U_E = E_{perp}/B$ has a roughly uniform value in that region.

The parallel electric field takes non-zero values within a limited region encircling the zone where the velocity shear is finite as illustrated by the right panel of figure **4.33**. The parallel component has a bi-polar signature, similar to the Region 1 parallel E-field obtained in the $PSEL1$ model. Note however that the value of the parallel field in the $PSPL1$ model is 10 times smaller than that obtained in $PSEL1$. The ratio between the amplitude of the parallel E-field in the two models is nearly proportional to the corresponding ratio between the values of V_x/V_0.

The $PSPL1$ model does not show a clearly identified Region 2 transition layer as in the electron dominated models. A Region 2 parallel electric field cannot be identified. This is probably due to the fact that the transition from moving to stagnant regime takes place over a distance of the order of several proton Larmor radius, exceeding the limits of the $2D$ domain considered in this model. Indeed, figure **4.34** shows that parallel gradients of the density and/or bulk velocity are much smaller than in $PSEL1$ model. They have only a significant peak within Region 1 as shown by figure **4.36**. The amplitude of the parallel gradients of the $PSPL1$ model is 2 orders of magnitude smaller than the corresponding values in the $PSEL1$ model.

The ion density, $n_i(y,z)$, and the total $j_x(y,z)$ current density are shown in figure **4.37**. The distribution of ion density clearly varies over a characteristic scale length of the order of several hundreds of electron Larmor radii or 5-10 proton Larmor radii. The dip inside the distribution of V_x shown in figure **4.32** on the left hand side of the simulation domain is accompanied by an increase of the density, n_i. The total current is ten times smaller than in the model $PSEL1$.

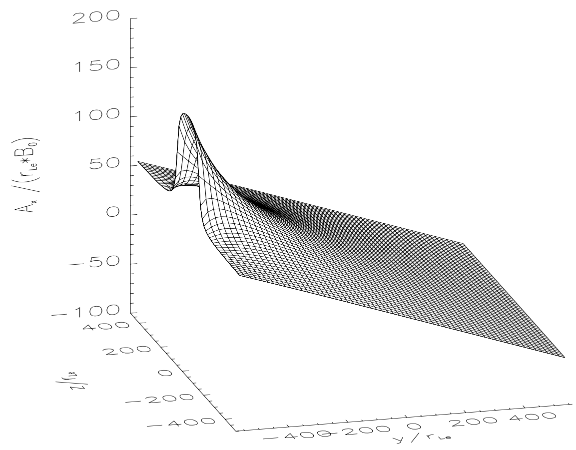

Figure 4.29: model PSPL1 - $2D$ distribution of the magnetic vector potential.

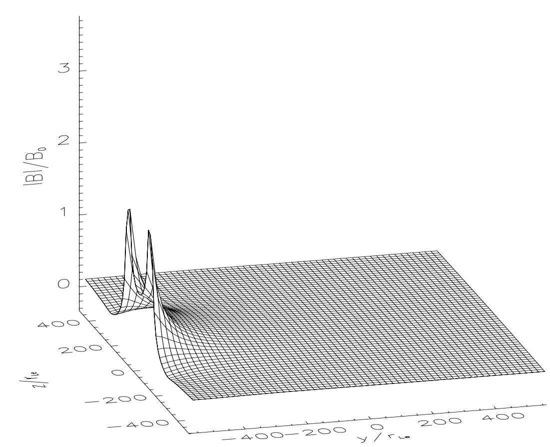

Figure 4.30: model PSPL1 - Total magnetic field.

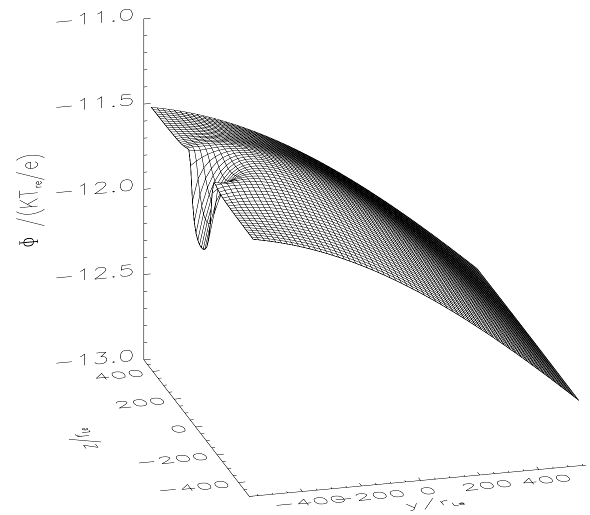

Figure 4.31: model PSPL1 - Distribution of the electric potential.

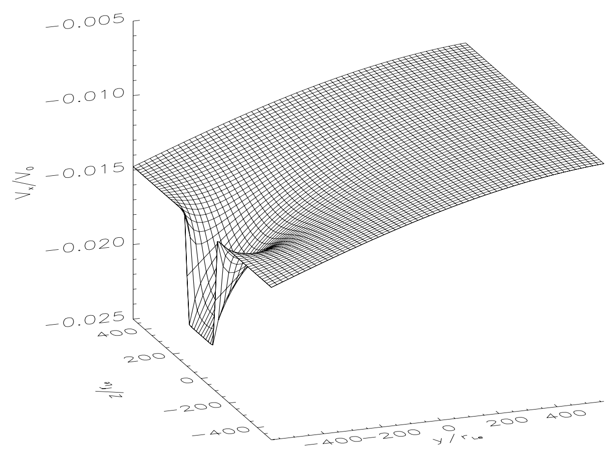

Figure 4.32: model PSPL1 - Distribution of the plasma average velocity.

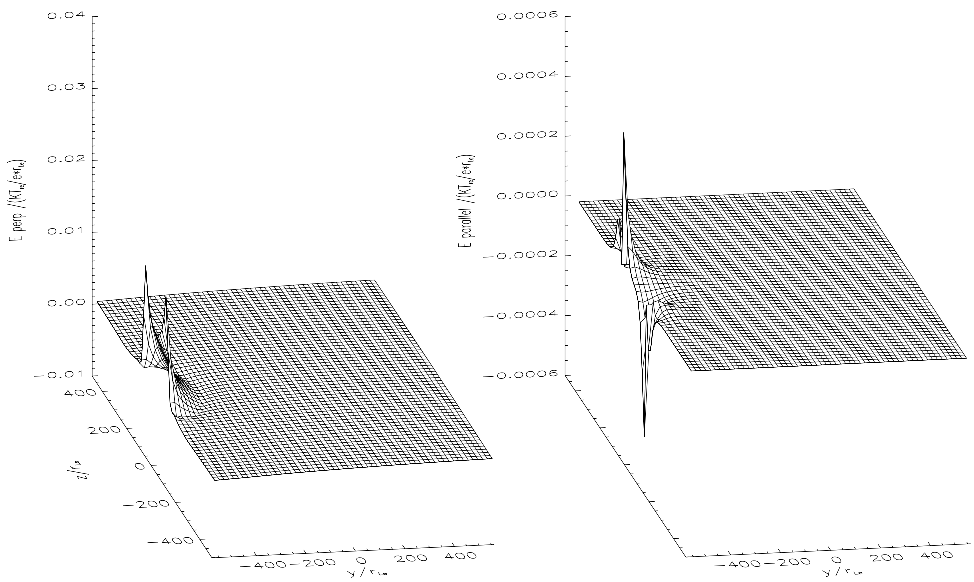

Figure 4.33: model PSPL1 - $2D$ distribution of the perpendicular component of the electric field (left panel) and of the parallel component (right panel).

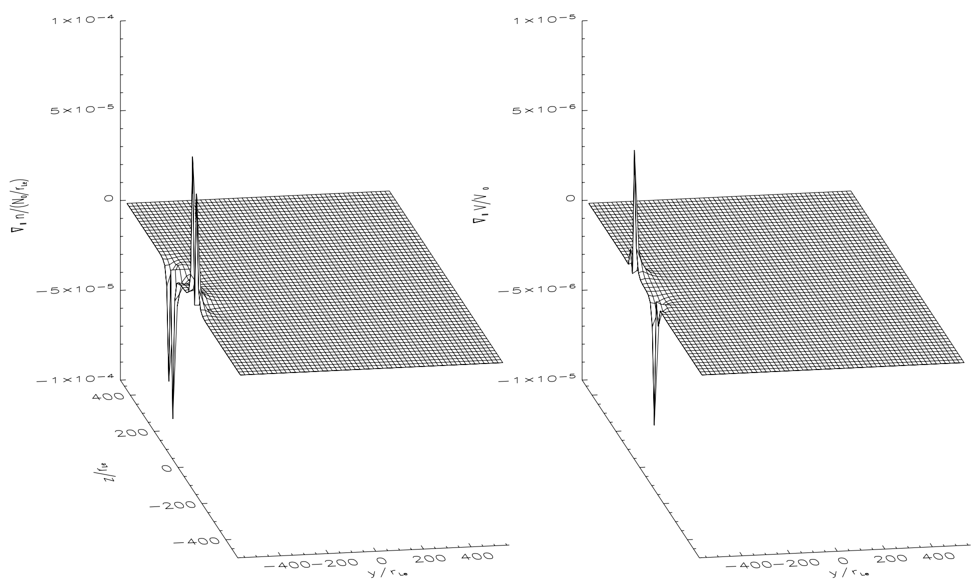

Figure 4.34: model PSPL1 - $2D$ distribution of the parallel gradient of the density (left panel) and of the V_x component of the plasma bulk velocity (right panel).

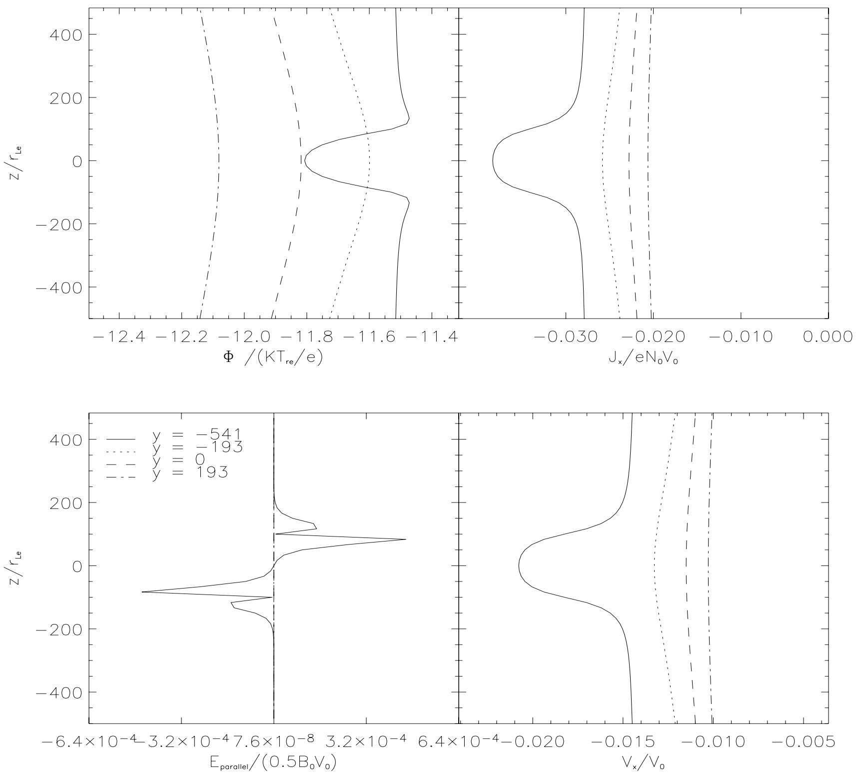

Figure 4.35: model PSPL1 - Electric potential (Φ), electric current (J_x), parallel E-field ($E_{parallel}$) and plasma bulk velocity (V_x) at 4 different y locations.

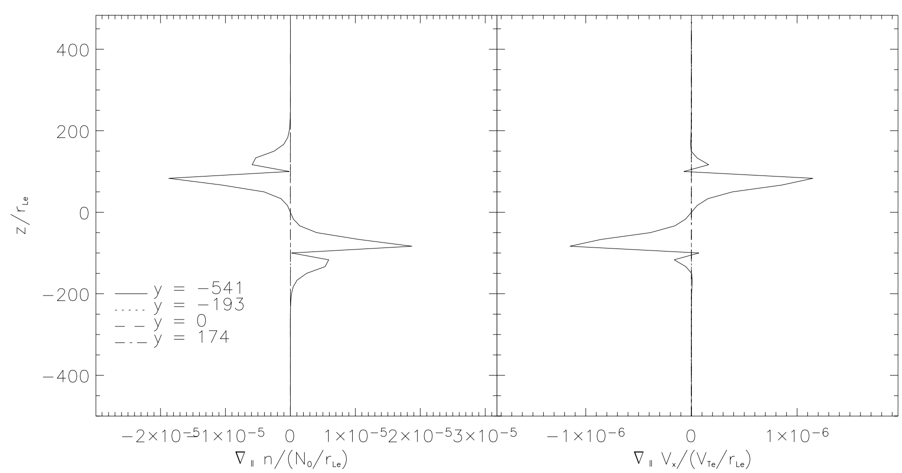

Figure 4.36: model PSPL1 - Gradient in the direction parallel to the magnetic field of the density (left panel) and bulk velocity (right panel) respectively.

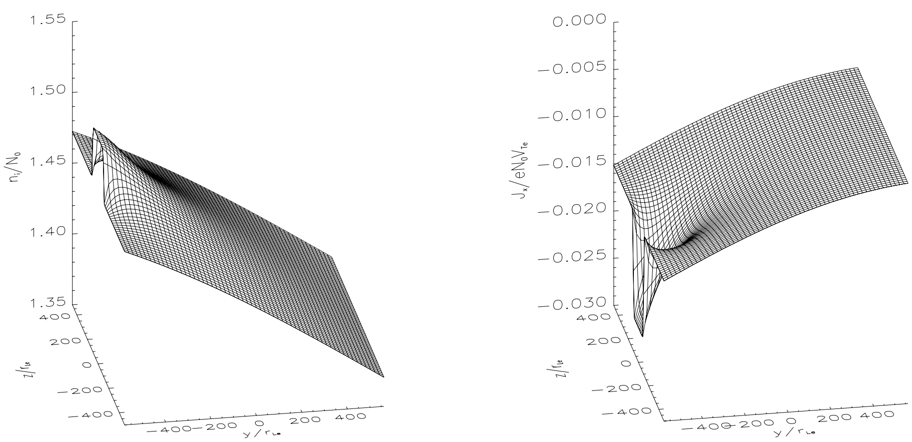

(a) Ion density (b) Electric current

Figure 4.37: model PSPL1 - Ion density and electric current for the $2D$ sheared plasma flow of case $PB1$.

4.3.5 Parallel Sheared Proton Layer - PSPL2

In the following subsection we discuss the results obtained by modifying some of the parameters of the proton model $PSPL1$. First let us increase the asymptotic density of the moving plasma, as we did previously for the $PSEL2$ model ($N^*_{i2} = N^*_{e2} = 10$, see Table 4.2). Furthermore we decrease the temperatures of all species by one order of magnitude ($\tau_i = \tau_e = \tau_{i2} = \tau_{e2} = 5$, see Table 4.2). The integration domain has been enlarged: $y^* \in [-2000, +2000]$, $z^* \in [-600, +600]$ (y^* and z^* are normalized with the electron Larmor radius, r_{Le}). The full set of the parameters of the **Parallel Sheared Proton Layer 2** ($PSPL2$) model is given in table **4.2**.

The bulk velocity profile shown in figure **4.38** has a maximum inside the region of transition from $V_x = -0.01V_0$ (approx. 10 km/s) to $V_x = 0$. Note that the velocity scale is normalized with respect to the electron thermal velocity $\sqrt{2\mathcal{K}T_{ref}/m_e}$. The change of V_x/V_0 extends over several proton Larmor radii. It has the same characteristic scale length as the transition of the density from the maximum value $N = 10N_0$ (in dimensional units 10 cm^{-3}) to the minimum value ($N = N_0$) at the right hand side of the integration domain.

Although very small and spread over large spatial distances, the density distribution has a gradient parallel to the magnetic field direction as well as a very small parallel velocity shear (note the faint "waves" in their distribution plotted in figure **4.39**). In non-dimensional units the parallel gradient of the density is 2 orders of magnitude stronger than the parallel shear of the velocity. The latter mechanism can be neglected in case of the model $PSPL2$ (see right panel in figure **4.42**).

The distributions of the perpendicular and parallel components of the electric field are shown in figure **4.40**. There is a smooth transition of the modulus of the perpendicular component of $\boldsymbol{E}$ from a maximum value at the left border toward a zero value at the right border. The peak value of E_{perp} is about 0.2 mV/m. It occurs precisely at the place where the magnetic field takes its maximum value of about 30 nT.

Low left panel of figure **4.41** shows that the parallel component of the electric field is almost 3 orders of magnitude smaller than the perpendicular one. The very small values of the parallel component is due to the small velocity of the moving plasma layer in addition to the small temperature of all species. Figure **4.42** shows that the $2D$ distribution of $E_{parallel}$ is anti correlated with the profile of the parallel gradient of density. This is expected according to eq. (4.24) for the electrons, since $Tr\left[n_e m_e \overline{\overline{\boldsymbol{V}_e \boldsymbol{V}_e}}\right] \ll Tr[\overline{\overline{p_e}}]$ and $\overline{\overline{p_e}} \approx n_{1e}\mathcal{K}T_e\overline{\overline{I}}$. The model $PSPL2$ gives an example of slow non-uniform plasma motion across B-field producing a small parallel component of $\boldsymbol{E}$ due to the parallel gradient of the electron pressure.

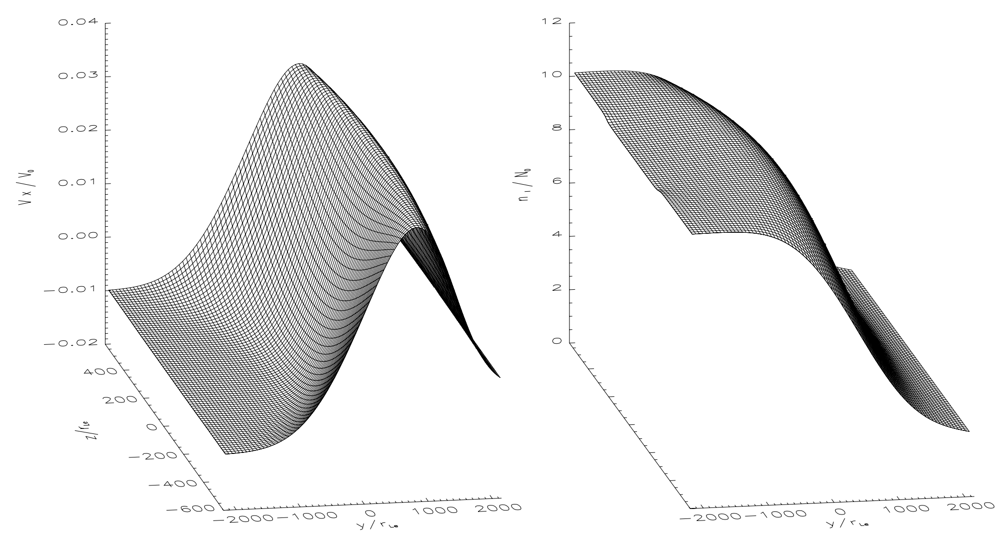

Figure 4.38: model PSPL2 - Plasma bulk velocity (left) and density (right).

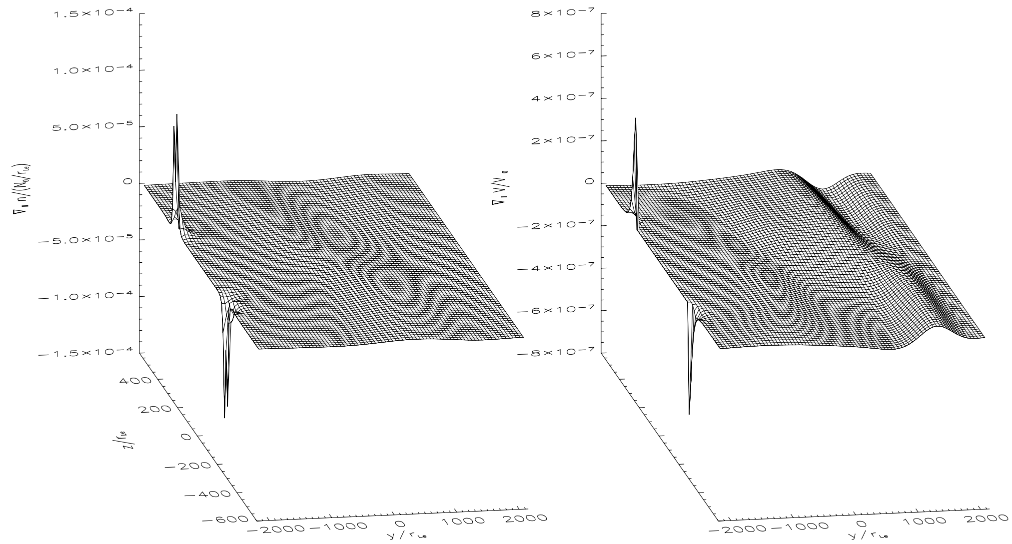

Figure 4.39: model PSPL2 - $2D$ distribution of the parallel gradient of the density (left panel) and of the V_x component of the plasma bulk velocity (right panel).

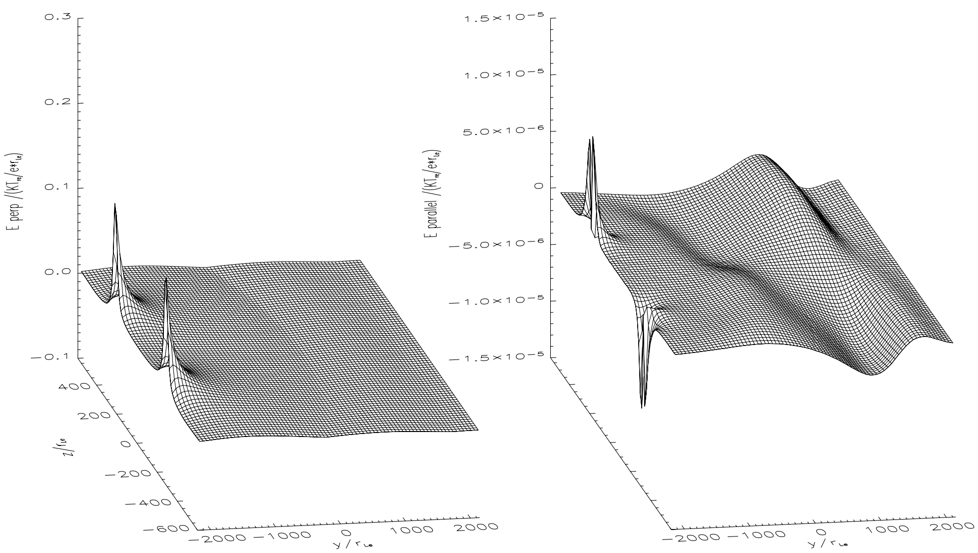

Figure 4.40: model PSPL2 - $2D$ distribution of the perpendicular component of the electric field (left panel) and of the parallel component (right panel).

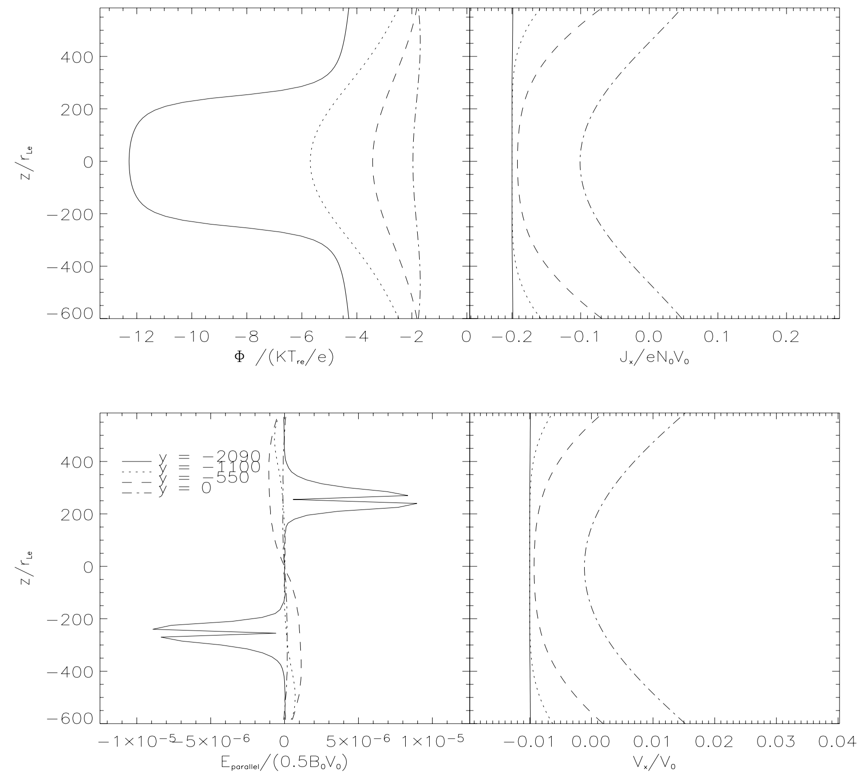

Figure 4.41: model PSPL2 - Electric potential (Φ), electric current (J_x), parallel E-field ($E_{parallel}$) and plasma bulk velocity (V_x) at 4 different y locations.

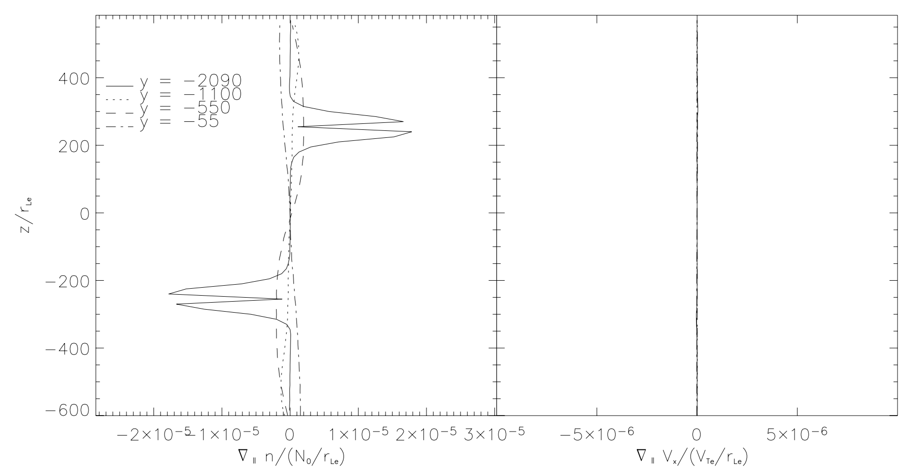

Figure 4.42: model PSPL2 - Gradient in the direction parallel to the magnetic field of the density (left panel) and bulk velocity (right panel) respectively.

4.3.6 Parallel Sheared Proton Layer - PSPL3

The next set of numerical results are obtained by increasing the temperature of the drifting plasma. This model will be further called **Parallel Sheared Proton Layer 3** ($PSPL3$). It simulates the slow propagation in the direction $-Ox$ of a hotter plasma slab or flat stream through a stagnant and colder background plasma. An external driving force sustains the streaming. A stationary solution for the flow and fields will be sought. The full set of the model parameters is given in Table **4.2**.

The $2D$ distribution of the plasma bulk velocity and density are shown in figure **4.43**. Embedded into a background flow there is an antiparallel plasma stream that moves with the imposed velocity $V_x = -0.02V_0$. The antiparallel stream has an excess of density as shown by the right hand side panel of figure **4.43**. The width of the excess density (or momentum) slab moving antiparallel to the Ox-axis is approximately 10 proton radii (or 900 kilometers for the parameters given in table **4.2**) in the Oy direction.

The gradient of the density in the direction of the magnetic field at the edges of the excess momentum slab is shown in the left panel of figure **4.44**. The boundaries separating the excess momentum slab form the rest of the plasma have a width of approximately 2 proton Larmor radii. These boundaries are the sites of a parallel velocity shear ($\nabla_{||}V$) shown in the right panel of figure **4.44**. The amplitude of $\nabla_{||}V$ is smaller and has a different aspect than that of $\nabla_{||}n$.

As in the previous models, the combined effect of both the parallel density gradients and parallel shear of velocities is to generate a non-zero parallel component of the electric field. The $2D$ distributions of both the perpendicular and parallel components of $\boldsymbol{E}$ are shown in figure **4.45**.

The parallel component has a maximum in the region where the shear of velocity is maximum, i.e. at the borders of the plasma slab moving in the direction $-Ox$. The peak values of $E_{parallel}$ are one order of magnitude greater than those obtained with model $PSPL2$. The modulus of the perpendicular E-field peaks at the left border, precisely where the intensity of the magnetic induction is maximum.

Figure **4.46** shows a series of distributions of the electrostatic potential (Φ), total electric current density (J_x), parallel electric field ($E_{parallel}$) and plasma bulk velocity (V_x) across the drifting plasma slab for a series of values of y. The characteristic scale length of variation of all these quantities is proportional to the proton Larmor radius (approx 90 km in this case). At the borders of the excess momentum slab one can note the two bipolar electric signatures or weak double layers (WDL) obtained also in the previous models. The parallel component of $\boldsymbol{E}$ has opposite polarization at the two edges.

Thus it has a confining effect, impeding the electron and ions to spread out along magnetic field despite their different thermal speeds.

The distribution of the parallel E-field can be compared with the distribution of the parallel gradient of density and of the parallel velocity shear. The latter are shown in figure **4.47**. The plots show that at the edges of the plasma stream both mechanisms concur to generate the parallel (magnetic-field-aligned) electric field component. The parallel E-field distribution has the same z-profile as the distribution of the parallel shear of velocity. In the $PSPL3$ the effect of the velocity shear appears to dominate that of the electric pressure gradient. Indeed, although the absolute magnitude in normalized units of $\nabla_{||}n$ is larger than $\nabla_{||}V_x$, the z-profile of $E_{parallel}$ (fig. **4.46**) is correlated with the z-profile of $\nabla_{||}V_x$ (fig. **4.47** right panel).

The kinetic treatment of plasma dynamics outlined in this chapter reveals important features undermined in certain macroscopic, or fluid, approximations. It demonstrates the existence of parallel electric fields for non-uniform, mixed sheared plasma flow across magnetic field. In the MHD approximation $E_{parallel}$ is always equal to zero since the magnetic field lines are considered electric equipotentials. Our simulations illustrate that this MHD postulate is generally violated in the case of a $2D$ sheared plasma flow. In the next section we will analyze the role of the parallel E-field in decoupling the plasma motion from the motion of so called "frozen-in" magnetic field.

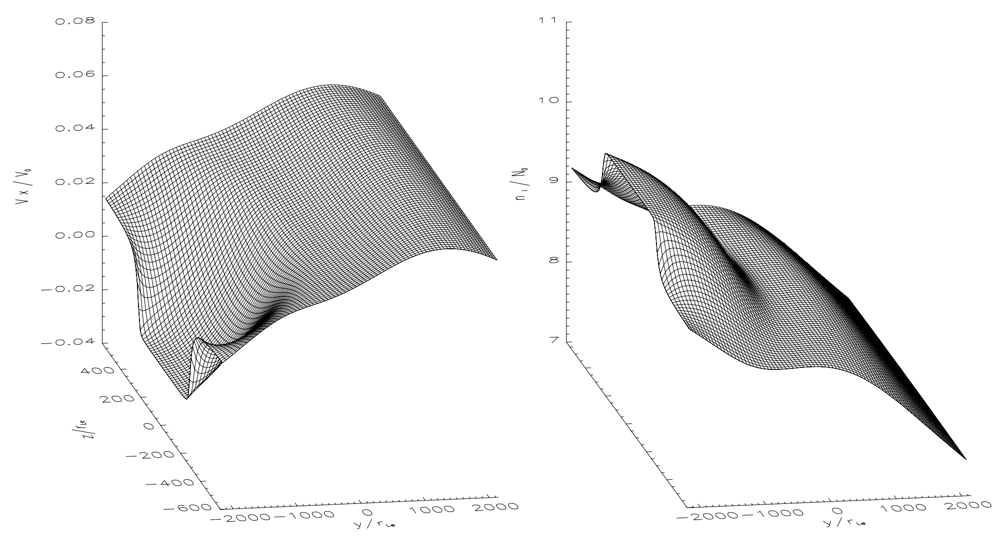

Figure 4.43: model PSPL3 - Plasma bulk velocity (left) and density (right).

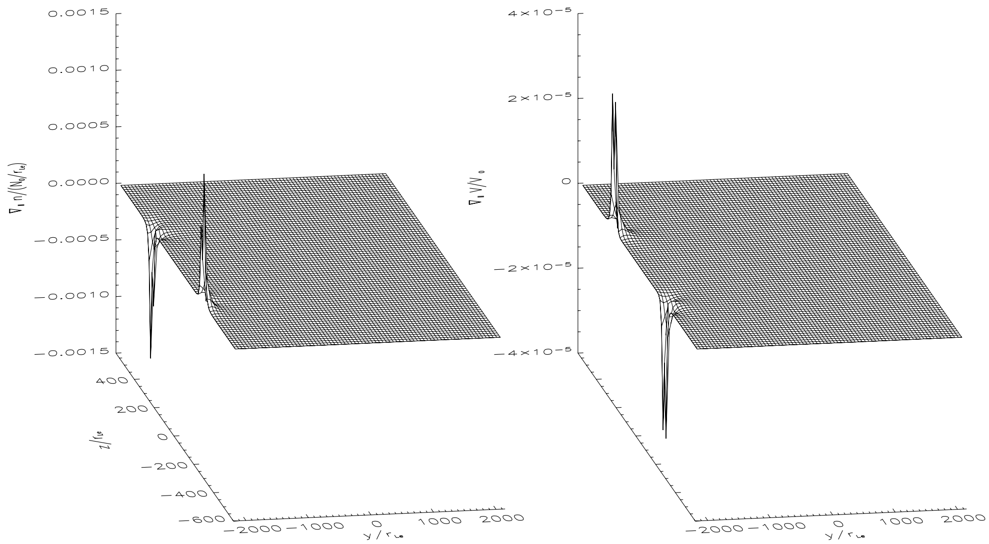

Figure 4.44: model PSPL3 - $2D$ distribution of the parallel gradient of the density (left panel) and of the V_x component of the plasma bulk velocity (right panel).

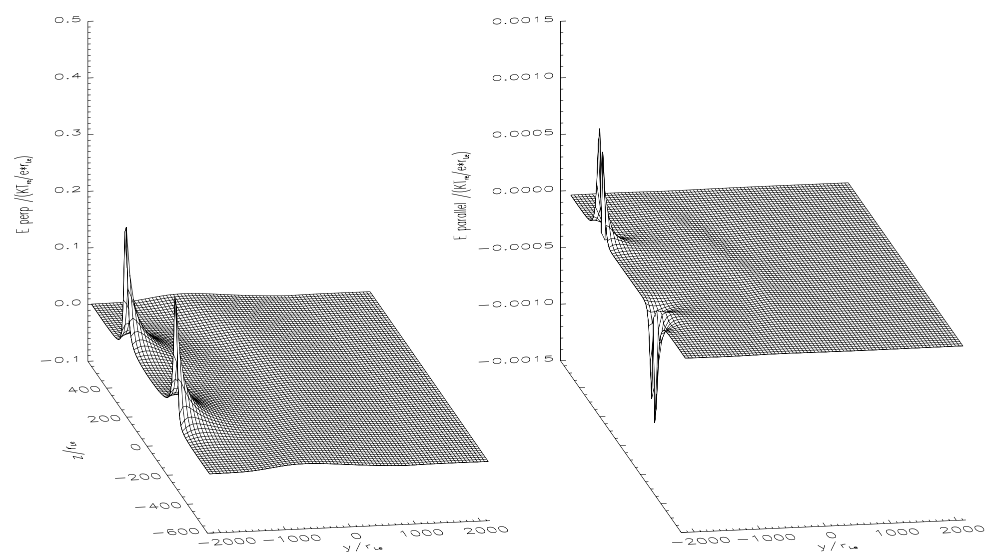

Figure 4.45: model PSPL3 - $2D$ distribution of the perpendicular component of the electric field (left panel) and of the parallel component (right panel).

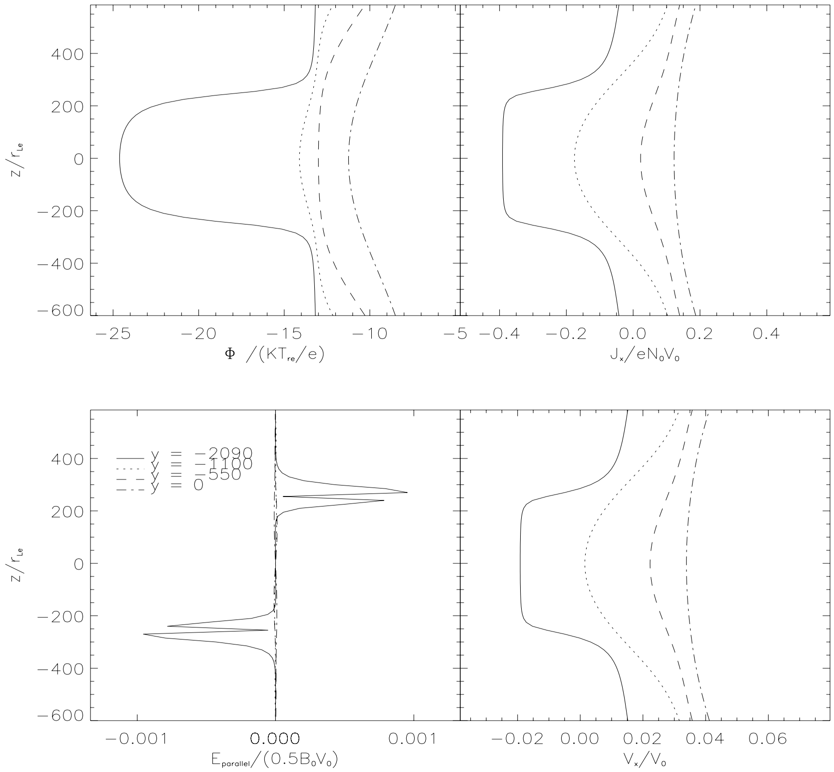

Figure 4.46: model PSPL3 - Electric potential (Φ), electric current (J_x), parallel E-field ($E_{parallel}$) and plasma bulk velocity (V_x) at 4 different y locations.

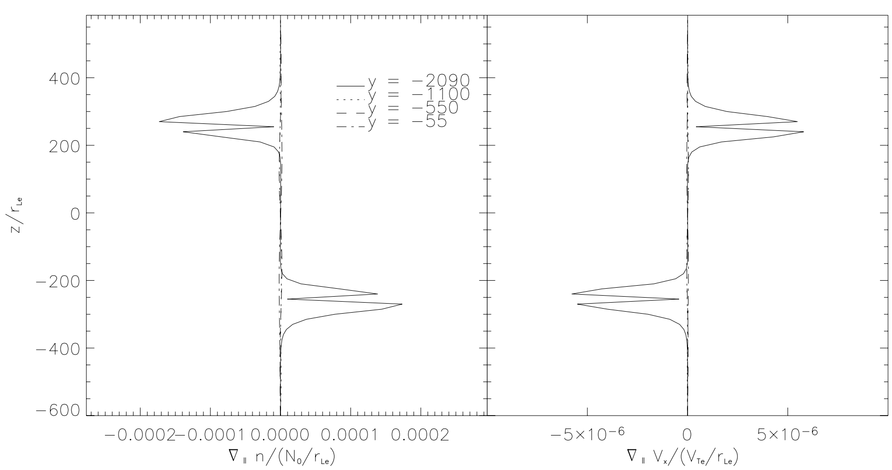

Figure 4.47: model PSPL3 - Gradient in the direction parallel to the magnetic field of the density (left panel) and bulk velocity (right panel) respectively.

4.4 Decoupling of plasma motion

In the magnetohydrodynamic-MHD approximation of plasma physics it is often stated that the plasma electrons and all positive have the bulk velocities are both equal to each other and can be approximated by that of a single fluid moving with the convection velocity:

$$\boldsymbol{U}_E = \frac{\boldsymbol{E} \times \boldsymbol{B}}{B^2}$$

Assuming infinite conductivity in the direction parallel to $\boldsymbol{B}$, *Alfven* (1953) showed that in the ideal MHD approximation $\boldsymbol{E} \cdot \boldsymbol{B} = 0$ and thus the magnetic field line are "frozen" in the plasma streaming with the velocity $\boldsymbol{U}_E$.

Alfven and Falthammar (1963) have shown, however, that a parallel electric field can be sustained in a non-uniform magnetized and quasineutral plasma, by an anisotropy of the pitch angle distribution of the electrons and ions. Even before Alfven, *Pannekoek* (1922) and *Rossland* (1924) computed the parallel electric field that is produced in the ionospheres of stars and planets by charge separation due to the difference between the gravitational force acting on the electrons and ions, $m_e\boldsymbol{g}$ and $m_i\boldsymbol{g}$,

Lemaire and Scherer (1970, 1971) have shown that along open polar wind or solar wind magnetic field lines an additional charge separation electric field can be the consequence of the electron Jeans evaporation rate which is larger than that of the slower thermal ions. There are additional physical mechanisms that produce polarization E-field that can have a component parallel to the magnetic field lines and violating therefore the usual MHD condition, $\boldsymbol{E} \cdot \boldsymbol{B} = 0$.

We were interested to describe the generation of parallel E-field, by parallel shears of velocity in convecting plasmas. The models presented in the previous subsections give examples for a range of asymptotic temperatures, densities and/or bulk velocities. Thus we can compare the bulk velocity distribution computed in these models with the zero order drift velocity (or convection velocity), $\boldsymbol{U}_E$, given by the distributions of total electric and magnetic fields obtained by our kinetic models. Thus one can obtain an evaluation of the errors introduced by assuming that plasma moves with the MHD convection velocity $\boldsymbol{U}_E$ and not with the bulk velocity $\boldsymbol{V}_x$. We will illustrate our conclusions with the results obtained for three of the six models discussed in the previous sections.

In figure **4.48** the distribution of the MHD convection velocity obtained by the model $PSEL1$ is shown in the left hand side panel. The MHD convection velocity, $\boldsymbol{U}_E$, decreases from a maximum value on the left boundary of the integration domain to a minimum value on the right hand side boundary. Its overall distribution can now be compared to $\boldsymbol{V}_x$, the plasma bulk velocity distribution shown in figure **4.12**. There are significant differences between the spatial distributions of the two velocities. They are illustrated in the right panel of figure **4.48**.

Indeed within the so-called Region 2 of the *Parallel Sheared Electron Layer 1* the plasma bulk velocity, $\boldsymbol{V}_x$, cannot be approximated by the MHD convection velocity, $\boldsymbol{U}_E$. In other words, using the MHD/fluid nomenclature, the plasma and B-field motion are *decoupled* across the slab Region 2. Second panel of figure **4.48** shows the "decoupling" of the plasma velocity or the un freezing of pseudo equipotential magnetic field lines within the Region 2 where $\boldsymbol{E} \cdot \boldsymbol{B} \neq 0$.

The physical mechanism that is responsible for this decoupling is precisely the parallel electric field. Figure **4.49** shows a set of profiles obtained by the $PSEL1$ model for the velocity difference $(V_x - U_E)$ and for the parallel component of the electric field $E_{parallel}$, as a function of y for 4 different values of z. These plots show that the decoupling takes place within the region where the parallel E-field is different from zero. The plasma flow and fields on both sides of the electron dominated layer are decoupled. The weak double layers formed due to the parallel gradient of plasma density and electron pressure as well as due to the parallel shear of bulk velocity act as "isolators" and "unfreezes" the magnetic field lines.

Similar conclusions can be reached in the case of proton dominated layers. The distribution of the convection velocity obtained with the model $PSPL3$ is shown in figure **4.50**. This model gives a peculiar distribution of the bulk velocity, for which there is an antiparallel stream, as already illustrated in figure **4.43**. Note that the distribution of the convection velocity, $\boldsymbol{U}_E$, also shows a region of reversed flow. Nevertheless there is a significant difference between the two velocities as illustrated by the right hand side panel of figure **4.50**. Figure **4.51** shows that although the parallel electric field is very small for $y > 0$, the plasma bulk velocity, V_x and the convection velocity, U_E, tend to different values. This proves that even small parallel components of the electric field act efficiently to decouple the plasma motion from the medium it originates from. Note however that in figure **4.51** the transition layer has a characteristic scale length of the order of the proton Larmor radius and extends therefore beyond the limits of the integration domain.

In order to study further the efficiency of the small parallel electric field we have computed the convection velocity, U_E, for the model $PSPL2$. The results are shown in figure **4.52**. Inside the transition layer which extends over several proton Larmor radius the difference $V_x - U_e$ is different from zero. The y-profiles of $V_x - U_E$ and of $E_{parallel}$ at 4 different z-values are given in figure **4.53**. One can see that at the right hand side border of the transition layer, the parallel electric field tends to zero as well as the difference between the convection and bulk velocity. A very small electric field component (with a maximum of about 0.018 $\mu V/m$) exists inside the layer that now extends over large distances. These results demonstrate that proton dominated transition layers also constitute decoupling mechanisms although in this case the parallel electric field is smaller and distributed over larger regions than in the case of electron dominated layers.

The associated effects of the velocity shear and parallel electric field is to confine the plasma and to keep it quasineutral precluding its spreading along the magnetic field lines, a process favored by the higher parallel mobility of the electrons. The role of the velocity shear in stabilizing plasma pinches has been recognized by laboratory plasma experimentalist (see *Smolyakov et al.*, 2001), but not yet by space plasma physicists who tend to restrict their limits within the framework of the MHD theory where the magnetic field lines are always electric equipotentials. This is, to our knowledge, among the first studies that develops a kinetic model showing that in a magnetized plasma the variation in the direction parallel to B of the cross-B plasma velocity produces a finite $E_{parallel}$ component that preserves the plasma quasineutrality and decouples the motion of plasma from the so-called motion of "frozen-in" field.

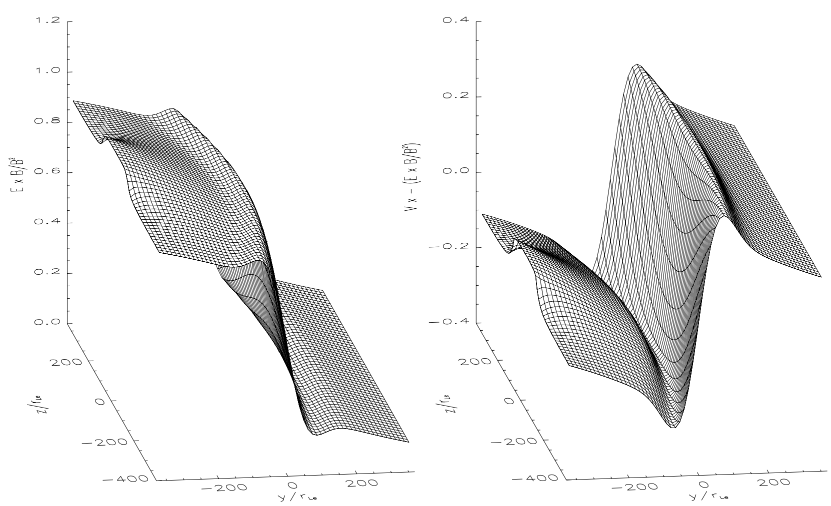

Figure 4.48: model PSEL1 - Convection velocity and decoupling velocity of plasma in case of an electron dominated sheath.

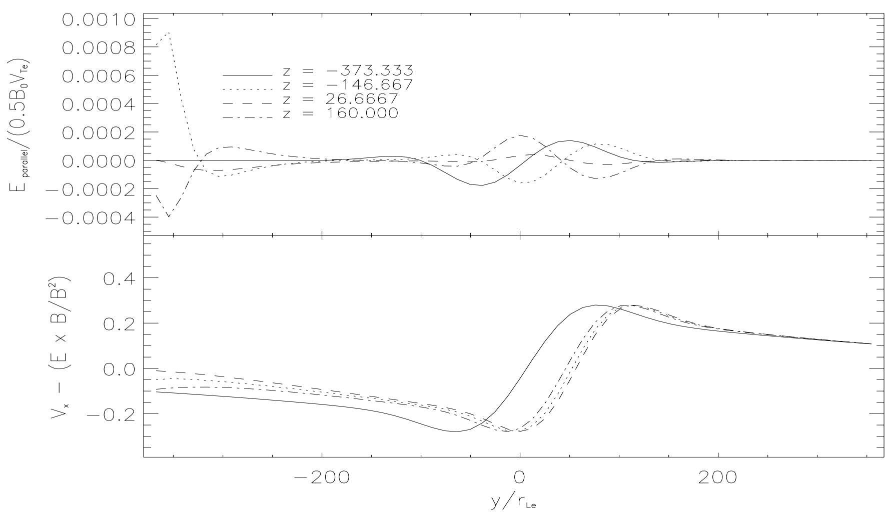

Figure 4.49: model PSEL1 - Decoupling velocity and parallel electric field vs. y coordinate at 4 different altitudes (model $EB1$).

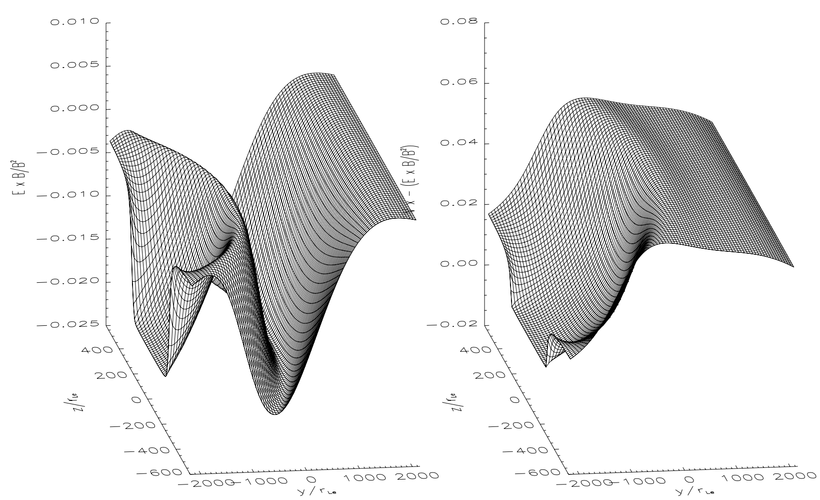

Figure 4.50: model PSPL3 - Convection velocity and decoupling velocity of plasma in the case of an proton dominated profile.

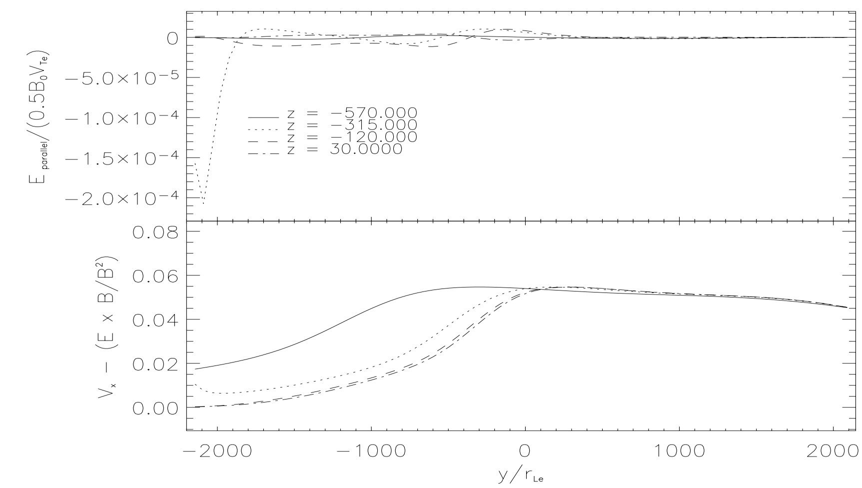

Figure 4.51: model PSPL3 - Decoupling velocity and parallel electric field vs. y coordinate at 4 different altitudes (model $PB3$).

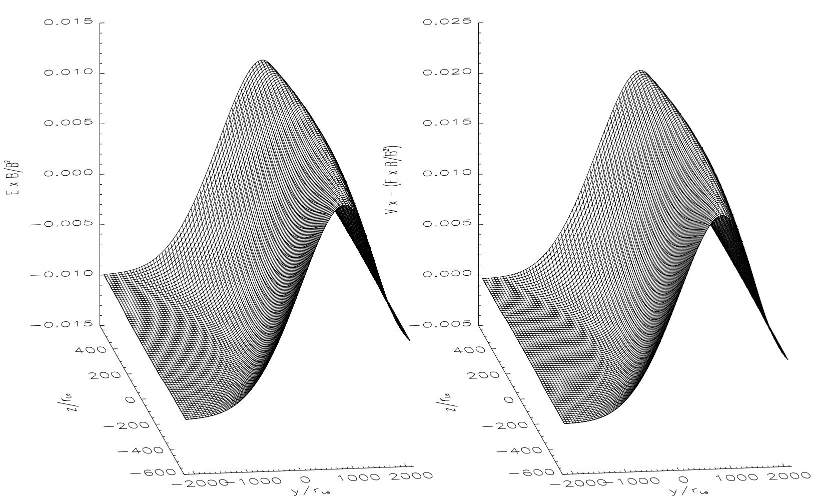

Figure 4.52: model PSPL2 - Convection velocity and decoupling velocity of plasma in the case of an proton dominated profile.

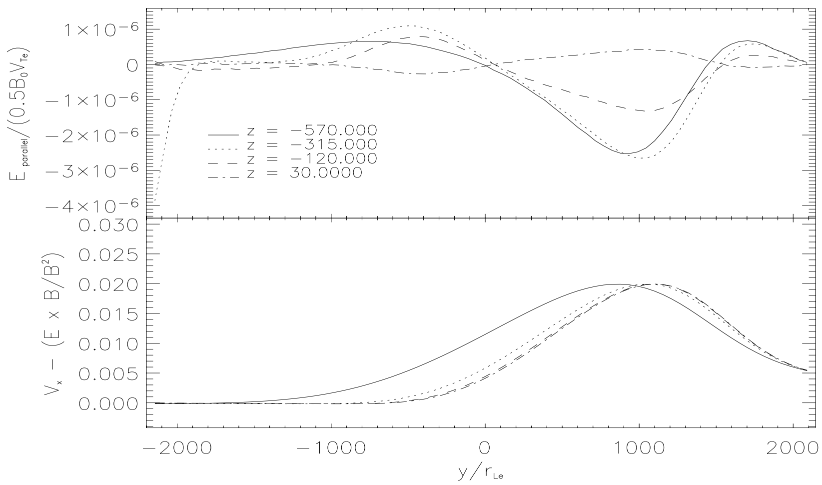

Figure 4.53: model PSPL2 - Decoupling velocity and parallel electric field vs. y coordinate at 4 different altitudes (model $PB3$).

4.5 Conclusions and comments

Cross-B convection of plasma has been treated in the kinetic models of tangential discontinuities proposed by *Sestero* (1967), *Lemaire and Burlaga* (1976), *Roth* (1978, 1984) and *Roth et al.* (1996). The transverse plasma flows considered in these models were sheared in the direction perpendicular to the magnetic field. Thus in TD models plasma layers were considered to be moving parallel to a surface of tangential discontinuity with the same velocity all along the magnetic field line.

Plasma flows sheared in the direction parallel to the magnetic field are observed in the region of the magnetospheric cusps, at the edges of plasma irregularities impulsively injected at the magnetopause (*Lemaire and Roth, 1991*), or propagating inside the magnetosphere (*Kelley et al., 2003*), artificial ion clouds (*Haerendel*, 1967; *Kazeminezhad*, 1993; *Delamere*, 2002), or in the laboratory during plasma gun experiments (*Baker and Hammel*, 1965; *Emmonds and Land*, 1962; *Wessel et al.*, 1988; *Hurtig* et al., 2003).

The kinetic model described in this thesis is a $2D$ development of the kinetic models of TDs. We assumed that the plasma is flowing in the direction parallel to the Ox-axis and perpendicular to $\boldsymbol{B} \equiv (0, B_y, B_z)$, but in addition to the $1D$ kinetic models, we considered that the plasma bulk velocity varies also with the coordinate z. This is a 2D flow in which we show that, under some circumstances, a shear of the perpendicular plasma velocity occurs in the direction parallel to the magnetic field.

We assume here that the plasma flow and fields are stationary. In Chapter 3 we gave a theoretical outline of the equations and approximations used to solve this problem. The beginning of Chapter 4 gives a description of the numerical method used to solve the equations. Complete solutions of the electrodynamics of a non-uniform plasma flow with a bulk velocity sheared in the direction perpendicular and parallel to the magnetic field have been illustrated in the figures of Chapter 4.

We have obtained 2D distributions for magnetic potential and magnetic field intensity, electric potential and field, electron and ion densities, bulk velocity, partial and total current densities. The parallel component of the E-field as well as of the gradient of density and bulk velocity were also computed. The kinetic treatment of plasma dynamics enabled us to study non-MHD phenomena like parallel electric fields or weak double layers.

The key point is that the differential velocity or sheared flow with a non-zero gradient parallel to the magnetic field produces a field aligned potential drop. The largest value of $E_{||}$, the parallel electric field, is indeed found where the parallel gradient of the perpendicular plasma bulk velocity has its maximum value. The results show that a parallel gradient of the electron pressure may also be present in $2D$ sheared flows, enhancing the parallel E-field generated by the parallel velocity shear.

We have evidenced two distinct regions where the parallel electric field occured: **Region 1** which is close to the left boundary and where we have studied the local effects of the imposed excess of bulk velocity and **Region 2** which is a $2D$ layer of transition from convecting to stagnant plasma regime. The latter can be considered a two-dimensional "deformation" of the $1D$ Sestero tangential discontinuity.

Our results show a bi-polar signature of the parallel electric field. The parallel component of $\boldsymbol{E}$ is positive on one side and negative on the other side of the excess momentum slab (Region 1) or inside the $2D$ layer (Region 2). This signature is retrieved in all six models simulated in Chapter 4.

The amplitude of the parallel electric field depends on the plasma properties. Thus we have shown that in case of a plasma moving in the positive direction of Ox-axis and in the case of a positive B_0, the parallel electric field is stronger. The characteristic scale length of Region 2 is in this case of the order of the electron Larmor radius. In case of a plasma moving in the negative direction of Ox-axis (for $B_0 > 0$) the characteristic scale length is of the order of the proton Larmor radius. The parallel shear is reduced in this case (the layer extends over larger distances) and the parallel electric field is smaller.

The models $PSEL1$ ($V_x(y,z) > 0$) and $PSPL1$ ($V_x(y,z) < 0$) show examples of a parallel electric field generated inside a $2D$ sheared flow of a

Table 4.4: Summary of the results obtained in Chapter 4

	$PSEL1$	$PSEL2$	$PSEL3$	$PSPL1$	$PSPL2$	$PSPL3$
$E_{parallel}$	Reg. 1 Reg. 2	Reg. 1 Reg. 2	Reg. 2	Reg. 1	Reg. 1 Reg. 2	Reg. 1
$\nabla_{\|\|} V_x$	Reg. 1	Reg. 1 Reg. 2	Reg. 2	Reg. 1	Reg. 1 Reg. 2	Reg. 1
$\nabla_{\|\|} n$	Reg. 1 Reg. 2	Reg. 1 Reg. 2	Reg. 2	Reg. 1	Reg. 1	Reg. 1

plasma that has the same asymptotic density ($N_{i2} = N_{e2} = N_{i1} = N_{e1}$) and temperature ($T_{i2} = T_{e2} = T_{i1} = T_{e1}$) at the borders of the $2D$ domain. Models $PSEL2$, $PSEL3$, $PSPL2$ and $PSPL3$ show that differences in asymptotic density ($T_{i2} = T_{e2} \neq T_{i1} = T_{e1}$) and/or temperature ($N_{i2} = N_{e2} \neq N_{i1} = N_{e1}$) enhances the parallel component of $\boldsymbol{E}$. A summary of the results obtained in Chapter 4 is presented in Table 4.4. It gives the regions where the parallel electric field, the parallel shear of velocity and the parallel gradient of density occured in each of the six models.

It is the parallel electric field that invalidates the MHD approach. Indeed, within the $2D$ layers studied in Chapter 4 we have verified that:

$$\boldsymbol{E} + \boldsymbol{V} \times \boldsymbol{B} \neq 0 \tag{4.26}$$

This is an important result indeed, since in the MHD paradigm, on which relies some models of plasma transfer at the magnetopause, the condition:

$$\boldsymbol{E} + \boldsymbol{V} \times \boldsymbol{B} = 0 \tag{4.27}$$

need necessarily be satisfied, i.e. the electric field has to be always perpendicular to $\boldsymbol{B}$ and has nowhere a component parallel to $\boldsymbol{B}$. The frozen-in field approximation according to which magnetic field lines "move" with the same velocity, $\boldsymbol{U}_E = \boldsymbol{E} \times \boldsymbol{B}/B^2$ as the plasma is also based on the assumption that equation (4.27) is satisfied.

Hence the results obtained in this chapter confirm that in a $2D$ non-uniform (sheared) flow of plasma perpendicular to B-field a parallel component of the electric field can be sustained. This additional mechanism must be added to the list of those already described in the literature for producing parallel electric fields: anisotropy of the pitch-angle distribution (*Alfvén and Fälthammar*, 1963), gravity (*Pannecoek*, 1922, and *Rossland*, 1924), temperature gradient (*Hultquist*, 1971), planetary or solar wind radial expansions or evaporation of plasma in ionized exosphere or coronae (*Lemaire and Scherer*, 1970, 1971a, 1971b; *Pierrard*, 1996, 1997).

In this work we have stressed the contribution of the velocity shear only with the aim to demonstrate its effectiveness. In space plasmas, however, all these mechanisms can be combined and may operate simultaneously. These are non-MHD processes that must be taken into account in order to complete the picture of plasma dynamics in magnetic fields.

The parallel electric field produced by the shear of plasma velocity contribute significantly to the propagation of plasma elements/plasmoids across magnetic field. Already in the 80ties *Lemaire* (1977, 1985) and *Lemaire and Roth* (1978, 1981, 1991) have suggested a theoretical/qualitative model for the dynamics of a plasma irregularity. They described the edges of the irregularity as sites of density and velocity gradients. They argued that the electric field should have a parallel component at the edges, decoupling the plasma element from the ambient plasma and field.

Our study determines quantitatively and self-consistently the solution for the E-field distribution at the plasmoid's edges, showing the existence of a parallel electric field or weak double layers sustained by the parallel shear of the perpendicular plasma velocity. The latter is due to the excess of velocity of the plasmoid with respect to the neighboring plasma layers. When the plasmoid has an excess of density and/or temperature with respect to the ambient plasma, the parallel electric component is even more enhanced due to thermoelectric effects. Furthermore when magnetic field lines are not parallel to each other, but diverging as in the polar wind and solar wind, the mirror force acting on the charged particles may also contribute to separate the electron and ions and thus produce additional parallel electric field component.

Chapter 5

Comparison with previous models for sheared magnetospheric plasma flows

In the previous chapters were presented models that are relevant for studying the dynamics of non-uniform plasma flows across magnetic field lines. In this chapter we recall the main results obtained with our kinetic models and how they relate to those obtained using other numerical methods or approximations like the Particle-In-Cell (PIC) method and MHD simulations.

5.1 Kinetic models

Kinetic approximation of plasma physics has been very successful in modeling the steady state tangential discontinuities (e.g. *Sestero*, 1964), exospheric models of the solar and polar wind (e.g. *Lemaire and Scherer*, 1970), stability of rotating plasmasphere (e.g. *Lemaire*, 1989). For a recent review on the kinetic treatment of space plasmas see *Lemaire and Pierrard* (2003).

The kinetic models of tangential discontinuities have been extensively described and discussed in the previous chapters. It is worthwhile to point out here that they are constructed with exponential functions of energy (Maxwellian) multiplied by truncation factors that can be step functions (*Lemaire and Burlaga*, 1978) or other smoother functions as for instance complementary error functions (*Lee and Kan*, 1979; *Roth et al.*, 1996). The cutoff functions determine the energy and pitch angle of particles that can penetrate from one side to the other side of the discontinuity as illustrated in the case studies of Part I.

The solutions presented in this thesis are two-dimensional solutions constructed with exponentials and step functions of the constants of motion. These solutions are not unique but they give one admissible configuration of the plasma and fields that is consistent both at the microscopic level and at the macroscopic level as well.

None of the earlier one-dimensional models did consider cross-B plasma flows with a gradient in the direction *parallel* to the magnetic field. Indeed, the treatment of parallel gradients of the velocity for a cross-B plasma flow is inherently two-dimensional.

In chapter **4** it has been discussed the role of the parallel component of the electric field in decoupling the plasma motion from the motion of the medium where it originates from. We give a quantitative assessment of this parallel component as well as of the "decoupling" between the plasma motion and the background generated by the parallel component of $\boldsymbol{E}$.

Our kinetic model assumes that an external driver sustains the sheared steady state plasma flow. In the case of a penetrating plasmoid the driving force is its inertia or excess of momentum. Nevertheless, time depending effects, like Alfven kinetic waves or other nonlinear modes must be taken into account in order to study the stability of the kinetic model discussed in Chapter 3 and 4.

5.2 Kinetic (PIC) simulations

Important advancement in studying the dynamics of $2D$ and $3D$ plasmoids moving across magnetic field were made by kinetic numerical simulations. These types of investigation take into account the dynamics of individual "macro-particles" or "clouds" that are used to approximate the plasma structure at the microscopic level (*Hockney and Eastwood*, 1981; *Birdsall and Langdon*, 1985).

The kinetic simulations by *Galvez* (1987), *Livesey and Pritchett* (1989) and *Koga et al.*(1989) are among the most successful. Using a two-dimensional geometry, they model correctly the charge separation and their accumulation at the lateral edge of a neutral beam injected normally to an external magnetic field. Indeed, they study the evolution in time of a plasma beam injected across magnetic field lines. These numerical simulation show that the plasma beam moves forward across magnetic field and penetrate over a distance that depend on its initial energy and momentum density. The polarization electric field perpendicular to $\boldsymbol{B}$ is correctly taken into account. It drives continuously charges to the later edges of the intruding plasma element. An example is given in figure **5.1** where the time evolution of the beam is given for three successive moments of time.

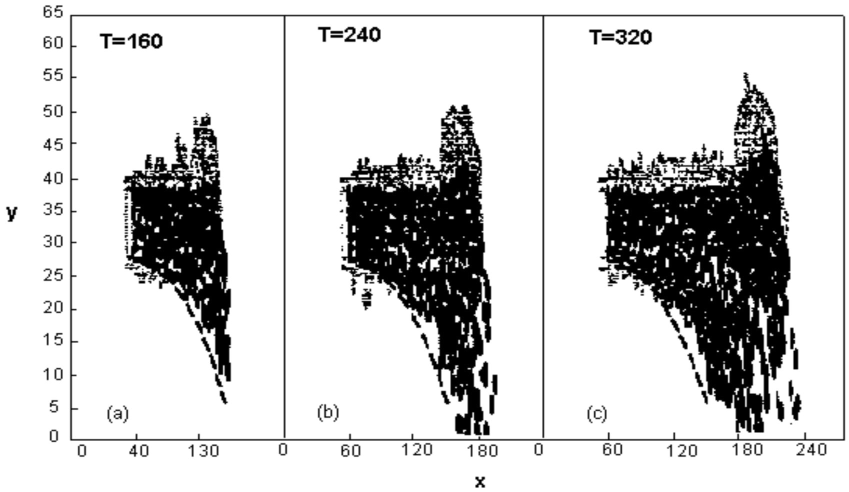

Figure 5.1: Results of two-dimensional PIC simulation for a narrow beam injected normally to the magnetic field (adapted from *Livesey and Pritchett*, 1989).

There are however two basic limitations of these numerical experiments: (**a**) the width of the beam is smaller than the ion Larmor radius, and (**b**) the length of the plasmoid along the magnetic field is infinitely long. Nevertheless the treatment of the electric field is self-consistent. Indeed, in order to take into account the effect of a polarization current which corresponds to the displacement current in Maxwell's equation the PIC modelers are able to solve the Poisson equation from the distribution of charged "macro-particles". But still they do not take into account the mass effects as they consider in general ion and electron mass ratio of the order of 10 or 100.

The kinetic simulations of *Neubert et al.* (1992) show the time evolution of a 3-D rectangular plasma cloud injected in the x-direction with an excess of density and velocity at time $t = 0$, perpendicular to a vertical uniform magnetic field parallel to the Oz axis. The evolution in time of the system shows the formation of space charge layers at the edges of the injected plasmoid. A sample of their results obtained for injection into vacuum is given in figure **5.2**. Similar simulations were performed by *Neubert et al.* (1992) to study the injection of a plasma cloud into an ambient plasma and B-field. They show that in both cases space charge layers are formed at the edges of the intruding plasma cloud. The space charge layers determined by the PIC simulations of *Neubert et al.* (1992) and illustrated in fig. **5.2** may be seen as the "sources" of the E-field distributions used in the numerical integrations presented in Chapter 2 of the Thesis.

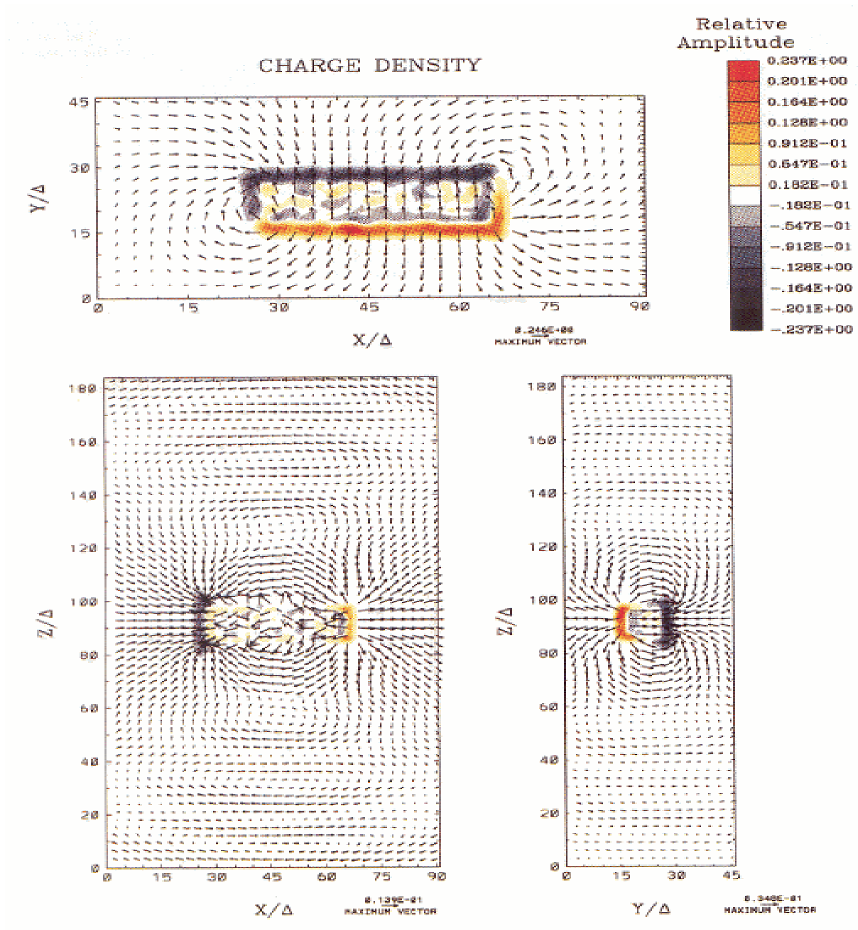

Figure 5.2: Time snapshot from a three-dimensional PIC simulation for a plasma cloud injected with the horizontal velocity, V_0, parallel to OX, normally to the vertical magnetic field, B_0, parallel to OZ (adapted from *Neubert et al.*, 1992). The three panels show the charge density in three planes, XOY, XOZ and YOZ respectively. The density is color coded, blue correspond to negative charge (electrons) and red correspond to positive charge (ions). The space charge layers formed at the edges of the moving plasmoid are seen in all three panels.

In the simulations of *Neubert et al.* (1992) the electron charge layer expands very rapidly along the magnetic field. In the case of injection into ambient plasma it seems that the quasi neutrality was very difficult to achieve by these PIC simulations. Indeed, the code used to solve the equation of motion for each of the particle of the system has to solve at each time step the Poisson equation in each grid point. The proton electron mass ratio used in these studies is $m_p/m_e = 16$. The number of simulated particles per Debye sphere is not specified.

An extension of the work of *Neubert et al.* (1992) was given by *Nishikawa* (1997) who studied the kinetic $3D$ motion of particles at the magnetopause. Nishikawa's simulations consider a 3-D model of the geomagnetic field and the superposition of an external, solar wind, magnetic field. These simulations introduce a rotation (shearing) in time of the orientation of the external B-field. The results show that the shearing of B-field seems to correspond to the penetration of the particles from outside into the magnetosphere. Direct, impulsive entry of the ions is observed in the cusp regions of the dipolar field. The numerical integration of test-particle orbits discussed in Chapter 2 evidenced also the penetration of particles across a sheared B-field distribution.

Very recent results of PIC simulations show interesting/novel results. *Hurtig et al.* (2003) have performed laboratory experiments and 3-D PIC numerical simulations to study the interaction of a moving plasma cloud in a curved magnetic field. It appears that the experimental results of *Hurtig et al.* (2003) support the theoretical results put forward in the chapters **3** and **4** of this thesis. Their laboratory experiment proves, as in the earlier *Schmidt's* (1960) experiment, that the streaming of plasma across a curved magnetic field is sustained by a perpendicular electric field, the Schmidt's convection electric field.

The computer simulations of *Hurtig et al.* (2003) show also the development of a parallel electric field immediately after the plasma moves across $\boldsymbol{B}$. The parallel component of the electric field is found at the edges of the plasma element. The parallel E-field is relatively strong and have antiparallel polarization at the upper and lower edge respectively.

The parallel electric field observed in the laboratory and numerical experiments of *Hurtig et al.* (2003) seems to correspond to the type of parallel E-field described by our kinetic model and presented in chapters **3** and **4**. *Hurtig et al.* (2003) find that, in their own words, "*the simulation reproduce several experimental results concerning the plasma's macroscopic behavior : ...the formation of a potential structure including (in the transition region) magnetic-field-aligned electric fields."* This supports the results presented in Part II of the thesis. Indeed, in Chapter 4 we have explained and assessed quantitatively the physical mechanism that produces a parallel electric field distribution as that reported by *Hurtig et al.*(2003), namely the parallel shear of the plasma bulk velocity and the parallel gradient of the electron density and pressure.

5.3 MHD models and numerical simulations

In a recent study by *Echim and Lemaire*, (2000) the numerical simulations devoted to the impulsive penetration mechanism at the frontier of the magnetosphere have been reviewed with the aim to outline their main approximations and results. All these numerical simulations investigating the interaction of an excess of momentum plasma element with a model magnetopause are based on the MHD approximation where $\boldsymbol{E} \cdot \boldsymbol{B} = 0$, i.e. the presence of a parallel electric field is ignored.

In ideal MHD models constructed to test the impulsive penetration mechanism *Dai and Woodward* (1994, 1995) and *Huba* (1996) took a vanishingly small electric resistivity, $\eta = 0$. The following equation holds true throughout the simulation domain :

$$\boldsymbol{E} + \boldsymbol{V} \times \boldsymbol{B} = 0 \tag{5.1}$$

This implies that $\boldsymbol{E} \cdot \boldsymbol{B} = 0$ and the electric field has no component parallel to $\boldsymbol{B}$. Resistive MHD models (*Ma et al.*, 1991) consider a finite resistivity that enables some kind of ohmic decoupling between plasma motion and B-field. The electric field is approximated in this case by:

$$\boldsymbol{E} + \boldsymbol{V} \times \boldsymbol{B} - \eta \boldsymbol{j} = 0 \tag{5.2}$$

But η is very small in space plasma and therefore the last term in eq. (5.2) is generally ignored. Furthermore in all MHD approximations the displacement current $(\partial \boldsymbol{D}/\partial t)$ is ignored in the incomplete form of the Ampere equation.

In Hall MHD an additional Hall term $\boldsymbol{\nabla} \times (\boldsymbol{j} \times \boldsymbol{B})/n_e e$ (*Huba*, 1995) is added such that the electric field is then approximated by:

$$\boldsymbol{E} + \boldsymbol{V} \times \boldsymbol{B} - (\boldsymbol{j} \times \boldsymbol{B})/n_e e = 0 \tag{5.3}$$

The MHD numerical simulations investigate the time evolution of the interaction of an excess momentum plasma element with adjacent layers of stagnant plasma. In general they suggest that the penetration would be possible only for certain orientation of the magentic field inside the plasmoid and the external magnetic field.

There are however two major limitations of these models. Both are common to all MHD simulations devoted to the investigation of the dynamics of plasmoids in the proximity of the magnetopause. The first limitation is the oversimplified treatment of the electric field : (**a**) equations (5.1) - (5.3) are not valid at the edges of the plasma elements where non-MHD processes, as those outlined in the Chapter 4 of this thesis, produce non-zero components of the electric field in the direction parallel to the magnetic field and (**b**) the displacement current is disregarded in the Ampere equation. Although small in amplitude, the displacement current $\epsilon_0(\partial \boldsymbol{E}/\partial t)$ has a key role in sustaining the formation of space charge layers. It is only recently that *Vasyliunas* (2001) realized that the displacement current carries the charges that sustain an electric field produced by the forward motion of a moving plasma. It is of course the same electric field as that discussed fourty years ago by *Schmidt* (1960).

In addition to the non-MHD processes considered in the past to produce parallel E-field, including the ohmic resistivity taken into account by MHD simulations (*Ma et al.*, 1991), we have shown in chapters **3** and **4** that a parallel shear of the convection velocity does produce a parallel electric field $E_{parallel} \neq 0$. Thus the assumption on which ideal and Hall MHD are based fails to be satisfied.

Chapter 6

Summary and perspectives

There is compelling evidence that in the laboratory plasma as well as in the magnetospheric plasmas an important role is played by the shearing of the plasma bulk velocity. Plasmoids fired by Q-machines and plasma guns, neutral beams simulated numerically, ion or neutral clouds injected from rockets and spacecraft or plasma irregularities plunging from the solar wind onto the exterior layers of the magnetosphere - all have an excess of velocity with respect to the ambient plasma.

The aim of this thesis is to improve our description from a kinetic point of view of the differential motion of plasma density irregularities across non-uniform magnetic field lines, as well as of the generation of a parallel electric field invalidating the ideal MHD approximation due to the shearing of their transverse convection velocity

Part I: In the first part we have analyzed the motion of individual particles, electrons and protons, moving across a sheared magnetic field distribution. We have computed numerically their orbits across a tangential discontinuity (TD) for three different electric field distributions. In the first case we examined the effect of a uniform electric field and showed that the particles are accelerated if the electric field is parallel to the sheared magnetic field lines at least at some portion in the assumed model of the tangential discontinuity. An example of sheared magnetic field penetrated all through by the drifting particles has been also given. The guiding center drift velocity diverges when $B \to 0$ but the equation of motion of the particle can be integrated and is not singular.

The second non-uniform electric field distribution satisfies everywhere the condition that $\boldsymbol{E} \cdot \boldsymbol{B} = 0$ as well as the requirement that the electric drift, $U_E = E/B$, is uniform even when $B \to 0$. In the limiting case of an antiparallel distribution of B-field there is a mathematical singularity where the first order guiding center approximation breaks down where $B \to 0$ and

$E \rightarrow 0$ but there is no singularity in the convection velocity (E/B) nor for the exact equation of motion of the charges particle drifting across the TD layer. The particle can drift across the non-uniform B-field to any depth even for large magnetic shear angles.

The third E-field distribution is a non-uniform electric field perpendicular everywhere to the local magnetic field lines and satisfying the additional requirement that the average magnetic moment of the drifting test particle is adiabatically conserved. In this case we find that the particle cannot always move to any arbitrary depth across the TD. The maximum distance of penetration depends on its initial convection energy. When the initial convection energy ($mv_{gc0}^2/2$) is too small on side 1 (the left hand side of the discontinuity) adiabatic deceleration of the particle can stop its forward motion while drifting toward the side 2 where the value of B is larger. The forward motion is stopped at the penetration depth where all the initial convection energy has been converted into energy of Larmor gyration.

We show that when the magnetic field directions on side 1 and side 2 are antiparallel the plane where $B = 0$ is a singularity for the zero and first order approximations, but not for the exact Newton-Lorentz equation of motion, i.e. no anomalous or reconnection-like acceleration is expected to take place.

We also demonstrate in the first part that it is not just enough to give and draw a distribution of magnetic field lines (as in 2D/3D reconnection models with or without X-lines or neutral points) to determine what will be the motion of plasma particles in this B-field distribution. Indeed, depending on the assumed distribution for the electric field, the charged particle will experience quite different drift motions among which that foreseen in magnetic reconnection models is just one special limiting case.

Without giving also explicitly (and not implicitly as in steady state reconnection models) the spatial distribution of the E-field intensity, a complete and realistic description of the motion of charged particle cannot be inferred in the magnetopause region. In Chapter 2 we have shown that the distribution of the electric field prescribed by the MHD fluid models is by no means unique, other distributions can be imagined and we gave two such examples.

Part II: In the second part we moved a step further by studying "ensembles" of electrons and protons forming a diamagnetic plasma, instead of individual charges as in Part I. The plasma is described by the velocity distribution function (VDF) of each component species. These VDFs are solutions of the Vlasov equation. The electric charge density and electric currents carried by these ensembles of electrons and ions determine the electric field distribution and perturb the magnetic field distribution according to the Maxwell's equations.

In a collisionless plasma any real, positive function of the constants of motion of the particle can be considered a solution of the Vlasov equation. First, we studied the simpler one-dimensional case where the VDF depends only on one spatial coordinate (y) perpendicular to the external magnetic field direction which is assumed to be directed in the Oz direction (see fig. 3.2). Eventually in Chapters 3 and 4 we examine two-dimensional cases where the VDF's are real functions of both y and z coordinates where plasma parameters are non-uniform in the direction *parallel* to the magnetic field (see fig. 3.3).

The two-dimensional problem studied in this second part of our memoire has two constants of motion: the total energy, $\mathcal{H}$ and the canonical momentum p_x. The magnetic moment, μ, is an adiabatic invariant used to determine the domains of the velocity space where the VDFs are defined. The VDF was specified in the plane $z = 0$ as a combination of exponentials and Heaviside step functions of the constants of motion. The velocity distribution function in this plane perpendicular to the magnetic field direction, corresponds to a plasma with a non-zero average bulk velocity, V_x, in the "left hand side" ($y \to -y_\infty$) and a stagnant plasma (having a zero average V_x velocity) in the "right hand side" ($y \to +y_\infty$).

The variation of the VDF with y and z is determined by the distributions of the electric and magnetic potentials, $\Phi(y, z)$, $A_x(y, z)$, which are solutions of Maxwell's equations. The variation of the electric and magnetic potentials with y and z restricts the region of accessibility of the plasma particles. Therefore the phase space is not uniformly populated, some regions are not accessible to all the particles. We have determined the boundaries of the accessibility regions in terms of the constants of motion. These boundaries were taken into account when the moments of the velocity distribution function are computed analytically.

The zero and first order moments of the VDF determine the charge densities and current densities contributed by electrons and ions. They were used to calculate the self-consistent electric and magnetic potentials as solutions of the Maxwell's equation. The electric potential, $\Phi(y, z)$, was found from the plasma quasineutrality condition which is a satisfying approximation of Poisson's equation when the VDFs of the component species do not change significantly over scale lengths of the order of the Debye length. This is indeed a good approximation for all known spatial structures observed in space plasmas. The magnetic vector potential was found by solving the Ampere equation with appropriate boundary conditions.

A test case - the Sestero sheath - has first been introduced into the kinetic and numerical model. We have obtained solutions that indeed reproduce the results obtained already by the one-dimensional kinetic models of the tangential discontinuities. Next we have imposed more general boundary conditions onto the magnetic potential and the asymptotic values of electron and proton temperatures and densities. Thus we have obtained several models of plasma convection across magnetic field, with the average velocity varying in both directions: normal and parallel to the magnetic field.

Our results show that the parallel (i.e. magnetic-field-aligned) gradient of the perpendicular plasma bulk velocity generates a parallel component of the electric field. Depending on the electron kinetic pressure distribution along the magnetic field lines, an additional thermoelectric field can also be generated with a non-zero component parallel to $\boldsymbol{B}$ as in exospheric models of the polar wind and solar wind (*Lemaire and Scherer*, 1970, 1971a, 1971b; *Pierrard and Lemaire*, 1996; *Pierrard*, 1997). It is the first time that the parallel electric field distribution generated by a $2D$ sheared plasma flow has been modeled quantitatively within the framework of kinetic theory of collisionless plasmas. This new mechanism must be added to those already known to produce parallel electric fields in space plasma: i.e. gravity, anisotropy of the pitch angle distribution, gradient of the temperature and kinetic pressure, different evaporation rates of electrons and ions out of planetary ionospheres or stellar coronae.

The role of this parallel electric field component is essential to understand and model the motion of plasma density irregularities across the magnetopause as a result of their excess of momentum density. It was already pointed out by *Lemaire and Roth* (1981) that at the edges of a plasma element having an excess of velocity with respect to the neighboring layers there is a parallel gradient of velocity. Our results give a quantitative assessment of the parallel component of the electric field generated by this parallel velocity shear. The parallel E-field component contributes also to confine the plasma element in a $3D$ shape and decouples its motion from the background medium.

Several future perspectives can be envisaged to improve/develop this work further. An important step would be to identify a third constant of motion to replace the adiabatic invariant, μ, used in our kinetic model. A third constant of motion was proposed in a new kinetic model of the rotational discontinuities (*Roth*, 2003, private communication). It is possible to identify a similar constant of motion in the case of parallel velocity shears.

Another possible future development would be to give the solution of the Vlasov equation in terms of Lorentzian(Kappa) functions instead of the Maxwellian that we used in our model. In the magnetosphere and solar wind the observed VDFs of particles are generally characterized by tails with an excess of suprathermal particles that can be conveniently fitted by kappa functions (*Lemaire*, 2003, private communication). Another possible improvement to our Vlasov solution would be to replace the step functions with other smoother functions that would then describe smoother VDFs in the velocity space.

The results obtained in Chapters 2, 3 and 4 offer very good perspectives for comparisons with experimental data collected by satellites. We envisage that in the near future some of the results described in the thesis will be tested against plasma and field data collected at the magnetopause by the Cluster quartet.

REFERENCES

Bibliography

[1] Abramowitz, M. and Stegun, I.A., **Handbook of mathematical functions**, Dover, New York, 1964

[2] Alfvén, H., "On the motion of a charged particle in a magnetic field", *Ark. Mat. Astr. Fys.*, **27A**, No 22, 1940

[3] Alfvén, H., **Cosmical Electrodynamics**, Oxford, The Clarendon Press, 1953

[4] Alfvén, H., Fälthammar, C.-G., **Cosmical Electrodynamics.Fundamental principles**, Oxford University Press, London, 1963

[5] Axford, W. I. and Hines, C. O., "A unifying theory of high-latitude geophysical phenomena and geomagnetic storms", *Can. J. Phys.*, **39**, 1433, 1961

[6] Baker, D.A. and Hammel, J.E., "Experimental studies of the penetration of a plasma stream into a transverse magnetic field", *Phys. Fluids*, **8**, 713, 1965

[7] Baños Jr., A., "The guiding centre approximation in lowest order", *J. Plasma Physics*, **1**, 305, 1965

[8] Berchem, J. and Russell, C.T., "Magnetic field rotation through the magnetopause: ISEE 1 and 2 observations", *J. Geophys. Res.*, **87**, 8139, 1982

[9] Bernhardt, P.A., Roussel-Dupre, R.A., Pongratz, M.P., Haerendel, G., Valenzuela, A., Gurnett, D.A., Anderson, R.R., "Observations and theory of the AMPTE magnetotail barium releases", *J. Geophys. Res.*, **92**, 5777, 1987

[10] Birdsall, C.K. and A.B. Langdon, **Plasma physics via computer simulation**, McGraw-Hill, 1985

[11] Born, M., **Atomic Physics**, Stechert, Berlin, 1936

[12] Bostick, W. H., "Experimental study of ionized matter projected across a magnetic field", *Phys. Rev.*, **104**, 292, 1956

[13] Buneman O., "Internal dynamics of a plasma propelled across a magnetic field", *IEEE Transactions on Plasma Science*, **20**, 6, 672, 1992

[14] Burlaga, L.F., "Nature and origin of directional discontinuities in the solar wind", *J. Geophys. Res.*, **76**, 4360, 1971

[15] Burlaga, L.F., Lemaire, J. and Turner, J.M., "Interplanetary current sheets at 1AU", *J. Geophys. Res.*, **82**, pp. 3191, 1977

[16] Büchner, J., Zelenyi, L.M., "Regular and chaotic charged particle motion in magnetotaillike field reversals 1. Basic theory of trapped motion", *J. Geophys. Res.*, **94**, 11821, 1989

[17] Celnikier, L.M., Muschietti, L. and Goldman, M.V., "Aspects of Interplanetary plasma turbulence", *Astron. Astrophys.*, **181**, 138, 1987

[18] Chapman, S. Ferraro, V.C.A., "A new theory of magnetic storms. 1. The initial phase", *Terr. Magn. and Atmosph. Electricity*, **36**, 77, 1931

[19] Chen, J., Palmadesso, P.J., "Chaos and nonlinear dynamics of single-particle orbits in a magnetotaillike magnetic field", *J. Geophys. Res.*, **91**, 1499, 1986

[20] Chew, G.F., Goldberger, M.L. and Low, F.E., "The Boltzmann equation and the one-fluid hydromagnetic equations in the absence of particle collisions", *Proc. R. Soc. London*, Ser. A 236, 112, 1956

[21] Chiu, Y.T., Schulz, M., "Self consistent particle and parallel electrostatic field distributions in the Magnetospheric-Ionospheric auroral region", *J. Geophys. Res.*, **83**, 629, 1978

[22] Chiu, Y.T., Cornwall, J.M. "Electrostatic model of a quiet auroral arc", *J. Geophys. Res.*, **85**, 543, 1980

[23] Dai, W. and Woodward P.R., "Two-dimensional simulations for the impulsive penetration of a solar wind filament into the magnetosphere", *J. Geophys. Res.*, **99**, 8577, 1994

[24] Dai, W. and Woodward P.R., "Interactions between a solar wind filament and an open magnetosphere", *J. Geophys. Res.*, **100**, 14843-14852, 1995

[25] De Keyzer, J. and M.Roth, "Equilibrium conditions for the tangential discontinuity magnetopause", *J. Geophys. Res.*, **102**, 9513-9530, 1997a

[26] De Keyzer, J. and M.Roth, Correction to "Equilibrium conditions for the tangential discontinuity magnetopause", *J. Geophys. Res.*, **102**, 19943, 1997b

[27] De Keyzer, J. and M.Roth, "Equilibrium conditions and magnetic field rotation at the tangential discontinuity magnetopause", *J. Geophys. Res.*, **103**, 6653-6662, 1998

[28] Delamere, D.A., Stenbaeck-Nielsen, H.C., Otto, A., "Reduction of momentum transfer rates by parallel electric fields: a two-fluid demonstration", *Phys. Plasmas*, **9**, 3130, 2002

[29] Delcroix, J.L. and Bers, A., **Physique des plasmas**, Savoirs Actuels - InterÉditions/CNRS Éditions, 1994

[30] Demidenko, I. I., Lomino, N. S., Padalka, V. G, Rutkevitch, B.G. and Sinel'nikov K.D., "Motion of a plasmoid in a non-uniform transverse magnetic field", *Soviet Physics-Technical Physics*, **11**, No 10, 1354, 1967

[31] Demidenko, I. I., Lomino, N. S., Padalka, V. G, Rutkevitch, B.G. and Sinel'nikov K.D., "Plasma stream in an inhomogeneous transverse magnetic field", *Soviet Physics-Technical Physics*, **14**, No 1, 16, 1969

[32] Demidenko, I. I., Lomino, N. S. and Padalka, V. G., 'Plasma flow in a strong transversal magnetic field', *Soviet Physics-Technical Physics*, **16**, No 7, 1096, 1972

[33] Dimonte, G., Wiley, L.G., "Dynamics of exploding plasmas in a magnetic field", *Phys. Rev. Lett.*, **67**, 1755, 1991

[34] Dolique, J.-M.,"Pénétration d'un faisceau neutralisé ions-electrons dans une barrière magnetique. Conditions portant sur la hauteur de la barrière", *Compt. Rend. Acad. Sci. Paris*, **256**, 3984, 1963

[35] Dongarra, J. J., Bunch, J. R., Moler C. B., Stewart, G. W., **LINPACK User's Guide**, SIAM Publications, Philadelphia, Pa., 1986
(For more information, see http://www.netlib.org/linpack/index.html.)

[36] Dungey, J. W., 'Interplanetary magnetic field and the auroral zones', *Phys. Rev. Lett.*, **6**,pp. 47, 1961

[37] Eastman, T.E., Hones, E.W., Bame, S.J. and Asbridge, J.R., 'The magnetospheric boundary layer: site of plasma, momentum and energy transfer from the magnetosheath into the magnetosphere', *Geophys. Res. Lett*, **3**, 685, 1976

[38] Echim, M.M., Lemaire, J., "Laboratory and numerical simulations of the impulsive penetration mechanism", *Space Science Reviews*, **92**, 565-601, 2000

[39] Echim, M.M., Lemaire, J. "Positive density gradients at the magnetopause: interpretation in the framework of the impulsive penetration mechanism", *Journal of Atmospheric and Solar-Terrestrial Physics*, **64**, 2019-2028, 2002a

[40] Echim, M.M., "Test-particle trajectories in "sheared" stationary field: Newton-Lorenz and first order drift numerical simulations", *Cosmic Research*, **40**, 534-547, 2002b

[41] Echim, M.M., Lemaire, J., "Advances in the kinetic treatment of the solar wind magnetosphere interaction: the impulsive penetration mechanism", **AGU**'s Geophysical Monograph 133 **Earth's Low Latitude Boundary Layer**, 169-179, ed. P. Newell and T. Onsager, Washington, 2003

[42] Emmons , H.W., Lamd. R.I., "Poiseuille plasma experiment", *Phys. Fluids*, **5**, 1489, 1962

[43] Erisman, D., **Direct Methods for Sparse Matrices**, Oxford, 1986

[44] Farrugia, C.J., Scudder, J.D., Freeman, M.P., Janoo, L., Lu, G., Quinn, J.M., Arnoldy, R.L., Torbert, R.B., Burlaga, L.F., Ogilvie, K.W., Lepping, R.P., Lazarus, A.J., Steinberg, J.T., Gratton, F.T., Rostoker, G., "Geoeffectiveness of three WIND magnetic clouds: a comparative study", *J. Geophys. Res.*, **103**, 17261, 1998

[45] Galvez, M., 'Computer simulation of a plasma streaming across a magnetic field', *Phys. Fluids*, **30**, pp. 2729, 1987

[46] Golub, G.H., Van Loan, C.F., **Matrix Computations**, Johns Hopkins Press, Baltimore, MD, 1989

[47] Haerendel, G., Lüst, R., Rieger, E., "Motion of artificial ion clouds in the upper atmosphere", *Planet. Space Sci.*, **15**, 1, 1967

[48] Haidvogel, D.B., Zang, T.A., “The accurate solution of Poisson's equation by expansion in Chebyshev polynomials”, *Journal of Computational Physics*, **30**, 167, 1979

[49] Heikkila, W. J., ”Impulsive plasma transport through magnetopause”, *Geophys. Res. Lett.*, **9**, 159-162, 1982

[50] Heikkila, W. J., ”Transport of plasma across the magnetopause”, in *Solar Wind-Magnetosphere Coupling*, edited by Y. Kamide and J. A. Slavin, 337, Terra Scientific, Tokyo, 1986

[51] Hockney, R. and J.W. Eastwood, **Computer simulation using particles**, McGraw-Hill, 1981

[52] Holt,E.H. and R.E. Haskell, **Foundations of plasma dynamics**, Macmillan, New York, 1965

[53] Huba, J.D., 'Hall magnetohydrodynamics in space and laboratory plasmas', *Phys. Plasmas*, **Vol. 2**, pp. 2504, 1995

[54] Huba, J.D., ”Impulsive plasmoid penetration of a tangential discontinuity: two-dimensional ideal and Hall magnetohydrodynamics”, *J. Geophys. Res.*, **101**, 24855-24868, 1996

[55] Hultqvist, B., ”On the production of a magnetic-field-aligned electric field by the interaction between the hot magnetospheric plasma and the cold ionosphere”, *Planet. Space Sci.*, **19**, 749, 1971

[56] Hurtig, T., Brenning N. and M.A. Raadu, 'Three-dimensional electrostatic particle-in-cell simulation with open boundaries applied to a plasma beam entering a curved magnetic field', *Physics of Plasmas*, **10**, 4291-4305, 2003

[57] Karimabadi, H., P.L., Pritchett, F.V. Coroniti, ”Particle orbits in two-dimensional equilibrium models for the magnetotail”, *J. Geophys. Res.*, **95**, 17153, 1990

[58] Karlson, E.T., ”Motion of charged particles in an inhomogeneous magnetic field”, *Phys. Fluids*, **5**, 476, 1962

[59] Karlson, E.T., ”Streaming of a plasma through a magnetic dipole field”, *Phys. Fluids*, **6**, 708, 1963

[60] Khazanov, G.V., Liemohn, M.W., Krivorutski.E.N. and T.E. Moore, Generalized kinetic description of a plasma in an arbitrary field-aligned potential energy structure, *J. Geophys. Res.*, **103**, 6871-6889, 1998

[61] Kazeminezhad, F., Dawson, J.M., Bingham, R., "Simulations and qualitative analysis of the AMPTE experiments", *J. Geophys. Res.*, **98**, 9493, 1993

[62] Kiendl, M.T., Semenov, V.S., Kubyshkin, I.V., Biernat, H.K., Rijnbeek, R.P., Besser, B.P., "MHD analysis of Petschek-type reconnection in non-uniform field and flow geometries", Space Sci. Rev., **79**, 709, 1997

[63] Kelley, M.C., Makela, J.J., Paxton, L.J., Kamalabadi, F., Comberiate, J.M., Kil H., "The first coordinated ground- and space-based optical observations of equatorial plasma bubbles", Geophys. Rev. Lett., **30**(14), doi: 10.1029/2003GL017301, 2003

[64] Koga J., Geary J.L., Fujinami T., Newberger B.S., Tajima T. and N. Rostoker, "Numerical investigation of a plasma beam entering transverse magnetic fields", *J. Plasma Physics*, **42**, 91-110, 1989

[65] Kruskal, M., "Asymptotic theory of Hamiltonian and other systems with all solutions nearly periodic", *J. Math. Physics*, **3**, 806, 1962

[66] Landau, L.D., Lifşiţ, E.M., **Mecanica**, (in Romanian) Editura Tehnică, Bucureşti, 1966

[67] Lee, L.C. and Kan, J.R., " A unified kinetic model of the tangential magnetopause structure', *J. Geophys. Res* ., **84**, 6417, 1979

[68] Lee, L. C. and Kan, J.R., "Structure of the magnetopause rotational discontinuity", *J. Geophys. Res.*, **87**, pp. 139-143, 1982

[69] Lehnert, B., **Dynamics of charged particles**, North-Holland Publishing, 1964

[70] Lemaire, J. and Scherer, M., Model of the polar ion-exosphere, *Planet. Space Sci.*, **18**, 103-120, 1970

[71] Lemaire, J., Scherer, M. "Kinetic models of the solar wind", *J. Geophys. Res.*, **76**, 7479, 1971a

[72] Lemaire, J., Scherer, M. "Simple model for an ion-exosphere in an open magnetic field", *Phys. Fluids*, **14**, 1683, 1971b

[73] Lemaire, J. and Scherer, M., "Plasma sheet particle precipitation: a kinetic model", *Planet. Space Sci.*, **21**, 281-289, 1973a

[74] Lemaire, J. and Scherer, M., "Kinetic models of the solar and polar winds", *Rev. Geophysics and Space Physics*, **11**, 2, 427, 1973b

[75] Lemaire, J. and Burlaga, L.F., Diamagnetic boundary layers: a kinetic theory, *Astrophys. Space Sci.*, **45**, 303-325, 1976

[76] Lemaire, J., Impulsive penetration of filamentary plasma elements into the magnetospheres of Earth and Jupiter, *Planet. Space Sci.*, **25**, 887, 1977

[77] Lemaire, J. and Scherer, M., Field aligned distribution of plasma mantle and ionospheric plasmas, *J. Atmos. Terr. Phys.*, **40**, 337-342, 1978

[78] Lemaire, J. and Roth M., Penetration of solar wind plasma elements into the magnetosphere, *J. Atmos. Terr. Phys.*, **40**, 337-342, 1978

[79] Lemaire, J., Roth, M., "Differences between solar wind plasmoids and ideal magnetohydrodynamic filaments" *Planet. Space Sci.*, **29**, 843-849, 1981

[80] Lemaire, J. and Scherer, M., "Field aligned current density versus electric potential characteristics for magnetospheric flux tubes", *Annales Geophysicae*, **1**, 81, 1983

[81] Lemaire, J., "Plasmoid motion across a tangential discontinuity (with application to the magnetopause)", *Journal of Plasma Physics*, **33**, part 3, 425-436, 1985

[82] Lemaire, J., "Plasma distribution models in a rotating magnetic dipole and refilling of plasmaspheric flux tubes", *Phys. Fluids*, **32**, 1519-1527, 1989

[83] Lemaire, J. and Roth M., Non-steady-state Solar Wind Magnetosphere Interaction , *Space Sci. Rev.*, **57**, 59, 1991

[84] Lemaire, J. and V. Pierrard, The kinetic treatment of space plasmas,**Rarefied Gas Dynamics:** 23^{rd} **International Symposium**, edited by A.D. Ketsdever and E.P. Muntz, American Institute of Physics, pp. 857-863, 2003

[85] Lepping, R.P., Burlaga, L.F., Szabo, A., Ogilvie, K.W., Mish, W.H., Vassiliadis, D., Lazarus, A.J., Steinberg, J.T., Faruggia. L.J., Janoo, L., Mariani, F., "The WIND magnetic cloud and events of October 18-20

1995: interplanetary properties and as triggers for geomagnetic activity", *J. Geophys. Res.*, **102**, 14049, 1997

[86] Liemohn, M.W., J. and Khazanov, G.V., Collisionless plasma modeling in an arbitrary potential energy distribution, *Physics of plasmas*, **5**, 580-589, 1998

[87] Livesey, W.A., Pritchett, P.L., "Two dimensional simulations of a charge-neutral plasma beam injected into a transverse magnetic field" *Phys. Fluids B*, **1**, 914, 1989

[88] Longmire, C.L., **Elementary plasma physics**, Interscience Publishers, New York, 1963

[89] Lu, G. **Computer Solution of Large Sparse Positive Definite Systems**, Prentice Hall, 1981.

[90] Lundin, R., Dubinin, E.M., "Solar wind energy transfer regions inside the dayside magnetopause: accelerated heavy ions as tracers for MHD-processes in the dayside boundary layer" *Planet. Space Sci.*, **33**, 891, 1985

[91] Ma, Z.W., Hawkins, J.G. and Lee, L.C.: 1991, "A simulation study of impulsive penetration of solar wind irregularities into the magnetosphere at the dayside magnetopause", *J. Geophys. Res.*, **96**, 15751, 1991

[92] Mahajan, S.M. and R.D. Hazeltine, "Sheared-flow generalization of the Harris Sheet", *Phys. Plasmas*, **7**, 1287-1293, 2000

[93] Mead, G. D. and Beard, D. B., "Shape of the geomagnetic field solar wind boundary", *J. Geophys. Res.*, **69**, 1169, 1964

[94] Morse P.M., Feshbach H., **Methods of Theoretical Physics**, McGraw-Hill, 1953

[95] Neubert T., Miller R.H., Buneman O. and K.I. Nishikawa, 'The dynamics of low-β plasma clouds as simulated by a three dimensional, electromagnetic particle code', *J. Geophys. Res.*, **Vol. 97**, 12057-12072, 1992

[96] Newman, D.L., Goldman, M.V., Ergun, R.E., "Evidence for correlated double layers, bipolar structures, and very-low-frequency saucer generation in the auroral ionosphere", *Physics of Plasmas*, **9**, No. 5, 2337, 2002

[97] Nishikawa, K.-I., "Particle entry into the magnetosphere with a Southward interplanetary magnetic field studied by a three-dimensional electromagnetic particle code", *J. Geophys. Res.*, **102**, 17631, 1997

[98] Northrop, T.G., **The Adiabatic Motion of Charged Particles**, Interscience Publishers, 1963

[99] Ortega, J.M., Rheinboldt, C.W., **Iterative Solution of Nonlinear Equations in Several Variables**, Academic Press, New York, 1970

[100] Pannekoek, A., "Ionization in stellar atmospheres", *Bull. Astron. Inst. Neth.*, **1**, 107, 1922

[101] Papamastorakis, I., Paschmann, G., Sckopke, N., Bame, S.J., and Berchem, J., " The magnetopause as a tangential discontinuity for large field rotation angle", *J. Geophys. Res.*, **89**, 127, 1984

[102] Perkins, F.W., Zabuski, N.J., J.H. Doles III, "Deformation and striation of plasma clouds in the ionosphere, 1", J. Geophys. Res., **78**, 697, 1973

[103] Peter, W. and Rostoker, N., "Theory of plasma injection into a magnetic field", *Phys. Fluids*, **25**, 730, 1982

[104] Petchek, H.E., "Magnetic field annihilation", in *AAS/NASA Symposium on the physics of solar flares*, edited by W.N. Ness, p. 425, NASA, Washington DC, 1964

[105] Phan, T.-D.,Paschmann, G. , "Low-latitude dayside magnetopause and boundary layer for high magnetic shear: 1. Structure and motion", J. Geophys. Res., 101, 7801, 1996a.

[106] Phan, T.-D., Paschmann, G. and Sonnerup, B.U.O., "Low-latitude dayside magnetopause and boundary layer for high magnetic shear: 2. Occurrence of magnetic reconnection", *J. Geophys. Res.*, **101**, 7817, 1996b

[107] Pierrard, V. and Lemaire J., "Lorentzian ion exosphere model", *J. Geophys. Res.*, **Vol. 101**, 7923, 1996

[108] Pierrard, V., "Fonctions de distribution des vitesses des particules s'échappant de l'ionosphère", **Ph. D. Thesis**, Université Catolique de Louvain-la-Neuve, 1997

[109] Press, W.H., Flanerry, B.P., Teukolski, S.A. and Vetterling, W.T., **Numerical recipes in FORTRAN: the art of scientific computing**, 2nd edition, Cambridge, England, 1992

[110] Pudovkin L. and Semenov, V.S., "Magnetic field reconnection theory and the solar wind - magnetosphere interaction: a review", *Space Science Reviews*, **41**, 1, 1985

[111] Raadu, M.A., "The physics of double layers and their role in astrophysics", Physics Reports, **178**, no. 2, 25-97, 1989

[112] Rosseland, S., "Electrical state of a star", *Mont. Not. R. Astron. Soc.*, **84**, 720, 1924

[113] Roth, M., "Structure of tangential discontinuities at the magnetopause: the nose of the magnetopause", *J. Atmospheric Terrest. Phys.*, **40**, 323, 1978

[114] Roth, M., "La structure interne de la magntopause", **Ph.D. thesis**, *Mmoires de la Classe des Sciences*, Acad. Royale de Belgique, Collection 8e, 2me Srie, T XLIV, Fasc. 7, 1984

[115] Roth, M., DeKeyzer, J. and Kuznetsova, M., "Vlasov theory of the equilibrium structure of tangential discontinuities in space plasmas", *Space Sci. Rev.*, **76**, 251, 1996

[116] Sanchez, E.R. and Siscoe, G. L., 'IMP-8 magnetotail boundary crossings: a test of the MHD models for an open magnetosphere', *J. Geophys. Res.*, **95**, 20771-20779, 1990

[117] Schield, M. A., 'Pressure balance between solar wind and magnetosphere', *J. Geophys. Res.*, **74**, 1275, 1969

[118] Schmidt, G, 'Motion of plasma across magnetic field lines', *Phys. Fluids*, **3**, 961, 1960

[119] Sestero, A., "Structure of plasma sheaths", *Phys. Fluids*, **7**, 44, 1964

[120] Sestero, A., "Charge separation effects in the Ferraro-Rosenbluth cold plasma sheath model", *Phys. Fluids*, **8**, 739, 1965

[121] Sestero, A., "Vlasov equation study of plasma motion across magnetic fields", *Phys. Fluids*, **9**, 2006, 1966

[122] Sestero, A., "Self-consistent description of a warm stationary plasma in a uniformly sheared magnetic field", *Phys. Fluids*, **10**, 193, 1967

[123] Sotirelis, T, Meng, C.I., "Magnetopause from pressure balance", *J. Geophys. Res.*, **104**, 6889, 1999

[124] Speiser, T.W., "Particle trajectories in model current sheets 1. Analytical solutions", *J. Geophys. Res.*, **70**, 4219, 1965

[125] Speiser, T.W., "Particle trajectories in model current sheets 2. Applications to auroras using a geomagnetic tail model", *J. Geophys. Res.*, **72**, 3919, 1967

[126] Speiser, T.W., D.J. Williams, H.A. Garcia, "Magnetospherically trapped ions as a source of magnetosheath energetic ions", *J. Geophys. Res.*, **86**, 723, 1981

[127] Sperling, J.L., Glassman, A.J., "Short-circuiting, ion-viscous and ion-inertial effects in striation freezing", *J. Geophys. Res.*, **90**, 8507, 1985

[128] Sperling, J.L., "On the effect of ion viscosity on the motion of two-dimensional plasma clouds", *J. Geophys. Res.*, **91**, 5859, 1986

[129] Störmer, C., "Sur les trajectoires des corpuscules électrisés dans l'espace sous l'action du magnétisme terrestre avec application aux aurores boréales", *Arch. Sci. Phys. Nat.*, 24, 317-364, 1907

[130] Störmer, C.,"Résultats des calculs numériques des trajectoires des corpuscules électriques dans le champ d'un aimant élémentaire", Videnskabs-Selskabets Skrifter (Norske), Videnskabs-Akademi i Oslo Math. Naturv. Klasse, 4, 1, 1913.

[131] Stratton, J. A., **Electromagnetic Theory**, McGraw-Hill, New York, 1941

[132] Vasyliunas, V.M., "Theoretical models of magnetic field line merging", *Rev. Geophys.*, **13**, 303, 1975

[133] Vasyliunas, V.M., "Electric field and plasma flow: what drives what?", *Geophys. Res. Lett.*, **28**, 2177, 2001

[134] Vlasov, A.A., **Many-Particle theory and its application to plasma**, *Gordon and Breach*, New York, 1961

[135] Walbridge, E., "The limiting of magnetospheric convection by dissipation in the ionosphere", *J. Geophys. Res.*, **72**, 5213, 1967

[136] Wessel, F. and Robertson, S., 'Polarization of an intense space-charge-neutral ion beam incident upon a magnetic field', *Phys.Fluids*, **24**, 739, 1981

[137] Wessel, F., Hong, R., Song, J., Fisher, A., Rostoker, N., Ron, A., Li, R., Fan, R.Y., "Plasmoid propagation in a transverse magnetic field and in a magnetized plasma", *Phys.Fluids*, **31**, 3778, 1988

[138] Willis, D.M., "The microstructure of the magnetopause", *Geophys. J.R. Astr. Soc.*, **41**, 355, 1975

[139] Willis, D.M., "The magnetopause: microstructure and interaction with magnetospheric plasma", *J. Atmos. Terr. Phys.*, **40**, 301, 1978

[140] Woch, J. and Lundin, R., "Magnetosheath plasma precipitation in the polar cusp and its control by the interplanetary magnetic field', *J. Geophys. Res.*, **Vol. 97**, 1421, 1992

[141] Wright, A.N., "Transfer of magnetosheath momentum and energy to the ionosphere along open field lines", *J. Geophys. Res.*, **101**, 13169, 1996

[142] Zabuski, N.J., J.H. Doles III and Perkins, F.W. "Deformation and striation of plasma clouds in the ionosphere, 2. Numerical simulation of a nonlinear two-dimensional model", J. Geophys. Res., **78**, 711, 1973

APPENDIX

Scaling factors

The electric potential is scaled with the potential necessary to accelerate an electron to the thermal energy $\mathcal{K}T_e$:

$$\Phi = \lambda_\Phi \Phi^*, \quad \lambda_\Phi = \frac{\mathcal{K}T_e}{e}$$

The magnetic vector potential is scaled with:

$$A_x = \lambda_{A_x} A_x^*, \quad \lambda_{A_x} = \frac{\sqrt{2m_e\mathcal{K}T_{re}}}{e}$$

and the electric current with:

$$\boldsymbol{j} = \lambda_j \boldsymbol{j}^*, \quad \lambda_j = (eN_0)\sqrt{\frac{2\mathcal{K}T_{re}}{m_e}}$$

The velocity is scaled with the electron thermal velocity:

$$V = \lambda_V V^*, \quad \lambda_V = \sqrt{\frac{2\mathcal{K}T_{re}}{m_e}}$$

we have also defined the non-dimensional quantities:

$$\gamma = \frac{m_e}{m_i}, \quad \tau_e = \frac{T_{re}}{T_{e1}}, \quad \tau_{e2} = \frac{T_{re}}{T_{e2}}$$

$$\tau_i = \frac{T_{re}}{T_{i1}}, \quad \tau_{i2} = \frac{T_{re}}{T_{i2}}$$

The spatial coordinate perpendicular and parallel to the magnetic field are both scaled with the electron Larmor radius:

$$y = \lambda_y y^*, \quad \lambda_y = \frac{\sqrt{2m_e\mathcal{K}T_e}}{eB}$$

$$z = \lambda_z z^*, \quad \lambda_z = \frac{\sqrt{2m_e\mathcal{K}T_e}}{eB}$$

Analytical moments of the truncated velocity distribution function

Given the velocity distribution function in terms of the constants of motion $\mathcal{H}$ and p_x and the adiabatic invariant μ :

$$
\begin{aligned}
f_\alpha \; = \; & N_{i1}\left(\frac{m_\alpha}{2\pi\mathcal{K}T_{i1}}\right)^{\frac{3}{2}}\eta\left(b_\alpha\frac{p_x}{\sqrt{m_\alpha\mathcal{K}T_{re}}}\right)\exp\left(-\frac{\mathcal{H}}{\mathcal{K}T_{\alpha 1}}\right) \\
& +N_{i2}\left(\frac{m_\alpha}{2\pi\mathcal{K}T_{\alpha 2}}\right)^{\frac{3}{2}}\eta\left(b_\alpha\frac{p_x}{\sqrt{m_\alpha\mathcal{K}T_{re}}}-\right. \\
& \left. b_\alpha\frac{m_\alpha V_0}{\sqrt{m_\alpha\mathcal{K}T_{re}}}\right)\exp\left(-\frac{\mathcal{H}+\frac{1}{2}m_\alpha V_0^2-p_xV_0}{\mathcal{K}T_{\alpha 2}}\right)
\end{aligned}
$$

where $b_\alpha = sign(q_\alpha)$ we have to compute its moments by integrating in the $(\mathcal{H},\mu,p_x)$ space within the limits of existence of the Jacobian of the transformation from the (v_x,v_y,v_z) to $(\mathcal{H},\mu,p_x)$:

$$
\begin{aligned}
Q_\alpha^{rst}(y,z) \; = \; & 4\int_{-\infty}^{+\infty}\int_{E_{c\alpha}}^{+\infty}\int_{\mu_{c\alpha}}^{+\infty}\left[[v_x(E,\mu,p_x)]^r[v_y(E,\mu,p_x)]^s[v_z(E,\mu,p_x)]^t\times\right. \\
& \left.\times\frac{\sqrt{B}f_\alpha(E,\mu,p_x)}{2m_\alpha^2\sqrt{E-E_{c\alpha}}\sqrt{\mu-\mu_{c\alpha}}}\right]dEd\mu dp_x
\end{aligned}
$$

where

$$
\begin{aligned}
E_{c\alpha} \; &= \; \mu B+\left[p_x-q_\alpha A_x(y,z)\right]V(y,z)+ \\
& \quad +q_\alpha\Phi(y,z)-\frac{m_\alpha V^2(y,z)}{2} \\
\mu_{c\alpha} \; &= \; \frac{m_\alpha}{2B}\left[\frac{p_x-q_\alpha A_x(y,z)}{m_\alpha}-V(y,z)\right]^2
\end{aligned}
$$

The factor 4 in front of the integrals is due to the summation of the integrals when both s and t are even. Whenever one of the two exponents is odd the moment is equal to zero:

$$Q_\alpha^{rst} = 0$$

A detailed discussion on the integration over the 4 quadrants of the (v_y, v_z) subspace mapped into the $(\mathcal{H}, p_x, \mu)$ space, is given in Chapter 3. As we are primarily interested to find a solution of the Maxwell's equations for the electromagnetic field we will compute the zero and first order moments.

Two dimensional density distribution

The numerical density of the species α is computed as:

$$Q_\alpha^{000} = 4\int_{-\infty}^{+\infty}\int_{E_{c\alpha}}^{+\infty}\int_{\mu_{c\alpha}}^{+\infty}\left[\frac{\sqrt{B}f_\alpha(E,\mu,p_x)}{2m_\alpha^2\sqrt{E-E_{c\alpha}}\sqrt{\mu-\mu_{c\alpha}}}\right]dEd\mu dp_x$$

Integration over $\mathcal{H}$ and μ gives:

$$Q_\alpha^{000} = 4I_{p_x}^I + 4I_{p_x}^{II}$$

where

$$I_{p_x}^I = \frac{N_{\alpha1}}{4}\left(\frac{e^{-\frac{m_\alpha V_0^2}{2\mathcal{K}T_{\alpha1}}}e^{-\frac{q_\alpha\Phi}{\mathcal{K}T_{\alpha1}}}}{\sqrt{2\pi\mathcal{K}T_{\alpha1}}}\right)\int_{-\infty}^{0}e^{-\frac{(p_x-q_\alpha A_x)^2}{2m_\alpha\mathcal{K}T_{\alpha1}}}dp_x$$

$$I_{p_x}^{II} = \frac{N_{\alpha2}}{4}\left(\frac{e^{-\frac{m_\alpha V_0^2}{2\mathcal{K}T_{\alpha2}}}e^{-\frac{q_\alpha\Phi}{\mathcal{K}T_{\alpha2}}}}{\sqrt{2\pi\mathcal{K}T_{\alpha2}}}\right)\int_{\frac{m_i V_0}{\sqrt{2m_\alpha\mathcal{K}T_{\alpha2}}}}^{+\infty}e^{\frac{p_x V_0}{\mathcal{K}T_{\alpha2}}}e^{-\frac{(p_x-q_\alpha A_x)^2}{2m_\alpha\mathcal{K}T_{\alpha1}}}$$

In finding $I_{p_x}^I$ and $I_{p_x}^I$ we used the integral:

$$\int_0^{+\infty}\frac{e^{-\frac{t}{\beta}}}{\sqrt{t}}dt = \sqrt{\pi\beta}$$

With the appropriate change of variables and using the integral:

$$\int_0^{+\infty}e^{-p^2x^2+qx}dx = \frac{\sqrt{\pi}}{p}e^{\frac{q^2}{4p^2}} - \frac{\sqrt{\pi}}{2p}e^{\frac{q^2}{4p^2}}erfc\frac{q}{2p}$$

we finally obtain the numerical density of the species α to be equal to:

$$\begin{aligned}Q^{000}(y,z) &= \frac{N_{\alpha1}}{2}e^{-\frac{e\Phi(y,z)}{\mathcal{K}T_{\alpha1}}}erfc\left(\frac{eA_x(y,z)}{\sqrt{2m_\alpha\mathcal{K}T_{\alpha1}}}\right) + \\ &\quad \frac{N_{\alpha2}}{2}e^{-\frac{e\Phi(y,z)}{\mathcal{K}T_{\alpha2}}}e^{\frac{eA_x(y,z)V_0}{\mathcal{K}T_{\alpha2}}}erfc\left(-\frac{eA_x(y,z)}{\sqrt{2m_\alpha\mathcal{K}T_{\alpha2}}}\right)\end{aligned}$$

The charge density of species α is equal to :

$$\rho_\alpha(y,z) = q_\alpha Q^{000}(y,z)$$

where q_α is the charge with algebraic sign.

Two dimensional current distribution

The current density, J_x, is obtained by calculating the first order moment of the VDF:

$$Q_\alpha^{100} = 4\int_{-\infty}^{+\infty}\int_{E_{c\alpha}}^{+\infty}\int_{\mu_{c\alpha}}^{+\infty}\frac{p_x - q_\alpha A_x}{m_\alpha}\left[\frac{\sqrt{B}f_\alpha(E,\mu,p_x)}{2m_\alpha^2\sqrt{E-E_{c\alpha}}\sqrt{\mu-\mu_{c\alpha}}}\right]dEd\mu dp_x$$

Integration over $\mathcal{H}$ and μ gives the same results as in the case of the number density and one can write:

$$Q_\alpha^{100} = 4J_{p_x}^I + 4J_{p_x}^{II}$$

where

$$J_{p_x}^I = \frac{N_{\alpha 1}}{4}\left(\frac{e^{-\frac{m_\alpha V_0^2}{2\mathcal{K}T_{\alpha 1}}}e^{-\frac{q_\alpha\Phi}{\mathcal{K}T_{\alpha 1}}}}{\sqrt{2\pi\mathcal{K}T_{\alpha 1}}}\right)\int_{-\infty}^{0}\left[\left(\frac{p_x - q_\alpha A_x}{m_\alpha}\right)e^{-\frac{(p_x - q_\alpha A_x)^2}{2m_\alpha\mathcal{K}T_{\alpha 1}}}\right]dp_x$$

$$J_{p_x}^{II} = \frac{N_{\alpha 2}}{4}\left(\frac{e^{-\frac{m_\alpha V_0^2}{2\mathcal{K}T_{\alpha 2}}}e^{-\frac{q_\alpha\Phi}{\mathcal{K}T_{\alpha 2}}}}{\sqrt{2\pi\mathcal{K}T_{\alpha 2}}}\right)\int_{\frac{m_i V_0}{\sqrt{2m_\alpha\mathcal{K}T_{\alpha 2}}}}^{+\infty}\left[\left(\frac{p_x - q_\alpha A_x}{m_\alpha}\right)e^{\frac{p_x V_0}{\mathcal{K}T_{\alpha 2}}}e^{-\frac{(p_x - q_\alpha A_x)^2}{2m_\alpha\mathcal{K}T_{\alpha 1}}}\right]dp_x$$

And finally the integration over p_x gives

$$Q_\alpha^{100} = N_{\alpha 2}\sqrt{\frac{\mathcal{K}T_{\alpha 2}}{2\pi m_\alpha}}e^{-\frac{e\Phi(y,z)}{\mathcal{K}T_{\alpha 2}}}e^{\frac{eA_x(y,z)V_0}{\mathcal{K}T_{\alpha 2}}}\left[\sqrt{\frac{\pi m_\alpha}{2\mathcal{K}T_{\alpha 2}}}V_0 erfc\left(-\frac{eA_x(y,z)}{\sqrt{2m_\alpha\mathcal{K}T_{\alpha 2}}}\right) + b_\alpha e^{\frac{(eA_x)^2}{2m_\alpha\mathcal{K}T_{\alpha 2}}}\right] -$$
$$-b_\alpha N_{\alpha 1}\sqrt{\frac{\mathcal{K}T_{\alpha 1}}{2\pi m_\alpha}}e^{-\frac{e\Phi(y,z)}{\mathcal{K}T_{\alpha 1}}}e^{-\frac{(eA_x(y,z))^2}{2m_\alpha\mathcal{K}T_{\alpha 1}}}$$

where $b_\alpha = sign(q_\alpha)$. The partial current of the species α is equal to

$$J_{x\alpha} = q_\alpha Q_\alpha^{100}$$

where q_α is the electric charge with algebraic sign.

The partial currents in the other two directions, $J_{\alpha y}$ and $J_{\alpha z}$, are obtained by computing other two first order moments:

$$Q_\alpha^{010}(y,z) = 4\int_{-\infty}^{+\infty}\int_{E_{c\alpha}}^{+\infty}\int_{\mu_{c\alpha}}^{+\infty}\left[[v_y(E,\mu,p_x)]\frac{\sqrt{B}f_\alpha(E,\mu,p_x)}{2m_\alpha^2\sqrt{E-E_{c\alpha}}\sqrt{\mu-\mu_{c\alpha}}}\right]dEd\mu dp_x$$

$$Q_\alpha^{001}(y,z) = 4\int_{-\infty}^{+\infty}\int_{E_{c\alpha}}^{+\infty}\int_{\mu_{c\alpha}}^{+\infty}\left[[v_z(E,\mu,p_x)]\frac{\sqrt{B}f_\alpha(E,\mu,p_x)}{2m_\alpha^2\sqrt{E-E_{c\alpha}}\sqrt{\mu-\mu_{c\alpha}}}\right]dEd\mu dp_x$$

which are identically equal to zero since the powers of $v_y(E,\mu,p_x)$ in $Q_\alpha^{010}(y,z)$ and of $v_z(E,\mu,p_x)$ in $Q_\alpha^{001}(y,z)$ are odd ($s = 1$ and $t = 1$ respectively) such that:

$$J_{y\alpha} = q_\alpha Q_\alpha^{010}(y,z) = 0$$
$$J_{z\alpha} = q_\alpha Q_\alpha^{001}(y,z) = 0$$

Analytical moments of the nontruncated velocity distribution function

In Chapter 4 the velocity distribution function of ions and electrons were simplified by taking into account the sign of V_0, the parameter entering the general solution given in Chapter 3:

- in case $V_0 > 0$, the VDF of ions satisfying the boundary conditions, can be written:

$$\begin{aligned} f_i(\mathcal{H}, \mu, p_x) &= N_{i1} \left(\frac{m_i}{2\pi \mathcal{K} T_{i1}} \right)^{\frac{3}{2}} e^{-\frac{\mathcal{H}}{\mathcal{K} T_{i1}}} + \\ & N_{i2} \left(\frac{m_i}{2\pi \mathcal{K} T_{i2}} \right)^{\frac{3}{2}} e^{-\frac{\mathcal{H}}{k T_{i2}} + \frac{p_x V_0}{k T_{i2}} - \frac{1}{2} \frac{m_i V_0{}^2}{k T_{i2}}} \end{aligned}$$

  in this case the VDF of electrons is equal to the general solution given in Chapter 3;

- in case $V_0 < 0$, the VDF of electrons satisfying the boundary conditions, can be written

$$\begin{aligned} f_e(\mathcal{H}, \mu, p_x) &= N_{e1} \left(\frac{m_e}{2\pi \mathcal{K} T_{e1}} \right)^{\frac{3}{2}} e^{-\frac{\mathcal{H}}{\mathcal{K} T_{e1}}} + \\ & N_{e2} \left(\frac{m_e}{2\pi \mathcal{K} T_{e2}} \right)^{\frac{3}{2}} e^{-\frac{\mathcal{H}}{k T_{e2}} + \frac{p_x V_0}{k T_{e2}} - \frac{1}{2} \frac{m_e V_0{}^2}{k T_{e2}}} \end{aligned}$$

  in this case the VDF of ions is equal to the general solution given in Chapter 3.

The densities and currents of the two VDFs were given in eqs. (4.16)-(4.17) and (4.20)-(4.21). The corresponding nondimensional values are equal to:

- in case $V_0 > 0$:

$$\begin{aligned} n_i^* &= N_{i1}^* e^{-\tau_i \Phi^*} + N_{i2}^* e^{-\tau_{i2}\Phi^*} e^{2\tau_{i2} V_0^* A_x^*} \\ J_{xi}^* &= N_{i2}^* V_0^* e^{-\tau_{i2}\Phi^*} e^{2\tau_{i2} V_0^* A_x^*} \end{aligned}$$

- in case $V_0 < 0$:

$$\begin{aligned} n_e^* &= N_{e1}^* e^{\tau_e \Phi^*} + N_{e2}^* e^{\tau_{e2}\Phi^*} e^{-2\tau_{e2} V_0^* A_x^*} \\ J_{xe}^* &= -N_{e2}^* V_0^* e^{\tau_{e2}\Phi^*} e^{-2\tau_{e2} V_0^* A_x^*} \end{aligned}$$

Fifth order Runge-Kutta algorithm to integrate ordinary differential equations

The second order differential equation;

$$\frac{d^2y}{dt^2} = f(y, x)$$

can be written as a system of two first-order differential equations:

$$\begin{aligned}
\frac{dy}{dx} &= v(x) \\
\frac{dv}{dx} &= f(v, x)
\end{aligned}$$

The numerical integration of the system of ODE is based on the evaluation of the derivative at the intermediate points between two successive samples, x_i, x_{i+1}. The fifth order Runge-Kutta algorithm gives the following series for successive approximation of the value y_{n+1} in x_{n+1} as a function of the value y_n in x_n:

$$\begin{aligned}
k_1 &= hf(x_n, y_n) \\
k_2 &= hf(x_n + a_2 h, y_n + b_{21} k_1) \\
k_3 &= hf(x_n + a_3 h, y_n + b_{31} k_1 + b_{32} k_2) \\
& \ldots \\
k_6 &= hf(x_n + a_6 h, y_n + b_{61} k_1 + \cdots b_{65} k_5) \\
y_{n+1} &= y_n + c_1 k_1 + c_2 k_2 + c_3 k_3 + c_4 k_4 + c_5 k_5 + c_6 k_6 + \mathcal{O}(h^6)
\end{aligned}$$

where h is the step size. By modifying the step size one modifies the accuracy of the solution. Cash and Karp have found a so called "embedded formula" that gives the value of the function y_{n+1} with a fourth order accuracy in the step h:

$$y^*_{n+1} = y_n + c^*_1 k_1 + c^*_2 k_2 + c^*_3 k_3 + c^*_4 k_4 + c^*_5 k_5 + c^*_6 k_6 + \mathcal{O}(h^5)$$

The difference between y_{n+1} and y^*_{n+1} gives an evaluation of the error of the integration:

$$\Delta = y_{n+1} - y^*_{n+1}$$

and is proportional to h^5. The coefficients b_{ij}, c_i and c^*_i computed by Cash and Carp for the fifth order RK integration algorithm have been taken from *Press et al.* (1991).

The estimate of the error of integration provided by Cash-Carp formula is very useful for adapting the step size such that a desired accuracy, ϵ, to be obtained. In practice the step size is modified and the value of the unknown function, y_n, recomputed until the integration error, Δ, is smaller than the minimum error, ϵ. Adaptive step size Runge-Kutta integration were performed in Chapter 3 to integrate the orbits of test particle injected into sharp varying electromagnetic field distributions.

Gauss-Seidel iterative method to solve sparse matrix linear systems

The discretization by finite differences of the Laplace operator in a two dimensional Poisson problem:

$$\frac{\partial^2 U}{\partial y^2} + \frac{\partial^2 U}{\partial z^2} = u(y, z)$$

generates a linear system whose unknowns are the values of the function on the grid points of the discrete mesh:

$$\begin{pmatrix} a_{11} & a_{12} & \cdots & a_{1(N^2-1)} & a_{1N^2} \\ a_{21} & a_{22} & \cdots & a_{2(N^2-1)} & a_{2N^2} \\ \vdots & & & & \vdots \\ a_{N1} & a_{N2} & \cdots & a_{N(N^2-1)} & a_{NN^2} \\ a_{(N+1)1} & a_{(N+1)2} & \cdots & a_{(N+1)(N^2-1)} & a_{(N+1)N^2} \\ \vdots & & & & \vdots \\ a_{[N(N-1)]1} & a_{[N(N-1)]2} & \cdots & a_{[N(N-1)](N^2-1)} & a_{[N(N-1)]N^2} \\ \vdots & & & & \vdots \\ a_{(N^2-1)1} & a_{(N^2-1)2} & \cdots & a_{(N^2-1)(N^2-1)} & a_{(N^2-1)N^2} \\ a_{N^2 1} & a_{N^2 2} & \cdots & a_{N^2(N^2-1)} & a_{N^2 N^2} \end{pmatrix} \begin{pmatrix} U_{11} \\ U_{12} \\ \vdots \\ U_{1N} \\ U_{21} \\ \vdots \\ U_{N1} \\ \vdots \\ U_{NN-1} \\ U_{NN} \end{pmatrix} = \begin{pmatrix} u_{11} \\ u_{12} \\ \vdots \\ u_{1N} \\ u_{21} \\ \vdots \\ u_{N1} \\ \vdots \\ u_{NN-1} \\ u_{NN} \end{pmatrix}$$

where the discrete values of the 2D unknown function distribution, $U_{j,l} = U(y_j, z_l)$, and of the source terms, $u_{j,l} = u(y_j, z_l)$, were written into one-column matrix. The $N^2 \times N^2$ matrix is the Laplace operator discretized with the 5-point Poisson finite differences method given in eq. (4.3) of Chapter 4.

The linear system can be written in a short form:

$$\mathcal{A}U = u$$

where U and u are one column matrix defined above. In the matrix $\mathcal{A}$ the most part of the elements on each row is equal to zero. Therefore a Gaussian elimination by pivoting may take unnecessary long computer time. The *Gauss-Seidel* method is developed to avoid such lengthy calculation. It implements an iterative method similar to the well known convergence of the array:

$$x_n = \frac{x_{n-1}}{2} + \frac{1}{x_{n-1}}, \qquad n = 1, 2, 3, \cdots$$

The method can be applied if the matrix $\mathcal{A}$ of the linear system is invertible and positive definite. That is precisely the case with the matrix obtained by the discrete transformation of the Laplace operator with the 5-point method given in eq. (4.3). Indeed, one can see that main diagonal elements of matrix $\mathcal{A}$ are equal to 4.

The first step in the Gauss-Seidel iterative method is to split the matrix $\mathcal{A}$ such that one can write:

$$\mathcal{A} = \mathcal{F} - \mathcal{G}$$

where the matrix $\mathcal{F}$ is defined as:

$$\mathcal{F} = \begin{pmatrix} a_{11} & 0 & \cdots & 0 & 0 \\ a_{21} & a_{22} & \cdots & 0 & 0 \\ \vdots & & & & \vdots \\ a_{N^2-11} & a_{N^2-12} & \cdots & a_{N^2-1N^2-1} & 0 \\ a_{N^21} & a_{N^22} & \cdots & a_{N^2N^2-1} & a_{N^2N^2} \end{pmatrix}$$

and the matrix $\mathcal{G}$ is defined as

$$\begin{pmatrix} 0 & 0 & \cdots & -a_{1(N^2-1)} & -a_{1N^2} \\ 0 & 0 & \cdots & -a_{2(N^2-1)} & -a_{2N^2} \\ \vdots & & & & \vdots \\ 0 & 0 & \cdots & -a_{(N^2-1)(N^2-1)} & -a_{(N^2-1)N^2} \\ 0 & 0 & \cdots & 0 & -a_{N^2N^2} \end{pmatrix}$$

One can rewrite the linear system as:

$$\mathcal{F}U = \mathcal{G}U + u$$

that defines the actual iterative scheme. Indeed, taking any initial guess, U_1, one can demonstrate that

$$\mathcal{F}U_n = \mathcal{G}U_{n-1} + u, \qquad n = 2, 3, 4, \cdots$$

the iteration converges to the solution.

In practice the convergence rate of the method is improved by implementing some matrix reordering algorithms based on the sparse nature of the matrix $\mathcal{A}$ (see *Dongarra et al.*, 1986). Indeed, since each component of the new iterate depends upon all previously computed components, the updates cannot be done simultaneously. The new iterate depends upon the order in which the equations are examined. The Gauss-Seidel method is sometimes called the method of successive displacements to indicate the dependence of the iterates on the ordering. If this ordering is changed, the components of the new iterate (and not just their order) will also change.

Bracketing and bisection method to find roots of a nonlinear equation

In Chapter 4 it has been solved the nonlinear equation derived from the quasineutrality condition. Indeed it has been obtained a nonlinear equation for the unknown Φ:

$$n_i(\Phi) - n_e(\Phi) = 0$$

where $n_i(\Phi)$ and $n_e(\Phi)$ are the densities of positive and negative charges. These are nonlinear functions of Φ involving exponentials and $erfc$ functions as shown in equations (3.57)-(3.58).

Since $n_i(\Phi)$ and $n_e(\Phi)$ are continuous functions of Φ one can find the solution of the quasineutrality equation by bracketing and bisection method. The procedure starts by defining a domain, $[-\Phi_m, +\Phi_m]$, within which the unknown Φ takes values. The domain is evenly sampled:

$$\Phi_i = \Phi_{i-1} + \Delta\Phi, \qquad i = 1, 2, \cdots, N$$

where $\Phi_0 = -\Phi_m$ and $\Delta\Phi = (2\Phi_m)/N$. For each value Φ_i one calculates:

$$n_i(\Phi_i) - n_e(\Phi_i) = \mathcal{R}(\Phi_i)$$

Whenever a change of sign of $\mathcal{R}$ occurs:

$$\mathcal{R}(\Phi_i)\mathcal{R}(\Phi_{i+1}) < 0 \qquad (C.1)$$

one has "*bracketed*" the solution of the nonlinear equation. In other words, assuming that $f(\Phi) = n_i(\Phi) - n_e(\Phi)$ is a continuous function of Φ and has no singularities in the interval $[\Phi_i, \Phi_{i+1}]$, one can be sure that at least one solution of $f(\Phi) = 0$ can be found if the condition (C.1) is satisfied.

Once the solution is bracketed several methods can be applied to find the solution with the required accuracy. We have chosen one that surely converge to the solution - the bisection method. When the condition (C.1) is satisfied for the interval $[\Phi_i, \Phi_{i+1}]$, one calculates

$$\mathcal{R}_{1/2} = \mathcal{R}(\Phi_i + (\Phi_{i+1} - \Phi_i)/2)$$

and check on which side of the interval, Φ_i or Φ_{i+1}, the functions $\mathcal{R}(\Phi_i)$ or $\mathcal{R}(\Phi_{i+1})$ have the same sign as $\mathcal{R}_{1/2}$. Thus one can reduce the size of the interval containing the solution to half of the initial interval $[\Phi_i, \Phi_{i+1}]$. The new interval is in turn halved and the same procedure repeated until the solution is determined with the desired accuracy.

If after n iterations the root is in an interval $\delta\Phi_n$ then after the next iteration the root is in an interval $\delta\Phi_{n+1} = \delta\Phi_n/2$. One knows in advance the number of iterations, N, needed to determine the solution with a given accuracy, ϵ:

$$N = log_2 \frac{\Phi_{i+1} - \Phi_i}{\epsilon}$$

List of Figures

1 Schematic illustration of a meridional, $(xOz)_{GSE}$, cross section through the main magnetospheric regions. 2

2 Laboratory experiment of *Baker and Hammel* (1965): a plasma flow injected normal to an external magnetic field into a vacuum chamber having insulating walls. An electrically conducting plate is attached to one of the walls. The stream is slowed down/stopped when it crosses the region where the magnetic field lines are connected to the conducting plate. Note the peculiar, elongated shape of the stream in the wedge of the conducting region resembling the Earth's magnetotail. Note that this tail is not formed by the presence of a non-uniform B-field distribution as in Birkeland Terella experiments or in *Demidenko et al.* (1967, 1969, 1972) ones. 4

3 Schematic illustration of a cross (xOy) section through an impulsive penetrating plasmoid at the dayside magnetopause. Differential drifts (grad-B and polarization) sustain the convection electric field. Space charge layers can exist for time scales less than that associated with the depolarization rate. Adapted from *Echim and Lemaire* (2002a). 7

1.1 Guiding center position, Larmor radius and particle position with respect to the local magnetic field line. Adapted from *Northrop* (1963). 16

1.2 Sheared magnetic field across a tangential discontinuity (from *Roth et al.* 1996) 19

1.3 Superposition of a sheared magnetic field (illustrated by black arrows) of a tangential discontinuity and a uniform electric field (blue arrows). 20

1.4 Superposition of a sheared magnetic field of a tangential discontinuity and a non-uniform electric field. $\boldsymbol{B}$ (solid black arrows) rotates and increase from "left" to "right" side of the discontinuity; when $\boldsymbol{B}$ rotates about the Ox-axis the vector $\boldsymbol{E}$ (solid blue arrows) rotates also and satisfies everywhere the condition $\boldsymbol{E}\cdot\boldsymbol{B} = 0$ and $\left|\frac{\boldsymbol{E}\times\boldsymbol{B}}{B^2}\right| = U_{E1}$; the convection velocity (red arrows) is everywhere parallel to the Ox direction. 21

1.5 Electric field (solid blue arrows) conserving the average magnetic moment of ions traversing the sheared TD magnetic field. It illustrates the situation when the particle is stopped at point (A) where its initial convection energy has been completely transformed into gyromotion perpendicular to the magnetic field $\boldsymbol{B}$. 22

2.1 *case* A'; panels show: $\boldsymbol{a}$) the B-field distribution; $\boldsymbol{b}$) the E-field distribution; $\boldsymbol{c}$) the xOy projection of trajectories: particle, guiding center (y_{gc}), and averaged gc ($< y_{gc} >$); $\boldsymbol{d}$) gives the xOz projections; panel $\boldsymbol{e}$) shows the velocities of the particle (v_x) and gc ($v_{gc,x}$); panel $\boldsymbol{f}$) shows the changes of B_y and B_z (solid thick line) and of E_y and E_z (dashed thick line) as "seen" by the drifting particle while it moves across the TD. 28

2.2 *Case A:* same panel distribution as in figure **2.1** but for a higher shear-angle α. The advancement in the Ox direction stops at $x \approx 500\ km$ where the magnetic field is parallel to the uniform E-field and $\boldsymbol{E} \times \boldsymbol{B}/B^2 = 0$; the particle is then accelerated in the parallel direction. 30

2.3 *Case A:* same panel distribution as in figure **2.1** but with $B_y \neq 0$ and a large magnetic shear angle, α. Different colors correspond to different initial energies of the three pairs ion-electron. Each electron is initialized with the same energy as the corresponding ion. 31

2.4 *Case A:* same panel distribution as in figure **2.1** but for a small magnetic shear angle α. 32

2.5 *Case* B': the first two panels show $\boldsymbol{a}$) Magnetic field distribution; $\boldsymbol{b}$) Electric field distribution; panel $\boldsymbol{c}$) gives the xOy projection of trajectories: particle (y), guiding center (y_{gc}), and averaged gc ($< y_{gc} >$); panel $\boldsymbol{d}$) gives xOz projections; in panel $\boldsymbol{e}$) is given the phase space plot for particle and gc; panel $\boldsymbol{f}$) shows the B and E fields as "seen" by the drifting particle. 36

2.6 *Case B* - large magnetic shear angle , $\alpha \approx 95^0$. The distribution of the graphs in the six panels is the same as in figure **2.5**. The initial energy of the test-proton is equal to 15 eV . . . 37

2.7 *Case B* - small magnetic shear angle ($\alpha \leq 6^0$); the distribution of the plots in the six panels is the same as that of figure **2.6** . 38

2.8 *Case B* - moderate magnetic shear angle and *adiabatic* motion of a 15 eV proton; the distribution of graphs in the six panels is the same as in figure **2.6** 39

2.9 *Case B*: orbits of three protons and three electron. The panels shows the same graphs as in fig. **2.5**; *gc* path is not shown. Each pair ion-electron is injected in the same point with the same initial "thermal" energy, $\mathcal{K}T_{e0} = \mathcal{K}T_{i0}$. The initial velocity of the guiding center of all particles: $v_{gc} = U_E = 100$ km/s. 40

2.10 *Case B*: orbits of three protons and three electrons of different energies. In this case each pair electron-ion is injected with the same "thermal" velocity, $v_{p0} = v_{e0}$. The initial velocity of the guiding center for the six particles is equal to $v_{gc} = U_E = 100$ km/s. 41

2.11 *Case C'* - non-penetrating proton trajectory : panel ***a***) gives the B-field distribution; panel ***b***) gives the E-field distribution; panel ***c***) shows the xOy projection of particle, guiding center, and averaged gc trajectories; panel ***d***) shows the xOz projections; panel ***e***) gives the (x, v_x) phase space plot for particle and guiding center; panel ***f***) shows the B and E fields as "seen" by the drifting proton of 430 eV. 46

2.12 *case C'* - penetrating proton trajectory; the distribution of the plots in the six panels is similar to figure **2.11** 47

2.13 *case C* - penetrating proton trajectory injected into a B-field distribution having a large angle of shear; the six panels show the plots of the same variables as figure **2.11** 48

2.14 *case C* - three penetrating protons and electrons across a *sheared* B-field distribution; the six panels give the distribution of the same variables as in figure **2.11** 49

3.1 Field and flow distribution with parallel shear ($\partial V_x/\partial z \neq 0$) illustrated in the case when the plasma magnetic perturbation is very small with respect to the external magnetic field ($B_y \ll B_0$). Dotted lines illustrate the magnetic field distribution, solid arrows illustrate the plasma bulk velocity profile that has a maximum in the plane $z = 0$. 59

3.2 Flow configuration of the Sestero Tangential Discontinuity. Plasma flows in the positive x-direction, out of the page. Plasma bulk velocity is represented by circles whose diameter is proportional to $V(y)$. The bulk velocity has a maximum at the left hand side ($y \to -y_\infty$) and decreases with increasing y, taking zero value at the right side ($y \to +y_\infty$). Dotted lines illustrate the B-field distribution. The TD is centered in $y = 0$. 62
3.3 $2D$ plasma flow across B-field - plasma bulk velocity is everywhere parallel to the positive x-direction, out of the page; it is illustrated by circles having the diameter proportional to $V(y,z)$. Dotted lines illustrate the distribution of the external magnetic field. Plasma internal perturbation of $\boldsymbol{B}$ is not shown but it is self-consistent computed. 64
3.4 Illustration of the integration subspace at $z = 0$; the particles whose velocity components are contained within the *intersection* of the interiorof the two parabolic surfaces reach the point (x, y, z). The two surfaces are solutions of (3.49)-(3.50) for arbitrary values of potentials. 75
3.5 Intersections of the parabolic surfaces plotted in figure **3.4** with the $v_{x_0}Ov_{y_0}$ and $v_{x_0}Ov_{z_0}$ planes at level $z = 0$. The hatched regions are the domain of integration to calculate the number of particles originating from the plane $z = 0$ that can reach the point (x, y, z). 76
3.6 Illustration of a possible shape of the integration region defined by (3.51); arbitrary units and potentials. 78
3.7 Illustration of a possible shape of the integration region defined by (3.51) at level $z = 0$: intersection with $H = 0$, arbitrary units and potentials. 78

4.1 SETD - distribution of the magnetic vector potential and total magnetic field given by eq. (4.14). 93
4.2 SETD - Electric field potential given by the quasineutrality equation (4.10) and the perpendicular component of $\boldsymbol{B}$. 93
4.3 SETD - 2D profile of the plasma bulk velocity. 94
4.4 SETD - Total density and net charge. 94
4.5 SPTD - magnetic vector potential and total magnetic field given by (4.14) with boundary conditions specified in table 4.1. 97
4.6 SPTD - Electric field potential given by the quasineutrality equation (4.10) and the perpendicular component of $\boldsymbol{B}$. 97
4.7 SPTD - 2D profile of the plasma bulk velocity. 98
4.8 SPTD - total density and total net charge. 98

4.9 model PSEL1 - $2D$ distribution of the magnetic vector potential component, A_x. A small perturbation was introduced in the boundary condition for the left border $y = Y_1$. 105
4.10 model PSEL1 - Total magnetic field given by the magnetic vector potential shown in figure **4.9** 106
4.11 model PSEL1 - Solution of the quasineutrality for a $2D$ sheared plasma flow. 106
4.12 model PSEL1 - Non-uniform distribution of the plasma average velocity; Oz is the direction of the main magnetic field. . . 107
4.13 model PSEL1 - Illustration of the magnetic field distribution: arrows are plotted according to the local amplitude and inclination of the magnetic field. Contours of equal amplitude of the $2D$ velocity field were over plotted. 107
4.14 model PSEL1 - Distribution in the yOz plane of the parallel shear of the plasma bulk velocity. 108
4.15 model PSEL1 - $2D$ distribution of the perpendicular component of the electric field (left panel) and of the parallel component (right panel). 108
4.16 model PSEL1 - Isocontours of $E_{parallel}$(in blue); B-field is shown by black arrows. 109
4.17 model PSEL1 - Gradient in the direction parallel to $\boldsymbol{B}$ of the density. 109
4.18 model PSEL1 - Electric potential (Φ), electric current (J_x), parallel E-field ($E_{parallel}$) and plasma bulk velocity (V_x) at 4 different y locations. 110
4.19 model PSEL1 - Gradient in the direction parallel to the magnetic field of the density (left panel) and bulk velocity (right panel) respectively. 110
4.20 model PSEL1 - Ion density and electric current for the $2D$ sheared plasma flow. 111
4.21 model PSEL2 - Electric potential (Φ), electric current (J_x), parallel E-field ($E_{parallel}$) and plasma bulk velocity (V_x) at 4 different y locations. 113
4.22 model PSEL2 - Plasma bulk velocity (left) and density (right). 114
4.23 model PSEL2 - Parallel (left) and perpendicular (right) components of the electric field. 114
4.24 model PSEL2 - Parallel gradient of density (left) and bulk velocity (right). 115
4.25 model PSEL3 - Plasma bulk velocity (left) and density (right). 116

4.26 model PSEL3 - Electric potential (Φ), electric current (J_x), parallel E-field ($E_{parallel}$) and plasma bulk velocity (V_x) at 4 different y locations. 117
4.27 model PSEL3 - Parallel gradient of density (left) and bulk velocity (right). 117
4.28 model PSEL3 - Parallel (left panel) and perpendicular (right panel) components of the electric field. 118
4.29 model PSPL1 - $2D$ distribution of the magnetic vector potential. 120
4.30 model PSPL1 - Total magnetic field. 120
4.31 model PSPL1 - Distribution of the electric potential. 121
4.32 model PSPL1 - Distribution of the plasma average velocity. . . 121
4.33 model PSPL1 - $2D$ distribution of the perpendicular component of the electric field (left panel) and of the parallel component (right panel). 122
4.34 model PSPL1 - $2D$ distribution of the parallel gradient of the density (left panel) and of the V_x component of the plasma bulk velocity (right panel). 122
4.35 model PSPL1 - Electric potential (Φ), electric current (J_x), parallel E-field ($E_{parallel}$) and plasma bulk velocity (V_x) at 4 different y locations. 123
4.36 model PSPL1 - Gradient in the direction parallel to the magnetic field of the density (left panel) and bulk velocity (right panel) respectively. 123
4.37 model PSPL1 - Ion density and electric current for the $2D$ sheared plasma flow of case $PB1$. 124
4.38 model PSPL2 - Plasma bulk velocity (left) and density (right). 125
4.39 model PSPL2 - $2D$ distribution of the parallel gradient of the density (left panel) and of the V_x component of the plasma bulk velocity (right panel). 126
4.40 model PSPL2 - $2D$ distribution of the perpendicular component of the electric field (left panel) and of the parallel component (right panel). 126
4.41 model PSPL2 - Electric potential (Φ), electric current (J_x), parallel E-field ($E_{parallel}$) and plasma bulk velocity (V_x) at 4 different y locations. 127
4.42 model PSPL2 - Gradient in the direction parallel to the magnetic field of the density (left panel) and bulk velocity (right panel) respectively. 127
4.43 model PSPL3 - Plasma bulk velocity (left) and density (right). 129

4.44 model PSPL3 - $2D$ distribution of the parallel gradient of the density (left panel) and of the V_x component of the plasma bulk velocity (right panel). 130
4.45 model PSPL3 - $2D$ distribution of the perpendicular component of the electric field (left panel) and of the parallel component (right panel). 130
4.46 model PSPL3 - Electric potential (Φ), electric current (J_x), parallel E-field ($E_{parallel}$) and plasma bulk velocity (V_x) at 4 different y locations. 131
4.47 model PSPL3 - Gradient in the direction parallel to the magnetic field of the density (left panel) and bulk velocity (right panel) respectively. 131
4.48 model PSEL1 - Convection velocity and decoupling velocity of plasma in case of an electron dominated sheath. 134
4.49 model PSEL1 - Decoupling velocity and parallel electric field vs. y coordinate at 4 different altitudes (model $EB1$). 135
4.50 model PSPL3 - Convection velocity and decoupling velocity of plasma in the case of an proton dominated profile. 135
4.51 model PSPL3 - Decoupling velocity and parallel electric field vs. y coordinate at 4 different altitudes (model $PB3$). 136
4.52 model PSPL2 - Convection velocity and decoupling velocity of plasma in the case of an proton dominated profile. 136
4.53 model PSPL2 - Decoupling velocity and parallel electric field vs. y coordinate at 4 different altitudes (model $PB3$). 137

5.1 Results of two-dimensional PIC simulation for a narrow beam injected normally to the magnetic field (adapted from *Livesey and Pritchett*, 1989). 143
5.2 Time snapshot from a three-dimensional PIC simulation for a plasma cloud injected with the horizontal velocity, V_0, parallel to OX, normally to the vertical magnetic field, B_0, parallel to OZ (adapted from *Neubert et al.*, 1992). The three panels show the charge density in three planes, XOY, XOZ and YOZ respectively. The density is color coded, blue correspond to negative charge (electrons) and red correspond to positive charge (ions). The space charge layers formed at the edges of the moving plasmoid are seen in all three panels. 144

List of Tables

2.1 Initial conditions for the integration of test-particle orbits . . . 26

3.1 Two-dimensional boundary/asymptotic values of the electromagnetic potentials and fields and of the plasma bulk velocity characterizing a Sestero-type tangential discontinuity 63
3.2 Robin-type boundary conditions used in the Sestero TD model to solve the Ampere equation (3.14) in the $2-D$ domain $[-y_\infty, +y_\infty] \times [-z_\infty, +z_\infty]$ 63
3.3 Two-dimensional boundary/asymptotic values of the electromagnetic potentials and fields and of the plasma bulk velocity characterizing a $2D$ sheared plasma flow. 65
3.4 Dirichlet-type boundary conditions used in the 2D sheared model to solve the Ampere equation (3.14) in the $2D$ domain $[-y_\infty, +y_\infty] \times [-z_\infty, +z_\infty]$ 65

4.1 Robin-type boundary conditions used in the Sestero TD model to solve the non-dimensional Ampere equation (3.14) in the $2D$ domain $[-y^*_\infty, +y^*_\infty] \times [-z^*_\infty, +z^*_\infty]$ 90
4.2 Boundary/asymptotic values of the plasma density and temperature used as input parameters to solve the Vlasov-Ampère-quasineutrality equations 100
4.3 Dirichlet-type boundary conditions used in the $2D$ sheared models to solve the non-dimensional Ampere equation (3.14) in the $2D$ domain $[-y^*_\infty, +y^*_\infty] \times [-z^*_\infty, +z^*_\infty]$ 101
4.4 Summary of the results obtained in Chapter 4 139